Report No.: TBD

AISI/DOE Technology Roadmap Program

Final Report

FORMABILITY CHARACTERIZATION OF A NEW GENERATION OF HIGH STRENGTH STEELS

By

Sriram Sadagopan, Principal Investigator
Dennis Urban, Program Manager

May 2003

Work Performed under Cooperative Agreement
No. DE-FC07-97ID13554

Prepared for
U.S. Department of Energy

Prepared by
American Iron and Steel Institute
Technology Roadmap Program Office

Pittsburgh, PA 15222

DISCLAIMER

“Any opinions, findings, and conclusions or recommendations expressed in this material are those of the author(s) and do not necessarily reflect the views of the US Department of Energy.”

Number of pages in this report: 171

For availability of this report, contact:
Office of Scientific and Technical Information
P.O. Box 62
Oak Ridge, TN 37831
(615) 576-8401.

TABLE OF CONTENTS

Contents **Page**

Table of Contents iii

List of Figures iv

List of Tables ix

Executive Summary xi

Acknowledgements xv

1. Introduction 1
2. Basic Mechanical Characterization 4
3. Medium Strain Rate Mechanical Behavior 15
4. Bauschinger Effect 34
5. Forming Limit Curves 47
6. Sheared Edge Stretching Limits 52
7. Bending Under Tension Limits 62
8. Springback and Curl 76
9. Stretch Formability 90
10. Stretch Drawability 103

References 123

Appendices

Appendix A: Data for Bending Under Tension Limits 126
Appendix B: Springback and Curl Data for the Channel Draw Test 130
Appendix C: Normalized Ratios for Channel Draw Test 138
Appendix D: The Scree Plot Analysis 139
Appendix E: Springback and Curl Analysis for Two Steel Groups 146
Appendix F: Data for Square Draw Test 151

LIST OF FIGURES

Figures **Page**

Section 2

2.1 Relationship between total elongation and ultimate tensile strength for the steel grades in the AISI/DOE formability project 5
2.2 Dependence of the n-bar value (6%-12%) on the ultimate tensile strength 6
2.3 Dependence of the r-bar value on the ultimate tensile strength 6
2.4 Instantaneous n-value vs. true strain for the baseline steel grades 11
2.5 Instantaneous n-value vs. true strain for the skin panel steel grades of nominal thickness 0.65mm 11
2.6 Instantaneous n-value vs. true strain for the skin panel steel grades of nominal thickness 0.95mm 12
2.7 Instantaneous n-value vs. true strain for some conventional high strength steels used for structural applications 12
2.8 Instantaneous n-value vs. true strain for DP600 and TRIP600 steel grades 13
2.9 Instantaneous n-value vs. true strain for the DP800 steel grades 13
2.10 Instantaneous n-value vs. true strain for the DP980 steel grades 14

Section 3

3.1 Engineering stress-strain curves for DQSK (Lot X1) 16
3.2 True stress-strain curves for DQSK (Lot X1) 17
3.3a Ultimate tensile strength vs. strain rate for six DP600 lots 25
3.3b Yield strength vs. strain rate for six DP600 lots 25
3.3c Uniform elongation vs. strain rate for six DP600 lots 26
3.3d Full curve n-value vs. strain rate for six DP600 lots 26
3.4 Yield strength vs. strain rate by steel grade 27
3.5 Tensile strength vs. strain rate by steel grade 27
3.6 Increase of ultimate tensile strength vs. quasi-static ultimate tensile strength, showing around 16 MPa increase for all steels except M190 28
3.7 Stress ratio of $UTS_{10}/UTS_{0.001}$ decreases with increasing steel strength 28
3.8a Uniform elongation vs. strain rate for steels of YS less than 300 MPa 29
3.8b Uniform elongation vs. strain rate for steels of YS equal and higher than 300 MPa 30
3.9a n-value vs. strain rate for steels of YS less than 300 MPa 30
3.9b n-value vs. strain rate for steels of YS equal and higher than 300 MPa 31

Section 4

4.1 Illustration of values used to calculate the Bauschinger Effect Factor: X1 (DQSK) 2% Pre-Strain 35
4.2 Bauschinger Effect Factor vs. True Plastic Strain for steel of different strength and microstructures 41
4.3 Bauschinger Effect Factor at 5% Nominal Prestrain vs. Yield Strength 41
4.4 Examples for curve fitting 43
4.5 Plot of Bauschinger power law fit constants for all steel grades 43
4.6 Comparison of forward flow and reverse yield stress for DP 600 & TRIP 600 46

Section 5

5.1 FLC displayed in terms of true strain for the 1.4mm CR TRIP600 steel lot (1T) 48
5.2 FLC displayed in terms of true strain for the 1.8mm GA RA830 steel lot (1W) 48
5.3 FLC displayed in terms of true strain for the 1.15mm DP980 steel lot (1S) 49
5.4 Comparison between the experimental FLC and standard FLC for the 1.4mm CR TRIP600 (1T) lot 50
5.5 Comparison between the experimental FLC and standard FLC for the 1.8mm GA RA830 (4W) lot 50
5.6 Comparison between the experimental FLC and standard FLC for the 1.15mm CR DP980 (1S) lot 51

Section 6

6.1 Photograph of the Hille-Wallace hydraulic press used for conducting the sheared edge stretching tests 54
6.2 Geometries of the hole expansion and hole extrusion test specimens 55
6.3 Correlation between the hole expansion and hole extrusion tests 55
6.4 Dependence of the sheared edge stretching limits on the ultimate tensile strength 57
6.5 Dependence of the sheared edge stretching limits on the r-bar value 58
6.6 Standard FLCs for 1K and 2K (BH300) and their strain paths for uniaxial tension 59
6.7 Schematic of a stretch flanging operation for an annular sample 59
6.8 Trend for characteristic flange parameter as a function of tensile strength 60

Section 7

7.1a Schematic of tooling for the ASB test. All dimensions in mm 63
7.1b ASB tooling as mounted in the press 63
7.2 Photograph of ASB test samples 64
7.3 Drawbead configurations used for sample lockout. The sample on top uses an equal clearance on either side of the male drawbead. The sample on the bottom uses an unequal clearance to prevent flow of the material through the drawbead 64
7.4 Formability of skin panel steels as a function of R/t ratio 65
7.5 Formability of structural steels as a function of R/t ratio 66
7.6 Observed failure locations for the smallest and largest R/t ratio samples 66
7.7 Dependence of the failure height for an R/t ratio of 5 as a function of the ultimate tensile strength of the steel grade 67
7.8 Location and orientation of strain axes on the ASB samples 68
7.9 Strain distribution in the unsupported sidewall region for 0.93mm BH210 for the R/t ratios experiencing punch failure 69
7.10 True strains for 0.93mm BH210 for the R/t ratios experiencing punch failure 70
7.11 Stretch bendability index as a function of R/t ratio for some skin panel steels 71
7.12 Stretch bendability index as a function of R/t ratio for some structural steels 71
7.13 Stretch bendability behavior of DP steels 72
7.14 Stretch bendability behavior as a function of tensile strength for three R/t ratios 73
7.15 Trend for critical R/t as a function of the tensile strength 73

Section 8

8.1 The tooling used for the channel draw test 77

8.2 Schematic drawing of the channel draw tooling 77
8.3 The drawbead fixture test 78
8.4 Measurement of a formed sample 80
8.5 Measurement of sidewall opening at a point 50.8mm (2.0”) above the punch face 80
8.6 The measurement system for measuring springback angle & sidewall curl 81
8.7 Schematic drawing of sidewall curl due to measurement uncertainty 82
8.8 The effect of tooling radii on springback 84
8.9 The effect of tool gap on springback 84
8.10 The effect of drawbead restraining force on springback 85
8.11 The effect of tooling radii on sidewall curl 85
8.12 The effect of tool gap on sidewall curl 86
8.13 The effect of drawbead restraining force on sidewall curl 86
8.14 Effect of tooling radii on springback of 0.70mm steels 88
8.15 Effect of tooling radii on springback of 1.20mm steels 88

Section 9

9.1 Geometry of the stretch form specimen. All dimensions in mm. 91
9.2 Stretch form/failure specimen 91
9.3 Biaxial stretch as a function of the forming height for 0.77mm DQSK, 1.19mm DQSK and 0.66mm DP500 92
9.4 Stretch form/failure test: Measurements of surface stretch using 100mm circles 94
9.5 Comparison of predicted and actual failure heights for the stretch form test 95
9.6 Correlation of the failure height as determined in the stretch form test to the n-bar value 96
9.7 Raw data for stretch form/dent test 98
9.8 Effect of thickness on the intercept of the load vs. dent depth trend line 100
9.9 Effect of as-received yield strength of the steel grade on the slope of the load vs. dent depth trend line 100
9.10 Failure height in the stretch form test for the EG steel lots of nominal thickness 0.65mm 102
9.11 Failure height in the stretch form test for the GA steel lots of nominal thickness 0.65mm 102

Section 10

10.1 Schematic of the Square Draw tooling showing the critical dimensions 104
10.2 Square Draw tooling as installed in the servohydraulic press 105
10.3 Set up to ensure alignment of the samples in the Square Draw die-set 105
10.4 Typical load-displacement curve for a sample experiencing significant draw-in from the flange. 106
10.5 Effect of binder force on formability of the material. The numbers are the binder forces for forming the samples. 107
10.6 Photograph of a formed and gridded sample for measurement of strains 108
10.7 Failure height vs. (UE*$\overline{R}$) for the largest blank size for all three thickness ranges 109
10.8 Effect of coating on the forming height for a few lots of steel of nominal thickness 0.95mm 110
10.9 Effect of coating on the forming height for the DP600 steels of nominal thickness 1.2mm 111
10.10 Binder Span of Control for steel grades of nominal thickness 0.65mm 113
10.11 Binder Span of Control for steel grades of nominal thickness 0.95mm 114

10.12 Binder Span of Control for some structural steels of nominal thickness 1.2mm 114
10.13 Effect of cup height, lubricant type and blank size on the binder span of control for 1.19mm CR DP600 (2P). 115
10.14 Major, minor and thickness strain distribution for lots 0.7 EG BH210 (B1), 0.66mm EG DP500 (G1) and 0.7mm DDQ+ (Y1) along the diagonal of the square cup. 116
10.15 Major, minor and thickness strain distributions for lots 0.74mm ULC BH340 (D1), 0.63mm IF-Rephos (E1) and 0.7mm DDQ+ (Y1) along the diagonal of the square cup. 117
10.16 Major, minor and thickness strain distributions for 0.77mm CR DQSK (X1), 0.93mm EG BH210 (B2), 1.02mm GA ULC BH340 (D2) along the diagonal of the square cup. 117
10.17 Major, minor and thickness strain distributions for 1mm EG BH280 (C2) and 1.04mm GA BH280 (C3) along the diagonal of the square cup. 118
10.18 Major, minor and thickness strain distributions for 0.8mm EG DP500 (G2) and 0.89mm GA IF-Rephos (E2) along the diagonal of the square cup. 118
10.19 Major, minor and thickness strain distributions for 1.24mm GA BH300 (1K), 1.19mm GI BH300 (2K) and 1.19mm CR DQSK (X2) along the diagonal of the square cup. 119
10.20 Major, minor and thickness strain distributions for 1.16mm GI HSLA350 (1L), 1.21mm CR HSLA350 (5L) and 1.24mm HS440W(1M) along the diagonal of the square cup. 119
10.21 Major, minor and thickness strain distributions for 0.96mm GI DP600 (1P), 1.19mm CR DP600 (2P) and 1.39mm GI DP600 (3P) along the diagonal of the square cup. 120
10.22 Major, minor and thickness strain distributions for 1.23mm GI DP600 (4P), 1.4mm CR TRIP600 (1T) and 1.19mm CR DDQ+ (Y2) along the diagonal of the square cup. 120
10.23 Major, minor and thickness strain distributions for 1.2mm GI DP800 (1R) and 1.15mm CR DP980 (1S) along the diagonal of the square cup. 121
10.24 Major, minor and thickness strain distributions for 1.32mm GI RA830 (1W), 1.25mm CR RA830 (3W) and 1.03mm CR M190 (1H) along the diagonal of the square cup. 121

Appendix D

D.1 The scree plot of effects of factors on springback (Baseline steel) 140
D.2 The scree plot of effects of factors on sidewall curl (Baseline steel) 141
D.3 The scree plot of effects of factors on springback (Skin panel steel) 141
D.4 The scree plot of effects of factors on sidewall curl (Skin panel steel) 142
D.5 The scree plot of effects of factors on springback (Structural HSS) 142
D.6 The scree plot of effects of factors on sidewall curl (Structural HSS) 143
D.7 The scree plot of effects of factors on springback (Structural AHSS) 143
D.8 The scree plot of effects of factors on sidewall curl (Structural AHSS) 144
D.9 The scree plot of effects of factors on springback (Structural UHSS) 144
D.10 The scree plot of effects of factors on sidewall curl (Structural UHSS) 145

Appendix E

E.1 The effect of tooling radii on springback (0.70mm group) 146
E.2 The effect of tool gap on springback (0.70mm group) 147
E.3 The effect of drawbead restraining force on springback (0.70mm group) 147
E.4 The effect of tooling radii on sidewall curl (0.70mm group) 148

E.5 The effect of tool gap on sidewall curl (0.70mm group) 148
E.6 The effect of drawbead restraining force on sidewall curl (0.70mm group) 149
E.7 The effect of tooling radii on springback (1.20mm group) 149
E.8 The effect of tool gap on springback (1.20mm group) 150
E.9 The effect of drawbead restraining force on springback (1.20mm group) 150
E.10 The effect of tooling radii on sidewall curl (1.20mm group) 151
E.11 The effect of tool gap on sidewall curl (1.20mm group) 151
E.12 The effect of drawbead restraining force on sidewall curl (1.20mm group) 152

LIST OF TABLES

Tables **Page**

Executive Summary

x.1 Summary of the different test methods used to characterize the formability of AHSS in this AISI/DOE project xiv

Section 1

1.1 Brief descriptions of the different steel grades used in the project 1
1.2 Summary of the different test methods used in the project 2

Section 2

2.1 Mechanical properties of the steel grades in the longitudinal (L) direction 7
2.2 Mechanical properties of the steel grades in the transverse (T) direction 8
2.3 Mechanical properties of the steel grades in the diagonal (D) direction 9
2.4 Average mechanical properties ((L+T+2D)/4) for all the steel grades 10

Section 3

3.1a Tensile Properties at Medium Strain Rates by Lot 17
3.1b Tensile Properties at Medium Strain Rates by Lot 18
3.1c Tensile Properties at Medium Strain Rates by Lot 19
3.1d Tensile Properties at Medium Strain Rates by Lot 20
3.1e Tensile Properties at Medium Strain Rates by Lot 21
3.1f Tensile Properties at Medium Strain Rates by Lot 22
3.2a Average Tensile Properties at Medium Strain Rates by Grade 22
3.2b Average Tensile Properties at Medium Strain Rates by Grade 23
3.2c Average Tensile Properties at Medium Strain Rates by Grade 24
3.3 Fit Constants for Additive and Multiplicative Constitutive Models 32

Section 4

4.1a Bauschinger Effect Factor 36
4.1b Bauschinger Effect Factor 37
4.1c Bauschinger Effect Factor 38
4.1d Bauschinger Effect Factor 39
4.1e Bauschinger Effect Factor 40
4.2a Constants A and B 44
4.2b Constants A and B 45

Section 5

5.1 n-values used for the determination of the FLC_0 for the three steel lots 49

Section 6

6.1 Sheared edge stretching results for all the steel grades 56

Section 7

7.1 Punch radii used for the different thicknesses in the ASB test 64

Section 8

8.1 Full factorial channel draw test 79
8.2 Factors used for process variables and their interactions 79
8.3 Grouping of steels of nominal thickness 0.70mm 87

8.4 Grouping of steels of nominal thickness 1.2mm 87

Section 9

9.1 Formability data for the Stretch Form test for the steels tested 93
9.2 Strain measurements from the Stretch form test 93
9.3 Regression analysis of the results of the stretch form test 94
9.4 Modified regression analysis of the failure height in the stretch form test 95
9.5 Summary dent test data for the skin panel steels 97
9.6 Reduced dent resistance data for the steels tested 99

Section 10

10.1 Blank dimensions for the square draw test for determination of failure heights 106
10.2 Sample conditions for binder span of control testing 107
10.3 Forming conditions for strain measurement 108
10.4 Binder force limits for wrinkling and splitting for all the steel lots in the experiment 112

Appendix A

A.1 Heights at failure and fracture locations for the Angular Stretch Bend test for all lots 126

Appendix B

B.1 Baseline Steels 130
B.2 Skin Panel Steels 131
B.3 Structural Steels 133

Appendix C

C.1 Ratios of tooling radii/thickness, tool gap/thickness and Drawbead Force/Plane Strain Yield Strength 138

Appendix D

D.1 Test results for 0.96mm GI DP600 steel (1P) 139
D.2 Normalized effects for 0.96mm GI DP600 (1P) 140

Appendix F

F.1 Failure heights for Square Draw test. The italicized entries are cups without splitting 153

EXECUTIVE SUMMARY

With a view to advancing the use of high strength and advanced high strength steels in the North American automotive industry, the American Iron and Steel Institute (AISI), in collaboration with the United States Department of Energy (DOE), commissioned a study to be performed by Ispat Inland Research Laboratories, to characterize the formability of several sheet steel products. The steels to be included in this study were grades of drawing quality and deep drawing quality steels, conventional high strength steels (HSS) including several bake-hardenable (BH) and high strength low alloy (HSLA) steels, advanced high strength steels (AHSS), such as Dual Phase (DP) and Transformation Induced Plasticity (TRIP) steels, and ultra-high strength steels (UHSS), such as Recovery Annealed (RA) and tempered martensitic sheet steels. A total of 40 different lots of steel, the majority of which were supplied by the member companies of Automotive Application Committee (AAC) of American Iron and Steel Institute (AISI) were characterized in this project. The main objective of this project was to conduct tests on the different steel grades to characterize intrinsic mechanical behavior and material limits under different forming conditions. The test results for AHSS could then be compared with data for "formable" steels and other conventional HSS evaluated using identical test practices, which could then assist in the development of die and process guidelines for AHSS.

The tests used in this project to characterize formability could be classified into three broad categories.

1. **Intrinsic Mechanical Behavior Tests:** Tests characterizing the intrinsic mechanical behavior of the material are classified as intrinsic tests. In addition to direct comparisons between the different steel grades, these data should assist in understanding behavior during stamping. In this project three intrinsic tests were used to characterize the mechanical behavior.
   - Standard Tensile test: Tensile tests were conducted using ASTM E-8 standards for testing of sheet materials. Standard properties such as 0.2% offset yield strength (YS), ultimate tensile strength (UTS), elongation, n-value and r-value were determined for the steel grades in the program. In addition, trends of the instantaneous n-value vs. true strain were determined in the transverse direction. Most steels showed a higher work hardening ability at the beginning of deformation, and a gradual decrease in work hardenability with increasing strain.
   - Medium Strain Rate Tensile test: This test consists of loading specimens at strain rates ranging from 10^{-3} to 10^{1}/s and using the test data to characterize the strain rate sensitivity of the steel grades. The maximum strain rate in this test was limited to 10/sec to be more applicable to the strain rates observed in a typical stamping. The test results showed that YS and UTS increased with increasing strain rate. The increase of UTS per order of magnitude increase of strain rate, was found to be 16 MPa for all the steels tested, except M190, which was 8 MPa. The n-value was found to decrease with strain rate, but the dependence decreases for high strength steels. For steels of YS higher than 300 MPa, n-value was found to be almost constant with increasing strain rate. Constants for two constitutive models: additive and multiplicative, were generated from the testing results for each lot of steel. These constitutive models could be used by finite element analysts to incorporate strain rate effects in formability simulations.
   - Bauschinger Effect: Bauschinger effect can be described as the reduction in yield strength when the direction of loading is reversed. The test results could be useful in interpreting springback behavior. In order to avoid buckling during compression for thin sheet steel specimens, dog-bone shape specimens with a small gage length, 7.62mm, were used. Testing consists of tensile loading to a specified strain, unloading and then reverse loading in compression till buckling was detected. The Bauschinger effect factor (BEF) determined by the ratio of reverse yield strength to the forward flow strength was determined for four prestrains.

A higher Bauschinger effect is characterized by a lower value of the BEF. It was found that the Bauschinger effect increased with the magnitude of the tensile prestrain. In general, higher strength steels exhibit a higher Bauschinger effect with mild steels showing the lowest, conventional high strength steels next and advanced high strength steels showing the highest. However, TRIP steels show a relatively lower Bauschinger effect than DP steels of the same strength.

2. **Tests for Splitting limits:** One of the most important failure modes limiting sheet metal formability is splitting caused by tensile loading. It is thus important to establish splitting limits for different forming modes to assist die and process engineers and also to provide trouble-shooting tools to press shop personnel. In terms of applicability to general part geometries, tests for splitting limits lie somewhere between intrinsic mechanical behavior tests, and simulative formability tests, where the ability of the sheet metal to resist strain localization under different conditions is characterized. Three tests were used to characterize splitting failures for different forming modes.
   - Forming Limit Curves: Severity analyses using Forming Limit Curves (FLCs) are used routinely in the North American stamping industry during die tryout and regular production. A FLC is a map of strains that indicate the onset of critical local necking for different strain paths. Experimental determination of FLCs involve forming the sheet specimens of different widths (to generate different strain paths) and measurement of resulting critical strains. Considerable prior work has been done with respect to characterizing the shape of the FLC as a function of n-value and thickness for different steel grades. In North America, for most steel grades, a standard shape for the FLC is used in the stamping industry. Recent work has shown that the standard shape is applicable for most dual phase steels. FLC determination was not part of this contractual agreement, but the importance of FLC for some AHSS such as TRIP, and UHSS such as DP980 and RA830 were recognized. As a result, experimental FLCs were determined for some of these lots. Ispat Inland determined the FLC for 1.15mm CR DP980, US Steel for the 1.4mm CR TRIP600 and Dofasco for 1.8mm GI RA830. Results showed that for negative minor strains, the experimentally determined FLC was in close agreement to the standard shape for the steels tested. For positive minor strains, only the TRIP600 showed close agreement with the standard shape, whereas the RA830 and DP980 steel showed significantly higher forming limits than suggested by the standard shape. This indicates that in the positive minor strain regime, the standard shape might be overly conservative for steels with complex microstructures.
   - Sheared Edge Stretching Limits: During manufacturing, the sheet metal goes through different dies on its way to a finished product. After deep drawing, the excess metal is usually trimmed off, and flanged. Flanging is often a strengthening requirement in the design or to provide a mating surface for subsequent joining operations. During stretch flanging, a tensile strain is usually imposed on the sheared edge, causing splitting failure in some cases. Determination of the sheared edge forming limits is usually conducted by stretching a punched hole, thereby evaluating formability of the sheared edge. In this project, holes were punched in square samples, and the stretching ability of the sheared holes were determined using a conical punch, where the % hole expansion at failure is used as a measure of sheared edge stretchability. It was found that sheared edge stretching limits were strongly related to the tensile strength, showing a significant decrease with increasing tensile strength for steels of tensile strength less than 700 MPa and then saturating for steels of higher strength. The TRIP600 steel lots studied did not seem to offer any significant advantages over the DP600 lots with respect to sheared edge stretching behavior. Interestingly, the sheared edge stretching limit for the DP980 lots was significantly higher than the observed trend, which suggests that it might be possible to maximize the sheared edge stretching performance for a given tensile strength level.
   - Bending Under Tension Limits: Metal behavior as it is bent over a tight radius with superimposed tensile load was recognized as an important deformation mode requiring more

complete characterization. Structural parts often have embosses and stiffening ribs with tight radii, where splits are possible. In this project the bending under tension limits are determined using the Angular Stretch Bend (ASB) test, which consists of forming wedge-shaped open channel specimens with punches of different radii. Two measures of bending under tension limits are presented: (a) failure heights for different Radius/thickness (R/t) ratios for the different materials and (b) normalized maximum allowable strain in the sidewall as a function of the R/t ratio. It was found that formability decreased with decreasing curvature of the punch nose (sharper radius). The dependence of formability on tensile strength was also significant, where formability decreased with increasing tensile strength. For this test, the formability of TRIP600 and DP980 were significantly above the observed trends of formability.

3. **Simulative formability tests:** These types of tests provide very specific information which are significantly dependent on lubrication conditions, tooling geometry, deformation mode and material behavior. The information generated is limited in applicability with respect to general panel shapes, but by combining most of the factors that make up the formability "system", the data provide information on steel performance under simulated press forming conditions. Results from simulative formability tests have a better correlation with actual press formability than tensile properties. The results from these tests could be used to gain insights on material behavior under production press forming conditions. Another important use of these results could be in conducting finite element (FE) simulations and comparing predictions with actual test results, whereby it is possible to improve on current simulation practices for AHSS. The forming attributes of the different steel grades studied included the following.
   - Springback Behavior: Springback and sidewall curl after unloading from stamping dies is a very important technical barrier to the widespread adoption and use of AHSS in vehicle platforms. Traditionally, press shops and process engineers have developed guidelines based on experience with mild steels for necessary tooling and process modifications to control springback. Lack of this experiential knowledge for AHSS coupled with the inability of commercial finite element analysis (FEA) codes to predict springback accurately have contributed to the resulting reluctance in the stamping plants for using AHSS for production parts. In this project, an open Channel die-set with an interchangeable construction for tooling radii, punch to die clearance and drawbead penetration was designed and used to characterize springback under a variety of testing conditions. A full factorial experimental design was used, whereby two levels of tooling radii, clearance and drawbead penetration were used. It was found that the most influential factors controlling springback and curl were the tooling radius and drawbead penetration. In general springback and curl increased with increasing strength level. It was also found that the springback for TRIP600 was lower than the trend.
   - Stretch Formability and Dent Resistance: Stretch formability and dent resistance were evaluated for the steel lots that are either currently in production or being considered for production for exposed body panels in automobiles. The test consisted of fully locking out the material beyond the die opening cavity and stretching the material using a 203.2mm diameter punch. The height at failure is used as a measure of formability. It was found that stretch formability was a strong function of the n-value. In addition, dent tests were conducted for the steel grades for a common geometry. The panels were formed to two different levels of surface strain to examine the effect of surface strain on dent resistance. The Auto/Steel Partnership procedure was used for conducting the dent tests. For the geometry that was used, for very low denting loads, it was found that the effect of thickness on dent resistance was very significant. At higher denting loads, the effect of the steel strength and the amount of stretch on dent resistance became more significant.
   - Stretch Drawability: Stretch drawability was evaluated using a round-cornered Square punch geometry and flat binder plates. This test was limited to steel lots of nominal thickness 1.2mm because of capacity restrictions of the formability press. Three measures of formability were

evaluated (a) failure heights (b) Strain distribution and (c) Binder span of control. Results for failure heights test were strongly influenced by the amount of draw-in from the flange. Analysis of the strain distribution revealed that at the eventual fracture location, the strain mode was biaxial, where a higher limit for material thinning was observed. Binder span of control is an interesting test method, where the safe operating window for split-free and wrinkle-free parts were determined for this square cup geometry. The safe operating window is a function of the amount of draw-in, which in turn is a complicated function of work hardenability, R-value, strength and the coating type. Once again, it was found that the operating window for the TRIP600 steel was higher than its counterparts.

In summary, the formability attributes characterized, the test methods used, and major factors influencing formability for the tests conducted in this project are presented in Table x.1.

Table x.1: Summary of the different test methods used to characterize the formability of AHSS in this AISI/DOE project

Formability attribute	**Test method**	**Formability parameters characterized**	**Factors influencing formability**
Forming Limits	100mm full dome test	FLC	n-value, thickness
Sheared edge stretching limits	Hole extrusion test	% Hole expansion	UTS, r-bar value
Bending Under Tension Limits	Angular Stretch Bend test	Height at failure, Stretch bendability index	UTS, r-bar value
Springback and Curl	Channel Draw test	Springback opening angle, radius of sidewall curl	YS, tool radii, drawbead restraining force, tool gap
Stretch Formability	Piepan forming, fully locked conditions	Height at failure	n-value, thickness
Stretch Drawability	Square Draw test	1. Height at failure 2. Binder span of control 3. Strain measurement	UE*(r-bar), blank size, lubrication, coating, thickness

ACKNOWLEDGEMENTS

As with all projects of this magnitude, this project would not be successful without the contributions of several individuals and organizations. The authors acknowledge the following organizations and individuals.

- American Iron and Steel Institute (AISI) and the U.S. Department of Energy (DOE) for providing the funding for the project
- Member companies of the Automotive Application Committee(AAC) of AISI for supplying the lots of steel
- Thyssen Krupp Stahl for supplying two lots of TRIP 600.
- Bernard S. Levy for developing the original project proposal and many of the test methods that were used in the project.
- The following members of the advisory committee for providing valuable input on test methodologies.
  - Ron Soldaat (Dofasco)
  - Alex Konieczny (US Steel)
  - Zeev Zimmerman , retired (Bethlehem Steel)
  - Wei Wang (Rouge Steel)
  - Roger Pradhan (Bethlehem Steel)
  - Dave Meuleman (National Steel)
- Ispat Inland technician staff for diligent conduction of all experiments
- Barb Kopko from Ispat Inland Research for excellent management of the logistical aspects of the project.
- Shrikant Bhat and Nassos Lazaridis of Ispat Inland Research for providing useful comments on the final report.

Section 1.0
Introduction

Stamping is one of the most common methods of shaping sheet metal into specified shapes. Many different modes of deformation are employed to impart the desired shape to the sheet metal during stamping, such as stretching, bending, deep drawing, embossing etc. Typically, a forming operation involves combinations of these different forming modes. Ability of the material to undergo these different forming modes without defects such as splitting, wrinkling, or springback is broadly termed as the "formability" of the material. Formability is a system characteristic depending on material properties, die geometry, lubrication conditions, press speed, and restraint conditions caused by binder pressure and/or drawbeads. Since sheet metal forming encompasses a diverse variety of processes and deformation modes, no one test can adequately characterize the "forming ability" of the material. This AISI/DOE (American Iron and Steel Institute/U.S. Department of Energy) formability project was therefore conceived to provide formability information under a variety of different simulated forming conditions for conventional and advanced high strength steels. The data generated from this project provides comparative formability data needed for development of die/process engineering guidelines as well as providing benchmark data needed to evaluate finite element analysis (FEA) formability methods for breakage and springback for advanced high strength steels. The duration of the project was two years, where majority of the time in the first year was spent in designing and constructing the experimental tooling and developing test methods, with the bulk of testing and data analysis conducted in the second year.

The steel grades in the program were supplied by the member companies of Automotive Application Committee (AAC) of AISI (with the exception of two lots of TRIP600, which were supplied by Thyssen Krupp Stahl). A total of 16 steel grades were evaluated in this program, which are listed below. Multiple lots of each steel grade were evaluated resulting in a total of 40 lots of steel for the program. The steel grades evaluated in the project are listed below. For a description of the different steel grades, Table 1.1 can be referred.

- Baseline Steels
  - DDQ+, DQSK
- Skin Panel Steels
  - BH210, BH280, IF-Rephos, ULC340BH, DP500
- Structural Steels
  - BH300, HSLA350, HS440W, DP600, TRIP600, DP800, DP980, RA830, M190

Table 1.1: Brief descriptions of the different steel grades used in the project

Grade	Brief Description
DDQ+	Interstitial Free **D**eep **D**rawing **Q**uality Steel
DQSK	**D**rawing **Q**uality **S**pecial **K**illed Steel
BHxxx	**B**ake **H**ardenable Steel of minimum yield strength xxx in MPa
IF-Rephos	A **Rephos**phorized **I**nterstitial **F**ree steel
ULC BH340	**U**ltra **L**ow **C**arbon **B**ake **H**ardenable Steel of 340 MPa minimum tensile strength
HSLA350	**H**igh **S**trength **L**ow **A**lloy steel with a minimum yield strength of 350 MPa
HS440W	**H**igh **S**trength (C-Mn) steel with a minimum tensile strength of 440 MPa
DPxxx	**D**ual **P**hase (ferrite+martensite) steel with a minimum tensile strength of xxx
TRIP600	**TR**ansformation **I**nduced **P**lasticity steel with a minimum tensile strength of 600 MPa. These steels contain retained austenite in the microstructure which transforms to martensite on application of plastic strain
RA830	**R**ecovery **A**nnealed steel of minimum tensile strength 830 MPa
M190	Tempered **M**artensitic steel of minimum tensile strength 190 ksi (1300 MPa)

The objective of the project was to provide formability information on the different steel grades. Because these steel grades come with different surface morphologies and different protective coatings with resulting different frictional behaviors, it was important to isolate formability differences arising from bulk mechanical properties of the steel sheet from the effects of the coating. All the formability tests were conducted under heavy lubrication conditions. In most cases, sheets of Teflon were used along with a lubricating oil between the tool and the sample interface. The effect of the coating was assessed somewhat in the Square Draw test, where the combined effect of the mechanical properties of the steel grade and the coating on formability was evaluated.

1.1 Experimental Methods

Table 1.2: Summary of the different test methods used in the project

Test method	Section	Attribute being characterized	Equipment	Tooling	Steels characterized
Standard tensile test	2	Mechanical properties	Tinius Olsen mechanical test frame	NA	All steels
Medium strain rate tensile test	3	Strain rate sensitivity for forming range	MTS 5kips mechanical test frame	NA	All steels
Bauschinger test	4	Bauschinger effect	MTS 5kips mechanical test frame	NA	All steels
Forming Limit Curves	5	Forming Limits	Servohydraulic press	100mm dome punch dieset	TRIP600, RA830, and DP980
Hole extrusion test	6	Sheared edge stretching limits	Hille-Wallace hydraulic press	38.1mm dia., 60^0 conical punch	All steels
Angular Stretch Bend test	7	Bending Under Tension limits	Interlaken servohydraulic press	Ispat Inland designed tooling	All steels
Channel Draw test	8	Springback and Curl behavior	Interlaken servohydraulic press	Ispat Inland designed tooling	All steels
Stretch form test	9	Formability under stretch-form conditions	Interlaken servohydraulic press	203.2mm diameter punch dieset	Skin panel steels
		Dent resistance	Ispat Inland dent tester	25.4mm indenter	
Square draw test	10	Formability under stretch-draw conditions	Interlaken servohydraulic press	Ispat Inland designed tooling	All steels of nominal thickness less than or equal to 1.2mm

Because of the diverse nature of sheet metal forming, many tests exist in the industry to characterize sheet metal formability. Companies use test methods based on the immediate requirement that needs to be satisfied, and existing testing capabilities. Development of experimental forming capability is capital-intensive, with the cost of a sophisticated research press and the associated tooling easily approaching half a million dollars of capital investment. As a result of these factors, there are no available ASTM or SAE standards for formability testing. Some tests are more widely accepted than others. In this project, several different experimental methods were used to characterize the formability of the steels in the project. These tests were used to characterize formability under different deformation conditions. The test methods in this project were either selected from existing test methods, or were developed in consultation with the advisory committee which consisted of experts in sheet metal formability from the member companies of AISI/AAC. In addition to simulative formability tests, data were generated on the intrinsic mechanical behavior of the different steel grades. The intrinsic mechanical behavior data could be used in commercial Finite Element (FE) programs to provide a better prediction of forming behavior for advanced high strength steels (AHSS). The test methods and the material attribute being characterized are given in Table 1.2. Also included in the table is a summary of the equipment, tooling, and steels characterized using the test method. The details for each test can be found in the relevant section describing the test.

Most of the testing for this project was conducted on a servohydraulic, computer controlled double action press manufactured by Interlaken Technologies. This press has a punch capacity of 500 kN, binder table capacity of 667 kN and a maximum attainable speed of 423.33 mm/sec. Significant amount of formability testing was conducted using specially designed tooling. The tooling was designed to be able to test steels of vastly different mechanical properties from DDQ+ to M190 and thicknesses ranging from 0.65mm to 1.6mm. All test equipment used in the program are accredited either by A2LA or QS9000.

1.2 Organization of the Report

This report is organized into 10 different sections, where sections 2-10 contain results from the different tests. Each section contains some background information, literature review (wherever applicable), description of the experimental methods, results, analysis and conclusions on the deformation mode being evaluated. It is to be noted that some test methods and deformation modes have been studied more than others, with the result that there are different extents of literature review in each section. Likewise, there are differences in the extent of analysis and data interpretation between the different test methods. By their very nature, some tests were found to be more amenable to extended analyses than others. Although this report contains a substantial amount of data analysis, by no means is it complete

It should also be noted that in the analysis and interpretation, the steel grades in the program are classified differently for each test. Attempts to come up with a single unified classification system for the steel grades to be used for all the tests were unsuccessful because of different material attributes highlighted in different tests. In that respect it was decided to adopt a more natural classification that would highlight specific aspects of the test results addressed in the individual sections.

Section 2.0
Basic Mechanical Characterization

2.1 Test Procedure

Basic mechanical characterization was performed by conducting tensile tests according to ASTM E-8 standards [2.1] for tensile testing of flat specimens, using a specimen width of 12.7mm and a gauge length of 50.8mm. Triplicate samples in the longitudinal (L), transverse (T) and diagonal (D) directions were tested and the properties averaged for each direction. Typically, the average n-value within a range of elongation is reported as a measure of the work hardening ability of the steel. For this study, the n-value (work hardening exponent) is reported for the elongation range of 6%-12%. The r-value (anisotropy strain ratio) was determined at a specified elongation less than the uniform elongation (UE). For the more ductile steels, the r-value was determined at 17% UE. For most of the high strength steels, where the uniform elongation was less than 17%, the r-value was determined at an elongation of UE less 1-2%. The r-value was not determined for steel grades of tensile strength greater than 800MPa. To get the average property of the steel lot, the average property was determined using the following standard relationship.

$$\text{Average property} = (L+T+2D)/4 \qquad (2.1)$$

In addition to the standard mechanical properties, the instantaneous work hardening behavior (n-value vs. true strain) was determined in the transverse direction for steels in the program that have a significant amount of work hardening. Steels for which this could not be achieved were the four lots of RA830 and two lots of M190. The procedure for determination of the instantaneous work hardening behavior is also described in this section.

2.1.1: Noise reduction and curve fitting

In describing the calculation procedure for instantaneous n-value, the variables x and y are used to avoid confusing the variables used in curve fitting with the true stress and true strain. The variables x and y are created from the same transformations that convert engineering stress and strain to true stress and strain, but are not true stress and strain since they include points beyond uniform elongation. The variables x and y are generated from $x = \ln(1+e)$ and $y = S(1+e)$ where e is engineering strain and S is engineering stress. A 4th order polynomial fit is applied to log y vs. log x. The 4th order fit takes the form: $\log y = A(\log x)^4 + B(\log x)^3 + C(\log x)^2 + D(\log x) + E$. Data are taken from the higher of either 1% true strain or the end of yield point elongation to the highest value of the variable x (beyond uniform elongation). This is necessary because the 4th order fit is sensitive to its end point since the fitting equation is unconstrained beyond the last stress-strain pair and the data-set beyond UE has been shown to generate a better curve fit [2.2].

The log-log 4th order polynomial approach is superior to directly determining uniform elongation from the raw data because the engineering stress-strain curve is flat in the vicinity of uniform elongation and noise is inherent in stress-strain data. Uniform elongation is calculated from the polynomial fit by applying Considere's criteria $\sigma = d\sigma / d\varepsilon$ (which is equivalent to $y = dy / dx$). The fitted log x and log y points are transformed back into x and y by exponentiation (i.e., $x = 10^{\log x}$). Uniform elongation is found at the point $y = dy / dx$ which can be determined by differentiation or taking the slope $(y_2 - y_1) / (x_2 - x_1)$. The latter method is used to determine uniform elongation. Thereafter, all data for strains higher than uniform elongation are discarded.

2.1.2: Instantaneous n value

The instantaneous n value is calculated by taking the derivative of the log true stress-log true strain curve and plotting it against total true strain up until the uniform elongation. The derivative of the fitted equation is: d log y / d log x = 4 A $(\log x)^3$ + 3 B $(\log x)^2$ + 2 C (log x) + D.

2.2 Results

Figure 2.1 shows a plot of the total elongation (TE) vs. the ultimate tensile strength (UTS) for all the steel grades in the project. The average properties ((L+T+2D)/4) are plotted here. Figures 2.2 and 2.3 show the dependence of the n-bar (average n) and r-bar (average r) values on UTS.

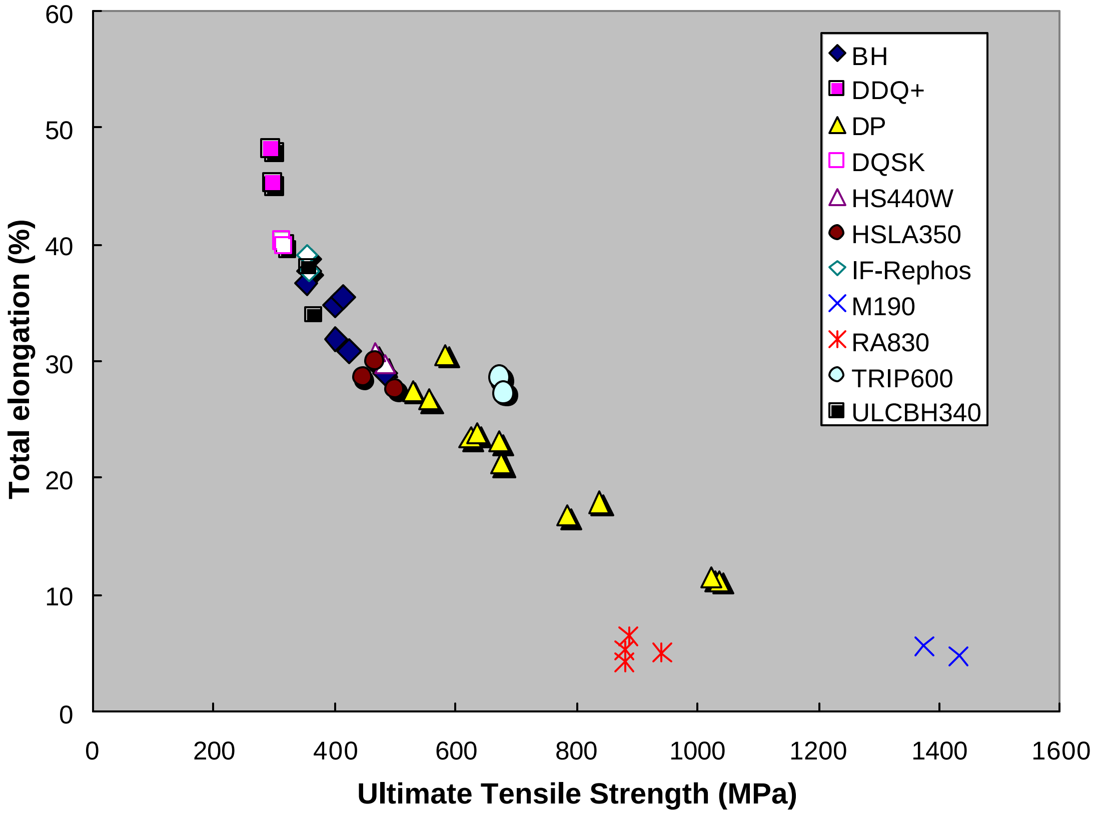

Figure 2.1: Relationship between total elongation and ultimate tensile strength for the steel grades in the AISI/DOE formability project

From Figure 2.2 it can be seen that DP steels can have n-bar values which are comparable to those of the BH grades. A wide range of n-bar values were observed for a given strength level. From Figure 2.3, the r-bar value seems to asymptotically approach a value of slightly less than 1.0 as the strength level increases. For steels with UTS less than 400 MPa, a wide range of r-bar values were observed. The effect of the r-bar value is important as it is a measure of the resistance of the sheet metal to change in thickness. This attribute is manifested as a resistance to thinning and wrinkling during stamping. The r-value is also instrumental in dictating the strain path during the stamping process.

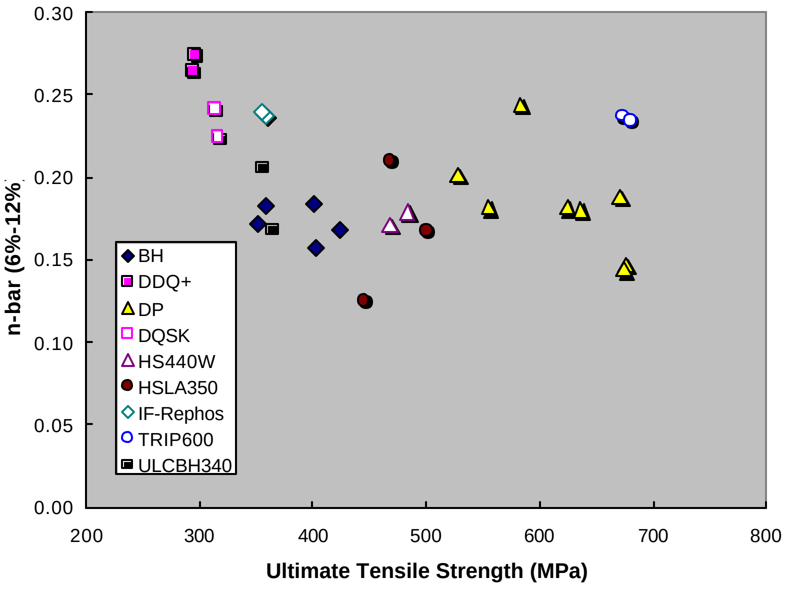

Figure 2.2: Dependence of the n-bar value (6%-12%) on the ultimate tensile strength

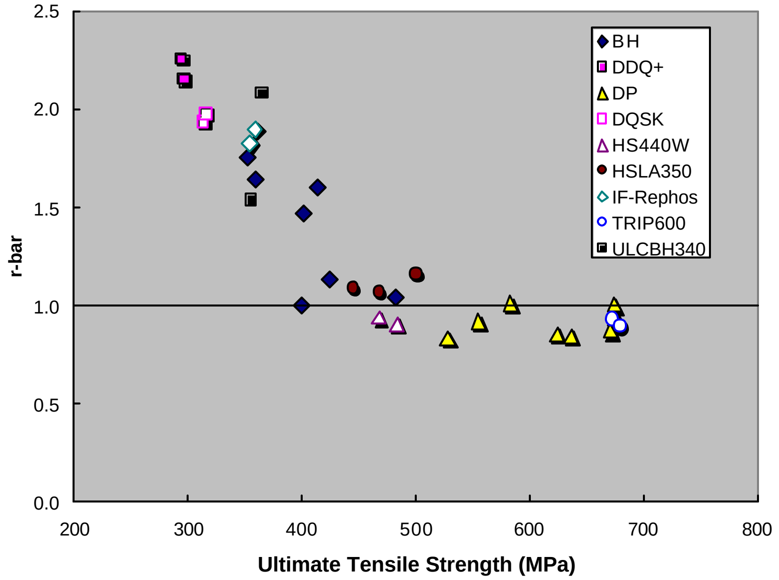

Figure 2.3: Dependence of the r-bar value on the ultimate tensile strength

Tables 2.1 through 2.3 show the mechanical properties for the steel grades in the L, T, and D directions. Tensile tests in the T directions for one of the RA830 lots (1W) were repeatedly unsuccessful and are not included in the tables. As seen in the tables, the r-values in the T-direction were higher than the L, and D directions for most of the steel lots. Table 2.4 shows the average mechanical properties (L+T+2D/4) for all the steel lots. For the RA830 steel grades, no work hardening was observed, thereby making it very difficult to distinguish between the yield point elongation (YPE) and uniform elongation (UE). For all the RA830 lots, only the total elongation (TE) is reported.

Table 2.1: Mechanical properties of the steel grades in the longitudinal (L) direction

	Grade	**Lot Code**	**Coating**	**Thickness (mm)**	**YS (MPa)**	**UTS (MPa)**	**YPE (%)**	**UE (%)**	**TE (%)**	**n (6-12%)**	**r**
Baseline	DQSK	X1	Bare	0.77	161	308	0.00	23.10	42.20	0.245	2.081
		X2	Bare	1.19	175	311	0.00	22.60	42.90	0.230	2.238
	DDQ+	Y1	Bare	0.70	138	294	0.00	24.90	48.40	0.266	2.317
		Y2	Bare	1.19	136	293	0.00	25.60	47.50	0.281	2.372
Skin Panel Steels	BH210	B1	EG	0.70	244	356	0.31	19.60	39.00	0.187	1.774
		B2	EG	0.93	237	348	0.07	19.87	37.40	0.183	1.680
	BH280	C1	EG	0.71	321	415	0.29	18.47	31.93	0.174	1.193
		C2	EG	1.00	277	394	0.00	16.87	34.27	0.162	1.645
		C3	GA	1.04	291	395	0.22	19.70	35.17	0.185	1.001
	ULC BH340	D1	GA	0.74	248	361	0.00	18.90	35.07	0.179	1.703
		D2	GA	1.02	221	351	0.00	22.17	39.20	0.212	1.667
	IF-Rephos	E1	GA	0.63	195	360	0.00	22.17	36.70	0.242	1.581
		E2	GA	0.89	192	358	0.00	22.37	37.67	0.245	1.411
	DP 500	G1	EG	0.66	305	521	0.00	19.23	29.80	0.202	0.891
		G2	EG	0.81	328	549	0.00	17.90	27.73	0.188	0.908
Structural Steels	BH300	1K	GA	1.24	342	476	0.96	16.93	29.43	0.183	1.049
		2K	GI	1.19	298	414	0.43	18.90	34.93	0.187	1.408
	HSLA 350	1L	GI	1.16	407	469	6.79	19.37	29.70	0.221	0.774
		5L	Bare	1.21	363	503	0.00	16.13	27.20	0.171	0.757
		2L	GI	1.62	356	446	0.00	15.13	28.60	0.133	0.892
	HS 440W	1M	GA	1.24	345	476	1.25	16.93	29.47	0.184	0.939
		2M	GA	1.58	340	457	0.28	17.67	33.67	0.180	1.069
	DP600	1P	GI	0.96	379	625	0.00	16.20	25.40	0.181	0.835
		2P	Bare	1.19	376	633	0.00	16.17	24.13	0.182	0.945
		3P	GI	1.39	382	668	0.00	16.21	23.06	0.188	0.869
		4P	GI	1.23	428	673	0.00	14.30	21.93	0.149	0.865
		5P	GI	1.64	337	582	0.00	18.37	31.10	0.248	0.908
		6P	GI	1.49	426	668	0.00	13.90	21.33	0.145	0.865
	TRIP 600	1T	Bare	1.40	424	670	0.05	20.60	29.73	0.247	0.908
		2T	Bare	1.60	420	671	0.00	20.53	29.40	0.246	0.875
	DP800	1R	GI	1.20	505	830	0.00	10.73	17.90		
		2R	GI	1.59	449	780	0.00	10.03	16.07		
	DP980	1S	Bare	1.15	902	1031	0.80	5.70	11.40		
		2S	Bare	1.52	861	1013	0.46	6.03	11.47		
	RA 830	1W	GI	1.32	516	888			0.47		
		2W	GI	1.53	831	865			6.90		
		3W	Bare	1.25	872	904			9.07		
		4W	GA	1.80	855	864			10.60		
	M 190	1H	Bare	1.03	1231	1437	0.00	2.53	4.72		
		2H	Bare	1.58	1202	1375	0.00	2.53	5.67		

Table 2.2: Mechanical properties of the steel grades in the transverse (T) direction

	Grade	Lot Code	Coating	Thickness (mm)	YS (MPa)	UTS (MPa)	YPE (%)	UE (%)	TE (%)	n (6-12%)	r
Baseline	DQSK	X1	Bare	0.77	164	303	0.00	21.30	42.40	0.239	2.583
		X2	Bare	1.19	183	306	0.00	20.60	42.10	0.218	2.646
	DDQ+	Y1	Bare	0.70	138	289	0.00	24.40	47.70	0.266	2.694
		Y2	Bare	1.19	144	290	0.00	23.50	45.40	0.271	2.761
Skin Panel Steels	BH210	B1	EG	0.70	247	354	0.00	18.80	38.30	0.184	1.872
		B2	EG	0.93	249	349	0.00	18.43	38.37	0.166	2.333
	BH280	C1	EG	0.71	328	417	0.42	18.00	31.03	0.170	1.594
		C2	EG	1.00	278	396	0.00	15.97	32.23	0.158	1.890
		C3	GA	1.04	302	400	0.41	18.87	33.13	0.178	1.293
	ULC BH340	D1	GA	0.74	263	364	0.00	17.53	33.00	0.160	2.608
		D2	GA	1.02	229	349	0.00	21.50	40.17	0.205	2.019
	IF-Rephos	E1	GA	0.63	204	359	0.00	21.50	37.47	0.236	2.253
		E2	GA	0.89	206	358	0.00	21.43	38.43	0.236	1.994
	DP 500	G1	EG	0.66	304	530	0.00	18.80	26.77	0.205	1.029
		G2	EG	0.81	329	567	0.00	17.70	27.73	0.185	1.111
Structural Steels	BH300	1K	GA	1.24	352	482	1.16	16.20	29.13	0.175	1.361
		2K	GI	1.19	314	412	0.46	18.43	35.33	0.172	1.845
	HSLA 350	1L	GI	1.16	420	475	8.51	18.53	29.70	0.183	1.19
		5L	Bare	1.21	399	522	0.00	15.00	25.23	0.161	1.045
		2L	GI	1.62	373	450	0.00	14.13	28.53	0.120	1.250
	HS 440W	1M	GA	1.24	354	484	0.40	16.40	28.30	0.179	1.119
		2M	GA	1.58	341	462	0.39	16.87	31.20	0.175	1.285
	DP600	1P	GI	0.96	379	631	0.00	14.97	22.10	0.180	0.869
		2P	Bare	1.19	367	630	0.00	16.17	24.53	0.184	1.063
		3P	GI	1.39	394	667	0.00	16.03	22.63	0.187	1.069
		4P	GI	1.23	431	677	0.00	13.80	21.47	0.147	1.064
		5P	GI	1.64	342	588	0.00	18.63	30.80	0.240	1.150
		6P	GI	1.49	439	683	0.00	13.60	21.60	0.141	1.093
	TRIP 600	1T	Bare	1.40	447	671	0.00	18.47	26.63	0.230	1.066
		2T	Bare	1.60	430	676	0.00	18.80	27.50	0.236	1.085
	DP800	1R	GI	1.20	489	850	0.00	10.27	16.70		
		2R	GI	1.59	462	791	0.00	10.27	15.53		
	DP980	1S	Bare	1.15	908	1044	0.50	5.73	10.13		
		2S	Bare	1.52	871	1037	0.15	5.50	10.50		
	RA 830	1W	GI	1.32	Not Included						
		2W	GI	1.53	508	959			3.93		
		3W	Bare	1.25	864	997			4.23		
		4W	GA	1.80	783	949			2.40		
	M 190	1H	Bare	1.03	1239	1443	0.00	2.50	4.35		
		2H	Bare	1.58	1228	1381	0.00	2.53	5.07		

Table 2.3: Mechanical properties of the steel grades in the diagonal (D) direction

	Grade	Lot Code	Coating	Thickness (mm)	YS (MPa)	UTS (MPa)	YPE (%)	UE (%)	TE (%)	n (6-12%)	r
Baseline	DQSK	X1	Bare	0.77	172	322	0.00	20.80	38.30	0.239	1.531
		X2	Bare	1.19	190	325	0.00	20.40	37.20	0.224	1.508
	DDQ+	Y1	Bare	0.70	143	298	0.00	23.00	48.30	0.262	2.003
		Y2	Bare	1.19	144	301	0.00	22.50	43.90	0.272	1.733
Skin Panel Steels	BH210	B1	EG	0.70	253	362	0.15	19.50	37.00	0.180	1.459
		B2	EG	0.93	252	357	0.00	18.90	35.43	0.168	1.502
	BH280	C1	EG	0.71	342	432	0.28	17.50	30.40	0.164	0.871
		C2	EG	1.00	287	408	0.00	15.63	30.00	0.154	1.143
		C3	GA	1.04	302	404	0.34	19.67	35.53	0.187	0.856
	ULC BH340	D1	GA	0.74	257	368	0.19	17.70	34.03	0.166	2.005
		D2	GA	1.02	234	361	0.00	20.47	36.57	0.203	1.226
	IF-Rephos	E1	GA	0.63	202	358	0.00	22.17	38.30	0.235	1.880
		E2	GA	0.89	200	351	0.00	22.47	40.13	0.238	1.955
	DP 500	G1	EG	0.66	315	531	0.00	18.77	26.77	0.199	0.707
		G2	EG	0.81	336	552	0.00	16.97	25.57	0.177	0.824
Structural Steels	BH300	1K	GA	1.24	356	486	0.62	16.50	28.77	0.178	0.881
		2K	GI	1.19	308	414	0.57	18.30	35.83	0.179	1.569
	HSLA 350	1L	GI	1.16	410	465	7.85	19.23	30.30	0.217	1.149
		5L	Bare	1.21	372	489	0.00	16.53	28.97	0.169	1.411
		2L	GI	1.62	364	443	0.00	14.50	28.60	0.123	1.099
	HS 440W	1M	GA	1.24	359	487	0.39	16.67	30.43	0.176	0.778
		2M	GA	1.58	354	477	0.19	16.07	29.23	0.165	0.699
	DP600	1P	GI	0.96	378	620	0.00	16.43	23.90	0.183	0.858
		2P	Bare	1.19	380	641	0.00	15.27	22.67	0.177	0.686
		3P	GI	1.39	405	675	0.00	16.40	23.63	0.187	0.811
		4P	GI	1.23	436	677	0.00	13.77	20.93	0.147	0.902
		5P	GI	1.64	335	581	0.00	18.40	30.17	0.244	0.991
		6P	GI	1.49	435	673	0.00	13.93	21.20	0.146	1.024
	TRIP 600	1T	Bare	1.40	441	676	0.00	20.27	29.00	0.235	0.873
		2T	Bare	1.60	435	687	0.00	18.83	26.10	0.227	0.800
	DP800	1R	GI	1.20	503	833	0.00	10.90	18.50		
		2R	GI	1.59	440	785	0.00	10.87	17.83		
	DP980	1S	Bare	1.15	914	1040	0.61	5.77	11.60		
		2S	Bare	1.52	858	1022	0.36	6.17	11.90		
	RA 830	1W	GI	1.32	738	875			6.10		
		2W	GI	1.53	801	859			7.47		
		3W	Bare	1.25	764	930			3.30		
		4W	GA	1.80	626	853			4.00		
	M 190	1H	Bare	1.03	1239	1423	0.00	2.53	4.77		
		2H	Bare	1.58	1203	1372	0.00	2.43	5.77		

Table 2.4: Average mechanical properties ((L+T+2D)/4) for all the steel grades

	Grade	Lot Code	Coating	Thickness (mm)	YS (MPa)	UTS (MPa)	YPE (%)	UE (%)	TE (%)	n-bar (6-12%)	r-bar
Baseline	DQSK	X1	Bare	0.77	167	314	0.00	21.50	40.30	0.241	1.931
		X2	Bare	1.19	184	316	0.00	21.00	39.90	0.224	1.975
	DDQ+	Y1	Bare	0.70	140	295	0.00	23.80	48.20	0.264	2.254
		Y2	Bare	1.19	142	296	0.00	23.50	45.20	0.274	2.150
Skin Panel Steels	BH210	B1	EG	0.70	249	359	0.15	19.30	37.80	0.183	1.641
		B2	EG	0.93	248	353	0.02	19.00	36.70	0.171	1.754
	BH280	C1	EG	0.71	333	424	0.32	17.90	30.90	0.168	1.132
		C2	EG	1.00	281	402	0.00	16.00	31.90	0.157	1.469
		C3	GA	1.04	299	401	0.33	19.50	34.80	0.184	1.002
	ULC BH340	D1	GA	0.74	256	366	0.10	18.00	34.00	0.168	2.080
		D2	GA	1.02	229	356	0.00	21.20	38.10	0.206	1.535
	IF-Rephos	E1	GA	0.63	201	359	0.00	22.00	37.70	0.237	1.898
		E2	GA	0.89	199	355	0.00	22.20	39.10	0.239	1.829
	DP 500	G1	EG	0.66	310	528	0.00	18.90	27.50	0.201	0.833
		G2	EG	0.81	332	555	0.00	17.40	26.70	0.182	0.917
Structural Steels	BH300	1K	GA	1.24	351	483	0.84	16.50	29.00	0.179	1.043
		2K	GI	1.19	307	414	0.51	18.50	35.50	0.179	1.598
	HSLA 350	1L	GI	1.16	412	468	7.75	19.10	30.00	0.210	1.065
		5L	Bare	1.21	376	501	0.00	16.10	27.60	0.167	1.156
		2L	GI	1.62	364	445	0.00	14.60	28.60	0.125	1.085
	HS 440W	1M	GA	1.24	354	483	0.61	16.70	29.70	0.179	0.903
		2M	GA	1.58	347	468	0.26	16.70	30.80	0.171	0.938
	DP600	1P	GI	0.96	379	624	0.00	16.01	23.51	0.182	0.855
		2P	Bare	1.19	376	636	0.00	15.72	23.82	0.180	0.845
		3P	GI	1.39	397	671	0.00	16.20	23.10	0.188	0.869
		4P	GI	1.23	433	676	0.00	13.90	21.30	0.147	0.933
		5P	GI	1.64	337	583	0.76	18.50	30.60	0.244	1.010
		6P	GI	1.49	434	675	0.00	13.80	21.30	0.144	1.002
	TRIP 600	1T	Bare	1.40	439	673	0.00	19.90	28.60	0.237	0.930
		2T	Bare	1.60	430	680	0.00	19.30	27.30	0.234	0.890
	DP800	1R	GI	1.20	500	837	0.00	10.70	17.90		
		2R	GI	1.59	448	785	0.00	10.50	16.80		
	DP980	1S	Bare	1.15	907	1037	0.60	5.80	11.20		
		2S	Bare	1.52	862	1024	0.33	6.00	11.40		
	RA 830	1W	GI	1.32	664	879			4.20		
		2W	GI	1.53	735	886			6.44		
		3W	Bare	1.25	816	940			5.00		
		4W	GA	1.80	723	880			5.25		
	M 190	1H	Bare	1.03	1237	1432	0.00	2.50	4.70		
		2H	Bare	1.58	1209	1375	0.00	2.48	5.57		

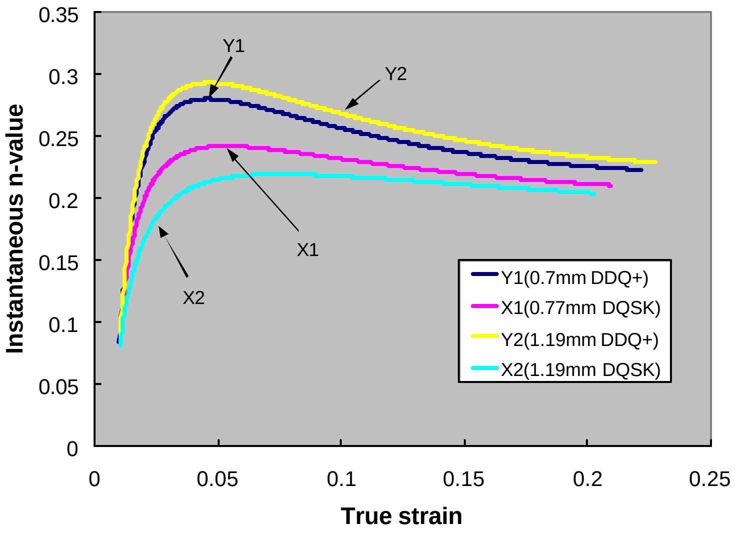

Figure 2.4: Instantaneous n-value vs. true strain for the baseline steel grades

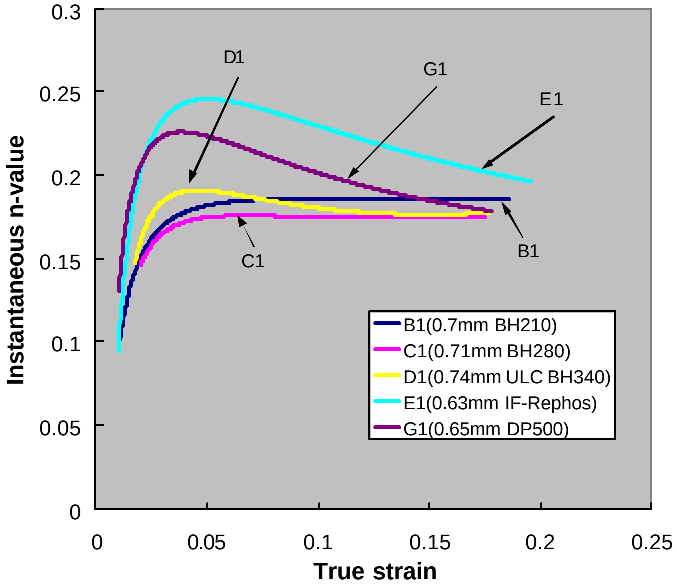

Figure 2.5: Instantaneous n-value vs. true strain for the skin panel steel grades of nominal thickness 0.65mm

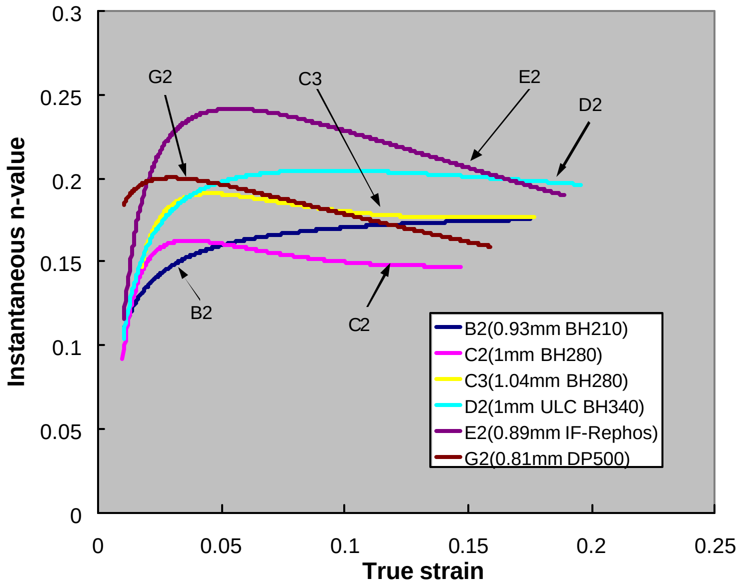

Figure 2.6: Instantaneous n-value vs. true strain for the skin panel steel grades of nominal thickness 0.95mm

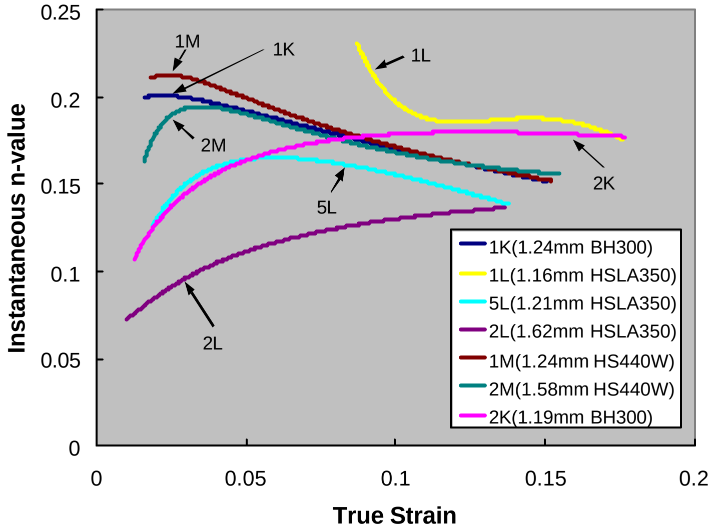

Figure 2.7: Instantaneous n-value vs. true strain for some conventional high strength steels used for structural applications

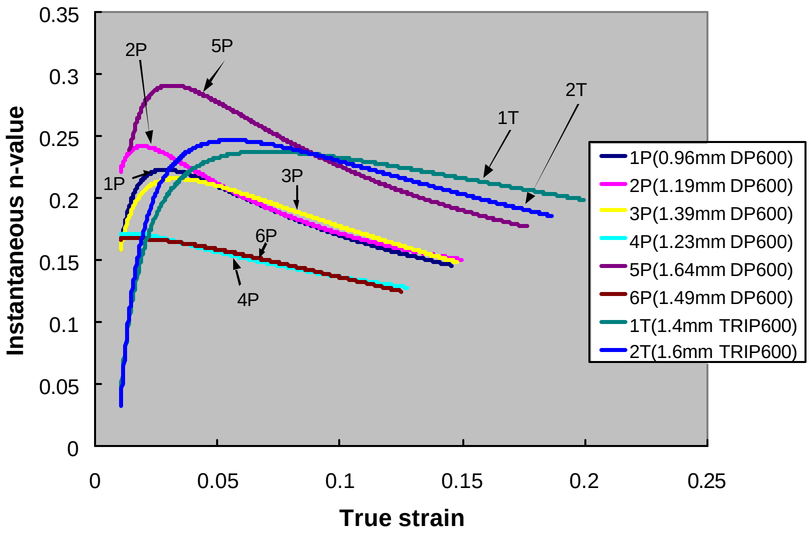

Figure 2.8: Instantaneous n-value vs. true strain for DP600 and TRIP600 steel grades

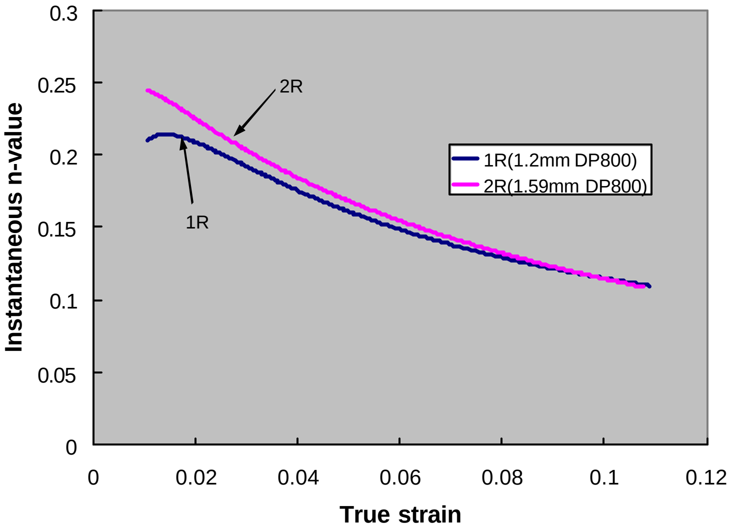

Figure 2.9: Instantaneous n-value vs. true strain for the DP800 steel grades

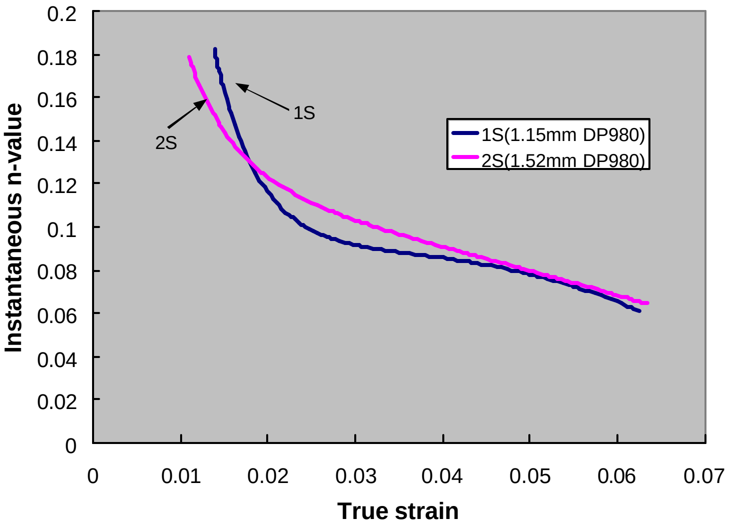

Figure 2.10: Instantaneous n-value vs. true strain for the DP980 steel grades

Figures 2.4 through 2.10 show trends of instantaneous work hardening behavior (n-value) as a function of the true strain. As seen in the figures, most of the steel grades have similar work hardening behavior showing a high rate of work hardening in the low strain region, which decreases with increasing strain. Notable exceptions to this observation were several traditional bake-hardenable steel grades such as B1, B2, C1, D2, 2K, where the n-value seems to approach some kind of a saturation value. For a given strength level the n-value of DP steels tends to reduce more significantly with increasing strain. This can be seen in Figure 2.6 where the reduction in n-value for the DP steels is higher than the TRIP steels. This difference in work-hardening might be important for stamping because the limit strains in a stamping could be dependent on the instantaneous work hardening behavior.

The trends of instantaneous n-value vs. true strain could be used to modify the simple power law of work hardening; $s = Ke^n$, by treating the n-value as a function of strain instead of a constant. Although most commercial FEA codes now have the ability to process true stress-strain behavior without the need for a constitutive equation, there are still many proprietary FEA codes used by researchers in universities and in the automotive industry, which were developed before the widespread use of commercial FEA software. These programs still rely on the traditional power law of work hardening for material hardening behavior. The trends of instantaneous n-value could assist these researchers working in the area of sheet metal forming in using more accurate representations of mechanical behavior of conventional and advanced high strength steels.

Section 3.0
Medium Strain Rate Mechanical Behavior

3.1 Summary

Stress-strain data have been generated in the strain rate region from 10^{-3} to 10^{1}/s for 36 lots of steel. This strain rate region is classified as the medium-rate regime [3.1]. The test results showed that YS and UTS increase while the modulus of elasticity does not change with strain rate. The increase of UTS per order of magnitude increase of strain rate, is 16 MPa for all the steels tested, except M190, which is 8 MPa. UE decreases with strain rate for DQSK and DDQ+, while the other steels show little strain rate dependence. The work hardening exponent (n-value) was found to decrease with strain rate, but the dependence decreases with higher steel strength. For steels of YS higher than 300 MPa, n-value is almost constant. Constants for two constitutive models, additive and multiplicative, are generated from the testing results for each lot of steel.

3.2 Testing Procedure

3.2.1 Materials

The program tested 36 out of 40 lots of steels from 15 steel grades. Four steel lots of RA830 were not tested since they showed low total elongation and tests at high strain rates were not successful.

3.2.2 Experimental Procedure

To achieve strain rates up to 10/s, the sub-size fatigue specimen (cut in the T direction) with a gage length of 7.62mm is used and is tested in the 5 kip MTS servohydraulic testing system. The maximum speed of the actuator is around 200mm/s, which corresponds to a maximum achievable strain rate of 26/s. Strain was measured by an extensometer to ensure measurement accuracy. Compared to the method commonly used at high strain rates that calculates strain by displacement, this direct measurement should provide the most accurate strain data. However, due to the structure limitations, the extensometer can only measure the strain up to 30% and at strain rates below 100/s. Therefore, no measurement was available for TE beyond 30%. Specimens were tested at 4 strain rates, 10^{-2}, 10^{-1}, 10^{0}, and 10/s. Two replicates were tested for each strain rate.

3.3 Results

A typical example of the engineering stress-strain data is given in Figure 3.1 for DQSK steel (Lot X1). The data are of excellent quality at strain rates below 10/s. The curves are very smooth and the slopes in the elastic regions are all close to the quasi-static Young's modulus. This confirms the finding by Yan et al. that the modulus of elasticity does not change significantly at high strain rates [3.2]. Oscillation starts to show at 10/s due to the ringing of the loading system that is typical for high strain rate testing. True stress-strain curves are shown in Figure 3.2. A Fourth order polynomial was used for curve smoothing and the smoothed curves are also shown in Figure 3.2. Tensile properties, YS, UTS, UE and full curve n-values were determined from each curve and are shown in Table 3.1a-f.

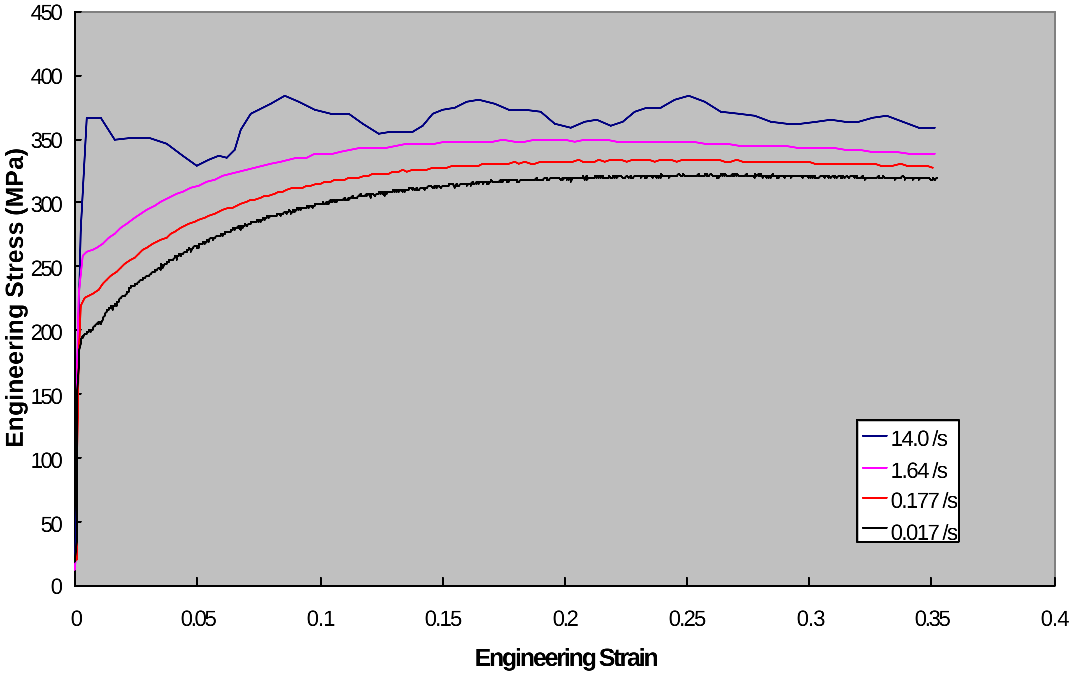

Figure 3.1: Engineering stress-strain curves for DQSK (Lot X1)

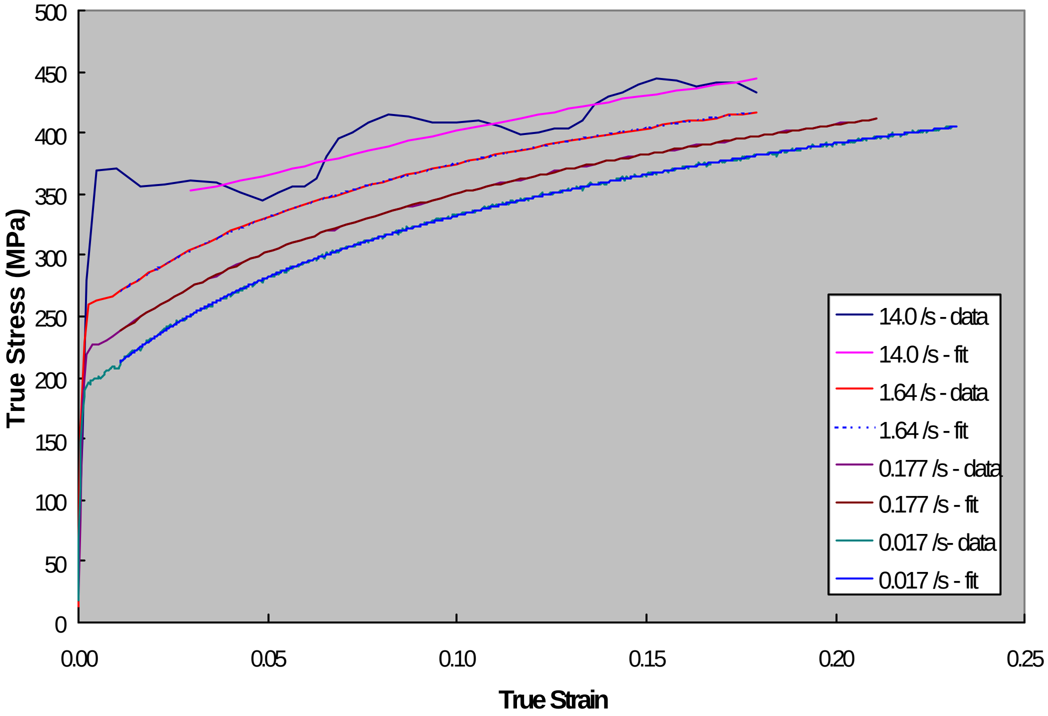

Figure 3.2: True stress-strain curves for DQSK (Lot X1)

Table 3.1a: Tensile Properties at Medium Strain Rates by Lot

Lot	Material	True Strain Rate	0.2% YS (MPa)	TS (MPa)	Uniform Elongation	n (2% - UE)
Baseline Steels						
X1	DQSK	0.001	167.1	313.9	0.215	0.24
		0.017	194.3	321.7	0.261	0.23
		0.177	222.6	333.1	0.235	0.21
		1.639	259.4	349.0	0.196	0.18
		14.018	366.8	362.1	0.196	0.15
X2		0.001	184.3	316.4	0.210	0.22
		0.018	204.3	313.8	0.246	0.21
		0.178	243.1	324.6	0.214	0.17
		1.656	281.7	344.7	0.179	0.15
		14.607	357.1	355.5	0.141	0.11
Y1	DDQ+	0.001	140.3	294.6	0.238	0.26
		0.017	173.8	307.2	0.269	0.26
		0.173	214.1	319.6	0.248	0.22
		1.626	253.3	337.3	0.203	0.17
		14.679	367.2	358.9	0.152	0.15
Y2		0.001	141.8	296.4	0.235	0.27
		0.016	169.0	307.7	0.275	0.26
		0.173	213.2	319.1	0.243	0.21
		1.619	251.8	336.3	0.211	0.17
		14.607	343.7	355.4	0.193	0.14
Skin Panel Steels						
B1	BH210	0.001	249.2	358.7	0.193	0.18
		0.018	266.7	357.7	0.206	0.18
		0.189	298.8	384.9	0.171	0.15
		1.658	336.5	369.7	0.188	0.16
		14.366	443.0	415.0	0.178	0.13
B2		0.001	247.8	352.7	0.190	0.17
		0.019	271.7	366.5	0.204	0.17
		0.189	294.8	375.4	0.183	0.15
		1.677	328.0	391.0	0.175	0.15
		14.438	420.9	405.2	0.180	0.13
C1	BH280	0.001	333.0	424.3	0.179	0.17
		0.019	345.2	422.8	0.192	0.17
		0.189	359.8	434.0	0.179	0.17
		1.654	386.0	449.7	0.173	0.16
		14.078	490.4	466.4	0.184	0.15

Table 3.1b: Tensile Properties at Medium Strain Rates by Lot

Lot	Material	True Strain Rate	0.2% YS (MPa)	TS (MPa)	Uniform Elongation	n (2% - UE)
C2	BH280	0.001	281.2	402.1	0.160	0.16
		0.018	290.8	404.4	0.173	0.17
		0.186	314.6	414.2	0.162	0.16
		1.606	347.5	429.3	0.156	0.16
		14.705	447.7	458.0	0.160	0.12
C3		0.001	298.9	400.6	0.195	0.18
		0.018	326.4	411.6	0.193	0.19
		0.188	339.4	414.3	0.181	0.18
		1.613	381.7	436.8	0.162	0.17
		14.238	461.5	457.7	0.151	0.13
D1	ULC BH 340	0.001	256.1	365.6	0.180	0.17
		0.019	280.1	369.2	0.178	0.16
		0.196	301.8	380.5	0.168	0.15
		1.663	336.2	396.0	0.161	0.14
		14.156	462.7	421.4	0.187	0.14
D2		0.001	229.4	355.6	0.212	0.21
		0.018	246.4	356.4	0.229	0.20
		0.184	274.5	368.7	0.204	0.18
		1.648	297.1	383.1	0.198	0.17
		14.320	398.7	395.0	0.215	0.15
E1	IF 340	0.001	200.6	358.6	0.220	0.24
		0.018	236.6	374.4	0.219	0.21
		0.182	256.3	385.0	0.201	0.20
		1.637	269.9	394.1	0.202	0.20
		13.845	359.8	400.7	0.206	0.19
E2		0.001	199.4	354.5	0.220	0.24
		0.018	223.6	365.9	0.228	0.24
		0.178	237.4	381.0	0.214	0.22
		1.608	275.7	396.7	0.202	0.20
		13.940	360.8	403.8	0.222	0.17
G1	DP500	0.001	309.8	528.3	0.189	0.20
		0.018	313.7	536.3	0.196	0.21
		0.179	325.2	546.1	0.177	0.21
		1.549	346.1	569.1	0.168	0.22
		13.390	431.3	585.5	0.172	0.21

Table 3.1c: Tensile Properties at Medium Strain Rates by Lot

Lot	Material	True Strain Rate	0.2% YS (MPa)	TS (MPa)	Uniform Elongation	n (2% - UE)
G2	DP500	0.001	332.1	555.0	0.174	0.18
		0.018	326.2	558.6	0.183	0.19
		0.183	345.3	570.0	0.164	0.19
		1.552	358.2	592.0	0.158	0.19
		14.551	439.2	608.3	0.176	0.18
Structural Steels						
1K	BH300	0.001	351.3	482.7	0.165	0.18
		0.018	361.0	493.1	0.177	0.19
		0.176	371.8	502.0	0.162	0.20
		1.521	398.8	519.7	0.158	0.20
		12.628	457.0	535.2	0.161	0.19
2K		0.001	307.2	413.5	0.185	0.18
		0.018	325.7	423.2	0.205	0.17
		0.186	342.9	435.3	0.186	0.17
		1.660	361.7	450.0	0.183	0.17
		13.425	445.0	463.2	0.181	0.15
1L	HSLA350	0.001	412.0	468.0	0.191	0.21
		0.016	436.5	476.0	0.201	0.191
		0.210	483.0	482.7	0.201	0.206
		1.737	534.1	502.5	0.207	0.194
		17.549	629.3	510.0	0.218	0.239
2L		0.001	364.0	445.4	0.146	0.13
		0.019	377.7	461.8	0.165	0.13
		0.188	390.2	473.2	0.152	0.12
		1.666	411.5	488.5	0.143	0.12
		13.855	466.7	510.9	0.121	0.11
5L		0.001	376.4	500.5	0.161	0.17
		0.018	412.5	541.5	0.159	0.16
		0.178	423.3	551.8	0.148	0.16
		1.593	446.9	565.2	0.146	0.16
		13.585	507.4	592.6	0.151	0.15
1M	440W	0.001	354.0	483.4	0.167	0.18
		0.017	363.7	500.2	0.174	0.19
		0.170	378.6	512.4	0.155	0.18
		1.563	397.8	527.9	0.154	0.19
		12.179	462.6	548.8	0.146	0.18

Table 3.1d: Tensile Properties at Medium Strain Rates by Lot

Lot	**Material**	**True Strain Rate**	**0.2% YS (MPa)**	**TS (MPa)**	**Uniform Elongation**	**n (2% - UE)**
2M	440W	0.001	347.3	468.1	0.167	0.17
		0.017	347.2	474.4	0.174	0.18
		0.176	354.2	482.2	0.164	0.19
		1.546	384.3	498.4	0.163	0.19
		13.218	445.3	511.7	0.169	0.18
1P	DP600	0.001	379.0	624.0	0.160	0.18
		0.017	398.5	651.2	0.160	0.19
		0.175	411.2	654.4	0.147	0.19
		1.498	429.3	677.3	0.144	0.19
		13.145	497.4	705.4	0.153	0.19
2P		0.001	375.8	635.1	0.157	0.18
		0.017	366.5	633.6	0.167	0.21
		0.175	371.9	640.8	0.157	0.20
		1.492	401.8	661.4	0.151	0.21
		13.043	479.1	674.8	0.168	0.20
3P		0.001	396.5	671.1	0.162	0.19
		0.016	410.7	685.4	0.169	0.20
		0.162	419.0	693.8	0.158	0.20
		1.448	428.5	721.6	0.144	0.19
		12.451	461.2	741.1	0.165	0.19
4P		0.001	432.7	676.0	0.139	0.15
		0.017	435.0	694.6	0.152	0.16
		0.172	443.6	709.1	0.134	0.16
		1.452	455.2	728.9	0.128	0.17
		12.900	511.3	754.0	0.136	0.16
5P		0.001	337.2	583.2	0.185	0.24
		0.015	346.2	605.2	0.193	0.25
		0.155	355.1	608.9	0.179	0.24
		1.402	375.5	626.2	0.174	0.26
		11.169	428.1	648.7	0.166	0.23
6P		0.001	434.0	674.5	0.138	0.14
		0.017	448.8	696.7	0.141	0.16
		0.169	458.5	709.8	0.129	0.15
		1.497	472.0	727.3	0.125	0.16
		12.443	504.7	750.1	0.111	0.16

Table 3.1e: Tensile Properties at Medium Strain Rates by Lot

Lot	Material	True Strain Rate	0.2% YS (MPa)	TS (MPa)	Uniform Elongation	n (2% - UE)
1R	DP800	0.001	499.5	836.7	0.107	-
		0.017	489.5	866.4	0.120	0.17
		0.166	506.6	884.0	0.113	0.17
		1.374	511.3	898.7	0.110	0.18
		11.357	521.5	918.8	0.102	0.19
2R		0.001	447.9	785.2	0.105	-
		0.017	452.5	806.8	0.131	0.17
		0.153	458.7	818.0	0.119	0.17
		1.391	465.6	842.1	0.117	0.18
		11.608	486.6	864.5	0.115	0.18
1S	DP980	0.001	907.1	1037.2	0.058	-
		0.017	918.0	1052.7	0.064	0.09
		0.172	931.5	1065.3	0.065	0.09
		1.553	942.3	1081.0	0.068	0.10
		11.709	969.2	1093.1	0.052	0.07
2S		0.001	862.0	1023.6	0.060	-
		0.017	854.5	1020.1	0.074	0.10
		0.169	871.9	1034.3	0.072	0.10
		1.546	888.3	1054.4	0.073	0.10
		12.769	929.1	1061.5	0.102	0.09
1T	TRIP600	0.001	438.5	673.4	0.199	0.24
		0.017	445.9	684.2	0.218	0.23
		0.168	465.3	690.1	0.188	0.22
		1.601	484.2	710.6	0.185	0.22
		12.158	541.7	736.2	0.184	0.21
2T		0.001	429.9	680.2	0.193	0.23
		0.017	445.6	696.7	0.204	0.24
		0.165	455.8	701.0	0.188	0.23
		1.566	471.2	720.4	0.175	0.24
		11.784	525.7	736.7	0.167	0.22
1H	M190	0.001	1237.0	1432.0	0.025	-
		0.017	1202.0	1426.9	0.037	0.06
		0.142	1231.9	1440.2	0.030	0.06
		1.372	1240.0	1444.0	0.035	0.05
		8.264	1219.2	1464.7	0.032	0.07

Table 3.1f: Tensile Properties at Medium Strain Rates by Lot

Lot	Material	True Strain Rate	0.2% YS (MPa)	TS (MPa)	Uniform Elongation	n (2% - UE)
2H	M190	0.001	1209.0	1375.0	0.025	-
		0.014	1204.2	1384.3	0.046	0.05
		0.160	1211.1	1390.2	0.035	0.05
		1.219	1214.9	1391.3	0.040	0.05
		12.291	1292.4	1394.5	0.034	0.04

3.3.1 Tensile Properties at Medium Strain Rates

The steels for a given lot show variability in tensile properties since they were supplied from different suppliers as shown in Table 2.4. This variability is also reflected at higher strain rates. Figures 3.3a through 3.3d show the range of the ultimate tensile strength, yield strength, uniform elongation and full curve n-value (2% to UE) for the 6 lots of DP600. Despite marked differences in the properties among the different lots of DP600, their dependence on strain rate is generally similar. Average tensile properties are thus used as representative values (shown in Tables 3.2a-c) to compare the strain rate dependence of tensile properties for each of these grades.

Table 3.2a: Average Tensile Properties at Medium Strain Rates by Grade

Material	True Strain Rate	0.2% YS (MPa)	TS (MPa)	Uniform Elongation	n (2% - UE)
Baseline Steels					
DQSK	0.001	176	315	0.213	0.233
	0.017	199	318	0.254	0.222
	0.177	233	329	0.224	0.191
	1.639	271	347	0.187	0.161
	14.018	362	359	0.169	0.126
DDQ+	0.001	141	296	0.237	0.269
	0.017	171	307	0.272	0.256
	0.173	214	319	0.246	0.216
	1.626	253	337	0.207	0.171
	14.679	355	357	0.172	0.143
Skin Panel Steels					
BH210	0.001	249	356	0.192	0.177
	0.018	269	362	0.205	0.172
	0.189	297	380	0.177	0.148
	1.658	332	380	0.182	0.158
	14.366	432	410	0.179	0.128

Table 3.2b: Average Tensile Properties at Medium Strain Rates by Grade

Material	**True Strain Rate**	**0.2% YS (MPa)**	**TS (MPa)**	**Uniform Elongation**	**n (2% - UE)**
BH280	0.001	304	409	0.178	0.170
	0.019	321	413	0.186	0.178
	0.189	338	421	0.174	0.173
	1.654	372	439	0.164	0.163
	14.078	467	461	0.165	0.132
ULC BH 340	0.001	243	361	0.196	0.187
	0.019	263	363	0.203	0.177
	0.196	288	375	0.186	0.165
	1.663	317	390	0.179	0.159
	14.156	431	408	0.201	0.145
IF 340	0.001	200	357	0.220	0.238
	0.018	230	370	0.224	0.228
	0.182	247	383	0.208	0.212
	1.637	273	395	0.202	0.198
	13.845	360	402	0.214	0.183
DP500	0.001	321	542	0.182	0.192
	0.018	320	547	0.189	0.204
	0.179	335	558	0.170	0.201
	1.549	352	581	0.163	0.204
	13.390	435	597	0.174	0.195
Structural Steels					
BH300	0.001	329	448	0.175	0.179
	0.018	343	458	0.191	0.183
	0.176	357	469	0.174	0.184
	1.521	380	485	0.171	0.183
	12.628	451	499	0.171	0.172
HSLA350	0.001	370	473	0.154	0.146
	0.019	395	502	0.162	0.146
	0.188	407	513	0.150	0.142
	1.666	429	527	0.144	0.142
	13.855	487	552	0.136	0.129
440W	0.001	351	476	0.167	0.175
	0.017	355	487	0.174	0.185
	0.170	366	497	0.160	0.184
	1.563	391	513	0.159	0.190
	12.179	454	530	0.158	0.180

Table 3.2c: Average Tensile Properties at Medium Strain Rates by Grade

Material	True Strain Rate	0.2% YS (MPa)	TS (MPa)	Uniform Elongation	n (2% - UE)
DP600	0.001	392	643	0.145	0.181
	0.017	401	661	0.164	0.194
	0.175	410	669	0.150	0.191
	1.498	427	690	0.144	0.196
	13.145	480	712	0.150	0.190
TRIP600	0.001	434	677	0.196	0.235
	0.017	446	690	0.211	0.231
	0.168	461	696	0.188	0.226
	1.601	478	716	0.180	0.230
	12.158	534	736	0.176	0.216
DP800	0.001	474	811	0.106	-
	0.017	471	837	0.126	0.171
	0.166	483	851	0.116	0.171
	1.374	488	870	0.113	0.180
	11.357	504	892	0.109	0.184
DP980	0.001	885	1030	0.059	-
	0.017	886	1036	0.069	0.095
	0.172	902	1050	0.069	0.095
	1.553	915	1068	0.071	0.097
	11.709	949	1077	0.077	0.079
M190	0.001	1224	1404	0.025	-
	0.017	1203	1406	0.041	0.054
	0.142	1221	1415	0.032	0.057
	1.372	1227	1418	0.037	0.055
	8.264	1256	1430	0.033	0.051

3.3.2 Yield Strength and Ultimate Tensile Strength vs. Strain Rate

The relationship of yield strength and ultimate tensile strength with strain rate is shown in Figures 3.4 and 3.5. As expected, yield strength and ultimate tensile strength exhibit positive strain rate dependence. While the increase of YS with strain rate is slightly higher for steels of lower strength, and is also higher at higher strain rates (> 1/s), the increase of UTS with increasing strain rate is almost the same for all steels (see Figure 3.5). By using the slope of the curves in the semi log plot, Figure 3.5, the increase of UTS (ΔUTS) per order of magnitude increase of strain rate can be calculated. This slope value, or increase of UTS, is plotted in Figure 3.6 vs. quasi-static UTS. It is obvious that the ΔUTS, is almost constant for all the steels, around 16 MPa. Only M190 shows lower ΔUTS, 8 MPa. The stress ratio, $UTS_{10}/UTS_{0.001}$ is shown decreasing in Figure 3.7 as the steel strength increases as widely known.

The phenomenon of constant ΔUTS has been reported by Yan et al. [3.2]. However, the ΔUTS reported was 22 MPa. This difference is attributed to the fact that the range of strain rates studied by Yan et al. was from 10^{-3} to 10^{3}/s. Since the strain rate dependence is much higher at strain rates higher than 100/s [3.2], it is expected that the results in this study should be lower since it represents the increase of UTS at a lower strain rate region.

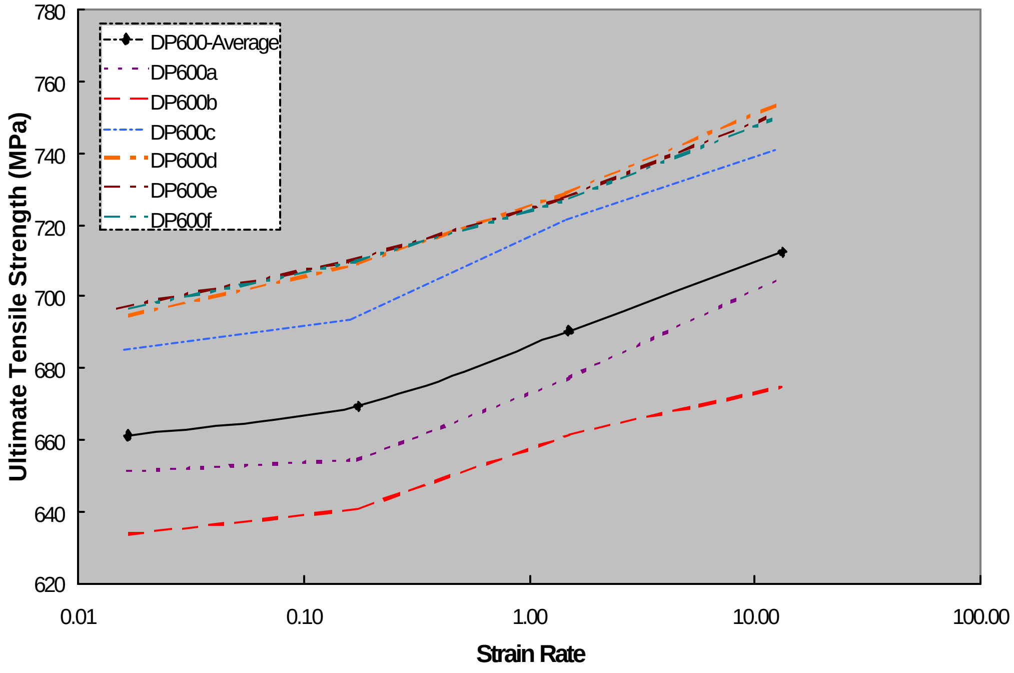

Figure 3.3a: Ultimate tensile strength vs. strain rate for six DP600 lots

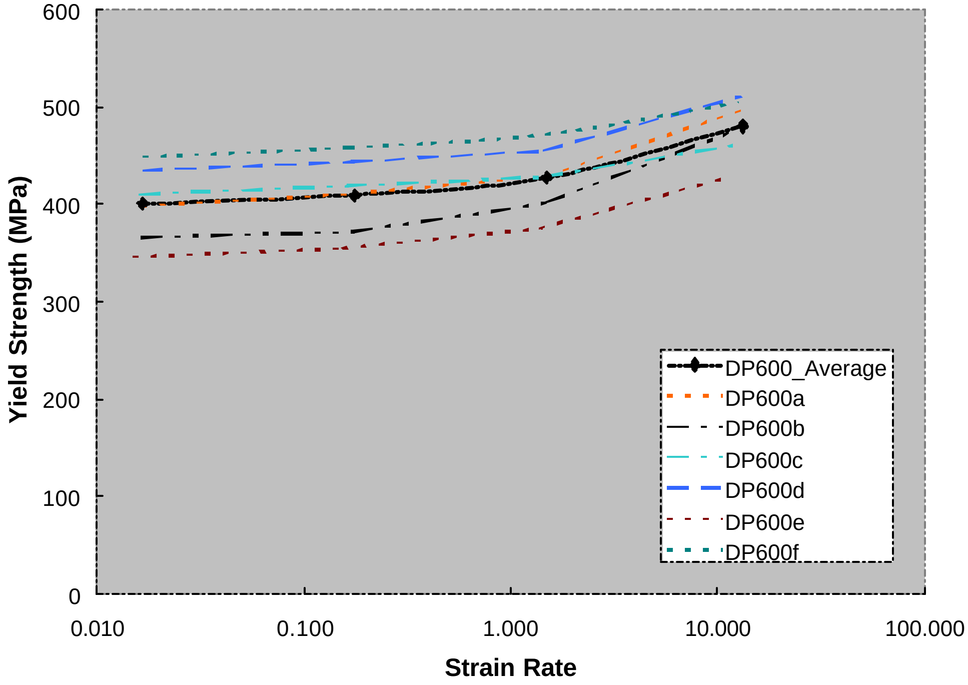

Figure 3.3b: Yield strength vs. strain rate for six DP600 lots

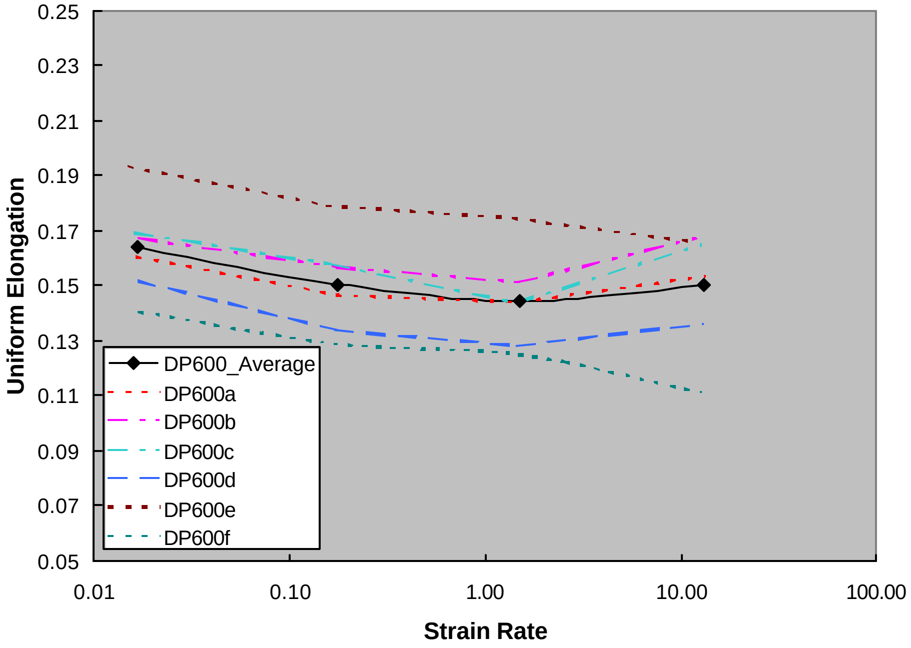

Figure 3.3c: Uniform elongation vs. strain rate for six DP600 lots

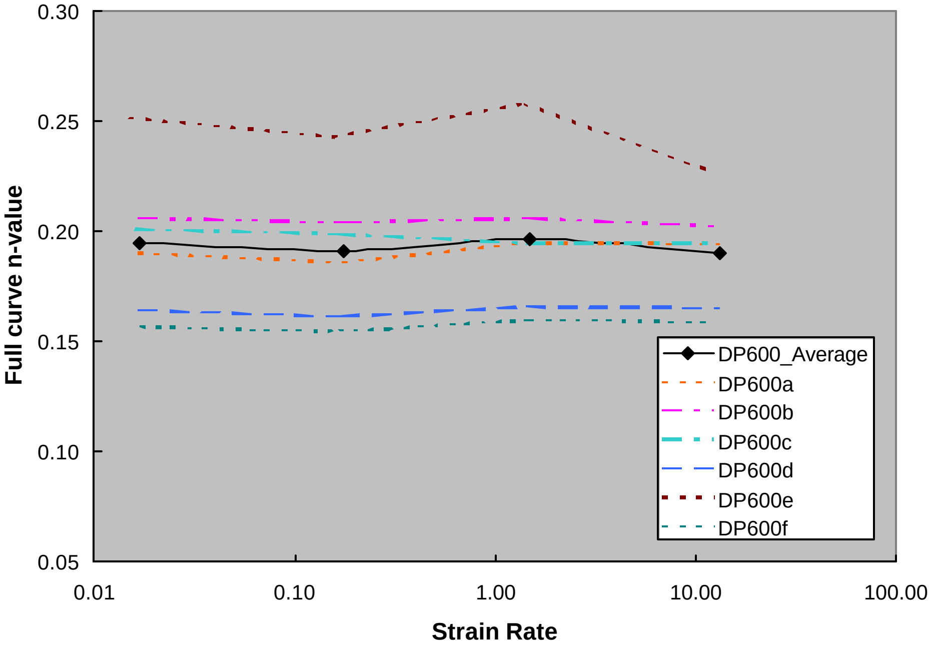

Figure 3.3d: Full curve n-value vs. strain rate for six DP600 lots

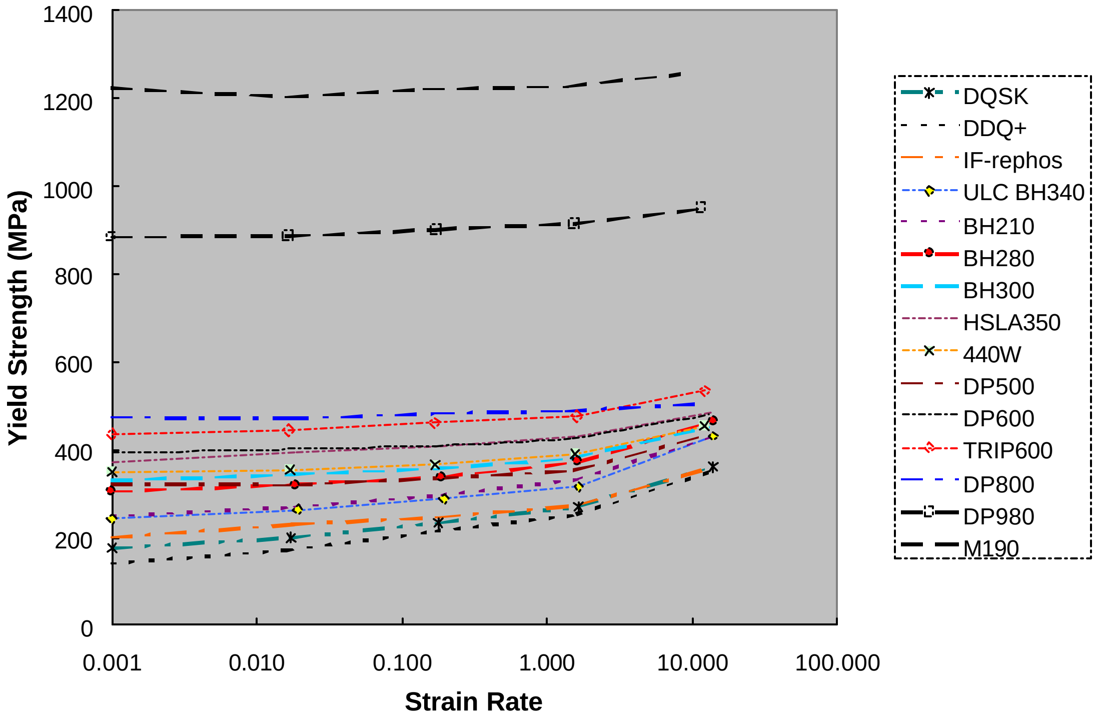

Figure 3.4: Yield strength vs. strain rate by steel grade

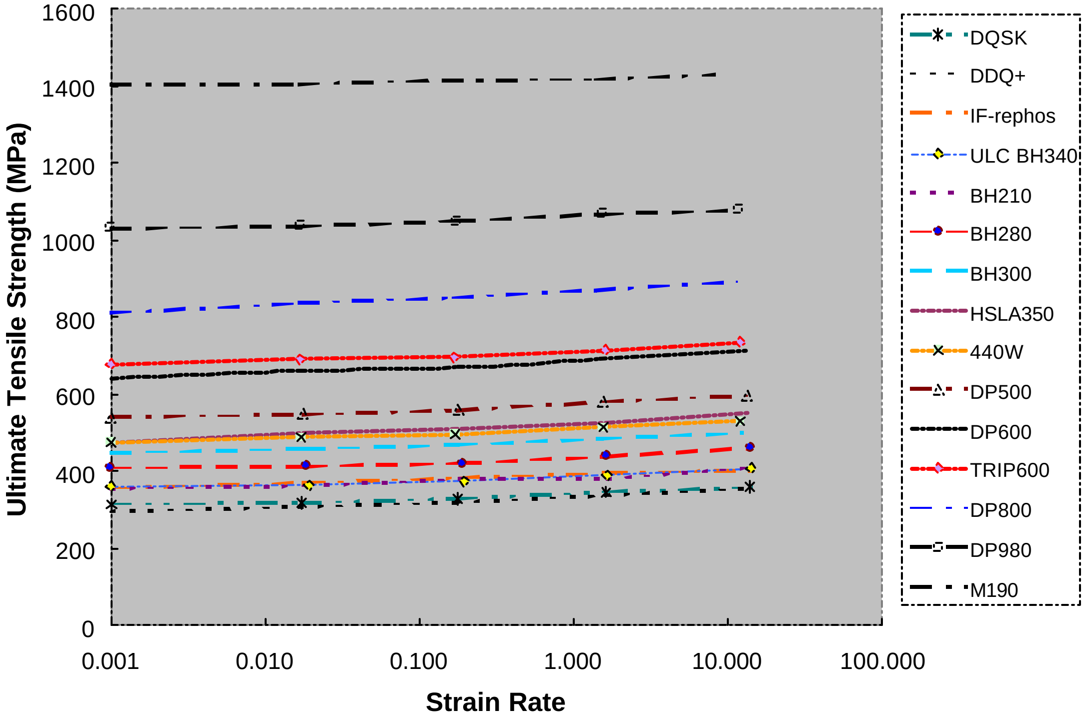

Figure 3.5: Tensile strength vs. strain rate by steel grade

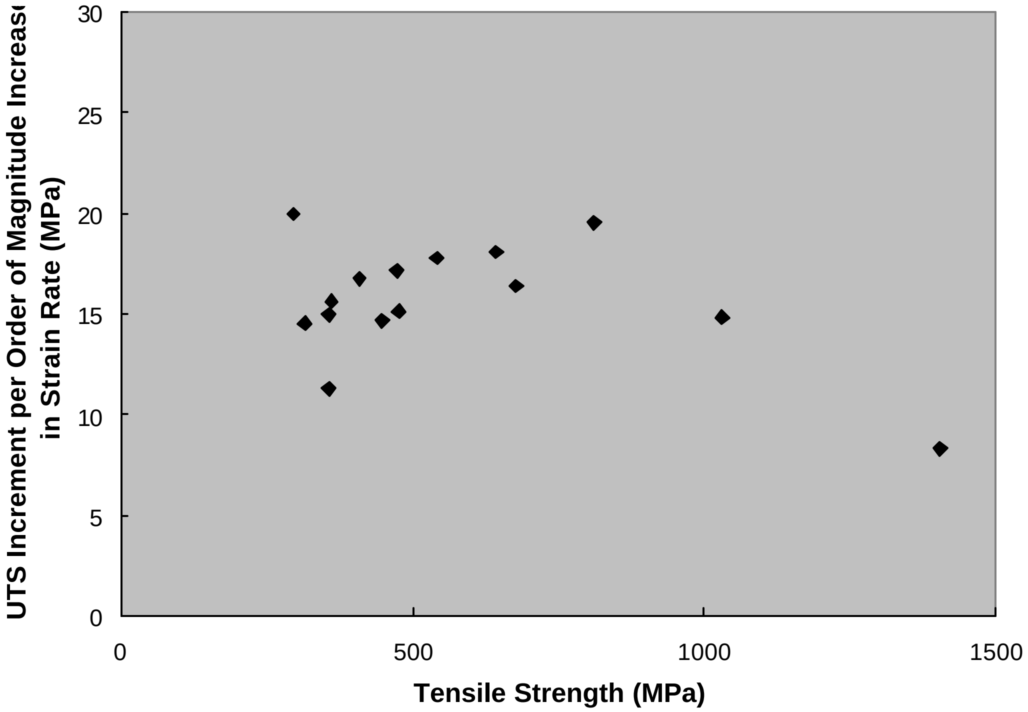

Figure 3.6: Increase of ultimate tensile strength vs. quasi-static ultimate tensile strength, showing around 16 MPa increase for all steels except M190

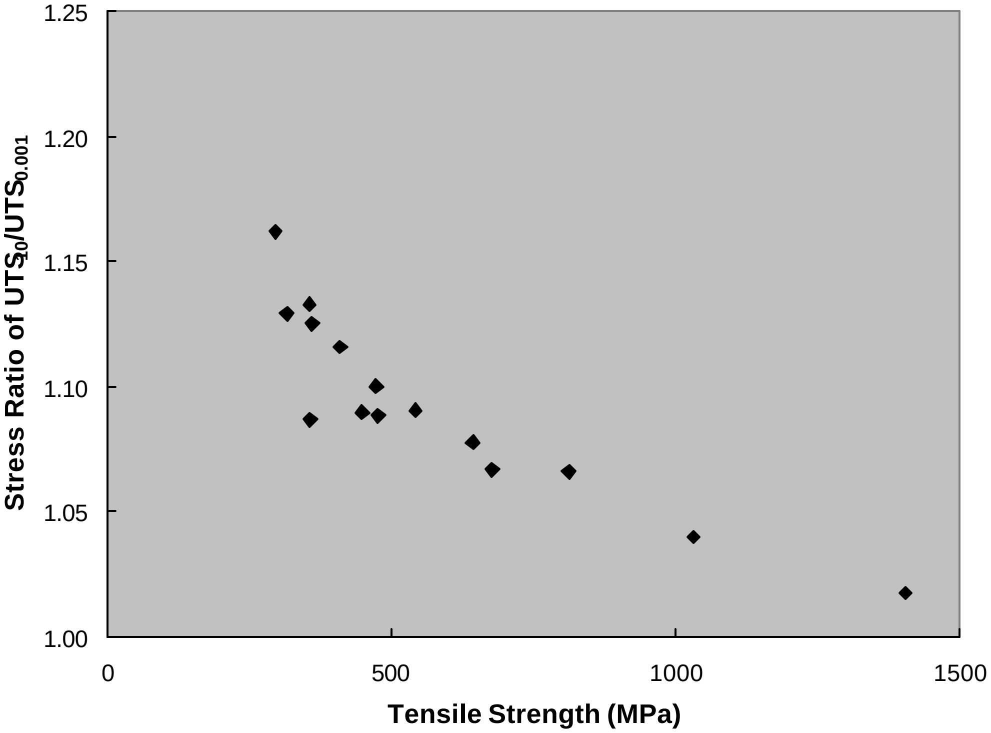

Figure 3.7: Stress ratio of $UTS_{10}/UTS_{0.001}$ decreases with increasing steel strength

3.3.3 Uniform Elongation vs. Strain Rate

Figures 3.8a and 3.8b show the relationship between uniform elongation and strain rate for the steels tested. Figure 3.8a is for steels of YS less than 300 MPa. Only two grades with the lowest strength, DQSK and DDQ+, exhibited marked decrease of uniform elongation with increasing strain rate. While BH210, BH280, BH300, HSLA 350, TRIP600 and DP800 showed slight decrease with strain rate, all the other steels exhibited very little changes.

3.3.4 n - Value (full curve)

The effect of strain rates on n-value is shown in Figures 3.9a and 3.9b. For steels in Figure 3.9a, i.e. i.e. yield strength below 300 MPa, the n-value decreases with increasing strain rate. The decrease is less for steels of higher strength. For steels of higher strength as in Figure 3.9b, there is little strain rate dependence for the full curve n-value, including DP and martensitic steels.

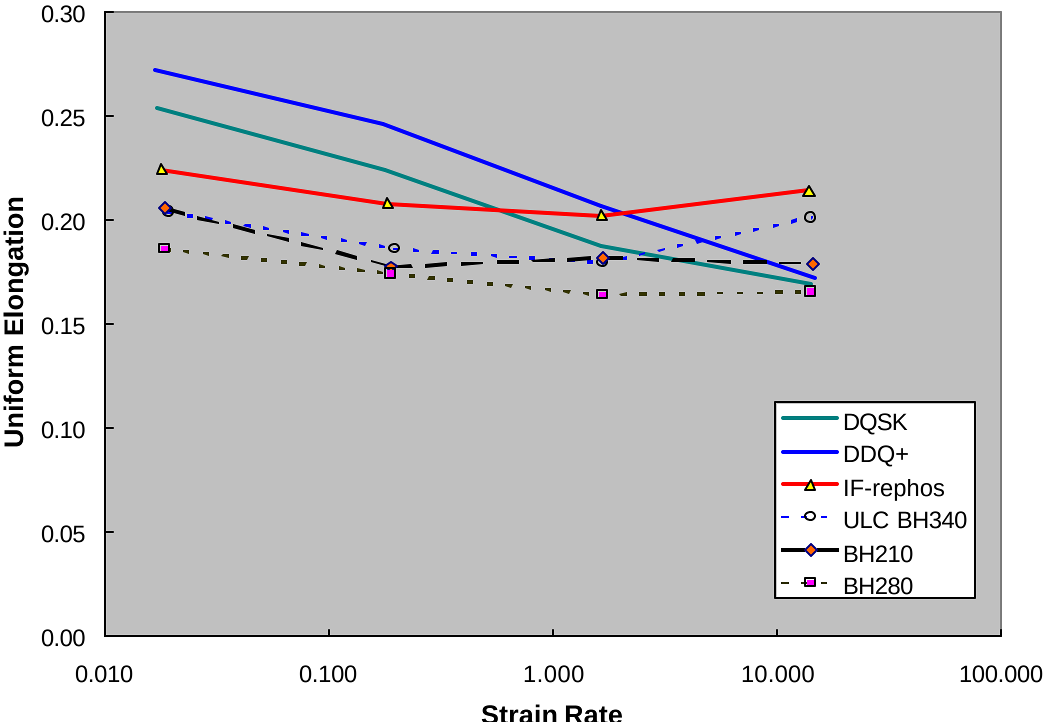

Figure 3.8a: Uniform elongation vs. strain rate for steels of YS less than 300 MPa

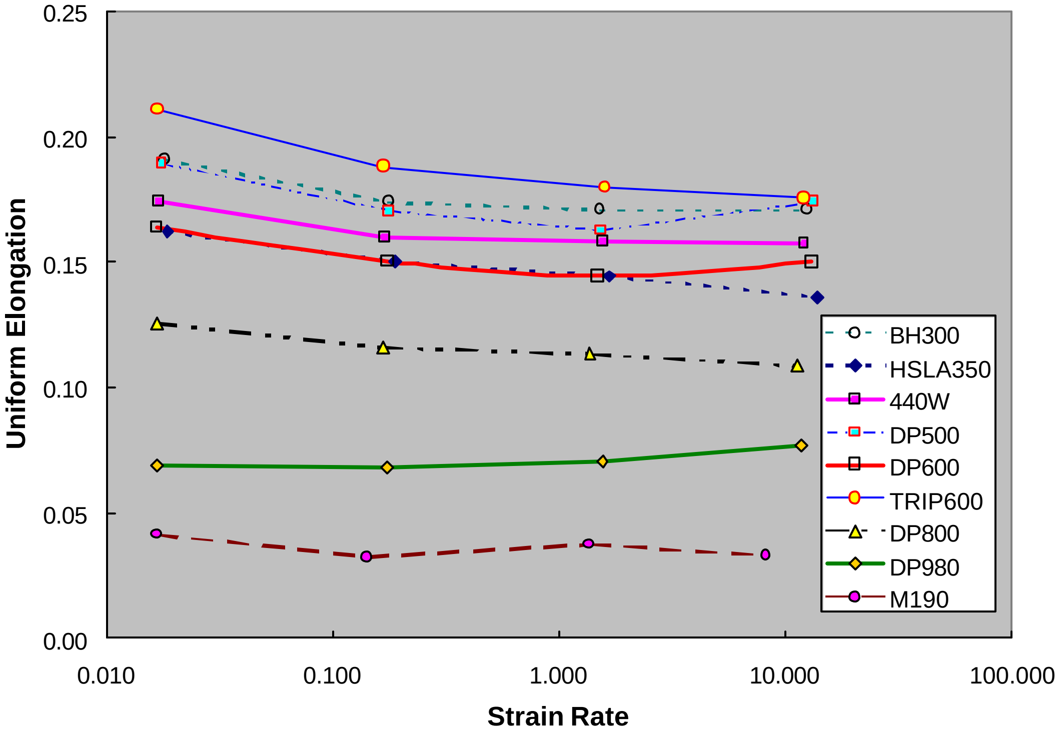

Figure 3.8b: Uniform elongation vs. strain rate for steels of YS equal and higher than 300 MPa

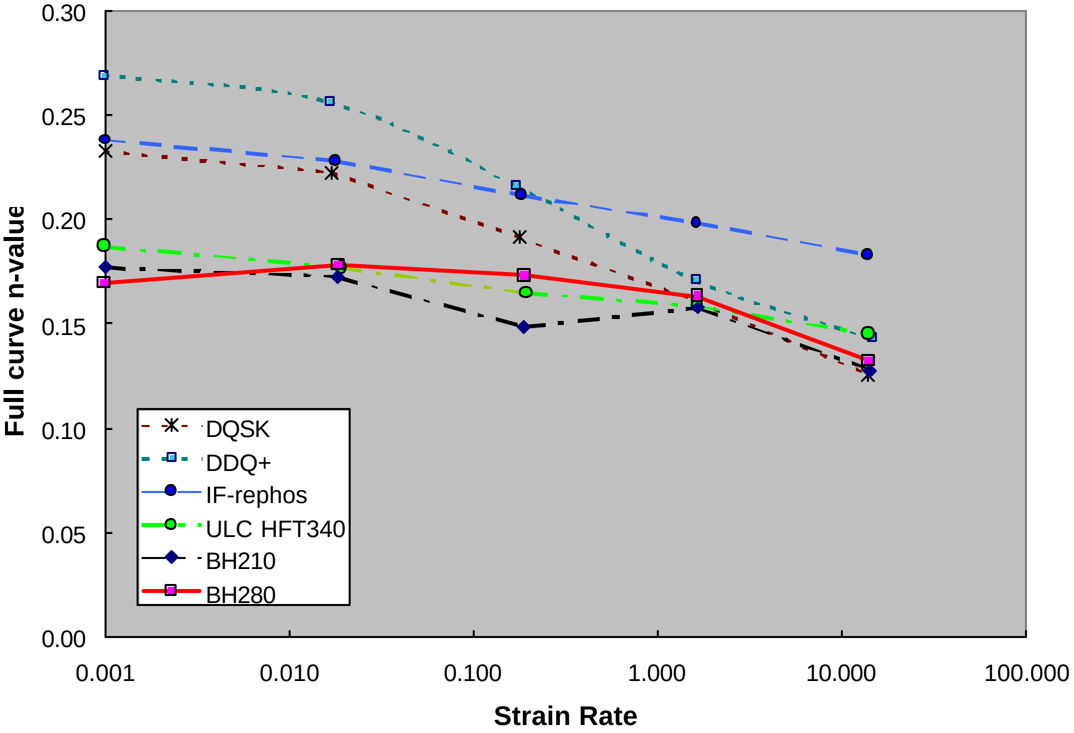

Figure 3.9a: n-value vs. strain rate for steels of YS less than 300 MPa

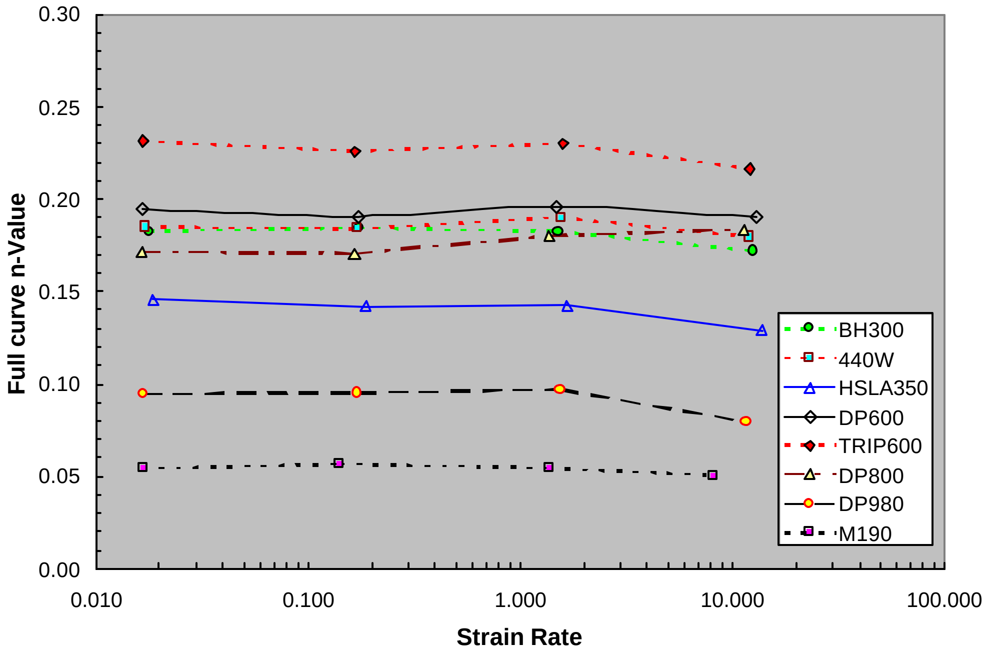

Figure 3.9b: n-value vs. strain rate for steels of YS equal and higher than 300 MPa

3.4 Constitutive Models

The testing data have been fitted into two constitutive models, additive and multiplicative.

3.4.1 Additive model

$$s = s_0 + m\ln\left(\frac{\dot{e}}{\dot{e}_0}\right)$$

where $\sigma_0 = A\,\varepsilon^B$, $m = C\,\varepsilon^D$, A, B, C and D are constants.

This model is an extension of the simple additive model where σ_0 and m are constant.

3.4.2 Multiplicative model

$$s = s_0 * \left(\frac{\dot{e}}{\dot{e}_0}\right)^m$$

where $\sigma_0 = e^{(A*\ln\varepsilon + B)}$, $m = C\ln\varepsilon + D$, A, B, C and D are constants.

This model is an extension of the simple multiplicative model where σ_0 and m are constant.

The fit constants for these models are summarized in Table 3.3 for each lot of the steels tested in this program. An average m value (strain rate sensitivity exponent) was calculated based on the multiplicative model.

Table 3.3: Fit Constants for Additive and Multiplicative Constitutive Models

Lot	**Material**	**Additive**				**Multiplicative**				**m**
		A	**B**	**C**	**D**	**A**	**B**	**C**	**D**	
Baseline Steels										
X1	DQSK	576.57	0.2437	5.920	-0.2511	0.2398	6.3514	-0.0144	-0.0037	0.031
X2		539.20	0.2204	5.948	-0.2921	0.2157	6.2828	-0.0164	-0.0058	0.036
Y1	DDQ+	577.54	0.2710	5.455	-0.3290	0.2651	6.3492	-0.0202	-0.0130	0.037
Y2		571.22	0.2674	5.810	-0.3052	0.2616	6.3390	-0.0192	-0.0098	0.036
Skin Panel Steels										
B1	BH210	585.43	0.1859	5.650	-0.2074	0.1838	6.3691	-0.0091	0.0013	0.024
B2		585.44	0.1723	4.709	-0.1803	0.1712	6.3708	-0.0064	0.0024	0.018
C1	BH280	690.55	0.1816	7.003	-0.0390	0.1810	6.5369	-0.0036	0.0077	0.017
C2		654.51	0.1775	5.712	-0.1754	0.1756	6.4808	-0.0073	0.0016	0.021
C3		688.66	0.1985	4.745	-0.2439	0.1964	6.5309	-0.0095	-0.0040	0.021
D1	ULC BH340	586.19	0.1665	5.958	-0.1003	0.1656	6.3724	-0.0049	0.0063	0.018
D2		600.58	0.2014	5.443	-0.1503	0.2001	6.3960	-0.0071	0.0030	0.020
E1	IF-Rephos	646.87	0.2152	7.425	0.0794	0.2149	6.4723	-0.0021	0.0102	0.014
E2		659.79	0.2368	5.805	-0.1619	0.2349	6.4888	-0.0087	0.0008	0.022
G1	DP 500	939.74	0.2171	11.990	0.1569	0.2169	6.8457	-0.0010	0.0117	0.014
G2		943.78	0.1961	9.089	0.0352	0.1958	6.8496	-0.0023	0.0081	0.014
Structural Steels										
1K	BH300	830.93	0.1957	13.022	0.2047	0.1956	6.7232	0.0001	0.0148	0.015
2K		676.42	0.1737	7.490	-0.0116	0.1731	6.5164	-0.0030	0.0091	0.017
1L	HSLA 350	745.91	0.1624	71.788	1.2265	0.1638	6.6179	0.0114	0.0339	0.010
2L		662.92	0.1218	9.946	0.0603	0.1216	6.4972	-0.0009	0.0142	0.017
5L		856.78	0.1640	7.296	-0.0079	0.1638	6.7531	-0.0022	0.0070	0.013
1M	HS 440W	836.48	0.1897	9.961	0.0868	0.1895	6.7294	-0.0015	0.0109	0.015
2M		784.49	0.1865	9.524	0.1353	0.1863	6.6653	-0.0006	0.0115	0.013
1P	DP600	1093.10	0.1909	15.016	0.2636	0.1909	6.9974	0.0007	0.0128	0.011
2P		1109.49	0.2100	9.957	0.1448	0.2100	7.0119	-0.0007	0.0086	0.010
3P		1176.96	0.2034	14.081	0.1067	0.2033	7.0711	-0.0014	0.0111	0.015
4P		1128.64	0.1703	12.176	0.1222	0.1702	7.0289	-0.0006	0.0102	0.012
5P		1156.82	0.2603	8.053	-0.0091	0.2598	7.0529	-0.0034	0.0047	0.014
6P		1101.77	0.1589	14.247	0.1719	0.1589	7.0051	0.0001	0.0124	0.012
1R	DP800	1444.99	0.1744	24.207	0.3898	0.1745	7.2763	0.0015	0.0132	0.009
2R		1342.92	0.1781	17.927	0.2352	0.1781	7.2030	0.0005	0.0124	0.011
1S	DP980	1573.68	0.1172	9.646	0.0531	0.1174	7.3620	-0.0005	0.0058	0.008
2S		1556.40	0.1273	3.350	-0.2771	0.1268	7.3490	-0.0042	-0.0054	0.009
1T	TRIP 600	1196.18	0.2242	10.590	0.0561	0.2240	7.0869	-0.0021	0.0078	0.015
2T		1254.46	0.2361	13.566	0.1669	0.2361	7.1348	-0.0008	0.0104	0.013
1H	M 190	2253.32	0.1195	5.323	0.0100	0.1195	7.7202	-0.0004	0.0020	0.004
2H		2208.68	0.1222	0.002	-1.9022	0.1219	7.6992	-0.0062	-0.0213	0.004

3.5 CONCLUSIONS

1. Stress-strain data at medium strain rates, 10^{-3} to 10^{1}/s, the practical strain rate region for forming, have been generated for 15 automotive sheet steels, of which 13 are high strength steels.
2. The following strain rate dependence is observed:
   - YS and UTS increase with strain rate.
   - There is no marked change of the modulus of elasticity with strain rate.
   - In the strain rate between 10^{-3} to 10^{1}/s, ΔUTS, the increase of UTS per order of magnitude increase of strain rate, is 16 MPa for all the steels tested, except M190, which is 8 MPa.
   - UE decreases with strain rate for DQSK and DDQ+; all the other steels show very little strain rate dependence.
   - n-value decreases with strain rate. However, the dependence decreases with higher strength steels. For steels of YS higher than 300 MPa, n-value is almost constant, including DP and martensitic steels.
3. Constants for two constitutive models, additive and multiplicative, are generated from the testing results for each lot of steel.

Section 4.0
Bauschinger Effect

4.1 Summary

The Bauschinger effect is defined as the lowering of the yield stress when deformation in one direction is followed by deformation in the opposite direction. The Bauschinger effect has been determined for 16 steel grades, including DP and TRIP steels. The results show that the Bauschinger effect is dependent on: the amount of plastic prestrain, the strength of the steel and its microstructure. The Bauschinger effect increases with increasing plastic prestrain. Higher strength steels exhibit a higher Bauschinger effect with mild steels showing the lowest, conventional high strength steels next and advanced high strength steels showing the highest. However, TRIP steels show a relatively lower Bauschinger effect compared to DP steels of the same strength. Martensitic steel, M190, also shows a relatively low Bauschinger effect for the strength of the steel.

4.2 Introduction

The Bauschinger effect is defined as the lowering of the yield stress when deformation in one direction is followed by deformation in the opposite direction. In other words, the Bauschinger effect describes material softening behavior when a reverse load is applied after forward loading.

Reverse loading occurs in stamping where metal undergoes bending and unbending as it is drawn over a die radius or through a draw bead. It also occurs in tube hydroforming where the tube making process involves compression followed by the hydroforming process where the tube is expanded in tension. However, the impact of the Bauschinger effect on forming operations involving reverse loading has usually been ignored due to the incomplete understanding of the Bauschinger effect and a lack of technical information.

The increasing use of advanced high strength steels (AHSS) in the automotive industry has emphasized the need for technical data about the Bauschinger effect. These advanced high strength steels show a stronger Bauschinger effect due to the presence of multiple phases that generate higher internal residual stresses during deformation. The impact of the stronger Bauschinger effect for these steels may significantly affect the formability of parts that use AHSS. In response to this need, this program included the Bauschinger effect in the project scope.

4.3 Testing Procedure

In this study, the specimens were cut in the transverse direction and loaded in tension to one of four (total) prestrain levels, 0.5%, 1%, 2% and 5%. The specimens were then loaded in the reverse direction to a compressive strain of 2%. The stress-strain data were recorded for each test for determining the Bauschinger effect factor. Two samples were tested for each steel lot and prestrain level. In order to avoid buckling during compression for thin sheet steel specimens, dog-bone shape specimens with a small gage length, 7.62mm, were used. Tests were conducted on a 5 kip MTS servohydraulic fatigue testing system. A load cell measured load and strain was measured by an extensometer attached to the gage section of the specimen.

4.4 Results

Figure 4.1 shows a typical test result from the Bauschinger test. The stress-strain response in the reverse (compression) direction was plotted in the positive stress region to better illustrate the response in the reverse loading region. The Bauschinger effect factor for each test was calculated as [4.1]:

Bauschinger Effect Factor (BEF) = reverse yield stress / maximum forward flow stress

The maximum forward flow stress is the highest stress in the forward (tension) direction. The reverse yield stress is determined with a 0.2% offset of the declining modulus to find the intercept with the reverse stress-strain response. Table 4.1a-e presents the values for true prestrain, forward flow stress, reverse yield stress and BEF. Lower BEF values reflect a greater difference between reverse yield stress and forward flow stress which are indicative of a larger Bauschinger effect.

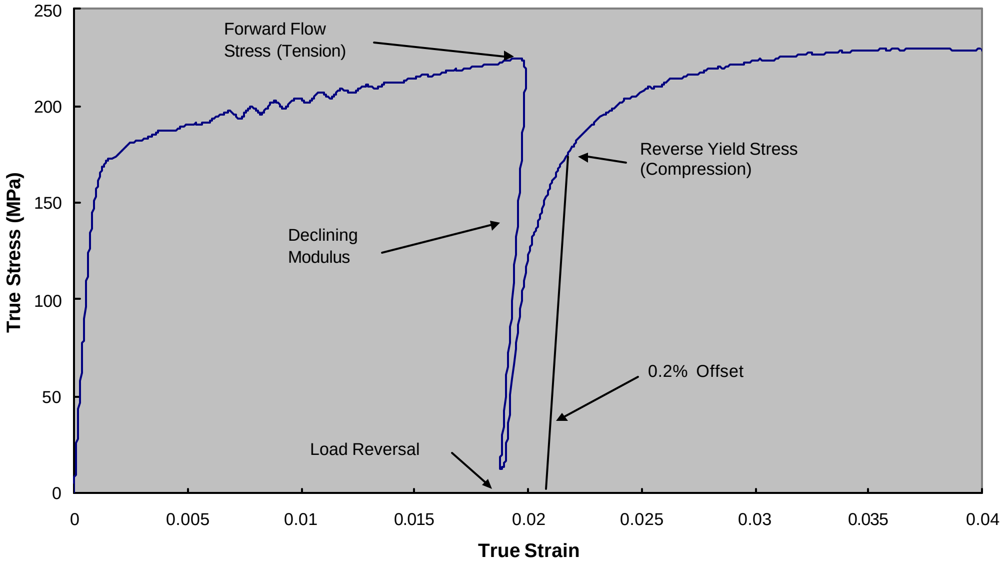

Figure 4.1: Illustration of values used to calculate the Bauschinger Effect Factor: X1 (DQSK) 2% Pre-Strain

From Table 4.1, it can be seen that the BEF for RA830, DP980 and M190 is greater than one for a prestrain of 0.5%. The strain required to reach the YS of these steels (800 MPa, 900 MPa, and 1230 MPa, respectively) is (YS/E)+0.002, i.e. 0.6%, 0.64% and 0.8%. At a prestrain of 0.5%, the forward flow stress is less than YS (tension) and no plastic strain occurs. When no plastic strain is applied to the specimen in the tensile direction, YS(compression) equals YS(tension). Thus, we have:

BEF = YS(compression)/forward flow stress = YS(tension)/forward flow stress > 1

Since the Bauschinger effect is only meaningful when a sufficient plastic strain is applied in the tension direction, data for RA830 and DP980 with a prestrain of 0.5% and M190 with a prestrain of 1% is ignored. The BEF for one HSLA350 lot at 0.5% prestrain is higher than one due to the large YPE, 7.75%, in forward loading and no YPE in reverse loading. This result is also ignored.

Table 4.1a: Bauschinger Effect Factor

Lot	Material	Nominal Engineering Pre-strain	True Pre-Strain	Forward Flow Stress (MPa)	Reverse Yield Stress (MPa)	Bauschinger Effect Factor
Baseline Steels						
X1	DQSK	0.005	0.004	190.65	171.77	0.90
		0.010	0.009	203.56	168.87	0.83
		0.020	0.019	224.51	178.71	0.80
		0.050	0.048	274.39	201.38	0.73
X2		0.005	0.004	207.86	197.20	0.95
		0.010	0.009	228.95	188.41	0.82
		0.020	0.019	239.76	191.07	0.80
		0.050	0.048	287.26	214.36	0.75
Y1	DDQ+	0.005	0.004	172.98	153.51	0.89
		0.010	0.009	191.30	156.41	0.82
		0.020	0.019	204.00	162.45	0.80
		0.050	0.048	259.23	189.57	0.73
Y2		0.005	0.004	162.84	154.06	0.95
		0.010	0.009	180.54	157.16	0.87
		0.020	0.019	202.75	165.34	0.82
		0.050	0.048	251.73	191.24	0.76
Skin Panel Steels						
B1	BH210	0.005	0.004	262.73	226.07	0.86
		0.010	0.009	269.08	219.10	0.81
		0.020	0.019	293.16	232.28	0.79
		0.050	0.047	334.36	250.88	0.75
B2		0.005	0.004	269.35	237.02	0.88
		0.010	0.009	284.20	231.29	0.81
		0.020	0.018	301.87	235.40	0.78
		0.050	0.047	345.60	256.45	0.74
C1	BH280	0.005	0.003	340.23	293.61	0.86
		0.010	0.008	349.51	271.32	0.78
		0.020	0.018	361.55	262.39	0.73
		0.050	0.047	422.62	279.76	0.66
C2		0.005	0.004	293.27	255.59	0.87
		0.010	0.009	307.81	242.77	0.79
		0.020	0.018	335.24	247.89	0.74
		0.050	0.047	392.52	268.19	0.68
C3		0.005	0.003	305.72	267.37	0.87
		0.010	0.008	312.51	239.41	0.77
		0.020	0.018	329.95	227.39	0.69
		0.050	0.047	384.47	241.42	0.63

Table 4.1b: Bauschinger Effect Factor

Lot	Material	Nominal Engineering Pre-strain	True Pre-Strain	Forward Flow Stress (MPa)	Reverse Yield Stress (MPa)	Bauschinger Effect Factor
Skin Panel Steels (continued)						
D1	ULC BH340	0.005	0.004	296.76	254.10	0.86
		0.010	0.009	307.41	240.96	0.78
		0.020	0.018	324.60	243.92	0.75
		0.050	0.047	370.11	264.02	0.71
D2		0.005	0.004	247.80	219.25	0.88
		0.010	0.009	262.90	213.41	0.81
		0.020	0.018	285.01	219.37	0.77
		0.050	0.047	333.48	240.65	0.72
E1	IF-Rephos	0.005	0.004	228.20	195.44	0.86
		0.010	0.009	249.01	201.14	0.81
		0.020	0.019	271.53	205.51	0.76
		0.050	0.048	330.59	231.35	0.70
E2		0.005	0.004	246.13	206.76	0.84
		0.010	0.009	265.54	206.51	0.78
		0.020	0.019	289.08	210.15	0.73
		0.050	0.048	346.76	234.42	0.68
G1	DP 500	0.005	0.003	367.48	305.37	0.83
		0.010	0.008	396.49	266.56	0.67
		0.020	0.018	424.21	257.29	0.61
		0.050	0.047	524.45	265.14	0.51
G2		0.005	0.003	363.56	293.06	0.81
		0.010	0.008	399.62	261.96	0.66
		0.020	0.018	451.35	262.32	0.58
		0.050	0.047	534.92	267.47	0.50
Structural Steels						
1K	BH300	0.005	0.003	375.36	313.42	0.84
		0.010	0.008	380.45	263.17	0.69
		0.020	0.018	419.18	257.32	0.61
		0.050	0.047	483.66	270.03	0.56
2K		0.005	0.003	328.06	284.42	0.87
		0.010	0.008	344.35	270.63	0.79
		0.020	0.018	362.26	275.72	0.76
		0.050	0.047	416.59	301.17	0.72

Table 4.1c: Bauschinger Effect Factor

Lot	Material	Nominal Engineering Pre-strain	True Pre-Strain	Forward Flow Stress (MPa)	Reverse Yield Stress (MPa)	Bauschinger Effect Factor
Structural Steels (continued)						
1L	HSLA 350	0.005	0.003	417.69	431.16	1.03
		0.010	0.008	429.86	389.80	0.91
		0.020	0.017	441.59	324.00	0.73
		0.050	0.046	427.81	296.40	0.69
2L		0.005	0.003	379.05	333.82	0.88
		0.010	0.008	388.12	306.14	0.79
		0.020	0.018	413.72	306.90	0.74
		0.050	0.047	454.09	304.16	0.67
5L		0.005	0.003	419.23	359.00	0.86
		0.010	0.008	432.08	319.34	0.74
		0.020	0.018	450.78	325.93	0.72
		0.050	0.047	520.10	348.94	0.67
1M	HS 440W	0.005	0.003	354.16	294.20	0.83
		0.010	0.008	361.73	245.66	0.68
		0.020	0.018	385.88	238.16	0.62
		0.050	0.047	463.78	257.77	0.56
2M		0.005	0.003	349.77	303.73	0.87
		0.010	0.008	360.70	269.28	0.75
		0.020	0.018	382.73	261.18	0.68
		0.050	0.047	456.26	275.18	0.60
1P	DP600	0.005	0.003	418.45	334.75	0.80
		0.010	0.008	442.52	287.81	0.65
		0.020	0.018	505.74	296.92	0.59
		0.050	0.047	621.83	296.94	0.48
2P		0.005	0.003	374.93	290.25	0.77
		0.010	0.008	412.21	254.83	0.62
		0.020	0.018	489.25	252.20	0.52
		0.050	0.047	606.51	269.19	0.44
3P		0.005	0.003	428.47	346.12	0.81
		0.010	0.008	476.07	299.65	0.63
		0.020	0.018	530.08	291.39	0.55
		0.050	0.047	648.40	304.08	0.47
4P		0.005	0.003	466.48	377.38	0.81
		0.010	0.008	530.48	321.01	0.61
		0.020	0.018	593.75	284.48	0.48
		0.050	0.047	691.63	277.04	0.40

Table 4.1d: Bauschinger Effect Factor

Lot	Material	Nominal Engineering Pre-strain	True Pre-Strain	Forward Flow Stress (MPa)	Reverse Yield Stress (MPa)	Bauschinger Effect Factor
Structural Steels (continued)						
5P		0.005	0.003	342.68	296.81	0.87
		0.010	0.008	356.53	260.52	0.73
		0.020	0.018	420.44	278.14	0.66
		0.050	0.047	545.44	302.36	0.55
6P		0.005	0.003	457.23	384.99	0.84
		0.010	0.008	520.96	326.12	0.63
		0.020	0.017	592.89	294.31	0.50
		0.050	0.047	688.26	286.27	0.42
1R	DP800	0.005	0.002	508.23	449.56	0.88
		0.010	0.008	614.05	364.74	0.59
		0.020	0.017	727.55	321.31	0.44
		0.050	0.046	872.55	283.17	0.32
2R		0.005	0.002	449.74	417.53	0.93
		0.010	0.008	553.50	333.27	0.60
		0.020	0.018	660.44	303.41	0.46
		0.050	0.047	794.26	286.82	0.36
1S	DP980	0.005	0.000	799.72	946.50	1.18
		0.010	0.006	933.92	472.08	0.51
		0.020	0.015	1008.79	379.66	0.38
		0.050	0.044	1102.20	403.34	0.37
2S		0.005	0.000	800.53	875.29	1.09
		0.010	0.006	885.51	440.63	0.50
		0.020	0.016	973.66	387.01	0.40
		0.050	0.045	1071.61	405.18	0.38
1T	TRIP 600	0.005	0.002	454.75	385.39	0.85
		0.010	0.008	481.53	331.72	0.69
		0.020	0.018	515.43	336.68	0.65
		0.050	0.047	612.31	368.25	0.60
2T		0.005	0.003	446.83	355.33	0.80
		0.010	0.008	465.11	318.24	0.68
		0.020	0.018	515.43	324.52	0.63
		0.050	0.047	615.52	347.47	0.56
1W	RA830	0.005	0.000	871.41	989.37	1.14
		0.010	0.005	979.73	670.18	0.68
		0.020	0.015	969.44	618.33	0.64
		0.050	0.044	1013.10	590.29	0.58

Table 4.1e: Bauschinger Effect Factor

Lot	Material	Nominal Engineering Pre-strain	True Pre-Strain	Forward Flow Stress (MPa)	Reverse Yield Stress (MPa)	Bauschinger Effect Factor
Structural Steels (continued)						
2W	RA830	0.005	0.000	801.02	989.84	1.24
		0.010	0.005	973.22	704.22	0.72
		0.020	0.015	976.21	600.56	0.62
		0.050	0.044	1001.19	612.53	0.61
3W		0.005	0.000	883.39	995.29	1.13
		0.010	0.005	1009.79	690.89	0.68
		0.020	0.014	1020.02	663.93	0.65
		0.050	0.044	1047.71	635.61	0.61
4W		0.005	0.000	833.13	1012.29	1.22
		0.010	0.005	974.89	733.74	0.75
		0.020	0.015	971.01	646.70	0.67
		0.050	0.044	990.51	566.74	0.57
1H	M 190	0.005	0.000	763.58	1232.05	1.61
		0.010	0.003	1252.24	1070.62	0.85
		0.020	0.014	1436.04	808.03	0.56
		0.050	0.043	1495.15	686.41	0.46
2H		0.005	0.001	711.80	1110.26	1.56
		0.010	0.004	1271.07	1069.28	0.84
		0.020	0.014	1386.15	770.65	0.56
		0.050	0.043	1449.56	624.84	0.43

Since the Bauschinger effect is the result of plastic deformation in the forward direction, the effect is better compared using plastic strain. The relationship between BEF and plastic strain is shown in Figure 4.2 for several steels, DQSK, HSLA350, DP500, DP600, DP800, TRIP600, DP980 and M190. The BEF values shown are the grade averages for the lots tested. It can be seen that the BEF approaches 1.0 when the true plastic strain is 0. With the increase of the tensile plastic strain, the BEF decreases significantly, i.e. more load drop in the reverse direction and more Bauschinger effect. The drop of BEF slows with the increase of the true plastic strain. When the true plastic strain is higher than 1.0 to 1.5%, the BEF decreases only slightly with the increase of the plastic strain applied in the forward direction, or the Bauschinger effect is almost stabilized.

It is clear that the BEF is related to the strength and microstructure of the steels. In general, steels of lower strength exhibit less Bauschinger effect, i.e. higher BEF values, such as DQSK and HSLA350. DP steels also show more Bauschinger effect than DQSK and HSLA350. However, TRIP600 exhibits less Bauschinger effect than DP600. Furthermore, M190 also shows less Bauschinger effect than DP800 and DP980 even though its tensile strength is higher. There is a cross over between DP800 and DP980. It is not clear if the cause is testing variation or the material behavior.

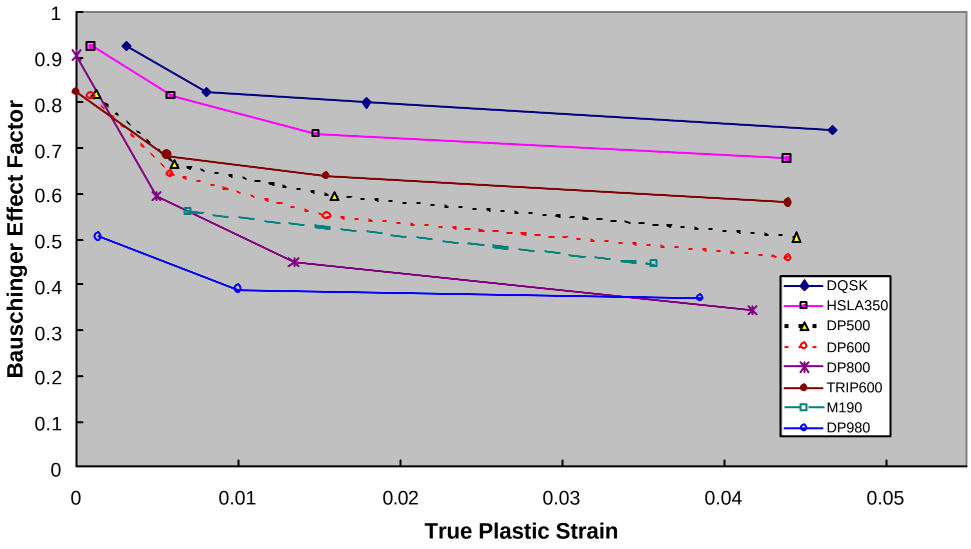

Figure 4.2: Bauschinger Effect Factor vs. True Plastic Strain for steel of different strength and microstructure

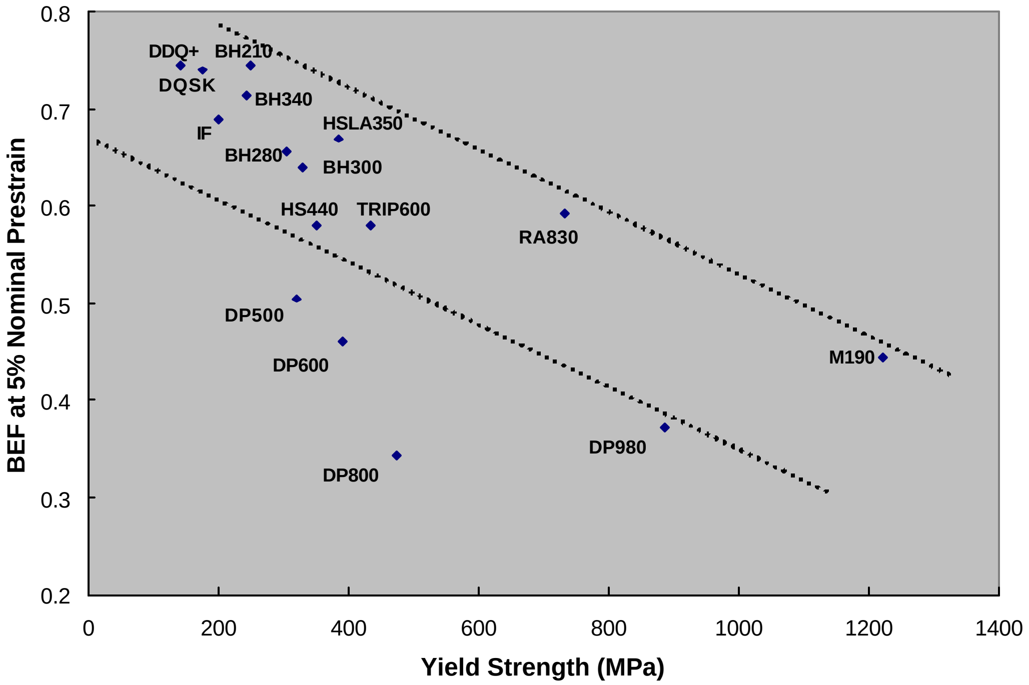

Figure 4.3: Bauschinger Effect Factor at 5% Nominal Prestrain vs. Yield Strength

Figure 4.3 plots the average BEF at 5% nominal prestrain against the average yield strength for each steel grade. It can be seen that for all steel grades except for the DP steels, the BEF falls in a roughly linear relationship with yield strength, i.e. BEF decreases with increasing YS. However, DP steels exhibit much lower BEF, and much higher Bauschinger effect.

As a means of characterizing the behavior of all of the steel grades, the BEF as a function of true strain was fitted with the power law:

$$BEF = A * \varepsilon^{B}$$

The power law constants A and B are indicators of how rapid the decline of BEF is as true strain increases. As both A and B decrease (B becomes more negative), the rate of decrease in BEF becomes more rapid. Figure 4.4 shows an example of the fitting for BH210 and DP500. Here, true strain, not the true plastic strain, is used because it is more convenient when comparing Bauschinger effect for different steels.

The constants A and B are presented in Tables 4.2a and 4.2b and plotted in Figure 4.5. Figure 4.5 presents the overall behavior of the steel in terms of the Bauschinger effect and it will be described as the Bauschinger Effect Factor Plot, or BEF Plot. It is a useful tool to compare the Bauschinger effect of different steels. The closer the A-B values of the steel to the bottom left side, the more rapid the drop in BEF, i.e. more drop in reverse load.

Figure 4.5 shows that the mild steels, DQSK, DDQ+, IF-Rephos, BH210 and BH340 (an ultra low carbon grade based on IF chemistry) have the highest values for A and B, indicating the lowest drop in reverse loading. Conventional high strength steels, BH280, BH300, and HSLA 350, have relatively lower values for A and B. The advanced high strength steels (AHSS), dual phase, TRIP, 440W and Martensitic steels, show the lowest A and B values, i.e. the most rapid drop in Bauschinger effect factor. As shown previously, for dual phase steels, the BEF seems to decrease with increasing yield strength, except DP980. TRIP600 also exhibits much higher BEF than DP600, i.e. less reverse load drop.

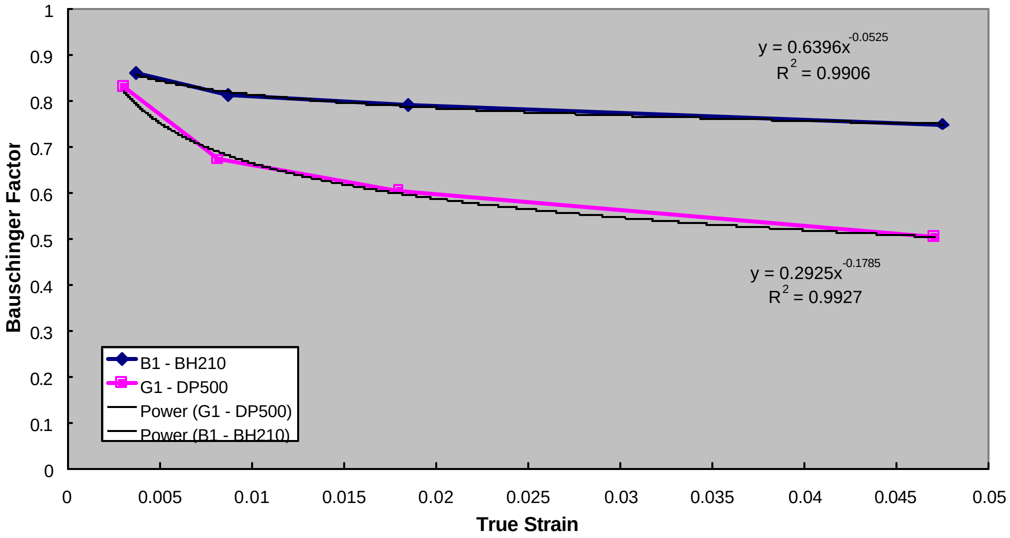

Figure 4.4: Examples for curve fitting

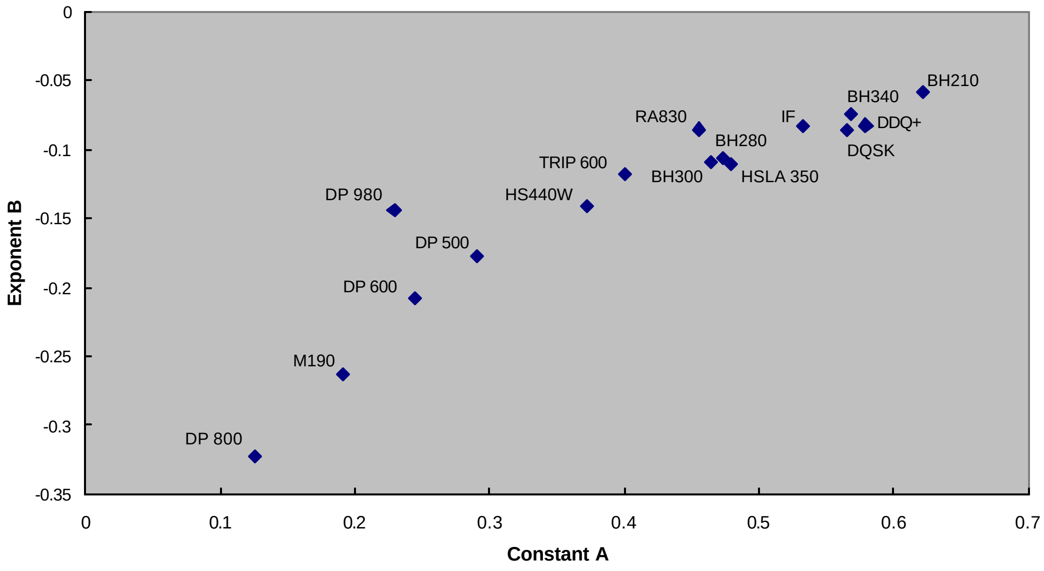

Figure 4.5: Plot of Bauschinger power law fit constants for all steel grades

Table 4.2a: Constants A and B

Lot	Material	A - Constant	B - Exponent
Baseline Steels			
X1	DQSK	0.574	-0.081
X2		0.557	-0.091
Y1	DDQ+	0.583	-0.076
Y2		0.576	-0.089
Skin Panel Steels			
B1	BH210	0.640	-0.053
B2		0.605	-0.065
C1	BH280	0.488	-0.099
C2		0.510	-0.094
C3		0.422	-0.126
D1	ULC BH340	0.572	-0.069
D2		0.565	-0.079
E1	IF-Rephos	0.548	-0.081
E2		0.518	-0.086
G1	DP 500	0.293	-0.179
G2		0.289	-0.176
Structural Steels			
1K	BH300	0.344	-0.151
2K		0.584	-0.067
1L	HSLA 350	0.427	-0.149
2L		0.495	-0.099
5L		0.514	-0.083
1M	HS 440W	0.346	-0.148
2M		0.397	-0.135
1P	DP600	0.275	-0.183
2P		0.231	-0.207
3P		0.254	-0.194
4P		0.181	-0.250
5P		0.337	-0.164
6P		0.188	-0.250
1R	DP800	0.115	-0.334
2R		0.135	-0.311
1S	DP980	0.216	-0.155
2S		0.242	-0.134
1T	TRIP 600	0.414	-0.114
2T		0.386	-0.121

Table 4.2b: Constants A and B

Lot	Material	A - Constant	B - Exponent
Structural Steels (continued)			
1W	RA 830	0.461	-0.076
2W		0.467	-0.078
3W		0.509	-0.057
4W		0.383	-0.130
1H	M 190	0.207	-0.245
2H		0.174	-0.282

4.5 Discussion

The Bauschinger effect has been explained by the behavior of dislocation substructure [4.2]. During forward strain, dislocation pile-up develops at barriers such as sessile dislocation segments, grain boundaries, precipitates or inclusions. This dislocation pile-up creates a back stress that tries to push the dislocations in the reverse direction. The back stress helps to reduce the external stress required when the load is applied in the reverse direction.

Another contribution to the Bauschinger effect is residual stresses developed due to inhomogeneous strains in the steel [4.3]. This is significant for steels with inclusions or second phases, such as dual phase (DP) steels. Due to the difference in strength and ductility, ferrite and martensite deform differently and residual stresses can develop after the steel undergoes plastic strain. This residual stress can also reduce the stress required for reverse deformation.

The relationship between the forward prestrain and the Bauschinger effect is that as prestrain increases, higher back and residual stresses develop which lead to a larger load drop in the reverse direction. Multiphase steels are expected to show a larger Bauschinger effect due to the additional contributions from long-range residual stresses. This is why DP steels show a larger Bauschinger effect. Higher strength DP steels possess a higher volume fraction of martensite, which develops higher residual stresses and hence a larger Bauschinger effect. In contrast, M190 is a single-phase steel, and the Bauschinger effect relies on the short range back stress only, and thus exhibits a lower Bauschinger effect than DP steels.

It is not clear why TRIP600 shows a lower Bauschinger effect than DP600 in this study. Figure 4.6 shows the forward flow and reverse yield stress for DP600 and TRIP600. TRIP600 and DP600 show similar hardening during the forward tensile deformation. However, the reverse yield stress of DP600 is much lower than that for TRIP600. It is speculated that the phase transformation of retained austenite in TRIP600 during reverse loading may overshadow the effect of back stress and residual stress, and resulting in a lower Bauschinger effect than DP600.

Higher Bauschinger effect means lower yield strength during a reverse loading. The practical importance may vary with the topic of concern. When reverse deformation occurs during a forming process, steels with a higher Bauschinger effect will have a lower strength than a process engineer assumes. Depending on the forming condition, the Bauschinger effect may play a significant role in the mechanisms involved in multiple stage forming, bending and unbending and springback. Data generated in this project provide the possibility to further quantitatively study these and other phenomena critical to the use of AHSS.

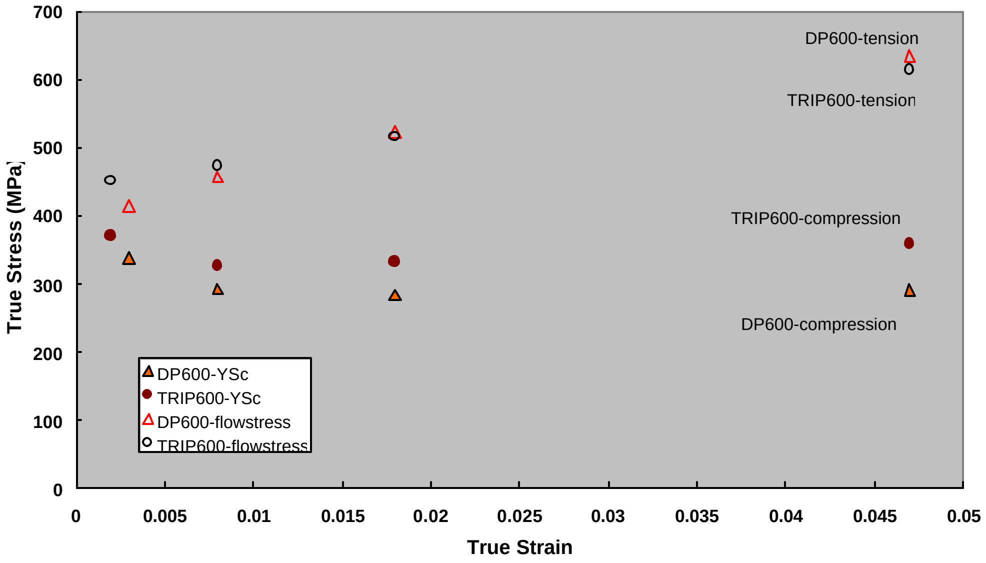

Figure 4.6: Comparison of forward flow and reverse yield stress for DP 600 & TRIP 600

4.6 Conclusions

1. Bauschinger effect factor has been generated for a series of automotive sheet steels.
2. Bauschinger effect is related with strength. In general, higher strength steels show more Bauschinger effect. Mild steels show the lowest Bauschinger effect, conventional high strength steels the second. AHSS show the highest Bauschinger effect.
3. Dual phase steels show a larger Bauschinger effect due to its martensite + ferrite microstructure. The two phases of different strengths can develop significant residual stress and thus enhance the Bauschinger effect. In contrast, the single phase M190 shows much less Bauschinger effect due to the relatively lower residual stress for its strength. TRIP steels exhibit a smaller Bauschinger effect than DP steels of similar strength possibly due to the effect of retained austenite.
4. A Bauschinger Effect Factor Plot is developed to evaluate Bauschinger effect for different steels. The plot can provide a general comparison for the Bauschinger effect in steels.

Section 5.0
Forming Limit Curves

5.1 Background

Forming Limit Curves (FLCs) are a very commonly used tool for evaluating stamping feasibility. FLC is a plot showing the limit strains for a range of strain paths. FLCs (or Forming Limit Diagrams, FLDs) are used to assess severity in a stamping operation in a production environment and also in conjunction with commercial FEA programs to predict splitting failures. FLCs have been studied in great detail by many researchers around the world for many years. In North America, the shape of the FLCs have been studied extensively for many low carbon formable steels and some high strength steels. Standard expressions are currently used by the stamping industry to determine the FLC [5.1]. These expressions [Keeler-Brazier (K - B) equations] are mentioned below and are given in terms of true strains.

$$FLD_0^{true} = \ln\left[1 + (23.3 + 14.13t)\cdot\frac{n}{0.21}\right]; n \le 0.21 \quad (5.1)$$

Where, n = Work hardening exponent, and t = Thickness

For $\varepsilon_2<0$; $e_1 = FLD_0^{true} - e_2$ (5.2)

For $\varepsilon_2>0$; $e_1 = \ln[0.6(\exp(e_2)-1)] + \exp(FLD_0^{true})$ (5.3)

In this project, experimental FLCs were determined for three steel grades by some of the member companies of AISI. The steel lot and the company performing FLC testing are given in the bulleted list below:

- 1.4mm CR TRIP 600 - US Steel
- 1.8mm GA RA830 - Dofasco
- 1.15mm CR DP980 - Ispat Inland

5.2 Test Procedure

The general procedure used for experimental determination of FLCs is given below. The actual details of the procedure might be slightly different between the performing companies.

- Samples of width ranging from 25.4mm to 177.8mm were sheared. Typically, multiple samples of 6-7 widths are prepared. Length of all samples was 177.8mm
- The surface of the tooling was cleaned with acetone after each sample is formed.
- One coat of ship oil was applied on the surface that would be in contact with the punch.
- The binder ring is closed applying the full binder capacity on the sample.
- The sample is formed using the 101.6mm spherical dome punch tooling.
- An iterative procedure is used to determine the punch travel such that incipient necking in the sample is detected.
- Once punch travel for incipient necking was determined, the rest of the samples are formed.
- Measurement of the samples was conducted using a strain measurement instrument. Great care is taken to determine the incipient necked circles. These are circles, for which there is no obviously visible neck. The presence of an incipient neck is determined mainly by touch and requires a great deal of experience to determine incipient necking.

5.3 Results

Figures 5.1 through 5.3 show the experimental FLCs for the three lots of steel. The FLCs are represented in terms of true strain in these figures. The solid line demarcating the safe points from the necked points is the experimental FLC.

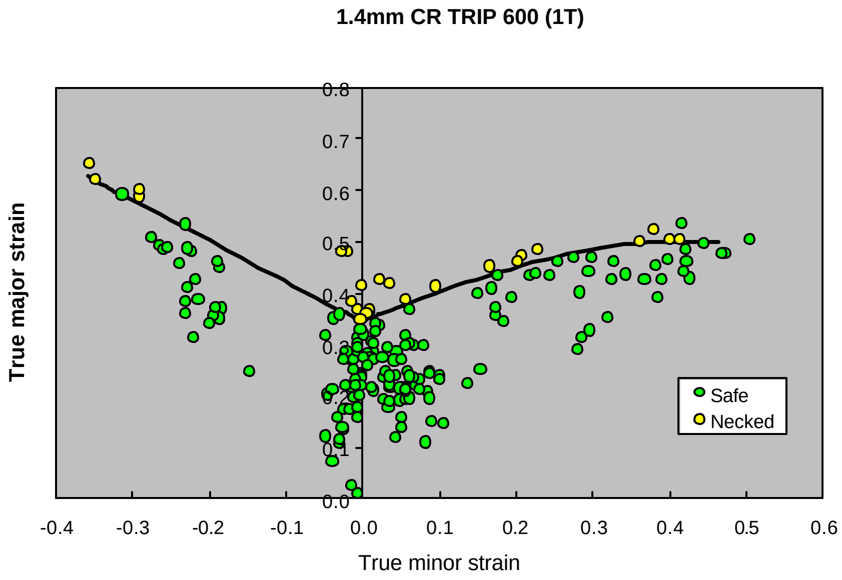

Figure 5.1: FLC displayed in terms of true strain for the 1.4mm CR TRIP600 steel lot (1T)

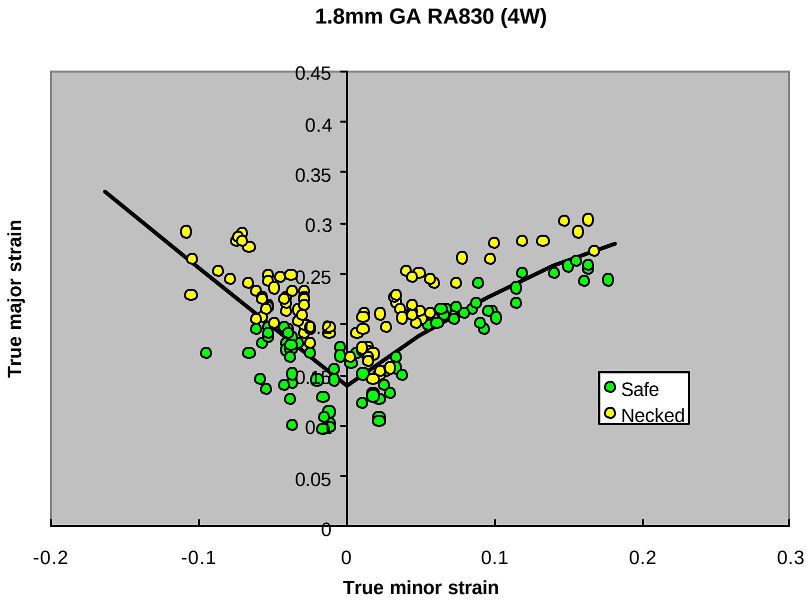

Figure 5.2: FLC displayed in terms of true strain for the 1.8mm GA RA830 steel lot (1W)

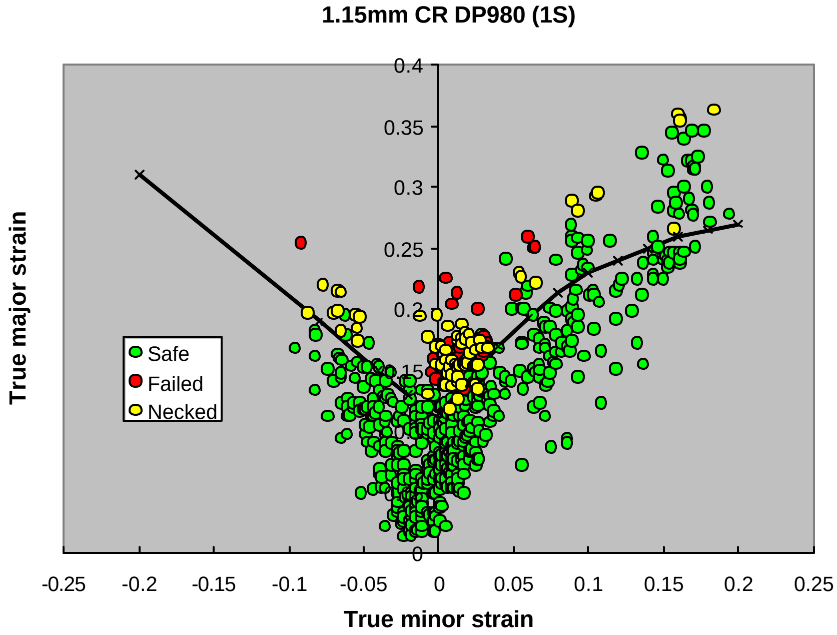

Figure 5.3: FLC displayed in terms of true strain for the 1.15mm CR DP980 steel lot (1S)

5.4 Discussion

In order to ascertain the applicability of the K-B equation to AHSS (TRIP600) and UHSS (RA830 and DP980), empirical FLCs were determined using equations (5.1) through (5.3). Because of the vastly different uniform elongations of the steels for which the FLCs were determined, it was not possible to use consistent definitions for the n-value to be used in the determination of FLC_0. The common industrial practice in determining FLC_0 is to use the average n-value for the elongation range of 10 -20% (or 10%-UE, if UE< 20%) to determine the FLC_0. Among the steels considered for FLC testing, only the TRIP600 lot had a high uniform elongation. The uniform elongations for the DP980 and the RA830 lots were less than 10%. Use of the terminal n-value (n-value at uniform elongation) has been recognized to yield a more accurate value for FLC_0 [5.2, 5.3], although it is more difficult to determine the terminal n-value on a routine basis. A special procedure as discussed in Section 2 needs to be implemented for accurate determination of the terminal n-value. Moreover the terminal n-value could not be determined for the RA830 lot, because in the transverse direction, the ductility of the RA steels was less than 1%. Because of these difficulties, the most easily available n-value is used in the determination of the empirical FLC_0. Table 5.1 shows the n-values used in the determination of the empirical FLC.

Table 5.1: n-values used for the determination of the FLC_0 for the three steel lots

Steel lot	**Definition of n-value to be used for determination of empirical FLC_0.**	**n-value**
1.4mm CR TRIP600 (1T)	10% - Uniform elongation (transverse direction)	0.21
1.8mm GI RA830 (4W)	3%-uniform elongation (longitudinal direction)	0.054
1.2mm CR DP980 (1S)	Terminal n-value (transverse direction)	0.066

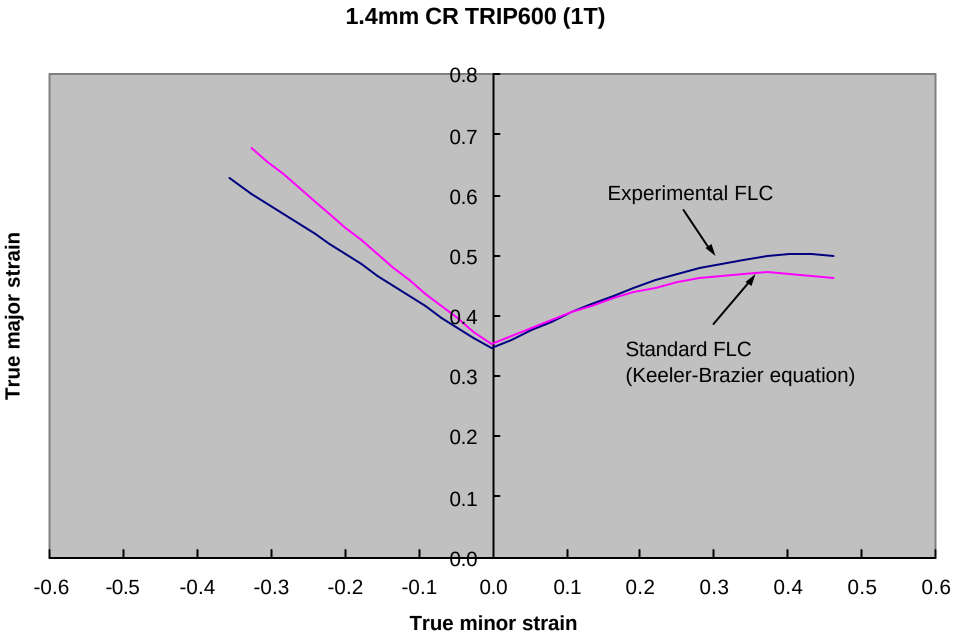

Figure 5.4: Comparison between the experimental FLC and standard FLC for the 1.4mm CR TRIP600 (1T) lot

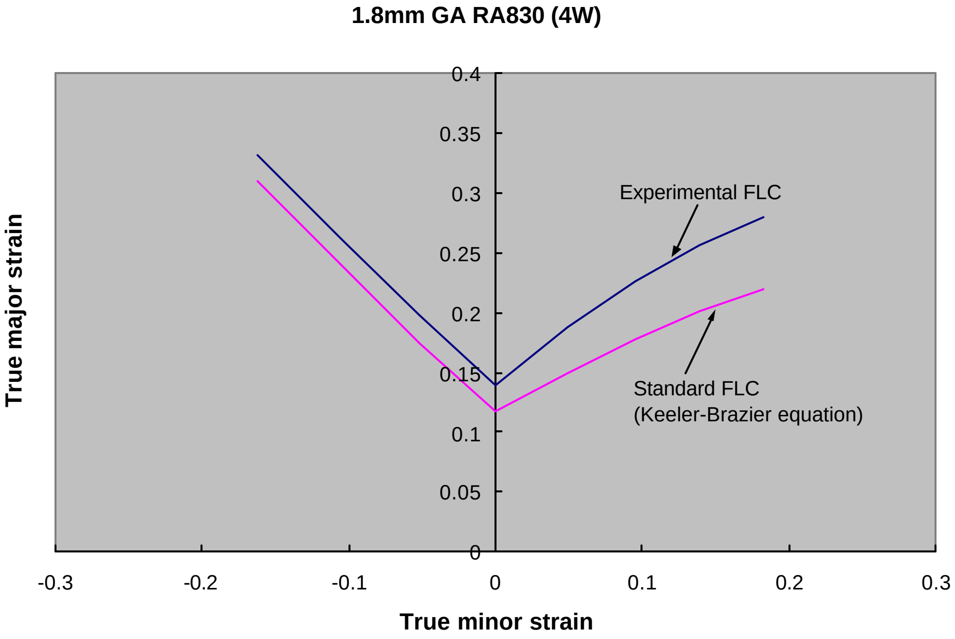

Figure 5.5: Comparison between the experimental FLC and standard FLC for the 1.8mm GA RA830 (4W) lot

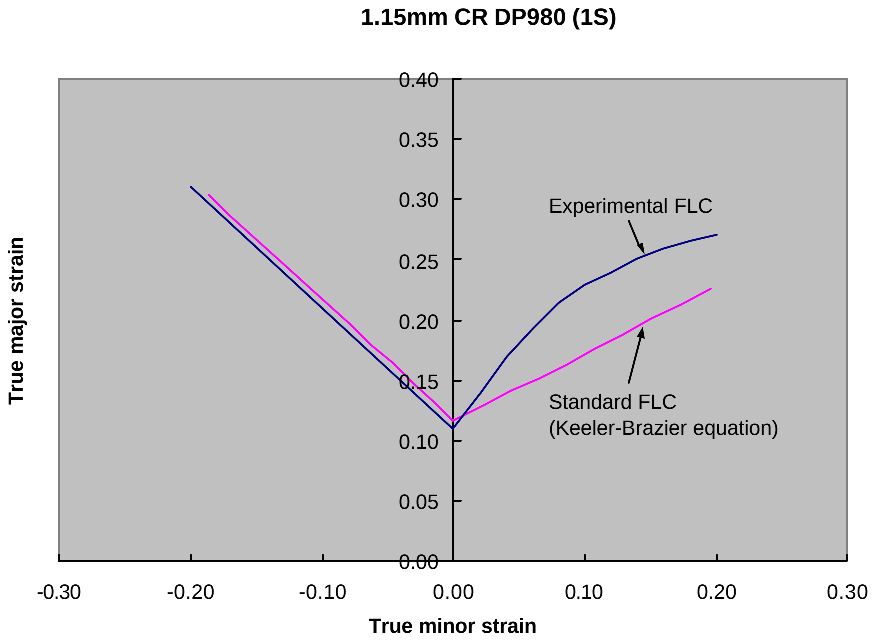

Figure 5.6: Comparison between the experimental FLC and standard FLC for the 1.15mm CR DP980 (1S) lot

As seen in Figures 5.4 through 5.6, the experimental FLC seems to agree with the standard FLC [as determined by equations (5.1), (5.2) and (5.3)] very well for the left hand side of the forming limit curve ($\varepsilon_2<0$) for all the steel lots. On the right hand side, ($\varepsilon_2>0$) the standard and experimental FLC showed the best agreement for the TRIP600 lot. For the RA830 and DP980 lots, the experimental forming limit curve was significantly higher than the standard FLC. This phenomenon indicates that for steels with complex microstructures, for $\varepsilon_2>0$, the standard FLC is conservative. More experimental work is needed to understand this phenomenon.

5.5 Conclusions

1. Experimental forming limit curves were determined for the 1.4mm CR TRIP600, 1.8mm GA RA830 and 1.15mm CR DP980 steel lots.
2. For negative minor strains, the experimentally determined FLC seems to match the standard FLC quite well for all the steel lots.
3. In the regime of positive minor strains, the match between experimental and standard FLC was good only for the 1.4mm TRIP600 steel lot. For the 1.8mm RA830 lot and 1.15mm CR DP980 lots, the experimental FLC was above the standard FLC, i.e., the standard FLC is conservative.

Section 6.0
Sheared Edge Stretching Limits

6.1 Summary

This section presents results from hole extrusion testing for all the steel grades in the project. The hole extrusion test is one of the tests that is typically used to characterize the formability of a sheared edge. The stress-state in the formed edge is simulative of the stress state at the sheared edge during stretch flanging. Results from the testing showed that as a first order effect, the hole extrusion limit is a strong function of the ultimate tensile strength of the material and the r-bar value. These trends are consistent with some previously reported trends in the literature. The applicability of these results to stretch flanging are also discussed.

6.2 Background

Sheared edge stretching limits are an important performance metric especially as they relate to material behavior during flanging operations. Flanging is carried out subsequent to the trimming operation to facilitate joining of components during assembly, or to provide stiffness to structural members. Depending on the geometry of the flange, flanges can be classified as either stretch flange (where the sheared edge is subjected to tensile stresses), a shrink flange (compressive stress), or a combination of the two types. Different punch geometries have been used to determine the sheared edge stretching limits. At Ispat Inland Research, this test is usually performed with either a 50mm flat punch (hole expansion test) or a conical punch with a 60^0 included angle (hole extrusion test).

Sheared edge stretching tests have been used extensively in the Japanese steel industry as one of performance metrics related to formability when developing new steel grades [6.1-6.14]. Most of the work on sheared edge stretching behavior also seems to have been performed for hot rolled steel grades, for both laboratory heats and production material. Researchers from Kobe Steel [6.2-6.5, 6.10-6.13] have done a significant amount of work in correlating the sheared edge stretching behavior of high strength dual-phase and TRIP steels to chemical composition and microstructure. There is considerable evidence in the literature that the sheared edge stretching behavior of F+B steels is better than that of the traditional F+M steels, where F stands for ferrite, B for bainite and M for martensite [6.2-6.5]. In some early work by M. Sudo and co-workers [6.2, 6.5], several laboratory heats were made for steels alloyed with Mn or Si, which were intercritically annealed and subsequently air-cooled, water quenched, or oil-quenched. Microstructures with differences in the morphology, hardness and amounts of low temperature transformation products (LTTPs) were obtained by this method. These steels were then subjected to a variety of mechanical tests, with the sheared edge stretching test being one of the tests. The % increase in hole diameter was represented by λ. The main findings of their studies are summarized below.

- λ decreases with increasing LTTP products.
- λ decreases rapidly with increasing tensile strength.
- λ increases with increasing r-value.
- λ decreases with an increase in hardness ratio between the ferrite and the LTTPs.

Most of the testing conducted by Japanese researchers use either a conical punch or a flat bottom punch for evaluation of sheared edge stretching ability. There have been other variations in test method [6.14, 6.15], with similar results. The effect of hole punching clearance on sheared edge stretching was examined by Milosevic and Moussy [6.14], where they found a very small effect of clearance on circumferential fracture strain (% hole expansion). Demeri [6.15] used a different measure of formability where the flange height before fracture is the measure of formability. The effect of prior work hardening on sheared edge stretching was also examined by biaxially stretching the sheet before hole punching. It was found that the hole expansion limit increased with prestrain.

In addition to steel grade development, the application of sheared edge stretchability on the design of stretch flanges and trimline development has been explored in several analytical/FEA studies [6.16-6.21]. One of the common elements in these studies is the discovery of the fact that the stress state at the edge of the stretch flange is uniaxial tensile. Attempts to design the flange or the trim-line were made for a "general" flange, where the flange length, root radius, flange angle and bend angle are treated as variables. The forming limit diagram is typically used as a failure criterion. The general applicability of these guidelines however seem to be limited and have not been demonstrated substantially in the papers reviewed. Moreover, the analytical work has mostly focussed on "soft" DQSK or IF steels, or in some cases Al alloys with very little work on high strength steels.

This project is thus unique because of the wide diversity of cold rolled and coated sheet steel products being tested. Comparison of test results for high strength steels with baseline DQSK or DDQ+ steels would highlight necessary areas for change in design/processing strategies when stamping high strength steels.

6.3 Testing Procedure

Hole Punching

- Samples of size 127mm X 127mm were cut and deburred.
- A special punch/lower die was used for aligning the punch and the die. The punch diameter is 9.474mm and the die diameter is 9.525mm. The punch and lower dies were mounted as a unit in the ram of the press. The bottom bed-plate was kept loose.
- Alignment between the punch and die was checked by moving the punch into the lower die. The clearance between the punch and die was visually checked from under the bed-plate of the machine to see if daylight is uniform all around the punch.
- A fixed punch of 10mm diameter was used. A lower die was ground specifically for each lot of steel to a 10% clearance per side, which is representative of typical production practice. Clearance is defined in terms of percentage of metal thickness.
- A new lower die was used for each lot of steel.
- Holes for a number of samples were punched for each steel lot. After hole punching, the samples were randomized.
- The initial diameters of the samples were measured in the L, T, and D directions and recorded.

Forming

- Forming was conducted using a 38.1mm diameter conical punch with a 60^0 included angle (hole extrusion test) for regular testing. For establishing a correlation with the hole expansion test, a 50mm flat bottom punch was also used for forming.
- The samples were placed in the press such that the shear burr was facing up.
- The specimens were clamped using a serrated plate to prevent draw-in.
- A teflon sheet and a light lubricant (LPS2) were used at the interface of the punch and the sample to minimize the effect of friction.
- Forming was conducted on the Hille-Wallace press, by moving the punch up so as to stretch the punched hole. Figure 6.1 shows a photograph of the Hille-Wallace hydraulic press. Typically, this test is conducted by visual inspection, where the movement of the punch is reversed when a through-thickness crack is detected. Since steels of vastly different mechanical properties (DDQ+ to M190) were tested, a more consistent test method of "sight gauges" was implemented. These gauges are cylindrical inserts with holes of predetermined % hole expansions (based on a 10mm punched hole) machined.

During testing, the position of the punched hole relative to the hole in the gauge was monitored. When the formed hole was just about to disappear behind the hole in the gauge, the punch travel was reversed. Using this approach, holes of different hole expansions were formed per lot. The final diameters of the samples were measured and recorded after forming. Samples with a big crack were discarded.

- The % hole expansion is considered as the measure of sheared edge stretching formability. Test specimens from each lot were examined to choose samples that exhibit a hairline through-thickness crack. The formed holes were measured in the L, T, and D directions and averaged to yield the % hole expansion for a given specimen.

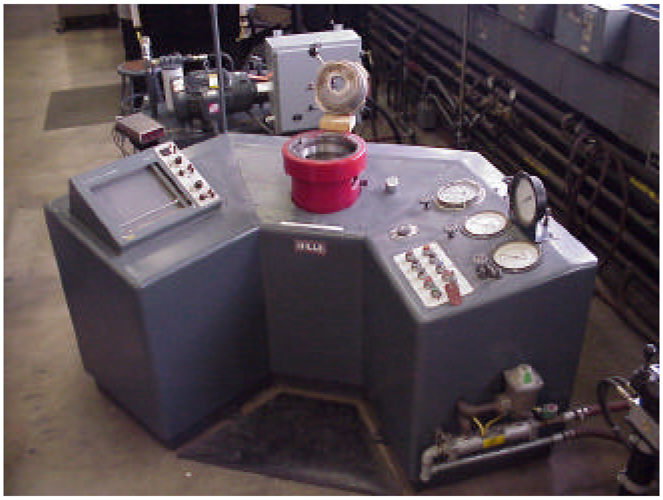

Figure 6.1: Photograph of the Hille-Wallace hydraulic press used for conducting the sheared edge stretching tests

6.4 Correlation between hole expansion and the hole extrusion tests

Figure 6.2 shows the geometry of the test specimens using the flat bottom punch and the conical punch. The correlation was established using 1.19mm CR DQSK (X2), 0.7mm EG BH210 (B1), 1mm EG BH280 (C2), 0.81mm EG DP500 (G2), and 1.2mm GI DP800 (1R). The samples were prepared, formed and measured according to the test procedure outlined previously, except the hole punching procedure, where the same punch and die-set were used for all the steel lots. Figure 6.3 shows the correlation between the hole expansion and hole extrusion tests. As seen in Fig. 6.3, excellent correlation between the two test methods was observed. It was observed the hole extrusion limits were consistently higher than the hole expansion limits. This could be a result of slightly different strain paths in the two tests. It is anticipated that strain analysis could provide further insight into the differences in the two tests. For the purposes of this project, it was sufficient to note that a correlation between the two test methods does exist and either one of the tests could be used. The hole extrusion test was chosen for "production" testing as it was more simulative of a stretch-flanging operation.

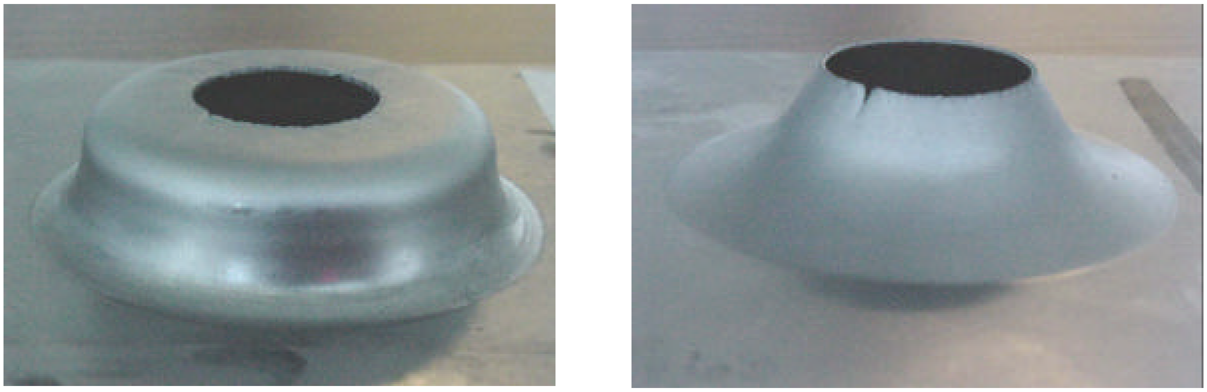

Figure 6.2: Geometries of the hole expansion and hole extrusion test specimens

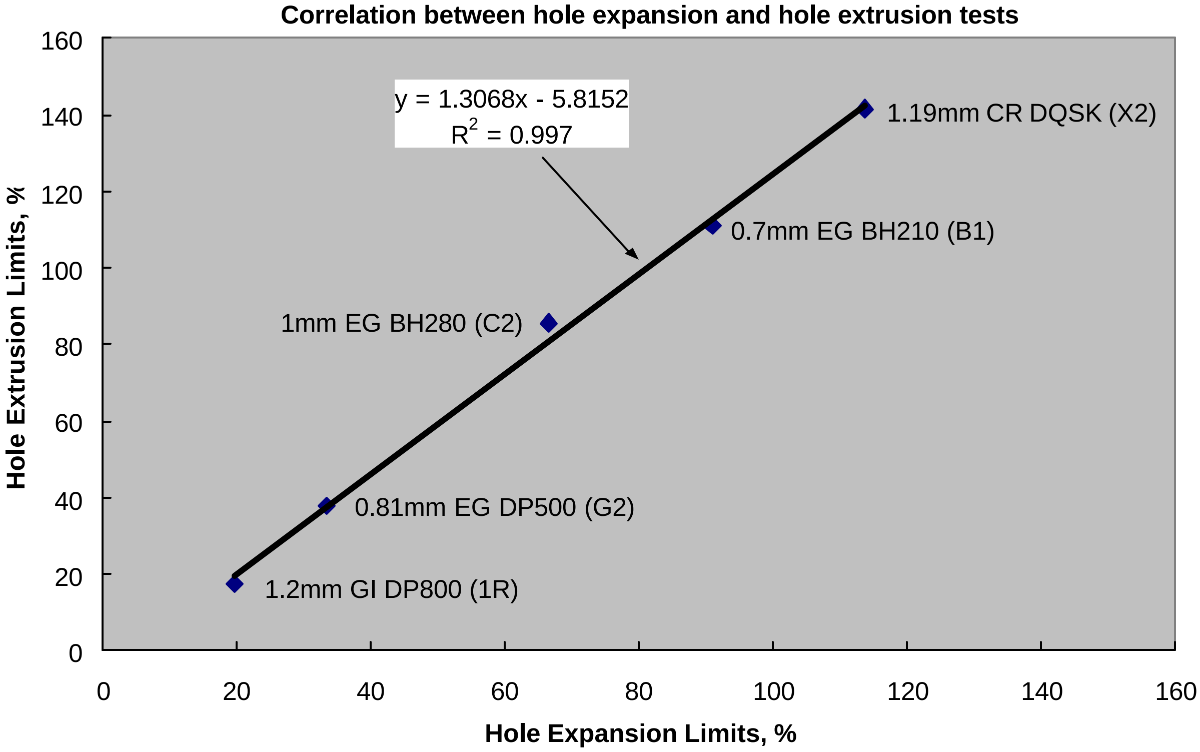

Figure 6.3: Correlation between the hole expansion and hole extrusion tests

6.5 Results

Table 6.1: Sheared edge stretching results for all the steel grades

	Grade	Thickness (mm)	Lot Code	Sheared Edge Stretching Limits		
				# of samples with thickness crack	Avg. % HE	Std. Dev.
Baseline	DQSK	0.77	**X1**	3	145.07	9.04
		1.19	**X2**	6	152.12	16.00
	DDQ+	0.70	**Y1**	8	150.49	5.67
		1.19	**Y2**	3	177.86	2.71
Skin Panel Steels	BH210	0.70	**B1**	5	151.96	2.84
		0.93	**B2**	5	151.45	4.70
	BH280	0.71	**C1**	3	98.87	2.16
		1.00	**C2**	6	98.60	3.49
		1.04	**C3**	5	101.07	9.73
	ULC BH340	0.74	**D1**	7	157.62	8.00
		1.02	**D2**	5	122.37	3.14
	IF-Rephos	0.63	**E1**	5	141.73	4.00
		0.89	**E2**	8	159.21	8.28
	DP 500	0.66	**G1**	9	55.97	5.57
		0.81	**G2**	3	57.24	6.59
Structural Steels	BH300	1.24	**1K**	6	66.63	13.53
		1.19	**2K**	7	123.84	7.78
	HSLA 350	1.16	**1L**	7	86.58	9.47
		1.21	**5L**	6	95.11	4.27
		1.62	**2L**	7	89.75	6.41
	HS 440W	1.24	**1M**	4	84.18	13.65
		1.58	**2M**	8	66.86	7.50
	DP600	0.96	**1P**	6	38.03	3.76
		1.19	**2P**	6	51.14	3.76
		1.39	**3P**	11	29.33	2.49
		1.23	**4P**	5	36.61	2.83
		1.64	**5P**	11	32.70	2.45
		1.49	**6P**	6	29.82	1.73
	TRIP 600	1.40	**1T**	6	50.95	6.54
		1.60	**2T**	6	39.98	3.01
	DP800	1.20	**1R**	3	21.93	2.55
		1.59	**2R**	4	18.72	2.21
	DP980	1.15	**1S**	6	53.66	15.10
		1.52	**2S**	5	61.13	7.41
	RA 830	1.32	**1W**	7	26.02	2.93
		1.53	**2W**	9	27.77	2.03
		1.25	**3W**	4	30.07	2.73
		1.80	**4W**	9	25.09	2.55
	M 190	1.03	**1H**	4	27.49	5.75
		1.58	**2H**	5	23.55	1.83

Table 6.1 shows results for the sheared edge stretching test for all the steel lots. Examination

of Table 6.1 reveals that within a certain steel grade, there is some variation in sheared edge stretching limits, which are not fully explainable by tensile properties. The reason for these differences may lie in some microstructural or chemical variables, and the volume fractions of the different phases. But these investigations are beyond the scope of this project. Also noteworthy is the fact that there seems to be almost no systematic dependence of sheared edge stretching limits on thickness of the steel grade.

Correlations between % HE and some standard tensile properties are shown in Figures 6.4 and 6.5. As seen in the figures, the correlation between %HE and the ultimate tensile strength of the material is very strong. The correlation between %HE and UTS shows an interesting dependence where the %HE is very sensitive to UTS in the strength range between 300 MPa to 700 MPa, beyond which, the results are fairly insensitive to changes in UTS. This suggests the importance of some microstructural variable contributing to the observed correlation. A high r-bar value is also beneficial to the sheared edge stretching limit. Interestingly, the % HE for DP980 is well above the trend line for its strength level.

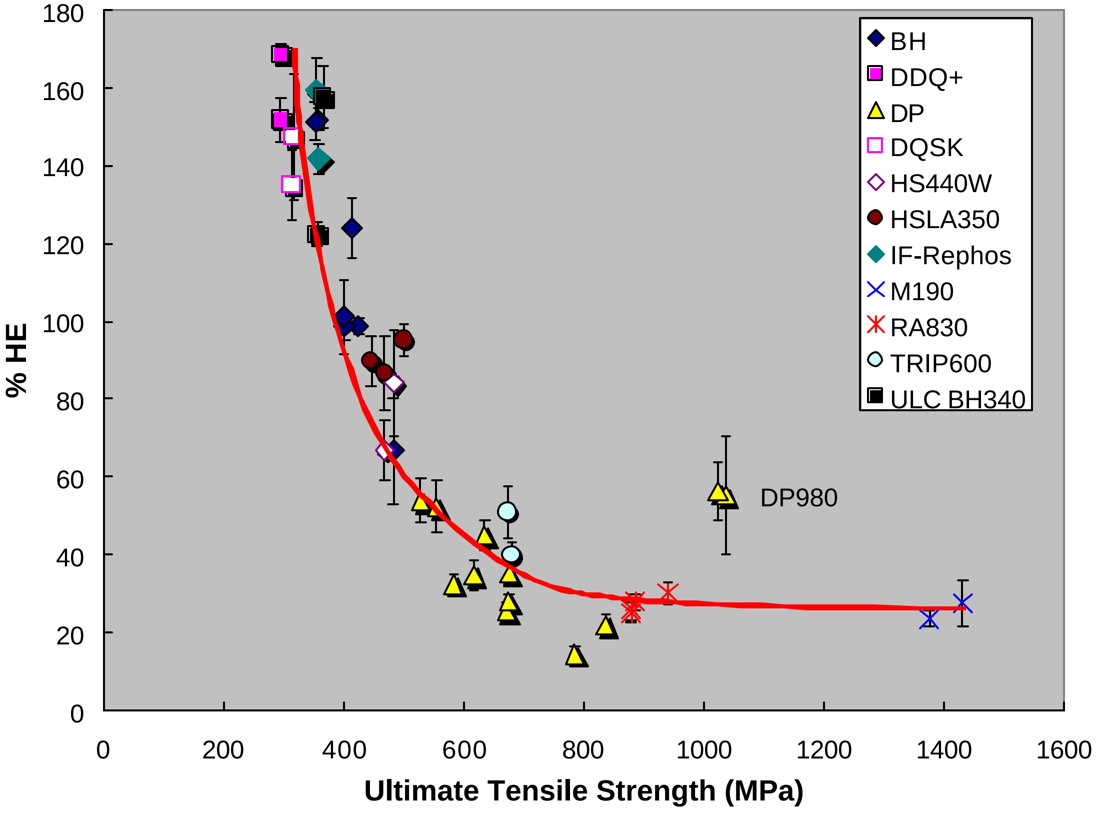

Figure 6.4: Dependence of the sheared edge stretching limits on the ultimate tensile strength

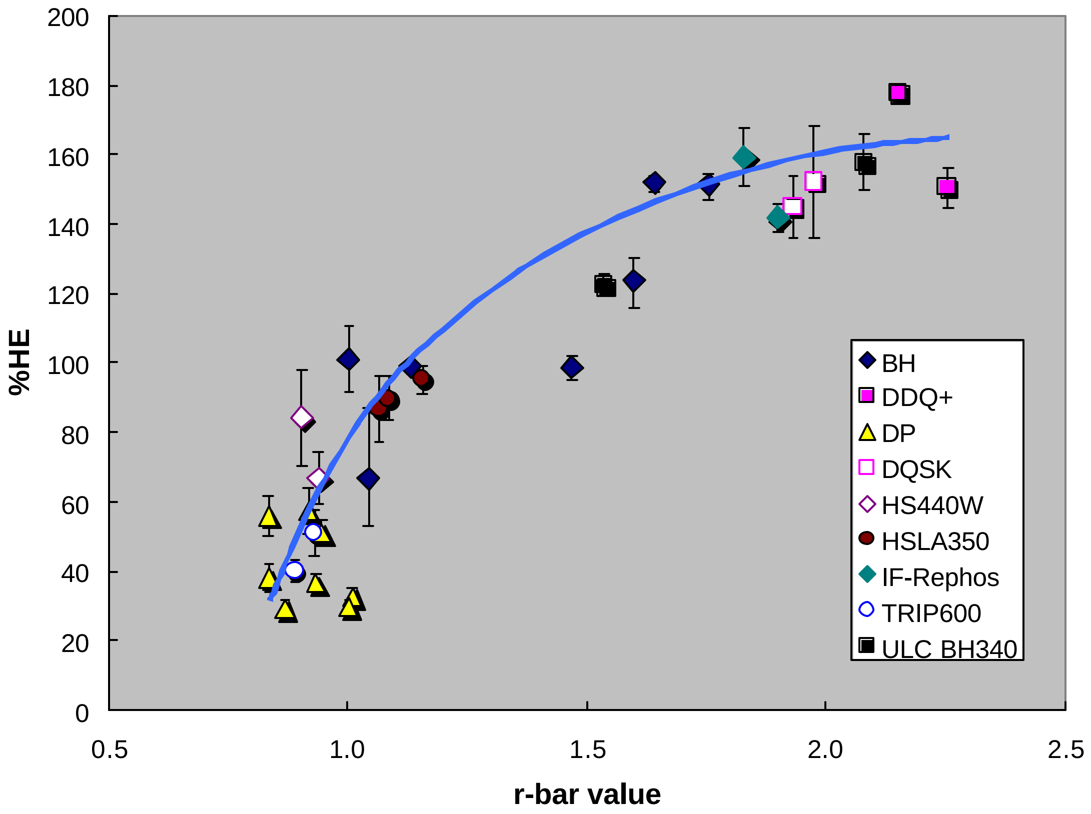

Figure 6.5: Dependence of the sheared edge stretching limits on the r-bar value

6.6 Discussion

The trends for %HE with respect to tensile strength and r-value are similar to prior findings reported in literature. The dependence of sheared edge stretching limits on tensile strength can be explained by the fact that higher strength steels have higher notch sensitivity. The action of punching a hole produces several "notches" in the immediate vicinity of the sheared edge, which would serve as nucleation sites for cracks to develop. The effect of r-value can be understood by examining the strain path for uniaxial tension. Prior work done by Wang and Wenner had established the stress state at the edge of the flange as being uniaxial tension [6.16]. The development below relates the uniaxial strain path to the r-value.

Invoking volume constancy: $e_1 + e_2 + e_3 = 0$ (6.1)

Where ε_1 is the circumferential strain; ε_2 is the radial strain, ε_3 is the thinning strain

For uniaxial tension strain path: $\frac{e_2}{e_3} = r$ (6.2)

Where r is the normal anisotropy factor. Substituting (6.2) in (6.1), we obtain an expression for the strain path ($\varepsilon_1/\varepsilon_2$) as a function of the r-value.

$$\frac{e_1}{e_2} = \frac{-(1+r)}{r} \tag{6.3}$$

As an illustration, the results for two lots of BH300: 1K and 2K can be considered. Examination of Table 6.1 reveals that the % HE for 2K is almost double that of 1K. Figure 6.6 shows the standard

FLC for 1K and 2K materials (BH300), with the same n-value but vastly different r-values. Also shown in the Figure are strain path lines corresponding to uniaxial tensile strain path determined from equation (6.3) for both the materials.

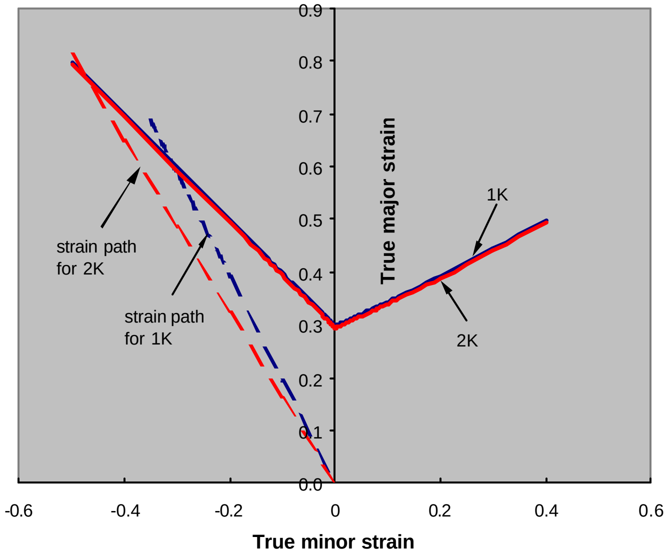

Figure 6.6: Standard FLCs for 1K and 2K (BH300) and their strain paths for uniaxial tension

As seen in the Figure, although the FLCs are almost identical for the two materials, the effect of the r-value is to yield a higher limit strain because of the different slope of the strain path line. Physically, a higher r-value represents the ability of the material to resist thinning for the same major strain yielding a higher % HE. Results from this test show that the sheared edge stretching test is very sensitive to gross mechanical properties and probably microstructural and compositional variables of the steel grade. However, because of the restrictions of the project, the study is only limited to correlations with standard tensile properties.

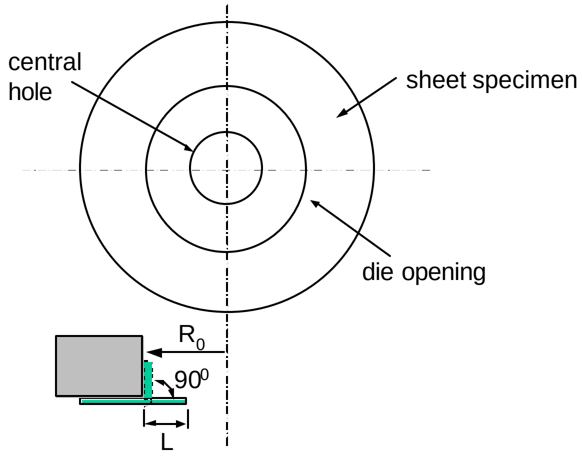

Figure 6.7: Schematic of a stretch flanging operation for an annular sample

The applicability of these test results to secondary finishing operations such as stretch flanging can be demonstrated by transforming the % HE to a characteristic variable describing the flange geometry. Figure 6.7 shows a schematic of an annular sheet specimen with a central hole, which is bent around a die to an angle of 90^0 as shown in the figure. The flange root radius, R_0 is the radius of the die opening. The flange length, L is the radial length from the edge of the hole to the flange root radius. For a 90^0 bend angle, the % hole extrusion expressed as a fraction is given by the following expression.

$$HE = \frac{R_0 - (R_0 - L)}{(R_0 - L)} \qquad (6.4)$$

$$\frac{L}{R_0} = \frac{HE}{1 + HE} \qquad (6.5)$$

Using equation 6.5, the experimental hole extrusion data can be represented as L/R_0, which can be considered as a dimensionless flange parameter. Figure 6.8 shows the correlation between L/R_0 and the ultimate tensile strength.

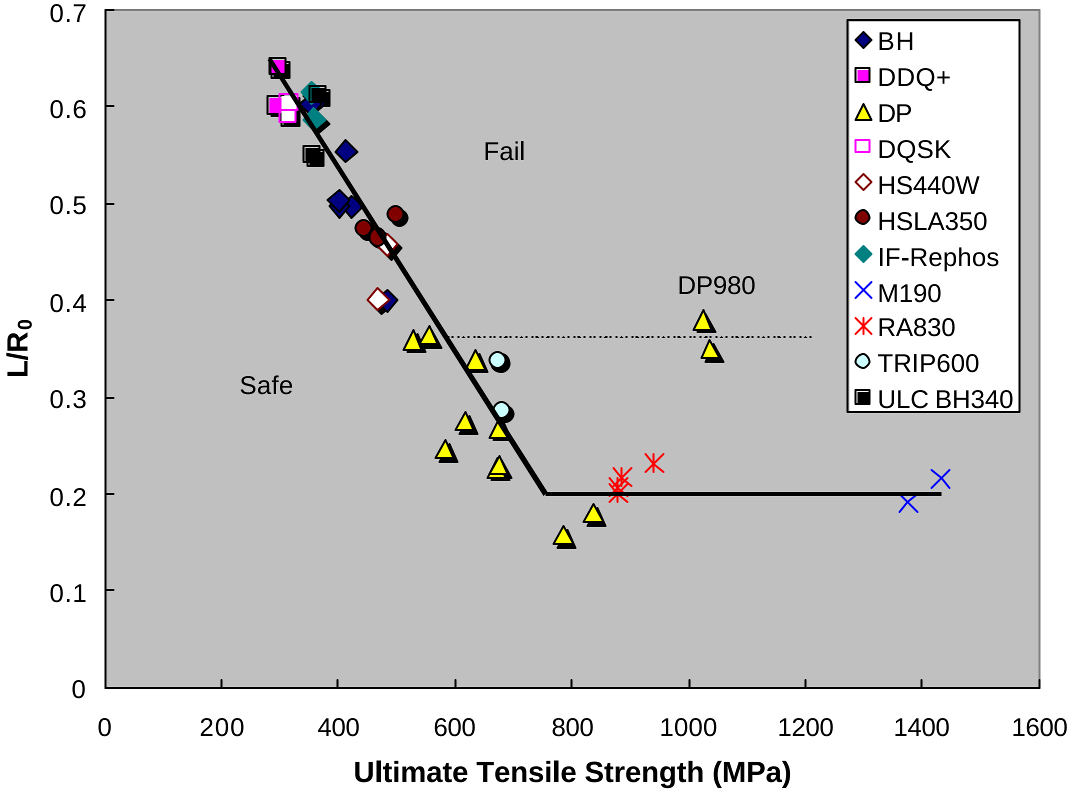

Figure 6.8: Trend for characteristic flange parameter as a function of tensile strength

As seen in Figure 6.8, for the geometry described in Figure 6.7, the trend line is an upper bound for severity of the flanging operation as a function of the ultimate tensile strength. As seen in Figure 6.8, the limit L/R_0 value for DP980 is significantly above the trend line. It is conjectured that DP980 might be a specially engineered steel, where it would be possible to obtain higher sheared edge stretching limits. As the length of the flange L, increases the severity of stretch flanging increases. Similarly as the flange root radius, R_0 decreases (higher curvature), the flange severity increases. When substituting a higher strength steel for a lower strength steel, for a given die (same

R_0), Figure 6.8 shows that the flange length would need to be decreased for a split-free flanging operation. As an illustration, from Figure 6.8, the L/R_0 for a 300 MPa material is approximately 0.62, and for a 500 MPa material is approximately 0.42. To ensure a split free flange, the flange length for the higher strength steel can be determined by the following expression.

$$\frac{L^{500MPa}}{L^{300MPa}} = \frac{0.42}{0.62} = 0.677 \tag{6.6}$$

The above illustration shows that the flange length would have to be decreased by 32%. It should be noted that the above treatment is an illustration describing the relevance of hole extrusion testing to stretch flanging, and should not be considered as a general failure criterion for complicated flange geometries. The usefulness of the testing lies in identifying the importance of appropriate die design practice for finishing operations when using advanced high strength steels such as DP and TRIP steels. Typically when running trials for advanced high strength steels, the common practice is to substitute the high strength steel for the production material without making adjustments to the die or the process. Although this method may appear to be the most cost-effective approach, and is suitable for performing quick trials, results of this study show that problems during stretch flanging should be expected. Fortunately solutions for reducing stretch flange severity exist when incorporated early on the process planning stage. Metal gainers are frequently used in the addendum to reduce the severity of stretch flanging operations. Another approach would be resort to a cam slide mechanism for trimming such as to avoid the need for stretch flanging. As in all engineering applications, the cost of implementing die/process engineering solutions have to be balanced with the multiple advantages of using AHSS in vehicle platforms.

6.7 Conclusions

The sheared edge stretching test has been completed for all the steels that were part of the AISI/DOE project on the formability of AHSS. The following are the conclusions of the study.

1. Sheared edge stretching limits are strongly dependent on the tensile strength of the steel grade. The %HE decreases significantly with an increase in tensile strength in the range of 350 - 700 MPa and then approaches a constant value with further increase in tensile strength.
2. Sheared edge formability increases with increasing r-values.
3. Considerable differences were found in the sheared edge formability between different lots for a given steel grade. The differences could be attributed to microstructural or chemical differences, which were not examined in this study.
4. The sheared edge stretching limits for DP980 were found to be significantly better than the observed trend. It is possible that specially engineered steels could have improved sheared edge formability than other steels of similar ultimate tensile strength.

Section 7.0
Bending Under Tension Limits

7.1 Summary

Bending under tension is an important deformation mode during stamping and has been observed to limit achievable ductility for high strength steels. This section presents results from Angular Stretch Bend (ASB) testing which has been used to characterize bending under tension behavior for the steels in this AISI/DOE formability project. Failure heights were determined under sample lockout conditions for different punch radii. A primary use of the test results is to compare formability measured by the failure height, which provides material ranking for different R/t ratios. In addition, strain distributions for all the samples were analyzed to provide bending under tension forming limits for the different steel grades. These forming limits can be used to develop die design and processing strategies for high strength sheet steels.

7.2 Background

The process of bending sheet metal over a radius with superimposed tension was recognized as an important deformation mode requiring more complete characterization for advanced high strength steels. This section presents the results of one simulative test, the Angular Stretch Bend (ASB) test which simulates the process of bending under the action of superimposed membrane tension. The influence of bending severity on achievable critical strains was studied by Charpentier [7.1], where domes of different curvatures were used to form sheet metal samples. Strains in the necked region and in the vicinity of the necked region of the sample were measured. Critically necked strains were found to increase with punch curvature for the same thickness. The ASB test was originally developed by Demeri [7.2]. The test consists of forming open channel shaped geometries with wedge shaped punches of different radii. Typically, the height at failure as a function of the R/t ratio is reported as a measure of formability under stretch bend conditions. The results were reported only for samples that experience failure in the punch contact region, as samples experiencing failure in the unsupported sidewall region essentially experience uniaxial tensile deformation as opposed to stretch bending. Narayanaswamy and Demeri [7.3] analyzed the results of the ASB test and determined that, irrespective of the failure height and frictional conditions at the punch-sheet interface, failure occurred at a constant critical strain for a given material.

This section presents the results of ASB testing for a variety of steel grades. Failure heights for different R/t ratios are presented as measures of overall formability. As previously observed [7.2] for most of the steel grades, failure moved from the punch contact region to the unsupported sidewall at the highest R/t ratios. Strains were measured in the failed samples in the unsupported sidewall region and resulting distributions analyzed to determine a critical R/t ratio beyond which the effect of bending severity on formability is minimal. Applicability of this measure of stretch bend formability in a general stamping is also discussed.

7.3 Experimental Procedure

Figure 7.1a and 7.1b show a schematic and the actual ASB tooling as mounted on the press. Essentially, the test consisted of using drawbeads and the binder table of the press to lock out material beyond the drawbead. The material is then formed using punches of different radii.

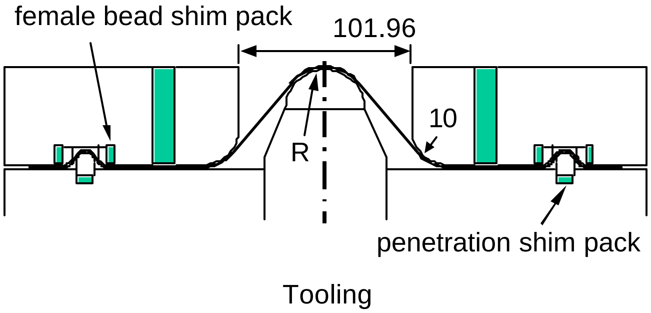

Figure 7.1a: Schematic of tooling for the ASB test. All dimensions in mm.

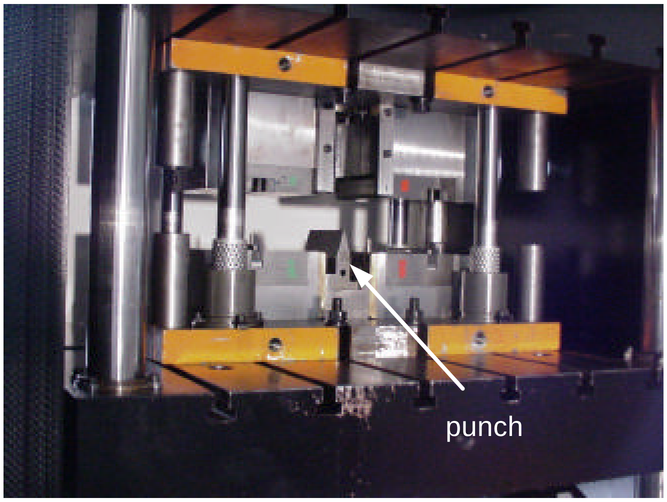

Figure 7.1b: ASB tooling as mounted in the press

Figure 7.2 shows the ASB test specimens for the different R/t ratios. Sample lockout was achieved by adjusting male drawbead penetration, and the clearance between male and female drawbeads. As shown in Figure 7.1a, these adjustments were made possible by the use of shim packs, controlling the bead penetration and clearance between the male and female drawbeads. To check for material slippage through the beads, one sample per lot was formed with only the drawbeads (bead sample). The test samples that were formed were stacked up on top of the bead sample and visually inspected for slippage. In case of slippage, the drawbead clearances were adjusted accordingly.

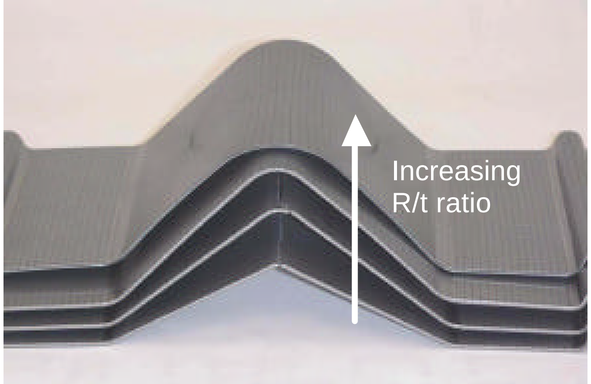

Figure 7.2: Photograph of ASB test samples

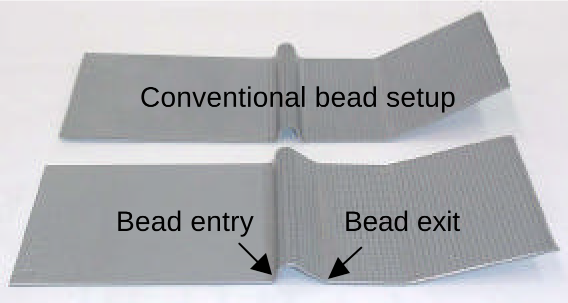

Figure 7.3: Drawbead configurations used for sample lockout. The sample on top uses an equal clearance on either side of the male drawbead. The sample on the bottom uses an unequal clearance to prevent flow of the material through the drawbead.

For some steels, to ensure sample lockout without splitting at the bead exit, the bead configurations were modified as shown in Figure 7.3, where a negative bead clearance was used for the bead entry with a larger clearance for the bead exit ensuring that the material beyond the drawbead was locked out. The flexibility made possible by the drawbead construction in the tooling was the key to successfully performing the test on materials with a wide variety of strength levels. Table 7.1 presents the punches used in the ASB test.

Table 7.1: Punch radii used for the different thicknesses in the ASB test

Nominal thickness (mm)	**Punch Radius (mm)**			
0.65	1.0	2.5	5.0	10
0.95	1.0	3.7	7.5	12.5
1.2	1.5	5.0	10	25
1.6	2.5	7.5	12.5	25

The other experimental conditions for ASB testing are summarized in the bulleted list below. To isolate steel substrate properties from surface conditions, teflon and a light lubricant (LPS2) were used on the punch nose to minimize friction.

- Die entry radius: 10mm
- Drawbead radius: 4mm

- Binder force: 556kN
- Speed: 4.24mm/sec
- Sample Dimensions: 101.6mm (Rolling) X 462.3mm (Transverse)
- Direction of Stretching: Transverse
- # of replicates: 3 samples per punch radius per lot.

7.4 Results

Two types of results were generated for the ASB test. As a first order view of material formability under stretch bending conditions, the height at failure is presented. During the test, the load and displacement signals for the punch actuator were recorded continuously. The punch displacement at maximum load is considered to be the failure height. This is one of the traditional ways of representing results for a simulative formability test, where material formability, measured by height at failure is a function of the tooling geometry, n-value, r-value, and lubrication conditions. This approach of representing formability is simple, and provides a relative ranking on the ability of the material. The main limitation of this approach is that extrapolation of test results as represented by forming height to general part geometries is almost impossible. A second type of results was obtained for the ASB test by measuring the strains for the samples, and comparing them with the achievable limit strain as determined by the empirical FLC.

7.4.1: Height at Failure

Figures 7.4 and 7.5 show the heights at failure for all skin panel steels and structural steels in the project. For ease of representation, the BH300, HSLA 350, HS440W have been grouped together as steels of tensile strength approximately equaling 450 MPa.

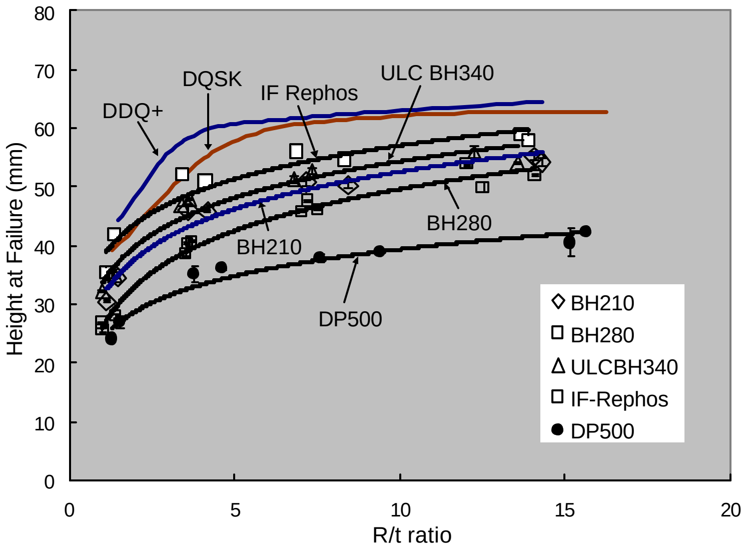

Figure 7.4: Formability of skin panel steels as a function of R/t ratio

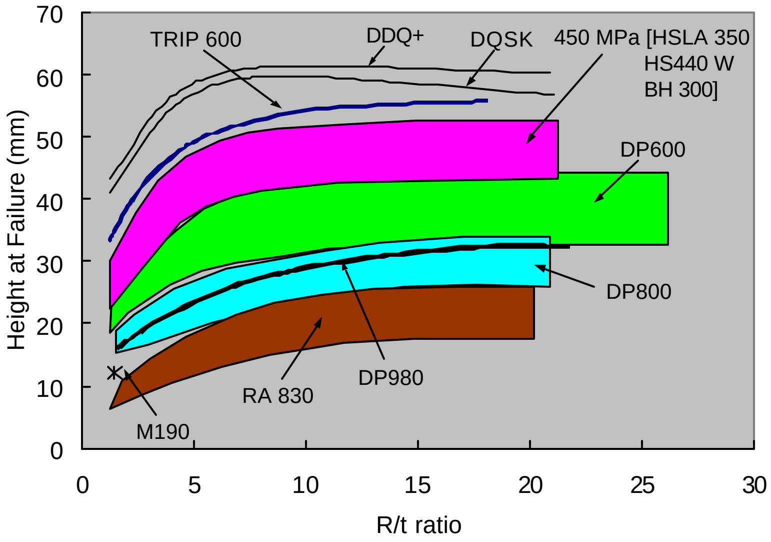

Figure 7.5: Formability of structural steels as a function of R/t ratio

A table with the failure heights and failure locations for all lots of steel is given in the Appendix A. As seen in Figures 7.4 and 7.5, at lower R/t ratios, the heights at failure are strong functions of R/t. At higher R/t ratios, formability of all the materials approaches some saturation limit, which is a function of the mechanical properties of the steel grade. Figure 7.6 shows the observed failure locations for the ASB test for the smallest and largest R/t ratio respectively. As seen in the figure, failure occurs at the punch nose radius across the width of the specimen for small R/t ratios. As R/t increases above some limit, failure moves from the punch to the sidewall. This observation is true for all the steels in the program except Dual Phase steels. The trends in Figures 7.4 and 7.5 are a manifestation of this phenomenon, where for smaller R/t ratios, failure occurs over the punch nose, whereas for the largest R/t ratio failure occurs in the sidewall. It can be considered that beyond a certain R/t ratio, the effect of bending severity on the ability to form the part is minimal.

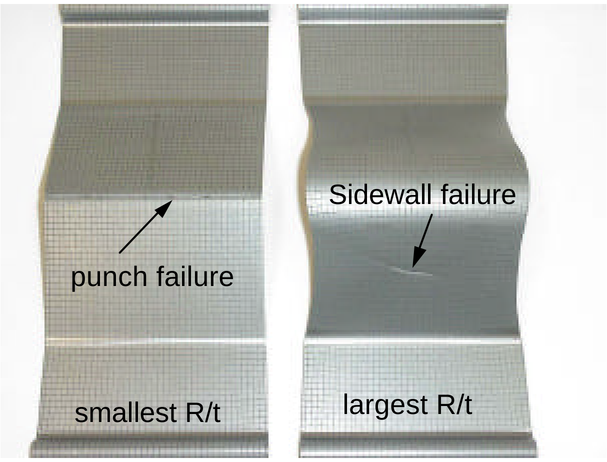

Figure 7.6: Observed failure locations for the smallest and largest R/t ratio samples

For Dual Phase steels, the largest R/t ratio did not produce sidewall failure as observed in the other steels. Samples continued to fail at the punch nose even for the largest R/t ratio for most of the DP steels in the program. This indicates that bending continued to limit the achievable formability for DP steels even as the R/t ratio was increased. The only exception was DP980, where failure occurred in the sidewall for the largest R/t ratio.

As seen in Figure 7.4, for different lots of a given strength level, formability results for the skin panel steels fell on the same line. Difference between the different lots of steel is magnified for structural steels, where significant variability in formability was observed for steels of a given strength level. As an example, from Figure 7.4 it can be seen that the formability of different lots of the BH280 grade were comparable. On the other hand, the formability of the different lots of DP600 showed significant differences. This is probably because the microstructures of the structural steels are more complicated than the skin panel steels. Considering DP600, it is possible to have lots of similar ultimate tensile strengths but with different dispersions and volume fractions of martensite which would influence bending under tension performance. The data shown in Figures 7.4 and 7.5 can be plotted for specific R/t ratios. Figure 7.7 shows the trend of the failure height as measured by the ASB test for all the steel grades in the study as a function of the UTS for an R/t ratio 5. From Figure 7.7, it can be seen that the formability of TRIP600 under stretch bend conditions is much better than the other structural steels. Also noteworthy is the superior formability of DP980, when compared to RA830 or even DP800. Results of ASB testing indicates that formability under stretch bending conditions is not only dependent on the specific mechanical properties of the steel lot, but microstructure and chemical composition may also have a significant effect. A study of the effect of microstructural attributes were beyond the scope of this project.

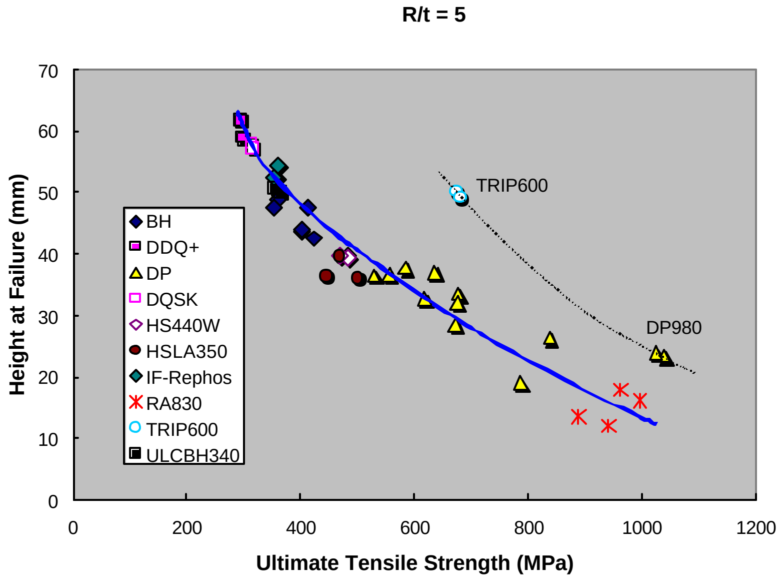

Figure 7.7: Dependence of the failure height for an R/t ratio of 5 as a function of the ultimate tensile strength of the steel grade

7.4.2: Strain Analysis

While results from the above section highlight differences in formability under stretch bend conditions, formability as measured by the failure height, is strongly dependent on typical mechanical properties. Determination of failure heights by itself does not provide distinct information about stretch-bendability of the material. Moreover, failure height although providing relative ranking of material formability under near identical conditions, is not particularly useful to provide guidance on critical R/t ratios for actual production parts. The purpose of strain analysis of ASB specimens was thus twofold: (1) Isolate and determine a performance metric of stretch-bendability and (2) Provide guidance on appropriate R/t ratios for general part geometries.

Figure 7.8 shows the orientation of the major and minor axes on the sample. Major and minor strains were measured on one side along the centerline of the sample as shown in the figure. Although strains were measured on the punch nose radius, wherever possible, for subsequent analysis only the strains in the unsupported sidewall region are used. Strains were measured in one sample per punch radius. Only the samples experiencing failure on the punch nose are used in the analysis. Figure 7.9 shows the strain distribution for the three R/t ratios, where punch failure is experienced for 0.93mm BH210 material. The X-axis shows the original distance of the undeformed grid point from the center of the sample, and the y-axis shows the true major and minor strain at the grid point. Strains were measured using an automated strain analysis system developed by FMTI systems. As seen in Figure 7.9, the strain distribution in the sidewall shows higher strains as the R/t ratio increases due to the reduction in bending severity at the punch nose. For small R/t ratios, the bending deformation at the punch nose is very severe and causes strain localization at the punch nose instead of distributing strains to the sidewall. At higher R/t ratios, the severity of bending deformation is reduced and strains increase in the unsupported sidewall. Beyond a critical R/t ratio, the severity of the bending deformation at the punch nose is overshadowed by the deformation in the unsupported sidewall. When this condition is reached, the failure location shifts from the punch nose to the unsupported sidewall.

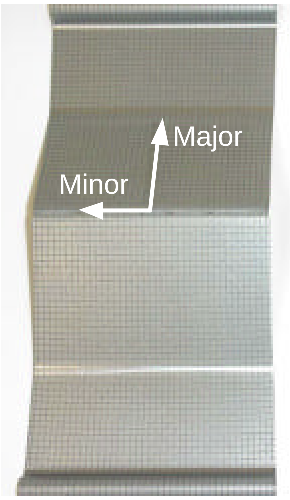

Figure 7.8: Location and orientation of strain axes on the ASB samples

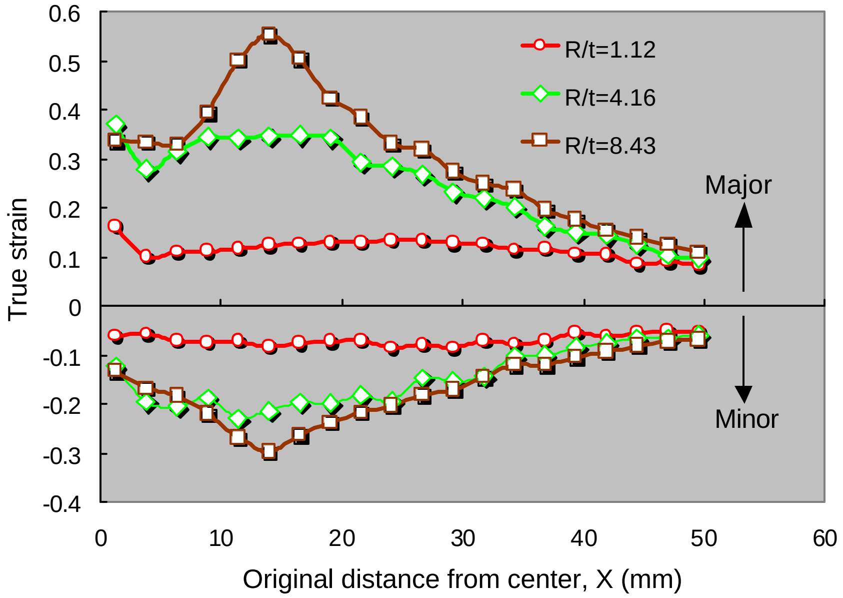

Figure 7.9: Strain distribution in the unsupported sidewall region for 0.93mm BH210 for the R/t ratios experiencing punch failure

These observations on the strain distribution for the different R/t ratios for a given steel lot can be compactly represented on a forming limit diagram as shown in Figure 7.10. Major and minor true strain distributions in the sidewall for all three samples (different R/t ratios) are plotted on the FLC, which is expressed in true strains. Also plotted on the figure is the empirical FLC, which is determined using the following equations [5.1].

$$FLD_0^{true} = \ln\left[1+(23.3+14.13t)\cdot\frac{n}{0.21}\right]; n \le 0.21 \qquad (7.1)$$

Where, n = Work Hardening Exponent, and t = Thickness

For $\varepsilon_2<0$; $$e_1 = FLD_0^{true} - e_2 \qquad (7.2)$$

For $\varepsilon_2>0$; $$e_1 = \ln\left[0.6\left(\exp(e_2)-1\right)\right] + \exp(FLD_0^{true}) \qquad (7.3)$$

In equation (7.1), the terminal n-value in the transverse direction is used to determine the empirical forming limits. This is because the stretch bend test was carried out in the transverse direction and for a significant number of high strength steels, the average n-value between 6% and 12% strain could not be determined, because of the uniform elongation being less than 12%.

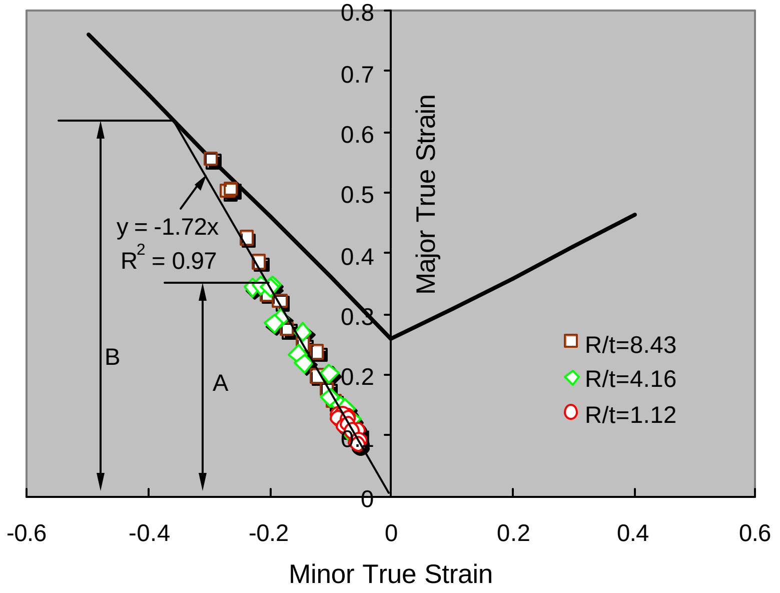

Figure 7.10: True strains for 0.93mm BH210 for the R/t ratios experiencing punch failure

As seen in the figure, the deformation mode for the samples with different R/t ratios is the same. A single straight line can be fit through the strain data points for the three R/t ratios as shown. The intersection of the straight line fit with the FLC is the limit strain (B), for the particular strain path (represented by the slope of the straight line fit). Also from the figure, it can be seen that for a given R/t ratio, the maximum distance along the strain path line increases, with increasing R/t ratio. The stretch bendability of the material can be thus be defined as a fraction of the forming limit for the sidewall.

$$\text{Stretch Bendability Index} = A/B \qquad (7.4)$$

The stretch bendability index represents ability of the material to tolerate membrane stretching in the presence of severe bending. In the above expression, B is the limit strain for a strain path. "A" is the maximum major membrane strain in the unsupported sidewall region for a given R/t ratio. The stretch bendability index is the normalized maximum sidewall strain for a given R/t ratio and is a measure of the proximity of the sidewall strain to the forming limit. The maximum achievable value of the stretch bendability index is 1. Figure 7.11 and 7.12 plot the stretch bendability index as a function of R/t ratio for some skin panel steels and structural steels respectively. As seen in both figures, for the non-DP steels, the trend is linear. The R/t value for a stretch bendability of 1 represents the critical R/t ratio, $(R/t)_c$, for stretch bending for the particular steel grade, which is the minimum R/t ratio required to achieve maximum possible sidewall stretch. For R/t ratios below $(R/t)_c$, there is a large influence of bend severity on the splitting behavior. For R/t ratios higher than $(R/t)_c$, the effect of bend severity on splitting behavior is minimal. Because the maximum sidewall strain for a given R/t ratio is normalized by the inherent forming limit for the steel grade, for a given deformation mode, this approach isolates bending under tension performance from traditional sheet forming limits determined by n-value and thickness.

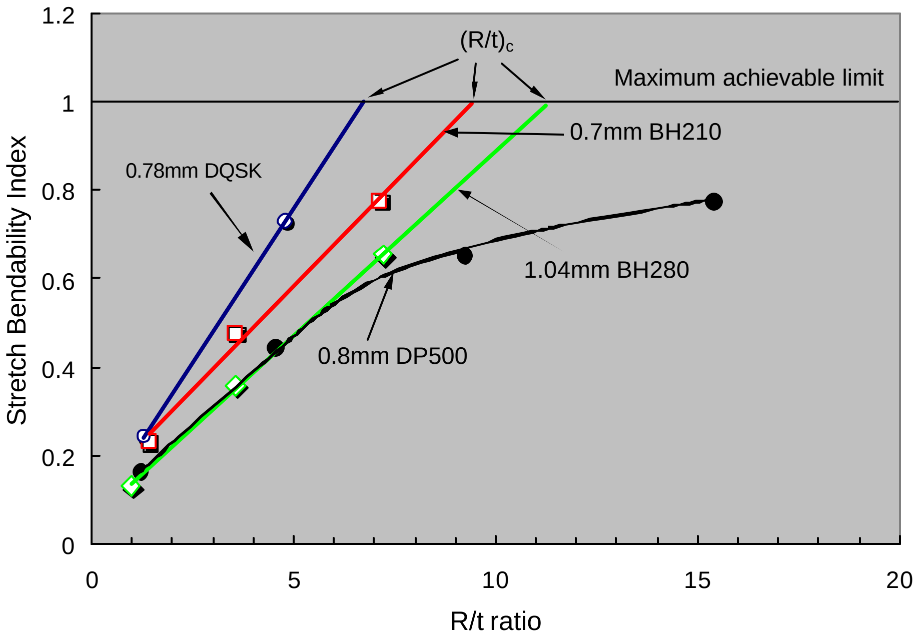

Figure 7.11: Stretch bendability index as a function of R/t ratio for some skin panel steels

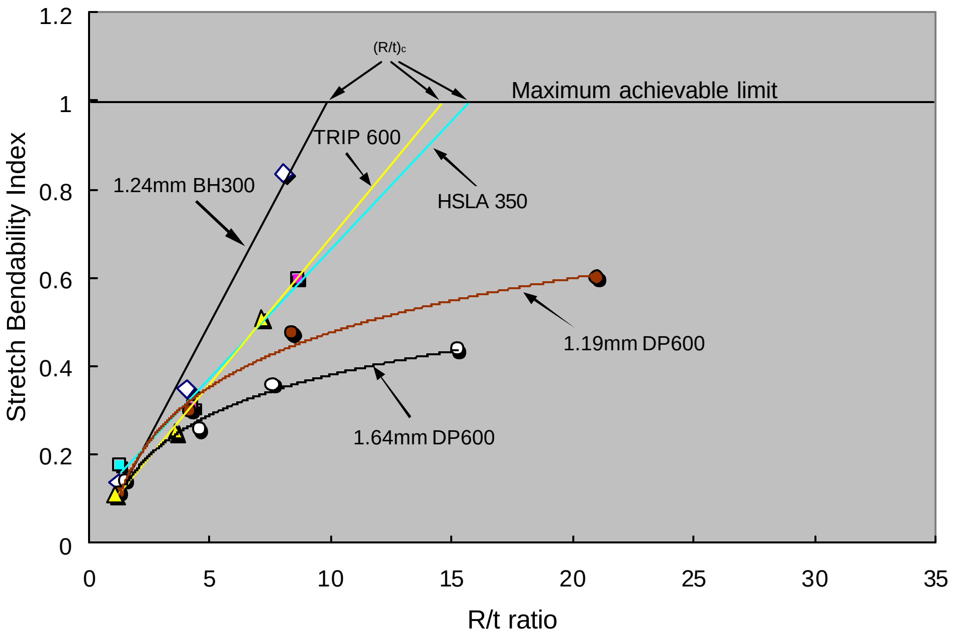

Figure 7.12: Stretch bendability index as a function of R/t ratio for some structural steels

Confirmation of the phenomenon shown in Figures 7.11 and 7.12 was provided by the fact that for all steels for the test conditions where the R/t ratio was higher than the critical value, failure occurred in the sidewall. The behavior of DP steels is demonstrated in Figure 7.13 where the stretch bendability index is plotted as a function of R/t ratio for DP steels. For most of the DP steels, the critical R/t ratio could not be determined because within the range of the punch radii used, all samples experienced punch failure, indicating that bending severity continued to influence splitting behavior even for the higher R/t ratios. These results underscore the fact that caution needs to be exercised while applying DP steels in predominantly stretch bending deformation mode.

The interrelationship between membrane stretching severity, bending severity and material characteristics is presented in Figure 7.14, where the stretch bendability index is plotted for three R/t ratios as a function of the tensile strength. Bending severity is represented by the R/t ratio, where a low R/t ratio represents severe bending. As seen in the figure, for a given material, the ability to tolerate tensile strain increases as R/t ratio increases. For a given bending severity, the stretch bendability index decreases as material strength increases. The decrease in the stretch bendability index with increasing material strength is more significant for higher R/t ratios. For steels with ultimate tensile strengths between 300 MPa and 400 MPa, an R/t ratio greater than 10 was sufficient to avoid localization at the bend radius thereby promoting localization in the unsupported region for this test. For higher strength steels, a R/t ratio of 10 was insufficient to avoid localization at the punch radius.

For the steels that experienced a change in failure location from the punch nose to the sidewall, the critical R/t ratio can be determined using the procedure described previously. The trend of the critical R/t ratio with respect to the UTS is presented in Figure 7.15.

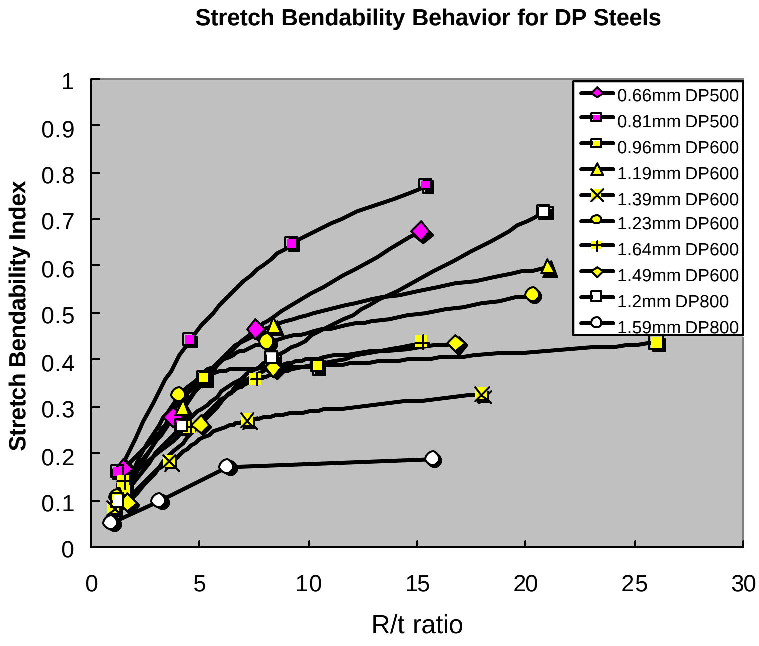

Figure 7.13: Stretch bendability behavior of DP steels

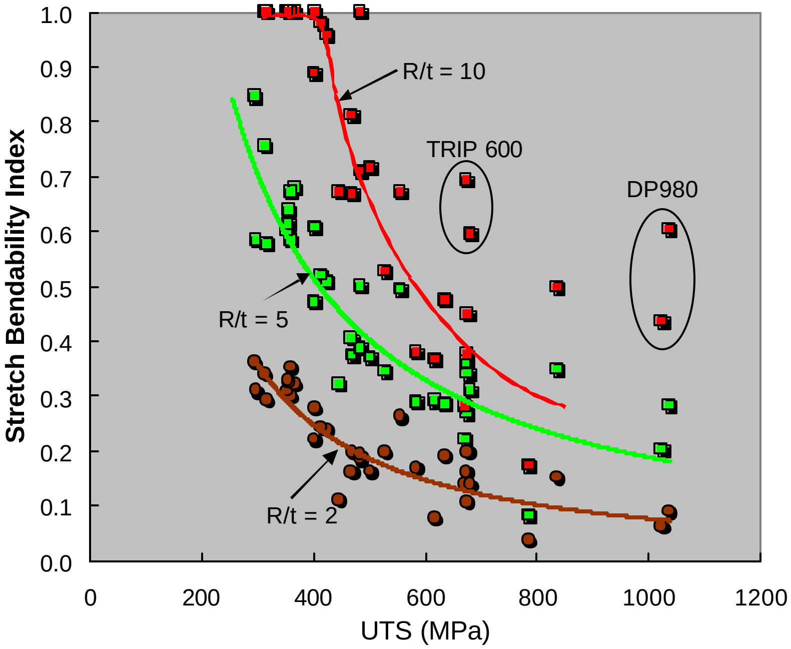

Figure 7.14: Stretch bendability behavior as a function of tensile strength for three R/t ratios

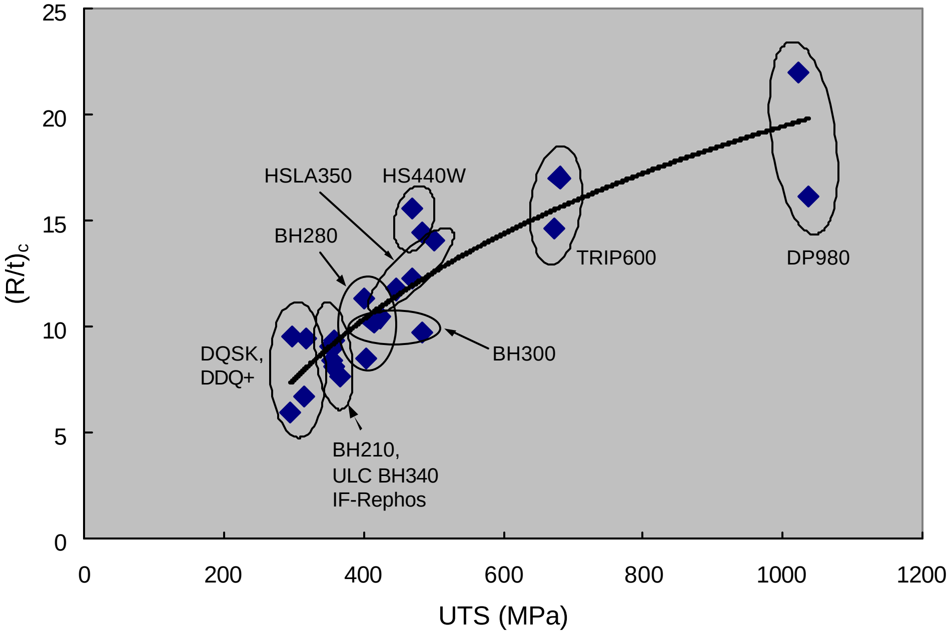

Figure 7.15: Trend for critical R/t as a function of the tensile strength

7.5 Discussion

From examination of Figure 7.14, it can be seen that for higher R/t ratios, for a given tensile strength level, there are considerable differences in the stretch bendability index that can be tolerated depending on the properties of the steel lot under consideration. This clearly indicates that bending under tension limits of the material is significantly dependent on the microstructural features of the steel grade, which are in turn functions of the chemical composition and steel processing. It is thus possible to optimize the microstructure of the steel grade to maximize stretch bend performance in addition to traditional measures of formability such as n-value and R-value. It is interesting to note from Figure 7.14 that the stretch bendability index for TRIP600 and DP 980 lie significantly above the trend lines.

The behavior of DP steels is also interesting. As opposed to all the other steels in the program, from Figure 7.13, it can be seen that the trend of stretch bendability index vs. R/t ratio is nonlinear. Figure 7.13 amplifies the differences between the different DP steels, where it is conjectured that differences in chemical composition and steel processing may influence the stretch bending performance significantly. Differences in steel processing and chemistries are known to yield different martensite volume fractions, distributions and hardness, which may be factors influencing the forming behavior. However this is beyond the scope of the project.

The use of strain analysis thus provides significantly more useful information than the forming heights at failure. The work on strain analysis of the ASB testing has yielded results that could provide guidelines for die design and process planning engineers when processing high strength steels to avoid stretch bending failures. One of the common approaches to minimize springback is to tighten die radii and increase membrane stretching. Results from this study provide lower bounds for R/t ratios for stretch bending. Using Figure 7.15, knowledge of the ultimate tensile strength of the material could help in specifying minimum die radii to avoid splitting at the bend radius while maximizing membrane stretching. Figure 7.14 provides a convenient approach to representing the relationship between stretch bendability and material strength. While conducting stamping feasibility analysis for a given steel grade using FEA, the stretch bend severity can be determined by evaluating the proximity of the maximum strain in a critical area to the forming limit strain for a given strain path. One can then assess the likelihood of stretch bend failures especially for tight bend radii. For example, from Figure 7.14, for a 600 MPa strength material, and R/t ratio of 5, the maximum stretch bendability index is determined to be approximately 0.3. This information can be used to adjust the forming process to limit the stretch bendability index to less than 0.3 such as to avoid splitting failure caused by stretch bending severity at the bend. It should be noted that Figure 7.14 has not been generalized for multiple strain paths. The same approach of isolating bending under tension limits from traditional forming limits can be applied to examine the influence of variables such as friction and lateral constraints on $(R/t)_c$. Testing can be conducted by increasing (or decreasing) sample width, to change the lateral constraint and hence the strain path. The effect of different lubrication conditions on $(R/t)_c$ can also be explored.

7.6 Conclusions

Bending under tension limits were determined for a range of steel grades. The following are the conclusions of this study.

1. Bending under tension formability as measured by the failure height is a strong function of the R/t ratio for small R/t values and saturates at higher R/t values. Location of failure moves from the punch nose to the sidewall (at higher R/t ratios) for all steels except most DP steels.

2. Most DP steels exhibit punch failure even at the highest R/t ratio indicating that bend severity continues to influence splitting behavior.

3. Using strain measurement and analysis, a procedure for isolating stretch bend performance as defined by the stretch bendability index was developed. The maximum value of the stretch bendability index is 1.

4. For non-DP steels, the trend for the stretch bendability index as a function of R/t ratio was linear. The R/t ratio corresponding to a stretch bendability index of 1 was defined as the critical R/t $[(R/t)_c]$ ratio.

5. The stretch bending performance of TRIP600 and DP980 was significantly better than their counterparts for a given level of ultimate tensile strength.

6. For DP steels, the trend for stretch bendability index as a function of R/t ratio was non-linear.

Section 8.0
Springback and Curl

8.1 Summary

This section summarizes the experiment and results of channel draw test, which is one of the simulative tests in this AISI/DOE formability project. The channel draw test has been widely used to examine the springback behavior of materials under plane strain stretch-draw conditions. Two springback parameters, springback angle and sidewall curl, were studied for the lots of steel in the program. Using a DOE (Design Of Experiment) approach, the effects of three process variables, namely tooling radii, tool gap and drawbead penetration, and their interactions on springback were characterized. Test results revealed that the single factor effect of three process variables were generally more important than their interactions. Among the three, tooling radii and drawbead penetration were found to be more influential than tool gap; this finding is in agreement with previous studies. Under all testing conditions, springback and curl were strong functions of strength and thickness of sheet metals.

8.2 Background

A major issue in the automotive application of Advanced High Strength Steel (AHSS) is the prediction and control of springback. Springback occurs in all metal forming processes but is especially important when bending is involved. It is caused by elastic recovery and residual stress distribution resulted from inhomogeneous strain in the material. It is related to the part geometry, material properties, friction and forming conditions [8.1]. In the last decade, springback has become a focus for the sheet metal forming research [8.2,8.3]. Although considerable progress has been made in terms of understanding springback for simple geometries, there is still a lack of technological breakthroughs to allow industrial practitioners to predict and control springback effectively for general part geometries. The present practice in springback control is still based on experience that was learned through a trial-and-error process. Experimental data on springback behavior of advanced high strength steels is thus desirable as it could provide much needed information on dimensional control and shape fixability that could be used to develop effective processing strategies for stamping. Experimentation of springback behavior using a Channel Draw test procedure has been widely used as a simulative test in the springback study of sheet metal stampings [8.4-8.7]. This is because most automotive structural components, such as rails, pillars, cross members and load beams, etc., are normally open channels. This section reports the results from a Channel Draw test for all the steel grades in the current project.

8.3 Materials

The mechanical properties of the steels are given in the Tables 2.1 through 2.4 in Section 2 of this report.

8.4 Testing

8.4.1 Channel Draw Test

The tooling and hydraulic press used for test are shown in Figure 8.1. A schematic drawing of the channel draw test is given in Figure 8.2. The tool set consists of a punch block, a die block, two binders (upper and lower), and two drawbead sets installed on binders. The punch and die blocks were constructed with inserts to change the punch and die entry radii and to use shims to control clearance. To eliminate the effect of binder force variations, a standoff was used to set the clearance between the upper and lower binders to 1.1 times the sample thickness. The samples were clamped by drawbeads only. A set of 4.0mm radius drawbeads was used for the entire study. A constant tool clearance between the male and female drawbead was set to the sample thickness plus 0.05mm at full drawbead penetration. For each lot of steel, the different clearances were checked with lead wires and adjusted to the proper setting. A pressure plate restraining the channel top on the punch face was used to prevent materials being pulled from one side of channel to the other. A constant punch speed of 85mm/second was used in the test. During testing, the lubricant, Ferrocote 61 MAL HCL 1 (Prelube), was thoroughly applied to both sides of the sample by a synthetic bristle paintbrush. Care was taken to apply equivalent amounts of lubricant on both sides of the sample. The samples were 508mm long (in the transverse direction) and 101mm wide. It was found that the effect of anticlastic curvature on the channel draw samples was minimal.

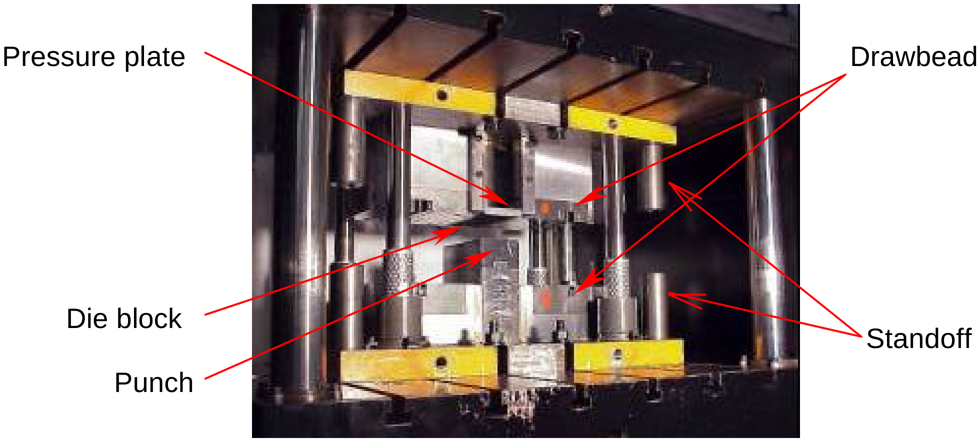

Figure 8.1: The tooling used for the channel draw test

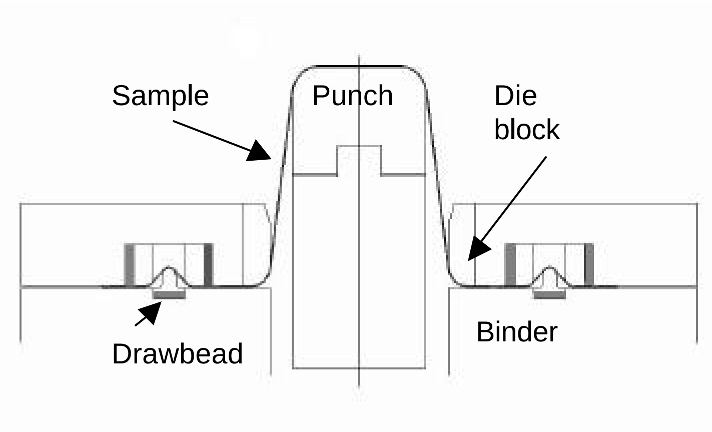

Figure 8.2: Schematic drawing of the channel draw tooling

Three process variables selected for the study are 1) tooling radii (die and punch radii), 2) tool gap and 3) drawbead restraining force. Two levels were used for each of these process variables in this study.

Two different drawbead restraining forces were obtained by setting the drawbead penetration at the maximum and 25%, respectively. The maximum drawbead penetration was chosen because of sample splitting experienced by some AHSS and UHSS under full drawbead penetration. The maximum drawbead penetration was determined for these materials through a series of tests in which the drawbead penetration was reduced stepwise until failure disappeared. In a few cases where the maximum drawbead penetration was smaller than 25%, the drawbead penetration levels were set to the maximum and 10% below the maximum penetration. The drawbead restraining forces were measured quantitatively for each penetration by pulling strips through the drawbeads in drawbead fixture tests.

Two sets of tooling were used for the tooling radii. The tooling set of small radii has a die entry radius of 6.5mm and a punch radius of 6.3mm, while the tooling set of large radii has a die radius of 10.0mm and punch radius of 10.1mm. For the baseline and skin panel steels, another set of small radii tooling with the die and punch radius of 3.0mm and 3.3mm, respectively, was used. Two different tool gaps of t+0.5t and t+0.05mm were used in all tests.

The drawbeads were positioned with enough distance from the die entry radii to provide sufficient material to form the channel. This is to ensure that no material passing through the drawbead would get into the channel wall section.

8.4.2 Drawbead Fixture Test

This test was designed to determine the drawbead restraining force by closely replicating the bending-unbending process experienced by the sample at the drawbead area in the channel draw test (Figure 8.3). During the test, the drawbeads are closed to clamp the sample strip using a hydraulic cylinder. The strip was then pulled through the drawbead by the punch actuator. The punch force recorded was used to obtain the drawbead restraining force. The drawbead setup and punch speed used in this test were exactly the same as those used in channel draw test.

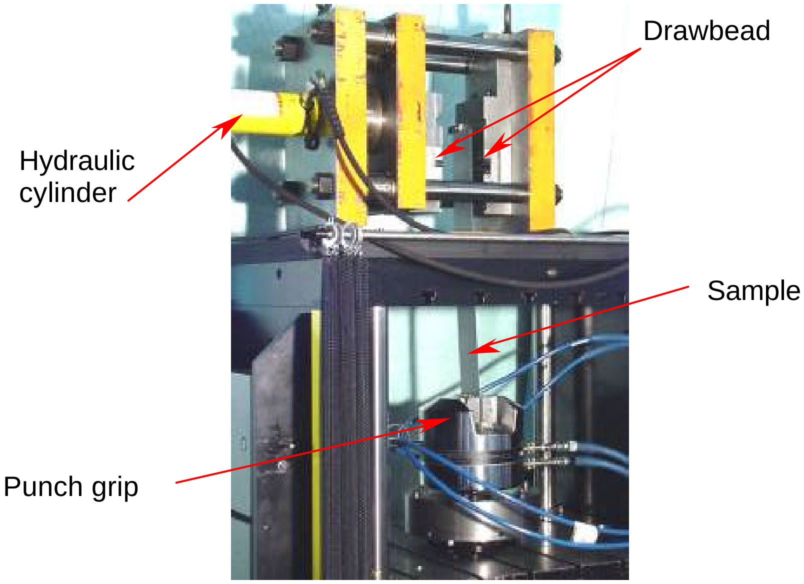

Figure 8.3. The drawbead fixture test

8.5 Design of Experiments

To examine the effects of process variables and their interactions on springback, a DOE (Design of Experiment) was developed for the study [8.8,8.9]. A full factorial design of experiment was used to identify the influential process variable(s) and their interactions. For a test with three factors (process variables) in two levels, a group of eight tests is required to fully evaluate the effect of all factors and interactions on springback. The testing runs resulting from the above full factorial design is shown in Table 8.1. In each run, at least four samples were repeated.

Table 8.1: Full factorial channel draw test

Testing Conditions		C (Drawbead Penetration)			
		C_S (25% Penetration)		C_L (Maximum Penetration)	
		B (Tool Gap)		B (Tool Gap)	
		B_S (1t+0.002”)	B_L (1.5t)	B_S (1t+0.002”)	B_L (1.5t)
A (Tool Radii)	A_S (6.5 &6.3 mm)	$A_SB_SC_S$	$A_SB_LC_S$	$A_SB_SC_L$	$A_SB_LC_L$
	A_L (10 & 10.1mm)	$A_LB_SC_S$	$A_LB_LC_S$	$A_LB_SC_L$	$A_LB_LC_L$

A full factorial experiment design allows us in examining the effects of seven factors that include all process variables and their interactions (Table 8.2)

Table 8.2: Factors used for process variables and their interactions

Factor	**Process Variables**
A	Tooling radii
B	Tool gap
C	Drawbead penetration
AB	Interaction of tooling radii and tool gap
AC	Interaction of tooling radii and drawbead penetration
BC	Interaction of tool gap and drawbead penetration
ABC	Interaction of all three process variables

8.6 Measurement

8.6.1 Springback Measurement and Measurement System

The plane view of a scanned channel draw sample is shown in Figure 8.4. The flanges outside the drawbeads were trimmed out. The scan result describes a 2D cross section view of the sample. The sidewall distortion due to anticlastic bending is small and negligible. By comparing the 2D cross section with punch profile, the springback angle and sidewall curl can be determined.

Two measurements, namely springback angle and sidewall curl, are used to characterize the springback of a channel draw sample. As there is no clear distinction to separate a cross section curve for individual measurement of springback and sidewall curl, some assumptions induced from the sample observations are introduced for the springback measurement. Firstly, it is assumed that the opening angle and sidewall curl varies independently and can be measured as such. Next, the springback angle can be assessed from the angle between a tangent of the cross section curve and punch sidewall. Finally, the sidewall curl could be approximated by a piece of circular arc.

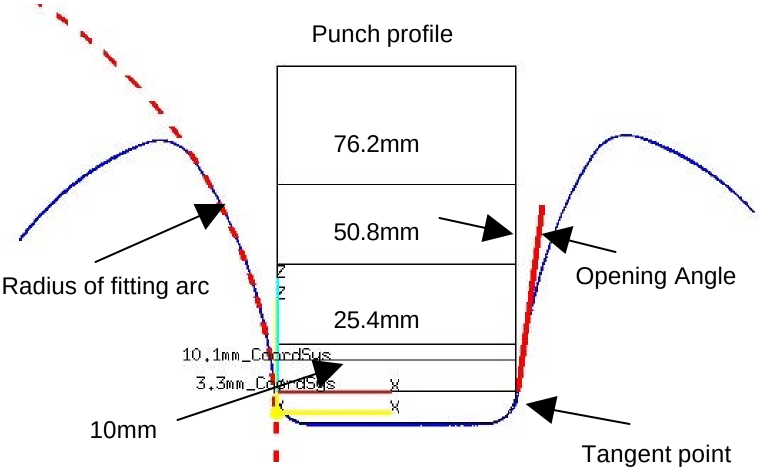

Figure 8.4: Measurement of a formed sample

The springback angle should be determined with a tangent of cross section curve before it starts to curl. As it was difficult to determine a tangent in practice, a straight line using two points on the cross section curve was used as an approximation. One point chosen for the straight line was the tangent point of nominal punch corner radius. The other was the point at 10.0mm above. Generally, the line constructed with these two points is a good approximation of the tangent (solid line in Figure 8.4).

To estimate sidewall curl, a curve fitting technique that employs three points to construct a circular arc is used. Three points selected from the cross section curve are at a distance of 25.4, 50.8 and 76.2mm from the punch face, respectively. After determining the coordinates of three points from measurement, a circular arc can be constructed (dotted line in Figure 8.4). The radius of the arc is taken as the radius of sidewall curl. In practice, the sidewall opening distances were measured at three heights as shown in Figure 8.5. As the sample is generally symmetrical, the measurements at three heights can be converted into XY coordinates of three points on the sidewall. The radius of sidewall curl was numerically calculated with the XY coordinates using the Newton-Raphson method.

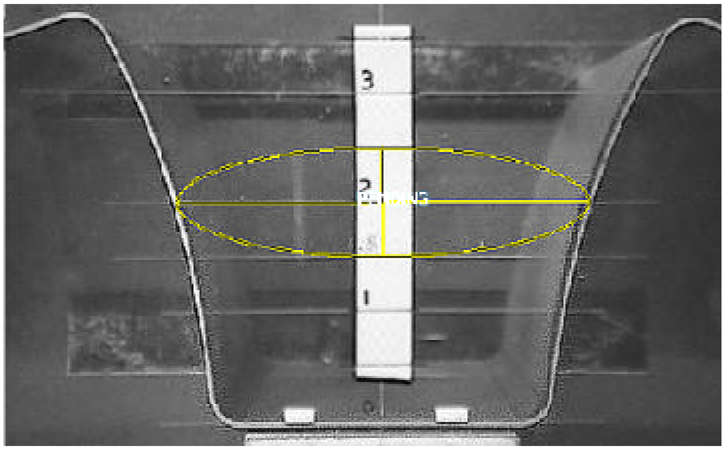

Figure 8.5: Measurement of sidewall opening at a point 50.8mm (2.0”) above the punch face

To prevent shape distortions caused by measurement equipment, a non-contact measurement system was built which included the FMTI 100A circle grid analyzer and a custom-made testing rig (Figure 8.6). A transparent template with a scale as shown in Figure 8.5 was used to assure the consistency and accuracy of measurements. Three replicates were measured for each testing condition. For each measurement, three readings were taken. The average of nine readings from three samples was used in the calculations of springback angle and curl radius.

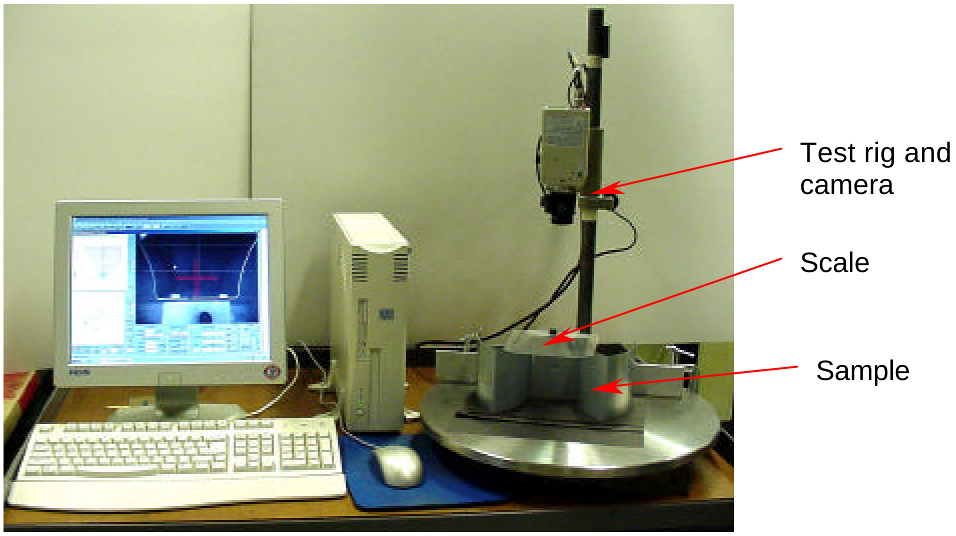

Figure 8.6: The measurement system for measuring springback angle & sidewall curl

8.6.2 Measurement Uncertainty

One major issue in the analysis and interpretation of measurement results is to understand sources of variations contained in the measurement [8.10]. The uncertainty caused by the accuracy of measuring equipment is one of the sources and needs to be analyzed. In the current study, some large variations were found in the curl measurements for the samples with nearly flat sidewalls.

The accuracy of a length measurement by FMTI circle grid analyzer is reported as 0.5% according to the manufacturer specifications. It was found that this measurement uncertainty might lead to an erroneous result for the sidewall curl in the situation described above.

A schematic illustration of a sample with perfectly straight walls is shown in Figure 8.7. Only a half of the channel is shown in the picture because of symmetry. The wall opening distance of the sample is measured at three points, A, B and C and the distance between them is 25.4mm (1.0”). As there is no curl in the sidewall, the radius of curvature of the sidewall should be infinity. Because of uncertainty in the measurement, however, we might get a measurement at point B with a difference of 0.5% from its true value. For the channel opening of 76.2mm (3.0”), a 0.5% difference is 0.382mm and a half of it is 0.191mm as shown from B to B’ in Figure 8.7. If there is no measurement variation for point A and C, an artificial sidewall curl would result from the above measurement variation.

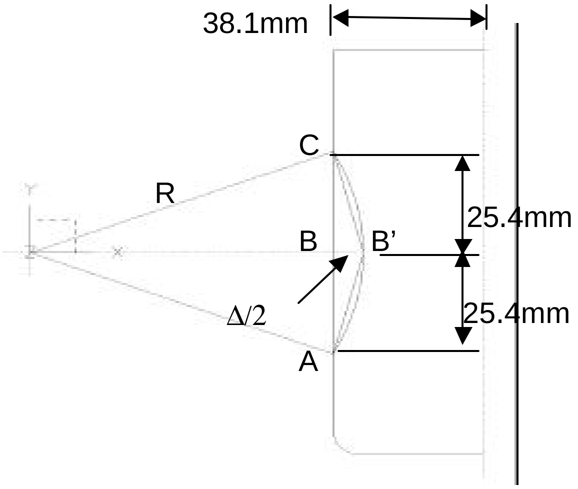

Figure 8.7. Schematic drawing of sidewall curl due to measurement uncertainty

The radius of sidewall curl can be determined from the above figure from simple trigonometry. For the triangle OBC in Figure 8.7, we have the following equation

$$R^2 = (R - 0.191)^2 + (25.4)^2 \qquad (8.1)$$

Solving equation (8.1), R was determined to be 1,690mm. The smaller the measurement variation is, the larger is the resulting R.

Thus, for any sample with nearly perfect straight walls, the measurement system was not able to measure the sidewall curl accurately. In another words, any value of the measured R greater than 1,690mm is not an actual radius of curvature of the sidewall curl. It is only a representative of the radius of curvature for a nearly straight wall. Similarly, the measurement uncertainty for the springback angle was determined to be 1.1^0.

8.7 Results

The springback results (springback angle and sidewall curl) for all materials tested for all the testing conditions are attached to this report (Appendix B). Ratios of tool radii/sample thickness, tool gap/sample thickness and drawbead restraining force/sample plane strain yield force are also attached (Appendix C

Because springback is a complicated issue and is sensitive to various factors, such as materials, tooling and process, no multiple regression analysis is attempted here to provide a general characterization of springback and curl behavior for all the steels tested. Instead, an analysis conducted using scree plots was performed to compare the effect of the three process variables and their interactions on springback. Also, an analysis is presented to show the dependence of springback and curl on the yield strength of the steels tested.

8.7.1 Major Process Factors in Springback - Scree Plot

The scree plot is a statistical tool designed to examine and rank the effects of the different factors on springback angle and sidewall curl in the experiment. The conclusions resulting from the scree plot analysis are discussed here. More details on the scree plot and analysis can be found in Appendix D.

From the scree plot analysis, it was found that, in most cases, the most influential factors are the three process variables but not their interactions. Among the three, the tooling radii and drawbead restraining force were found to be more important than tool gap. Under current testing conditions, it was found that the drawbead penetration (restraining force) played a major role in the sidewall curl with little impact made by the tool gap. For the UHSS, the effect of drawbead penetration on springback and sidewall curl was found to be significantly reduced. This was caused by a narrower range of drawbead penetrations that had to be used because of the limited ductility of these steel grades. As observed in Figure D.2, a large variation was observed in the sidewall curl of the baseline steels (DQSK and DDQ+). This was caused by the measurement uncertainty in a situation of nearly perfect channel walls as was discussed previously.

Since the material springback behavior in channel draw test is essentially controlled by the main factors, we will consider only the three process variables in the following analysis.

8.7.2: Springback and Curl of Different Steels

In Figures 8.8 to 8.13, the effects of three process variables on springback and curl are compared for all steels. In these figures, the curvature of the curl (1/curl radius) is plotted. It should be noted that the springback angle and curvature of curl have been multiplied by a thickness factor to exclude the effect of thickness in the analysis. It was found that springback and curl curvature increased with yield strength showing some significant variations to the trend. The variations are attributed to material, geometric, surface and process variables inherent in the test. As the materials tested in this project covered a large variety of steel grades and coatings, the variations in the springback results are inevitable. For materials having similar tensile properties, examination of their microstructures could help to understand the noticeable differences in springback results. However, an examination of microstructure was beyond the scope of the current project.

Other results obtained from Figure 8.8 to 8.13 are listed below.

1. Springback and curl results all fall in a band and increase with yield strength. However, they seem to increase slowly or to saturate for materials of yield strength above 500MPa before climbing again for the martensitic steel.
2. Dual Phase steels show larger springback and curl than conventional HSLA steels. TRIP steels have springback and curl in between the DP and HSLA steels.
3. Curl was observed to exhibit larger variations than springback in general, which indicates that the sidewall curl is more sensitive to the material and testing conditions.

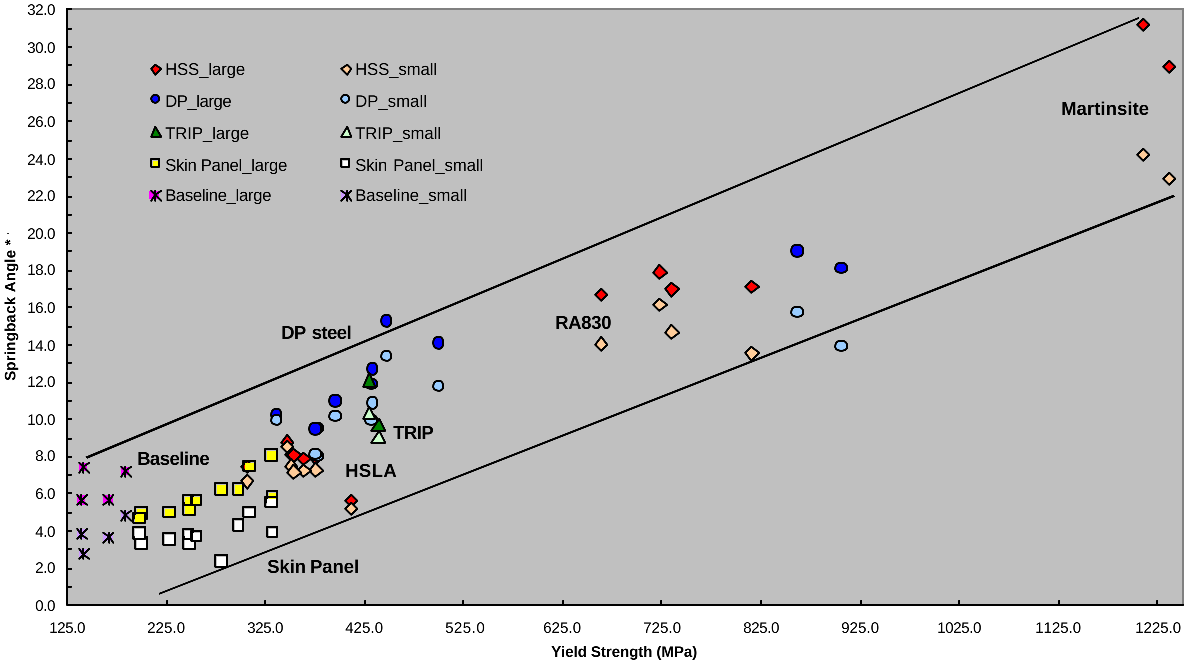

Figure 8.8: The effect of tooling radii on springback

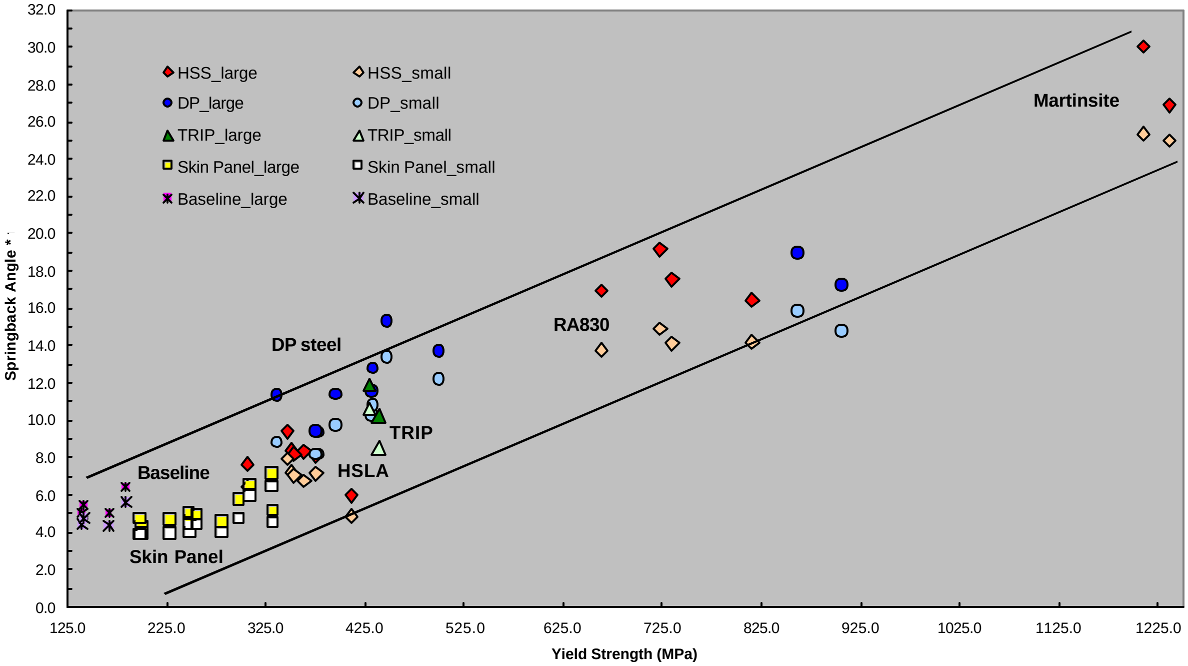

Figure 8.9: The effect of tool gap on springback

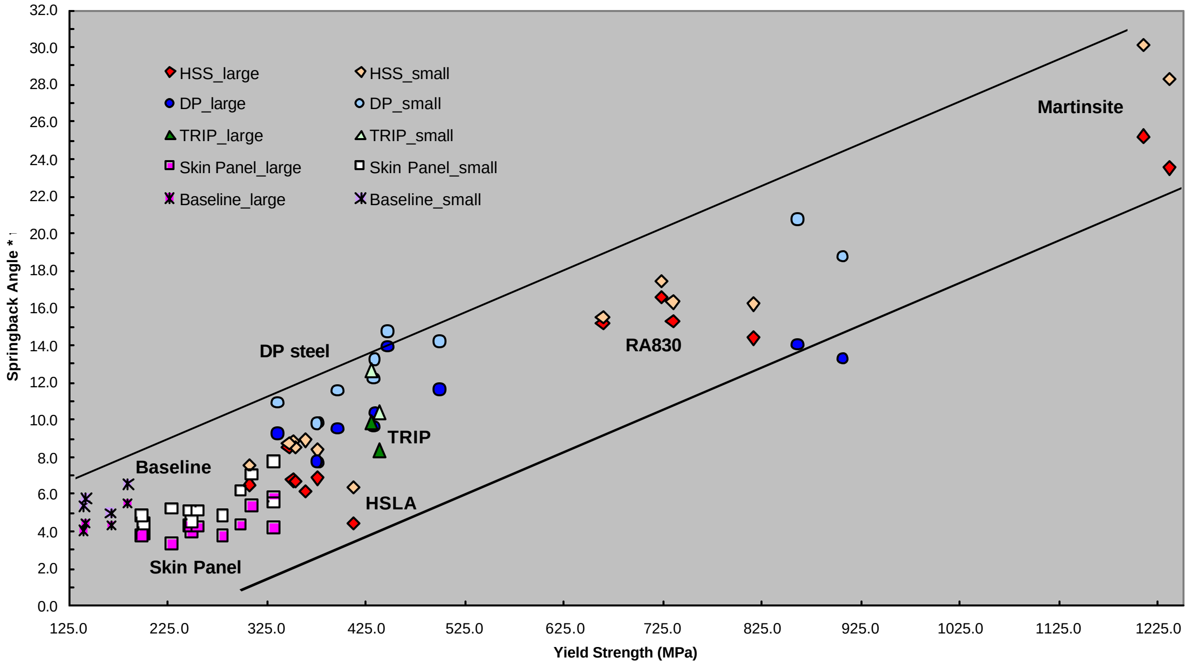

Figure 8.10: The effect of drawbead restraining force on springback

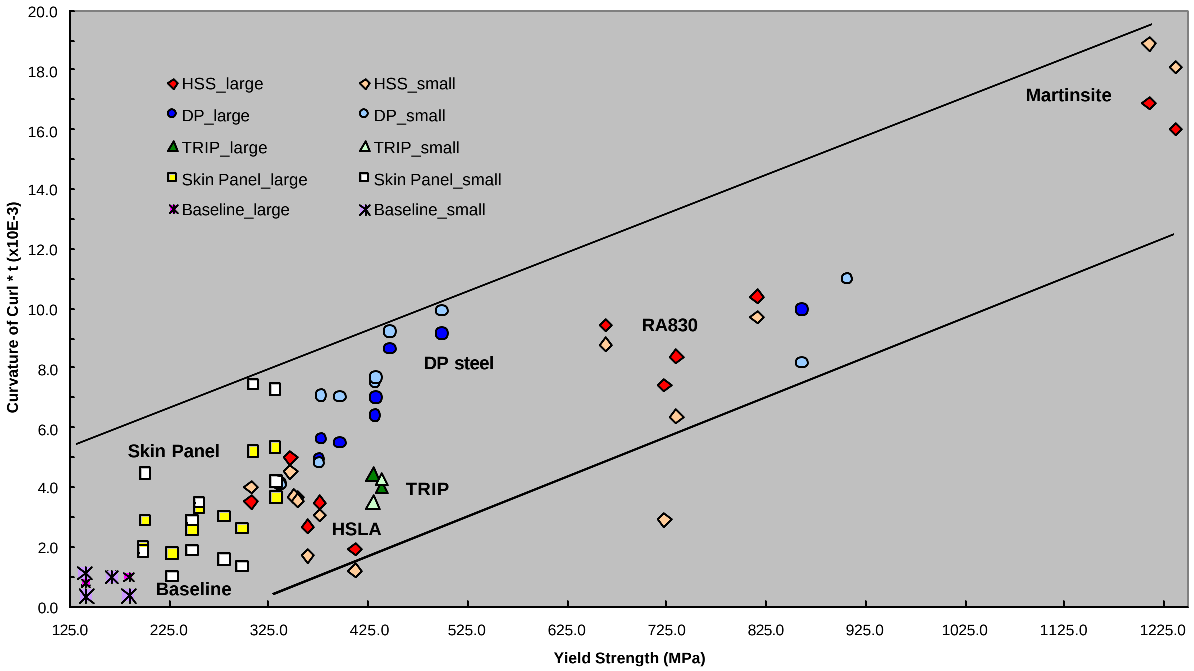

Figure 8.11: The effect of tooling radii on sidewall curl

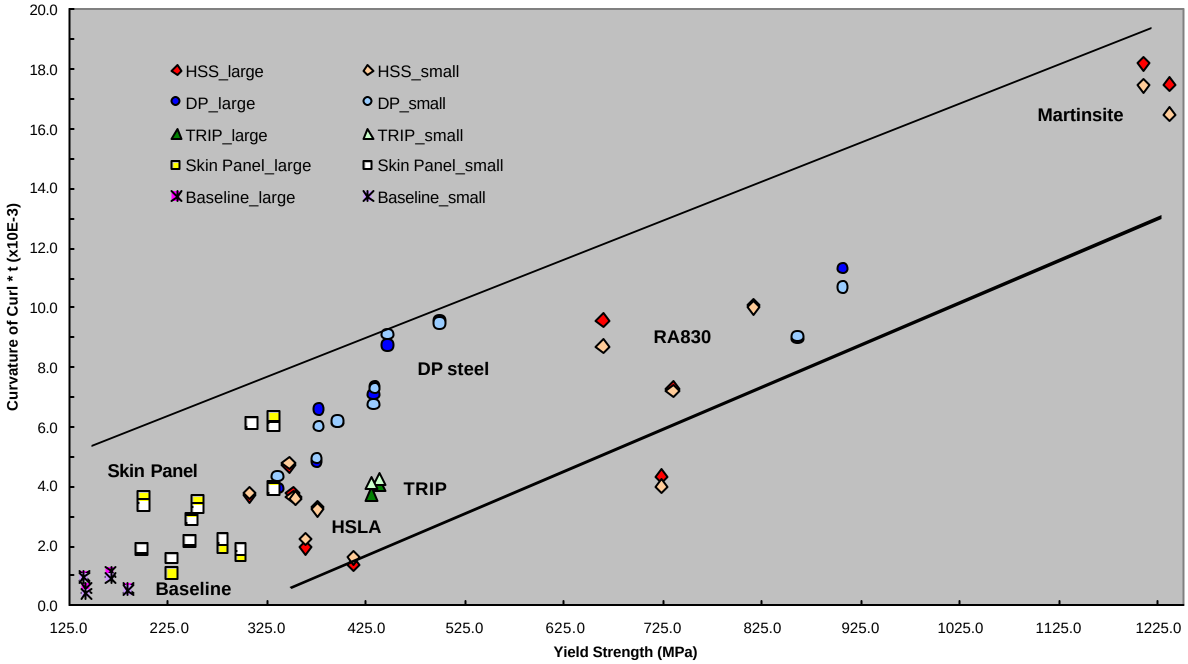

Figure 8.12: The effect of tool gap on sidewall curl

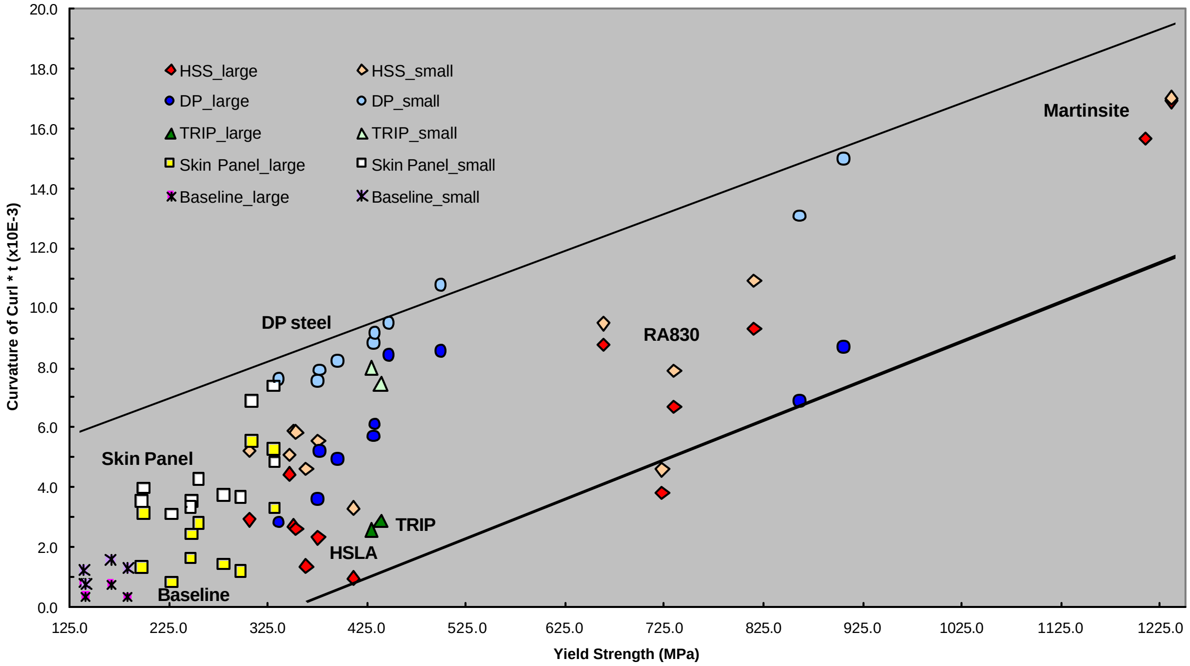

Figure 8.13: The effect of drawbead restraining force on sidewall curl

To further examine the springback behavior of different steels, steels of similar thickness were organized into the following two groups (Table 8.3 and 8.4). Each group has steels of different grades, coatings and strength levels.

Table 8.3: Grouping of steels of nominal thickness 0.70mm

Code	Steel	Coating	Thickness (mm)	Yield Strength (MPa)
Y1	DDQ+	Bare	0.70	140
X1	DQSK	Bare	0.77	167
E1	IF-Rephos	GA	0.63	201
B1	BH210	EG	0.70	249
D1	ULC BH340	GA	0.74	258
G1	DP500	EG	0.66	310
G2	DP500	EG	0.81	332
C1	BH280	EG	0.71	333

Table 8.4: Grouping of steels of nominal thickness 1.2mm

Code	Steel	Coating	Thickness (mm)	Yield Strength (MPa)
Y2	DDQ+	Bare	1.19	142
X2	DQSK	Bare	1.19	184
2K	BH300	GI	1.19	307
1K	BH300	GA	1.24	351
1M	HS440W	GA	1.24	354
5L	HSLA350	Bare	1.21	376
2P	DP600	Bare	1.19	376
1L	HSLA350	GI	1.16	412
4P	DP600	GI	1.23	433
1R	DP800	GI	1.20	500
3W	RA830	Bare	1.25	816
1S	DP980	Bare	1.15	907

The springback and curl analysis of the above two groups is listed in Appendix E. The results of 0.70mm group showed that the sidewall curl has a larger variation than springback. Springback seemed to increase linearly with the yield strength in a range below 350MPa (Figure 8.14). On the contrary, results for curl demonstrated a nonlinear trend. Also, springback generally decreased with smaller tooling radii, tool gap and larger drawbead restraining force. Although curl decreased with larger drawbead restraining force, the changes in tooling radii and tool gap had mixed effects on curl. In some cases, curl was found to increase with smaller tooling radii and tool gap.

Steels of 1.20mm group are compared in the Figures E. 7 - E.12 in Appendix E. Similar conclusions can be drawn for this group except that the springback increases much slower with YS for YS>500 MPa (Figure 8.15).

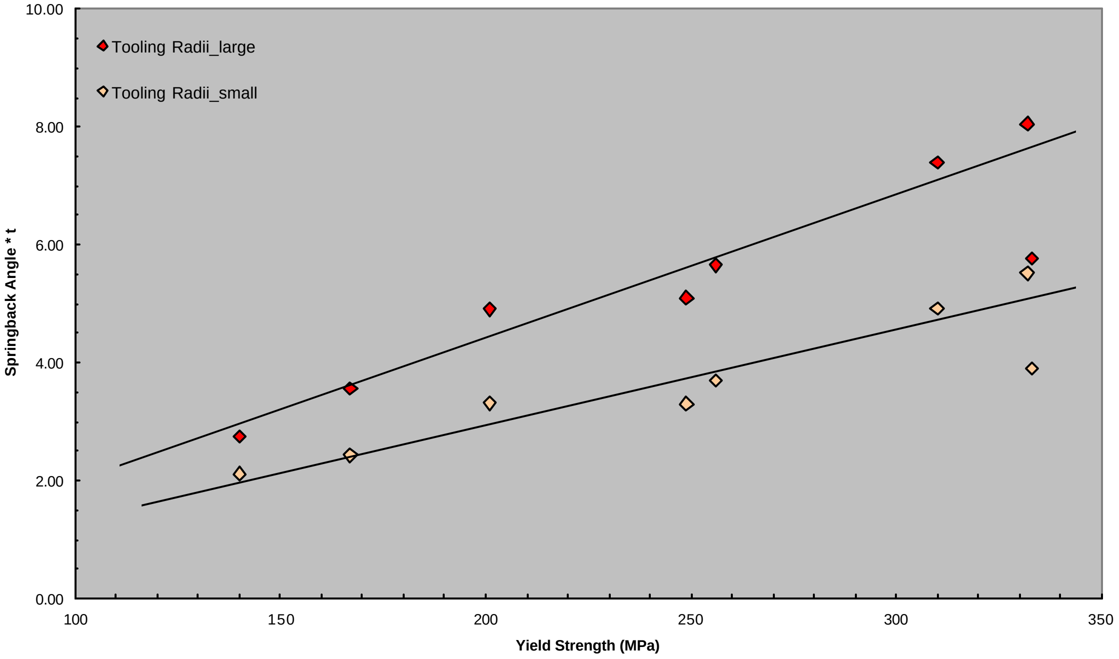

Figure 8.14 Effect of tooling radii on springback of 0.70mm steels

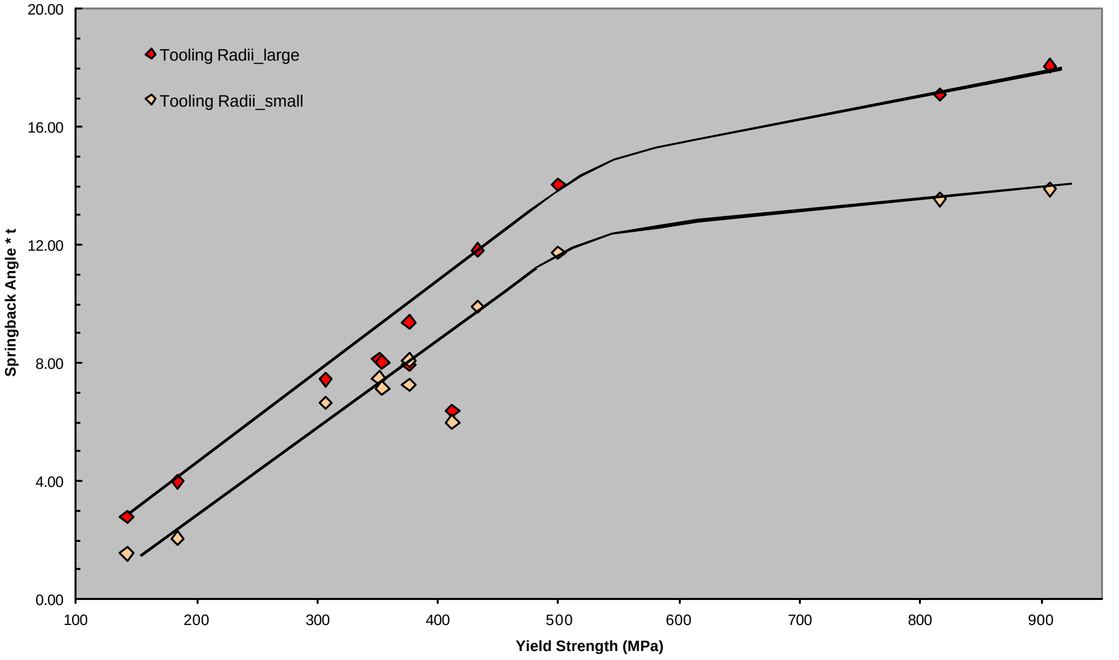

Figure 8.15 Effect of tooling radii on springback of 1.20mm steels

8.8 Conclusions

1. The single-factor effects of the process variables studied, such as tooling radii, tool gap and drawbead restraining force were generally found to play a more important role in material springback behavior than their interactions.
2. Among the three variables, tooling radii and drawbead restraining force were found to be more influential than tool gap.
3. The springback and curl increase with increasing yield strength and decrease with increasing material thickness.
4. Dual Phase steels exhibit more springback and curl than conventional HSLA steels. The springback behaviors of TRIP steels are between DP and HSLA.
5. The curl seems to be more sensitive to the material and setup in a channel draw test.
6. The springback decreases with smaller tooling radii, tool gap and larger drawbead restraining force. On the contrary, curl shows mixed results for smaller tooling radii and tool gap.

Section 9.0
Stretch Formability

9.1 Summary

This section presents results from formability testing of the skin panel steel grades under stretch forming conditions. Test results show that for stretch formability as measured by this geometry is primarily dependent on the n-value of the material. The r-value does not seem to be as important for stretch formability. Dent testing results are also included for some representative conditions, for one panel geometry for these materials

9.2 Background

This section presents the results from one such simulative test called the stretch form test, which simulates the forming of skin panels. The die-set designed by the Auto/Steel Partnership (A/SP) dent test task force [9.1] is used for this test. The test consists of locking out the material with stinger beads, applying a high binder force and forming the material to failure. Failure height is considered as the measure of formability. Strains on the surface of the panels were measured with 100mm circles scribed in the region of the sample in contact with the punch face. In addition to formability, dent resistance behavior of skin panel steels is also of great interest. Dent testing was conducted on samples formed with the same die-set to two different stretch levels: 1% X 1% and 2% X 2%. Apart from providing data on comparative formability for the different steel grades, the test data could also be used for benchmarking Finite Element models for formability and dent resistance.

9.3 Materials

Only the skin panel steels and baseline steels were tested. Complete mechanical properties of the skin panel and baseline steels is given in Section 2 of this report.

9.4 Testing Procedure

9.4.1 Stretch Formability

The procedures for the test are outlined below. Figures 9.1 and 9.2 show the geometry of the Stretch Form sample and a failed specimen. The tooling used for this test was purchased from Interlaken Technologies and is the same tooling as developed by the standardized dent test task force of the A/SP [9.1]. This test simulates the stamping and the splitting mode often observed in the first draw operation of outer panels. A high binder force is applied so as to prevent draw-in of the material outside the stinger beads. As the punch moves, the metal begins to stretch across the punch face and wrap around the punch nose. At a certain punch height, the combination of high membrane strain coupled with bending around the punch entry radius results in failure of the material.

- Samples of size 304.8mm square were cut and deburred prior to testing. The failure height was determined for 25 samples per lot of steel.

- 100 mm circles were scribed in the center of the blanks prior to forming
- The blanks were formed using the tooling with the following conditions

  - Punch speed: 4.24 mm/sec
  - Lubricant: Teflon + LPS2 lubricant on the punch face and oil on both sides of the blank. This lubrication was used to eliminate the effects of different coatings on stretch formability.
  - Binder Force: 622kN
- Failure was detected using the load-drop feature in the control software of the press.

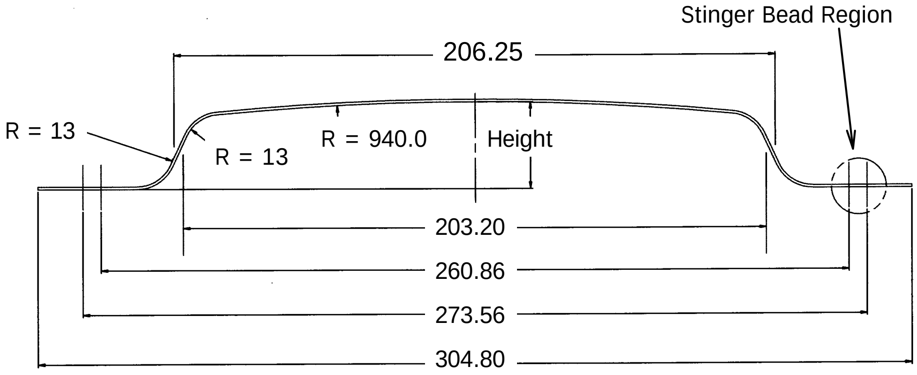

Figure 9.1: Geometry of the stretch form specimen. All dimensions in mm.

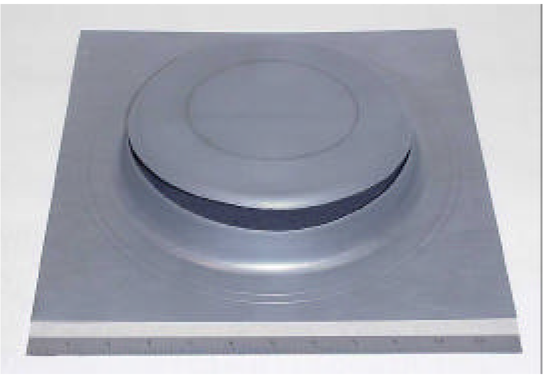

Figure 9.2: Stretch form/failure specimen

9.4.2 Dent Resistance

- For this test, dent resistance information was desired for stretch values of 1% X 1% and 2% X 2%. Prior to forming the materials, calibration experiments were conducted to determine the heights necessary to achieve the given values of stretch. These experiments were conducted for 0.77mm DQSK, 1.19mm DQSK and the 0.66mm DP500. Figure 9.3 shows the results of these experiments where it is seen that for these different materials, the stretch obtained was a pure function of the punch height and independent of the material.
- 3 samples per lot were dent tested per value of stretch, resulting in 6 samples per lot. Dent testing was carried out using the A/SP procedure [9.1].

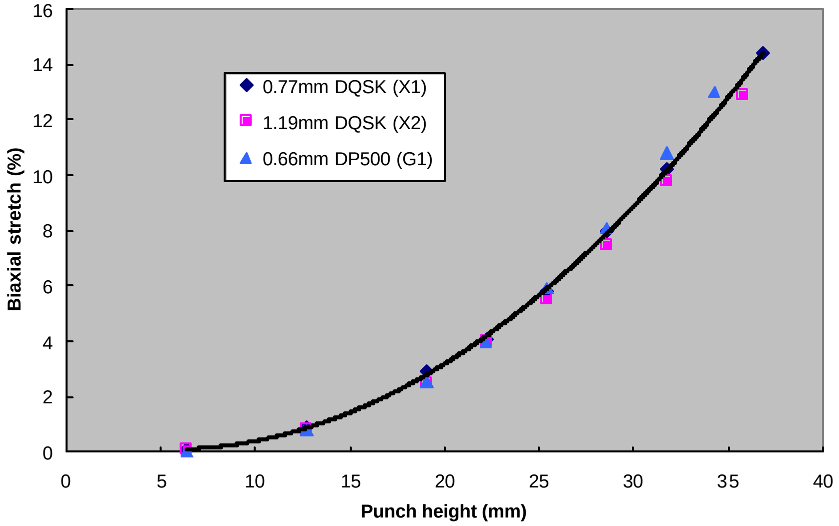

Figure 9.3: Biaxial stretch as a function of the forming height for 0.77mm DQSK, 1.19mm DQSK and 0.66mm DP500

9.5 Results

9.5.1 Stretch Formability

Table 9.1 shows formability data for the steels tested. The standard deviation is also presented as a measure of the variability during testing. As seen in the table, the test was very repeatable. The average standard deviation for the failure height was 0.48mm. The numerical value of the failure height does not seem to change very significantly with changing the steel grade. This is probably a function of the geometry of the tooling and the specimen. For this geometry and fully locked boundary conditions, the evolution of strains with increasing punch height might be very rapid. This could be manifested as a small difference in failure heights between the different steel grades. In addition to the failure heights, L and T strains on the punch face were measured using 100mm circles for the failed samples. Twelve samples per lot were chosen for strain measurement. Table 9.2 shows results of the strain measurements. Figure 9.4 shows the average biaxial stretch plotted as a function of the failure height. As seen in the figure, the maximum achievable stretch in this geometry is a function of the failure height.

Table 9.1: Formability data for the Stretch Form test for the steels tested

	Lot Code	Lot	Average failure height (mm)	Std. dev. (mm)
Skin Panel Steels	B1	0.7mm BH210	34.82	0.274
	B2	0.93mm BH210	33.93	0.424
	C1	0.71mm BH280	34.01	0.996
	C2	1mm BH280	33.99	0.287
	C3	1.04mm BH280	34.93	0.262
	D1	0.74mm ULC BH340	34.26	0.378
	D2	1.02mm ULC BH340	34.99	0.340
	E1	0.63mm IF-Rephos	35.64	0.635
	E2	0.89mm IF-Rephos	35.64	0.470
	G1	0.66m DP500	34.75	0.450
	G2	0.81mm DP500	34.85	0.325
Baseline Steels	X1	0.77mm DQSK	36.20	0.404
	X2	1.19mm DQSK	34.06	0.864
	Y1	0.7mm DDQ+	37.11	0.671
	Y2	1.19mm DDQ+	36.04	0.429

Table 9.2: Strain measurements from the Stretch form test

Lot Code	Lot	L (%)		T (%)	
		Average	Std. Dev	Average	Std. Dev.
B1	0.7mm BH210	16.19	1.08	16.08	1.10
B2	0.93mm BH210	13.68	0.71	12.87	0.59
C1	0.71mm BH280	15.11	1.59	14.77	1.53
C2	1mm BH280	14.61	0.54	14.20	0.86
C3	1.04mm BH280	16.31	0.78	15.87	0.80
D1	0.74mm ULC BH340	18.91	1.97	18.12	2.19
D2	1.02mm ULC BH340	16.63	0.57	15.77	0.62
E1	0.63mm IF-Rephos	18.02	2.16	17.33	2.26
E2	0.89mm IF-Rephos	17.72	0.97	17.26	0.75
G1	0.66m DP500	18.47	1.47	18.17	1.64
G2	0.81mm DP500	18.96	1.50	18.88	1.48
X1	0.77mm DQSK	19.77	0.84	19.42	0.74
X2	1.19mm DQSK	12.49	1.79	12.05	2.09
Y1	0.7mm DDQ+	23.05	1.86	22.53	1.29
Y2	1.19mm DDQ+	18.34	0.43	17.64	0.50

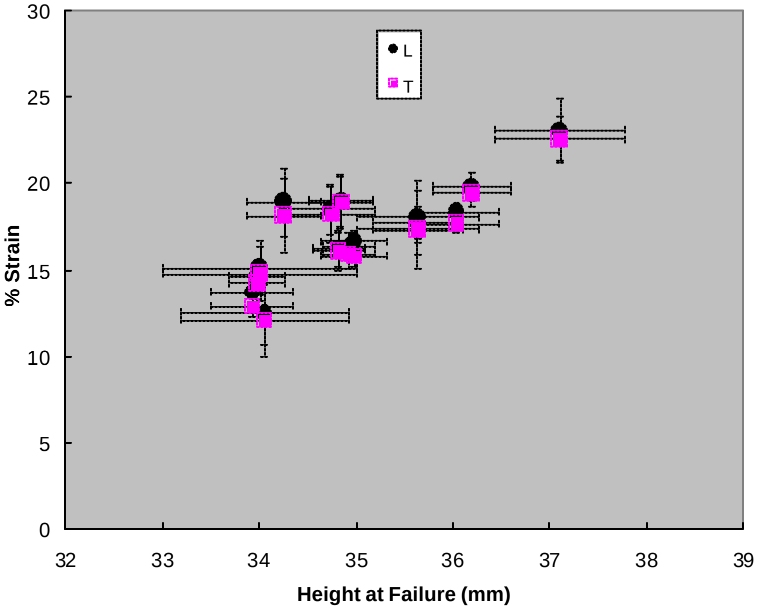

Figure 9.4: Stretch form/failure test: Measurements of surface stretch using 100mm circles

Although the difference in failure heights between the different steels was not significant, to obtain a better understanding of the material factors controlling stretch formability, a multiple linear regression of the failure height as a function of the thickness, n-bar, and r-bar, was conducted. The n-bar and r-bar values for the individual lots of steel are reported in Table 2.4 in Section 2 of this report. The regression analysis was conducted without considering interactions between the variables. Table 9.3 shows the results of the regression analysis, where the first column is the factor, the second column is the coefficient, which is the multiplier to the numerical value of the factor, and the third column is the p-value. The p-value is the probability of the particular factor being statistically insignificant. The lower the p-value, the higher is the statistical significance of the factor. As seen in Table 9.3, for this test geometry and forming conditions, the thickness of the steel grade and the n-bar were the most significant. The effect of r-bar was found to be insignificant. The table also shows a negative coefficient for thickness. From examination of Table 9.1, it can be seen that the forming height for the 1.19mm DQSK and DDQ+ were lower than the 0.77mm DQSK and 0.7mm DDQ+ respectively. This behavior is possible because the decreased R/t ratio for the thicker lots of steel which might cause higher bending severity and thus strain localization at a lower punch height.

Table 9.3: Regression analysis of the results of the stretch form test

Factors	Coefficients	p-value
Constant	31.68318467	5.53E-13
Thickness (mm)	-1.494303889	0.045886043
n-bar	23.25542732	0.000137511
r-bar	-0.120028429	0.722870414

Using the insights obtained from Table 9.3, another regression analysis was conducted for the height at failure as a function of n-bar and thickness leaving out r-bar, as it was found to be statistically insignificant. The data points for the 1.19mm DQSK and DDQ+ were also left out because they seemed to be outside the normal range for skin panel materials. Table 9.4 shows the results of the modified regression analysis.

Table 9.4: Modified regression analysis of the failure height in the stretch form test

Factors	Coefficient	*p-value*
Constant	29.9676441	2.13298E-11
Thickness (mm)	-0.074586388	0.917482968
n-bar	25.40541086	5.54047E-06

Using the regression analysis, predictions of the stretch form height can be obtained using the properties of the steel lot. Figure 9.5 shows a comparison of the actual failure height in the stretch form test vs. the predicted failure height. As seen in Figure 9.5, the predicted failure height compares very well with the experimental failure height. The average % difference between predicted and actual heights was found to be 0.75%.

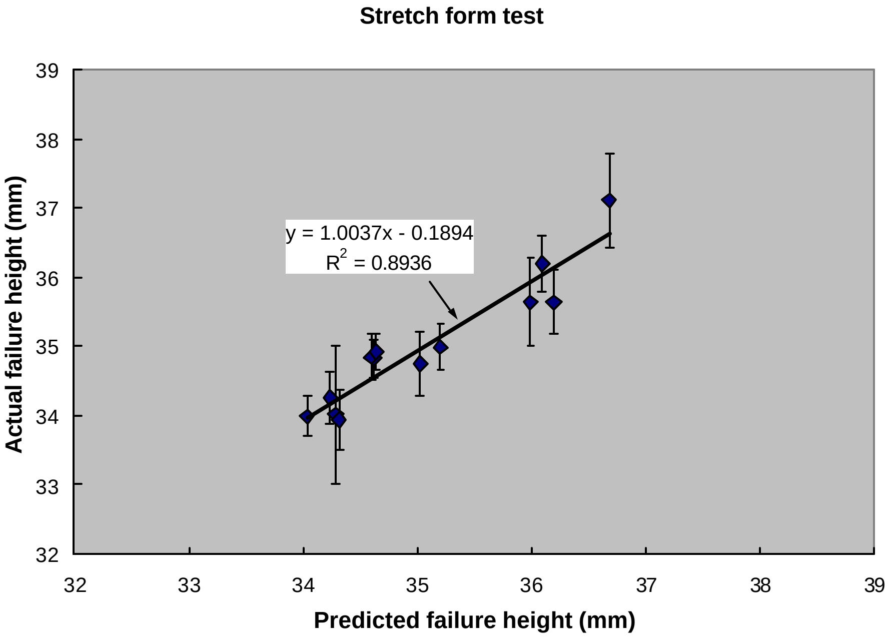

Figure 9.5: Comparison of predicted and actual failure heights for the stretch form test

As seen in Table 9.4, the n-bar value is the most significant material attribute influencing the height at failure in the stretch form test. Once the results for the 1.19mm DQSK and DDQ+ were taken out, the effect of thickness was also insignificant. Figure 9.6 shows a plot of the failure height as a function of the n-bar value for the different steels. The results are sorted by the coating type and thickness. Although, the frictional effects of different coatings are minimized by the use of Teflon, the effect of coating is significant in that it highlights the type of commercial product (and hence the mechanical properties) available with the coating.

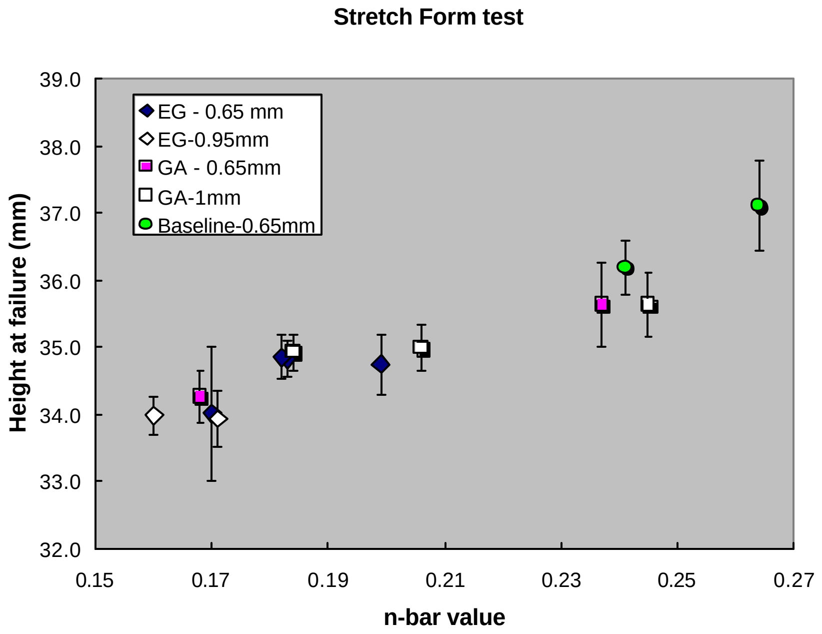

Figure 9.6: Correlation of the failure height as determined in the stretch form test to the n-bar value

9.5.2 Dent Resistance

Table 9.5 shows load for 0.1mm dent depth, which is a commonly accepted measure of dent resistance for all the lots of steel tested. Because the mean values for the different cases are very different, the standard deviation is expressed as a percentage of the mean value. The average standard deviation for dent testing was 9%. As seen in the table, for this geometry, the dependence of the 0.1mm dent load on thickness overwhelms the effect of material strength and stretch. It has been shown before that dent resistance has a complicated dependence on panel curvature, thickness, stretch and yield strength [9.2-9.3]. For highly curved panels, as is the case with the A/SP experimental sample, the dent load is mainly governed by the local geometry and thickness of the steel. For panels with gentler curvature, the effect of stretch and material strength level on the dent load is more pronounced. A good understanding of dent resistance involves inclusion of panel curvature as a test variable, which was beyond the scope of the project.

Table 9.5: Summary dent test data for the skin panel steels

Lot Code	Grade	Stretch (%)	0.1mm Dent Load (N)	% Std. Dev.
B1	BH210	1	147.68	6.49
		2	179.73	10.40
B2	BH210	1	284.60	1.59
		2	312.22	10.69
C1	BH280	1	182.15	11.61
		2	208.09	11.51
C2	BH280	1	352.68	0.87
		2	441.74	5.85
C3	BH280	1	351.96	0.46
		2	394.82	9.86
D1	ULC BH340	1	190.28	1.79
		2	206.83	11.95
D2	ULC BH340	1	357.31	7.06
		2	363.94	8.42
E1	IF Rephos	1	105.76	11.30
		2	113.75	8.36
E2	IF Rephos	1	246.30	20.14
		2	275.70	10.53
G1	DP500	1	133.96	5.35
		2	184.28	10.54
G2	DP500	1	226.48	5.14
		2	228.27	0.60
X1	DQSK	1	192.20	20.00
		2	200.03	17.93
X2	DQSK	1	526.54	8.57
		2	524.57	7.71
Y1	DDQ+	1	119.74	9.93
		2	138.12	8.23
Y2	DDQ+	1	413.54	22.21
		2	520.67	6.05

To better isolate the thickness effect from material strength and stretch effects, an alternative approach of using the entire load vs. dent depth data was adopted and will be discussed below. Figure 9.7 shows the complete dent resistance data for 0.66mm DP500 material, where the applied load is plotted as a function of dent depth. Data for all three replicates for both stretch values are plotted. As seen in the figure, the data can be approximated by a linear relationship, and the entire dent resistance data can be reduced to two values, the y-intercept and the slope of the trend line. The y-intercept is the dent initiation load (which is the minimum load required to form a dent). The slope of the trend line can be considered analogous to panel stiffness, where the higher the slope, the "harder" it is to cause dents of greater depth in the panel. Although the 0.1mm dent load is a commonly used measure of dent resistance, use of the intercept and slope approach allows for more complete characterization of the dent resistance behavior of the panel allowing for the determination of the dent resistance at any applied load. If P is the applied load, the resulting dent depth, δ can be determined by: δ=(P-intercept)/slope. The intercepts and slopes of the characteristic dent resistance curves were determined and are presented in Table 9.6.

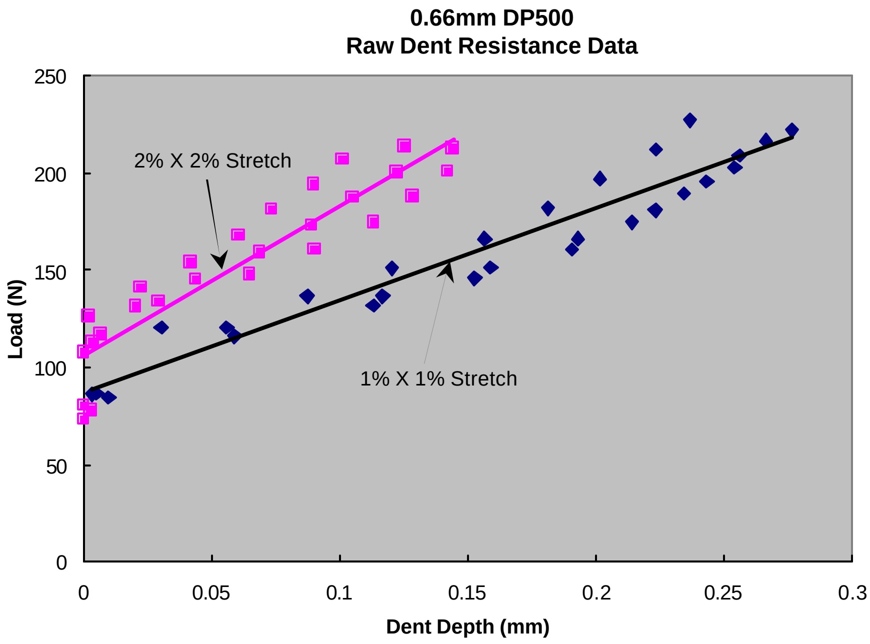

Figure 9.7: Raw data for stretch form/dent test

Using these data, it is possible to examine the effects of the different variables on dent resistance for this particular geometry. Figure 9.8 shows the dependence of the intercept on the steel thickness. As seen in the figure, the effect of steel thickness is very significant. Figure 9.9 shows the effect of the yield strength on the slope. The fit is not as good as for the intercept, because the effect of stretch is ignored in this plot, where from Table D.2, it can be seen that increasing the stretch also increases the slope.

Table 9.6: Reduced dent resistance data for the steels tested

Lot Code	Grade	Stretch (%)	Intercept (N)	Slope (N/mm)
B1	BH210	1	111.17	300.83
		2	127.07	465.23
B2	BH210	1	225.23	334.41
		2	247.23	391.57
C1	BH280	1	133.88	462.94
		2	140.22	649.54
C2	BH280	1	274.5	450.55
		2	318.28	735.28
C3	BH280	1	287.24	370.83
		2	315.48	418.23
D1	ULC BH340	1	137.94	401.68
		2	151.89	483.16
D2	ULC BH340	1	297	297.07
		2	291.3	351.3
E1	IF Rephos	1	84.26	190.74
		2	80.2	185.41
E2	IF Rephos	1	216.83	202.34
		2	216.57	300.56
G1	DP500	1	87.69	470.26
		2	106.12	771.74
G2	DP500	1	158.39	536.84
		2	150.98	665.78
X1	DQSK	1	165.09	168.35
		2	164.52	199.67
X2	DQSK	1	429.15	282.2
		2	418.62	330.7
Y1	DDQ+	1	101.77	111.1
		2	107.69	176.54
Y2	DDQ+	1	382.66	193.52
		2	395.7	320.1

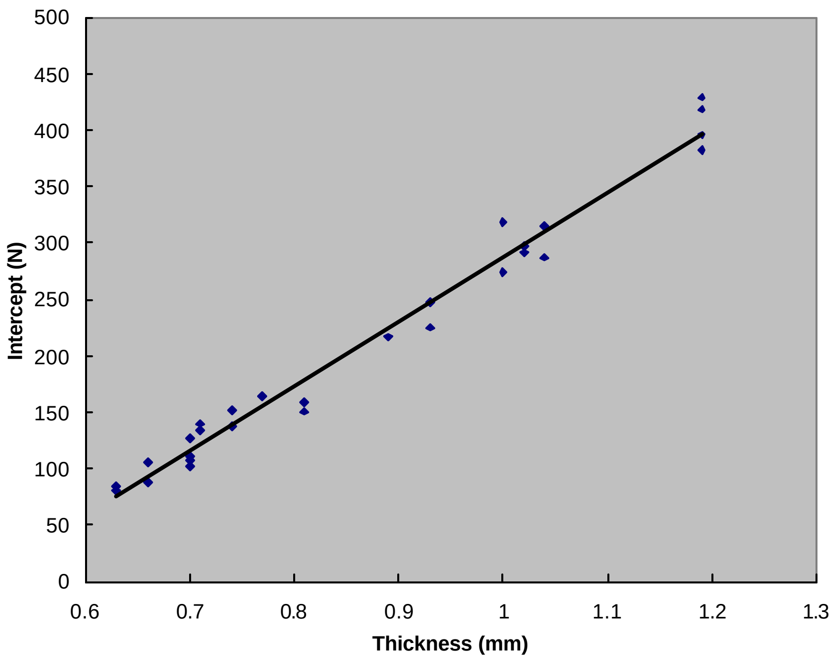

Figure 9.8: Effect of thickness on the intercept of the load vs. dent depth trend line

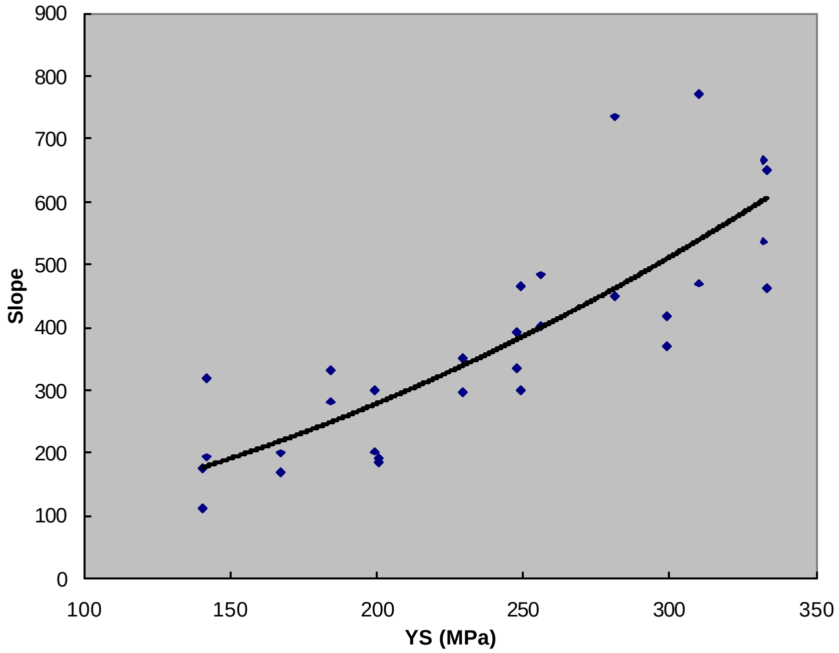

Figure 9.9: Effect of as-received yield strength of the steel grade on the slope of the load vs. dent depth trend line.

9.6 Discussion

In the first draw die of an outer panel, a variety of forming modes such as drawing, stretching, bending are observed in different regions. The stretch form mode can be typically observed where material is pulled across the punch entry radius in the presence of membrane strains. The correlation of the stretch formability of the material to the n-value and the lack of correlation to the r-value are not surprising because of the boundary conditions of the test.

Figure 9.6 shows some interesting differences among the different classes of materials. As seen in the figure, the difference in failure heights for the EG steel lots was not as high as the difference for the GA lots. Figures 9.10 and 9.11 show the failure heights for the EG and GA lots for the steel lots of nominal thickness 0.65mm. As seen in the two figures, when the error bars are considered, the failure heights for the EG lots are practically indistinguishable. On the other hand, the GA lots seem to have different forming heights. This implies that substitution of a currently available commercial higher strength EG steel for a "lower" strength EG steel might not result in a loss of stretch formability performance. A similar substitution using GA steels might result in some stretch forming issues. From Table 2.4 in Section 2, it can be seen that the yield strength of the IF-Rephos lot (E1) is lower than the ULC BH340 lot (D1). The GA lots in Figure 9.7 are ultra-low carbon substrates, where it might be possible to obtain steels of vastly different n-values for similar ultimate tensile strength levels.

With regard to dent resistance, since curvature was not a test variable, results from this test are valid only for this geometry. For this geometry, for very low applied loads, the effect of thickness on dent resistance is very significant. For higher applied loads, the effect of material strength and stretch on dent resistance starts to increase in importance.

9.7 Conclusions

The following conclusions can be drawn from the stretch/form test.

- Stretch formability is predominantly a function of the n-value of the material
- Differences in stretch formability for the GA steel lots in the program were higher than the EG lots.
- For this geometry, for lower applied loads the effect of thickness was found to be more significant than the steel grade. The effect of steel grade increased in significance for higher applied loads.

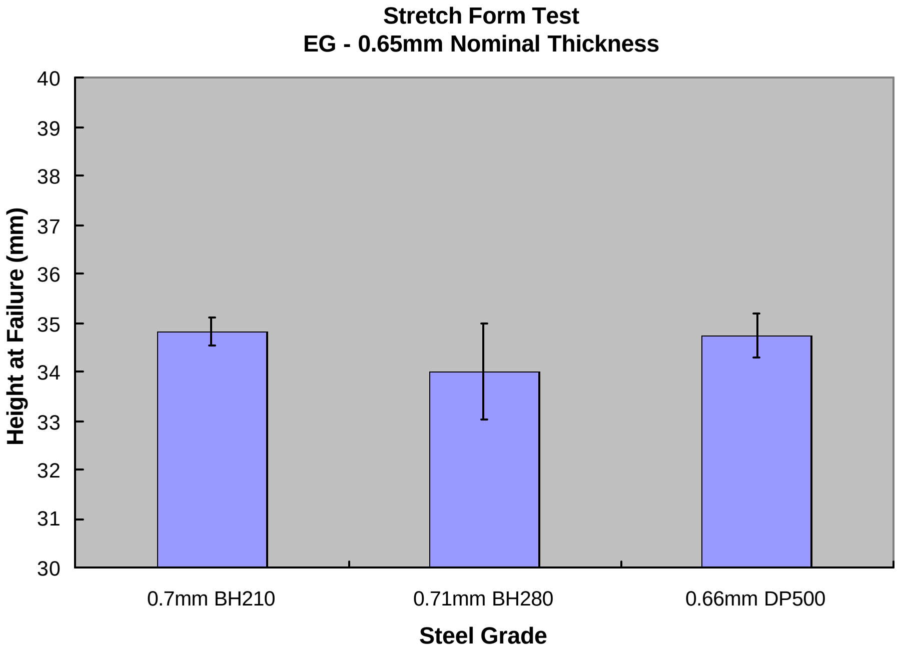

Figure 9.10: Failure height in the stretch form test for the EG steel lots of nominal thickness 0.65mm

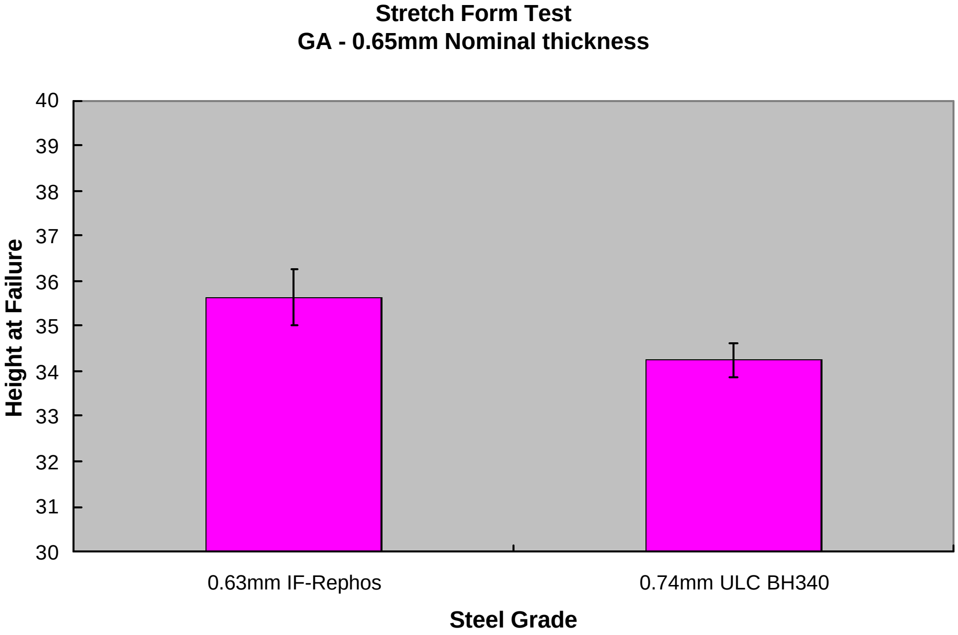

Figure 9.11: Failure height in the stretch form test for the GA steel lots of nominal thickness 0.65mm

Section 10.0
Stretch Drawability

10.1 Summary

This section presents results of the Square Draw test, which is one of the simulative tests under this AISI/DOE formability project. The Square Draw test was designed to evaluate the formability of the steel grades under stretch-draw conditions. Three different measures of formability were used to characterize the forming performance of the steel grades: (a) Failure height (b) Strain distribution for one common condition and (c) Binder Span of Control. Test results indicate that the failure height was a strong function of the tensile strength of the material. Analysis of the strain distributions indicates that strain localization takes place under biaxial stretching conditions at the corners of the square cups, which were the eventual fracture locations. The localization behavior was similar for all the steels studied in the program. Additional insights on formability were obtained by the determination of the binder span of control, where the importance of friction between the steel sample and the binder surface on formability was highlighted.

10.2 Background

The Square Draw test is a simulative formability test, where the forming performance of the steel grade is evaluated under stretch-draw conditions. The purpose of this test is to provide a relative comparison of the forming behavior of the steel under a set of fixed conditions. The tooling was designed by Ispat Inland to enable the forming of a square cup even for the ultra-high strength steels in the test program. The testing was restricted to steels with a nominal thickness of 1.2mm and lower due to capacity restrictions of the Interlaken press. To minimize the cost associated with designing dies to be suitable for steels ranging from DDQ+ to M190 for thicknesses ranging from 0.65mm to 1.2mm, the die-set has flat binders, where the restraint to metal movement comes only from the applied binder force on the blank. The binder force can be varied to control the amount of draw-in from the flange into the die cavity. The metal flow can also be controlled by changing the blank size. The die-set was designed to maximize testing flexibility such as to enable evaluation of the different factors influencing formability such as the mechanical properties of the steel, coating type, lubrication, binder pressure and tooling geometry, and sample size. The downside to this flexibility lay in the development of a robust test method, that could provide meaningful information for steel lots with vastly different mechanical properties. Considerable experimentation (both physical and FEA) and discussions with the advisory committee were conducted to help determine appropriate test methods. Based on the results from these initial experiments, three measures of formability were chosen to be evaluated for the steels in the program.

1. Height at Failure: Height at failure would be determined for the steel lots under investigation for three blank sizes. It was recognized that for smaller blank sizes, failure might not be observed because of draw-in. In those cases, the maximum cup height would be reported. These failure heights would be determined at a binder load of 94kN.
2. Binder Span of Control: Binder Span of Control is a test method that determines the working range of binder force such as to produce a defect free part (wrinkle-free and split-free). For the different lots of steel, the relative working range of the binder force for defect free parts is used as a measure of formability. This test was to be conducted for one blank size and punch height.
3. Strain Distribution: Major and minor strains would be measured on the formed samples for one common condition along three lines.

The height at failure and strain distribution at a common condition evaluate the integrated effects of the n-value, r-value and steel strength on formability. Strain distribution at a common condition could be used by FEA analysts for comparing predicted strain distributions with experimental results for AHSS. Binder span of control is a test method used to evaluate product formability, where the effect of the protective coating is also examined in addition to the substrate mechanical properties.

10.3 Tooling

Figure 10.1 shows a schematic of the tooling that was built to conduct the Square Draw test. Three sets of punches and upper binder plates were made for the three different nominal thickness ranges, 0.65mm, 0.95mm and 1.2mm. The critical dimensions of the tooling are given in the bulleted list below. All dimensions are in mm.

- Punch entry radius, A: 10t
- Clearance between punch and upper binder, B: 2.5*t + 0.127
- Plan view radius of the upper binder, C: 12.7+B

Figure 10.2 shows the photograph of the tooling as installed in the Interlaken servohydraulic press. The overall binder table capacity of the press was 667kN, which made it difficult to achieve repeatable control of the binder force for values less than 10% of the rated capacity using servohydraulics. Realization of low forces was necessary to perform binder span of control experiments. To achieve the objectives of the test, the tooling was designed with eight nitrogen springs, where the nitrogen pressure could be adjusted so as to change the binder force. The actual pressure in the die-set upon binder closure was read by a pressure gauge. Since the effective area of the spring cylinders were known, the pressure reading was easily converted to binder force.

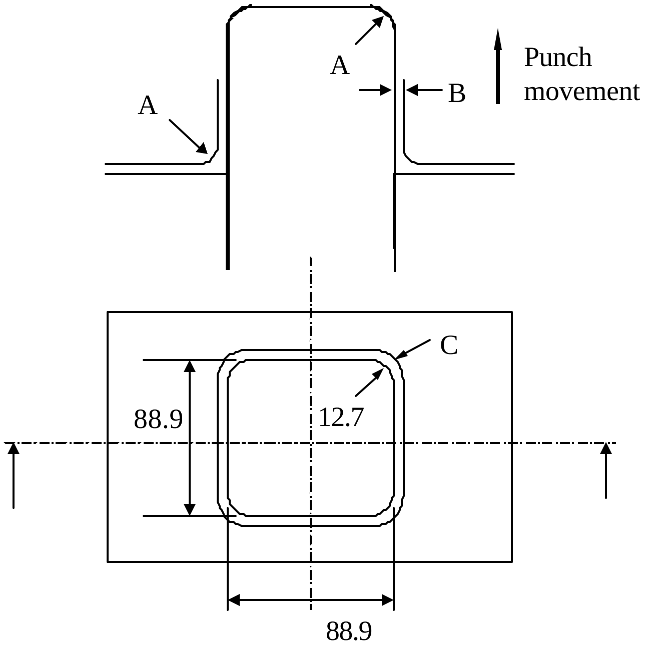

Figure 10.1: Schematic of the Square Draw tooling showing the critical dimensions

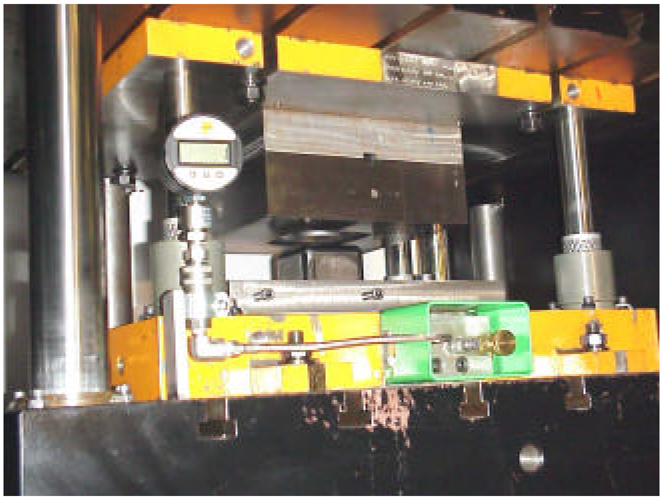
Figure 10.2: Square Draw tooling as installed in the servohydraulic press

10.4 Steel Grades

This test was conducted for all steel lots of nominal thickness less than or equal to 1.2mm. Lots of thicknesses slightly higher than 1.2mm were also included. Steel lots of thickness greater than 1.4mm were excluded from testing.

10.5 Experimental Procedure

Sample Alignment

Since the tooling was designed to accommodate blanks of different sizes, a fixture was designed to ensure accurate alignment of the samples in the tooling. Figure 10.3 shows the alignment fixture. It consists of an L-shaped bracket that could be moved in a 45^0 groove to adjust the centering of the blank. For a given blank size, once a nominal setting was determined, the bolts holding the bracket were tightened to set the gauge. It was found that minor adjustments were needed to be made from lot to lot to ensure accurate alignment.

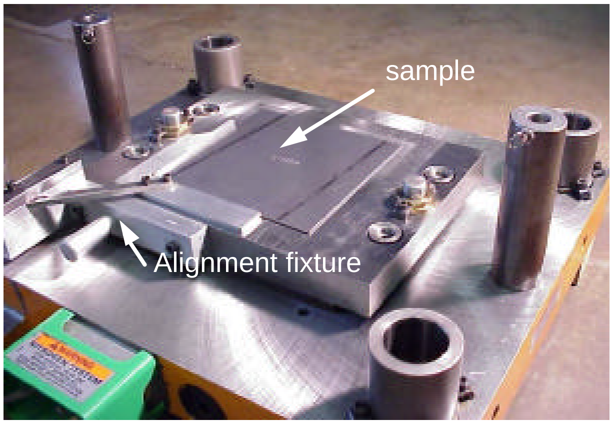

Figure 10.3: Set up to ensure alignment of the samples in the Square Draw die-set

Lubrication: Ferracote 61 MAL HCL 1 (Prelube)

Determination of Failure Heights

For processes with material draw-in, the load-displacement behavior shows a characteristic drop with the onset of easy draw-in from the flange. Figure 10.4 shows a typical load-deflection curve for the Square Draw test. In this case, the material did not experience any localized necking even at the maximum cup depth. Because of this feature of the process, the typically used procedure of detecting a drop in the load-displacement data for determination of failure heights is inappropriate. Hence, for this portion of the test, for the different blank sizes, an iterative procedure was used to form the cups, starting with an initial forming height. For a given blank size, if the formed cup showed splitting, the forming height was adjusted so as to produce a cup with an incipient local neck. Once this setting was determined, five cups were formed at this height. The failure heights were determined by a depth gauge for three replicates per blank size per lot. Measurements were taken at three separate locations per replicate.

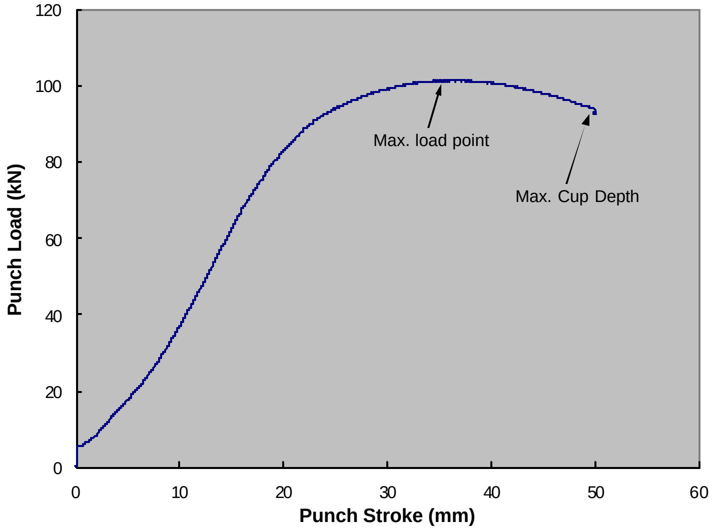

Figure 10.4: Typical load-displacement curve for a sample experiencing significant draw-in from the flange.

Failure heights were determined for three blank sizes. These sizes were different for the different thickness groups. The blank sizes for the different thickness groups are listed in Table 10.1. These blank sizes were determined by initial experimentation and were chosen to maximize differences in forming behavior. For the cases, where failure did not occur by incipient necking, the maximum cup depth is reported as the result. The binder force for this test was chosen as 94kN.

Table 10.1: Blank dimensions for the square draw test for determination of failure heights

	0.65mm thick	0.95mm thick	1.2mm thick
Small (mm)	190.5	190.5	203.2
Medium (mm)	203.2	203.2	228.6
Large (mm)	228.6	228.6	279.4

Binder Span of Control

Binder Span of Control is a procedure frequently used in stamping plants, where for a given press condition, the binder pressure is varied to determine the safe operating window (wrinkle-free and split-free parts) for production. The procedure is a very good indicator of the robustness of the stamping process, whereby the sensitivity to variations in incoming material, lubricant, and die condition can be evaluated. Figure 10.5 shows some samples, which were formed with different binder forces resulting in wrinkled, safe or split part. The numbers in the figure correspond to the binder forces used to form the samples. Two views are presented for each sample. The photographs in the figure show the effect of the binder pressure on forming a cup of the same depth using the same material.

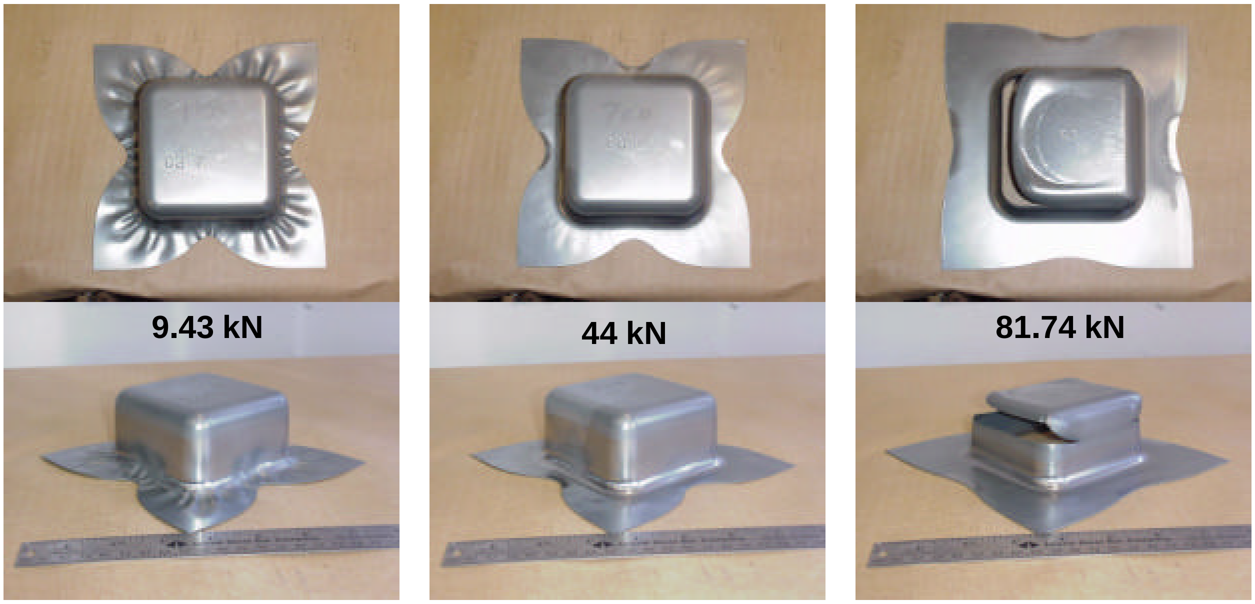

Figure 10.5: Effect of binder force on formability of the material. The numbers are the binder forces for forming the samples.

Binder span of control testing was conducted for one blank size and punch height for each nominal thickness range. Initial discussions with the advisory committee revealed an interest in the forming behavior when forming a deep cup. To achieve this goal, the punch height and blank size were chosen such that a deep square cup could be formed leaving a small amount of metal on the flange for all the steel lots. The combination of blank size and cup height that would be appropriate for all lots was determined by experimentation. Similar to Table 10.1, the combinations for the different nominal thickness ranges are different owing to the different tooling associated with each thickness group. Table 10.2 shows the blank dimension and forming height for each thickness range. These experimental conditions for binder span of control testing are different from those of failure height determination, because for binder span of control, forming of a "full" cup was of interest.

Table 10.2: Sample conditions for binder span of control testing

	0.65mm thick	0.95mm thick	1.2mm thick
Blank Dimension (mm)	177.8	190.5	203.2
Cup Height (mm)	38	50	50

For each lot, about 10-20 samples were formed. Each sample was formed with a different binder force. An efficient procedure was devised to minimize the number of samples being formed. For binder forces less than 94kN, the binder force was adjusted by varying the Nitrogen pressure in the die-set. After forming, the samples were examined for splits (or incipient necking) and perceptible wrinkling. For a given lot, the binder force limit for splitting is the lowest binder force producing incipient necking and below which the resulting sample is free of necking. In some high strength steels, there was no incipient necking, and the sample either split or did not neck. The wrinkling limit is the binder force below which, perceptible wrinkling on the flange can be observed. The onset of perceptible wrinkling was determined using touch and the unaided eye. The actual wrinkling pattern (number of wrinkles and height of wrinkles) was found to be very sensitive to the steel grade. For more complete characterization of wrinkling behavior, it is necessary to characterize the number of wrinkle lines and the height of the wrinkles, which would necessitate the use of a more sophisticated (and expensive) measurement technique for each sample, which was beyond the scope of the project. For this program, determination of the wrinkling limit focussed on the perception of wrinkle depth determined by touch. The splitting and wrinkling limit forces were recorded for all the steel lots.

Strain Measurement

For strain distribution, samples from the different lots were formed under common forming conditions. Table 10.3 shows the forming conditions for the different nominal thickness groups. The blank sizes were kept the same as the binder span of control experiment. Based on results from failure height determination and binder span of control testing, the binder force and cup height were chosen such as to form cups without splitting (or incipient necking) for all steel lots.

Table 10.3: Forming conditions for strain measurement

	0.65mm thick	0.95mm thick	1.2mm thick
Blank Dimension (mm)	177.8	190.5	203.2
Binder Force (kN)	94	94	94
Cup Height (mm)	25.4	25.4	25.4

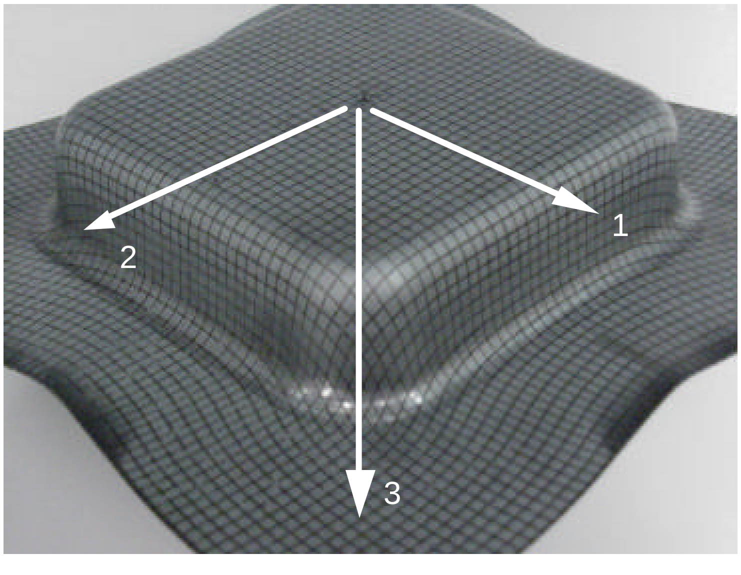

Figure 10.6: Photograph of a formed and gridded sample for measurement of strains.

Figure 10.6 shows a photograph of a formed and gridded sample for strain measurement. As seen in the Figure, strains were measured from the center of the specimen along three lines. Line 1 is parallel to the rolling direction, Line 2 is parallel to the transverse direction and line 3 is aligned along the diagonal direction. Since eventually, splitting failure occurred at the punch entry radius along line 3, the strain distributions along line 3 are presented in this report.

10.6 Results

10.6.1:Failure Heights

Results for the failure heights for all the sample sizes, for all lots are reported in Appendix F. For the smaller blank sizes, it was found that failure heights were a strong function of the amount of draw-in from the flange. In these cases, formability as measured by failure height is not just a function of material ductility, but also the ease with which metal can be drawn in, which in turn depended on material strength, coating type and r-value. However for larger blank sizes, draw-in is limited by the large area of the surrounding material. Therefore substrate properties become the dominant factor influencing formability. Initial analyses indicated that for the largest blank size, failure height increased with higher %uniform elongation and the r-bar value. Both these dependencies are reasonable as the uniform elongation is a measure of the overall ductility of sheet metal and r-bar represents the resistance of the metal to thinning. To highlight differences in formability arising from the substrate properties of the grades, Figure 10.7 shows the trend of failure heights vs. UE*(r-bar) . The results are presented only for the largest blank size for each nominal thickness group, for which the draw-in is minimized.

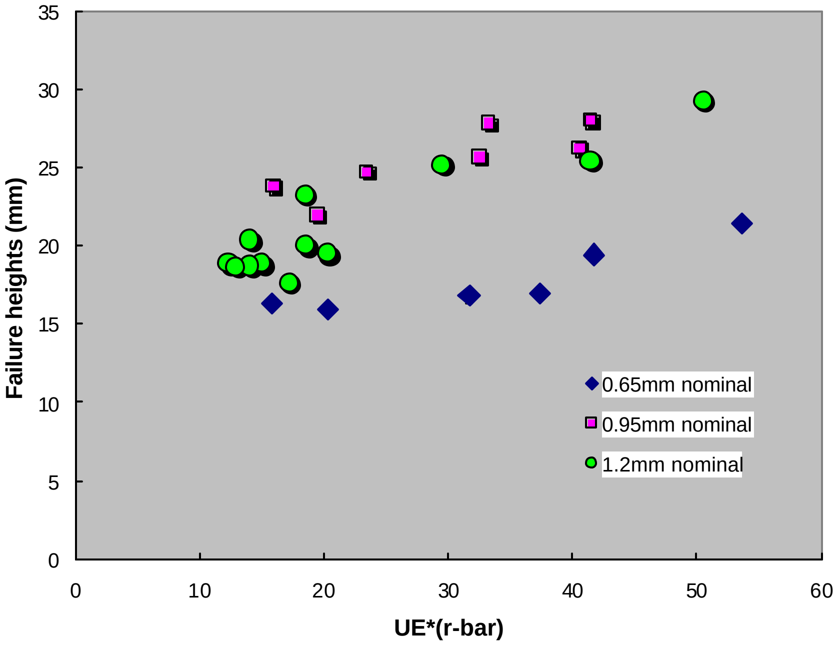

Figure 10.7: Failure height vs. UE*(r-bar) for the largest blank size for all three thickness ranges

As seen in Figure 10.7, as the value of UE*(r-bar) increases, the height at failure increases. This trend is physically reasonable as a higher value of UE*(r-bar) represents a higher overall ductility and ability to resist thinning both of which are desirable for stretch-drawing applications.

The effect of surface coating on formability is illustrated in Figures 10.8 and 10.9, where the forming heights are presented for different lots of steel. Figure 10.8 compares the forming height for BH210, ULCBH340 and BH280 products. The BH210 and the ULCBH340 products have similar mechanical properties but different coatings. The figure shows that with the lubricant that was used

(Ferracote 61 MAL HCL 1), the forming performance of the EG steels was better than the GA steels. The difference is very significant for the 203.2mm blank, where for both strength levels, the EG steels outperform the GA steels. The trend might be somewhat different with another lubricant. Figure 10.9 shows a similar plot for the DP600 steels that were evaluated. In this case, for the smaller blank size, the performance of the GI steels were better than the uncoated steel. For larger blank sizes, the difference between the different DP600 lots was marginal. The surface friction characteristics of the steel can thus play a very significant role in formability. Although the draw-in amounts were not measured, it is presumed that because of different frictional conditions at the surface, different lots of steel pulled in differently thereby influencing the forming height.

From Figures 10.8 and 10.9 it can be seen that a blank size of 203.2mm seems to highlight differences in formability caused by differences in frictional behavior of the different protective coatings. Blanks smaller than 203.2mm resulted in easy draw-in whereas larger blanks tended to prevent material flow into the die cavity irrespective of the coating.

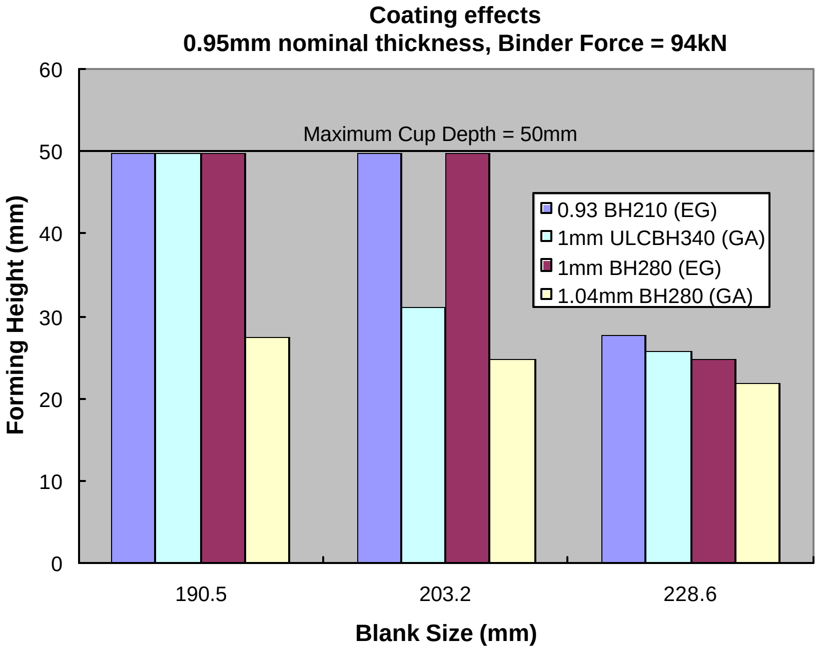

Figure 10.8: Effect of coating on the forming height for a few lots of steel of nominal thickness 0.95mm

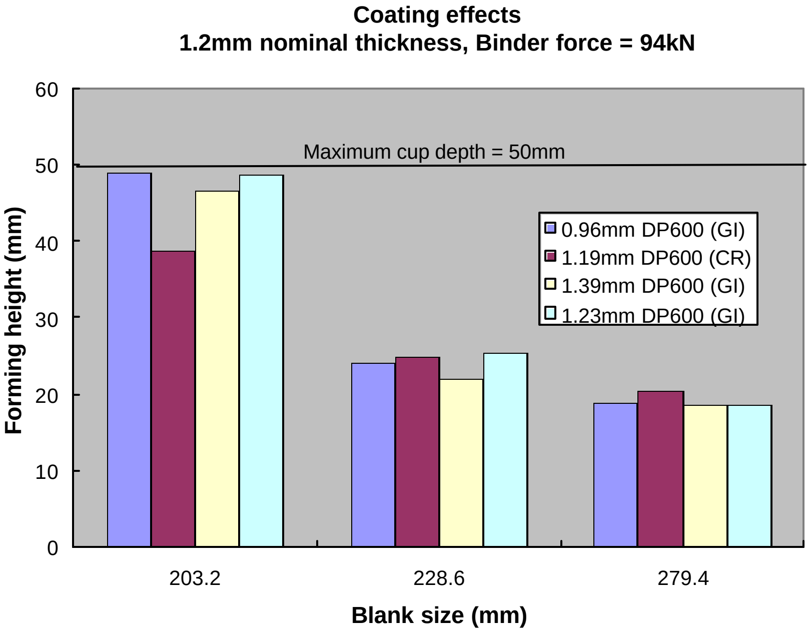

Figure 10.9: Effect of coating on the forming height for the DP600 steels of nominal thickness 1.2mm

10.6.2:Binder Span of Control

Table 10.4 shows the results from binder span of control testing for all the lots of steel that were tested. The table is divided into three sections, with each section corresponding to a given nominal thickness. The forming conditions for binder span of control testing are given in Table 10.2. For each nominal thickness, the rows in the table are arranged according to increasing tensile strength of the steel. The wrinkling limit is the value of the binder force below which perceptible wrinkling was observed. The splitting limit is the value of the binder force above which incipient necking or splitting was observed. For most cases, the splitting limit is higher than the wrinkling limit. The difference between the splitting limit and the wrinkling limit is the safe binder force range for the steel lot. For some lots, there is no window for defect-free parts, which means that the transition from wrinkling to splitting is immediate. The interpretation of this result is that for the particular combination of blank size and lubrication condition, the part cannot be formed to the specified cup height. For the 1.24mm GA BH300, the limit for wrinkling was higher than the limit for splitting, which means that the blank size would have to be changed to make a good part out of this lot of steel.

Although this test is an excellent test to evaluate product formability, where the effect of all components that make the forming system are simulated, it is difficult to separate the effect of coating, lubricant and the mechanical properties of the steel grade. On the positive side, this is a very useful test to evaluate the forming performance of different lubricants, coatings, and surface texture of the steel grade.

Table 10.4: Binder force limits for wrinkling and splitting for all the steel lots in the experiment

Nom. thickness (mm)	Grade	Coating	Lot Code	Wrinkling Limit (kN)	Splitting Limit (kN)	Safe Window (kN)
0.65	0.7mm DDQ+	CR	**Y1**	19.61	122.87	103.26
	0.7mm BH210	EG	**B1**	19.61	128.54	108.93
	0.63mm IF Rephos	GA	**E1**	9.94	129.12	119.18
	0.74mm ULC BH340	GA	**D1**	9.82	125.39	115.57
	0.71mm BH280	EG	**C1**	46.66	58.04	11.38
	0.66mm DP500	EG	**G1**	59.79	59.79	0.00
0.95	0.77mm DQSK	CR	**X1**	19.61	120.09	100.48
	0.93mm BH210	EG	**B2**	33.07	247.65	214.58
	0.89mm IF-Rephos	GA	**E2**	32.95	166.88	133.93
	1mm ULCBH340	GA	**D2**	32.95	125.44	92.49
	1.04mm BH280	GA	**C3**	46.67	59.49	12.83
	1mm BH280	EG	**C2**	46.67	247.65	200.98
	0.8mm DP500	EG	**G2**	97.95	216.63	118.67
1.2	1.19mm DDQ+	CR	**Y2**	9.69	139.21	129.52
	1.19mm DQSK	CR	**X2**	9.94	120.66	110.73
	1.19mm BH300	GI	**2K**	19.87	666.18	646.31
	1.16mm HSLA350	GI	**1L**	45.91	181.90	135.99
	1.24mm BH300	GA	**1K**	45.77	19.93	-25.84
	1.24mm HS440W	GA	**1M**	33.39	33.39	0.00
	1.21mm HSLA350	CR	**5L**	45.77	162.52	116.75
	0.96mm DP600	GI	**1P**	98.71	183.65	84.94
	1.19mm DP600	CR	**2P**	84.83	84.83	0.00
	1.39mm DP600	GI	**3P**	71.87	85.83	13.96
	1.4mm TRIP600	CR	**1T**	71.62	224.17	152.56
	1.23mm DP600	GI	**4P**	100.34	165.02	64.68
	1.2mm DP800	GI	**1R**	120.33	120.33	0.00
	1.25mm RA830	CR	**3W**	166.66	166.66	0.00
	1.32mm RA830	GI	**1W**	98.10	98.10	0.00
	1.15mm DP980	CR	**1S**	224.17	224.17	0.00
	1mm M190	CR	**1H**	224.09	263.70	39.61

Examination of Table 10.4 reveals that the wrinkling limit tends to increase as the strength of the steel increased, which is reasonable because higher strength steels would require more binder pressure to close the binder so as to prevent wrinkling. The splitting limit also shows some dependence on the strength level. Higher strength steels have a larger tendency to pull the material under the binder, thereby necessitating a higher binder force to prevent draw-in and thus causing splitting failures. A higher r-bar value is also considered to be beneficial to reduce wrinkling, which means that a lower binder force would be required to suppress wrinkling. A high value of the uniform elongation tends to increase the splitting limit, because even at higher binder forces, a cup is able to be formed because of the higher ductility. A better understanding of wrinkling and splitting limits could be obtained by plotting the binder force limits normalized by the tensile strength of the steel lot as a function of the previously defined parameter: UE*(r-bar) which are shown in Figures 10.10 through 10.12. The normalized minimum binder force for wrinkling and maximum binder force for splitting are plotted in the graphs for each steel lot. The difference between the two binder force limits is the safe operating binder force window for the particular lot. When $BF_{wrinkle} > BF_{split}$, there is no window to make the part to the specified height. As seen in the figures, as UE*(r-bar) increases, the safe operating window increases. From Figure 10.11 it can be seen that for similar values of UE*(r-bar), the safe window of EG steels was higher than GA steels.

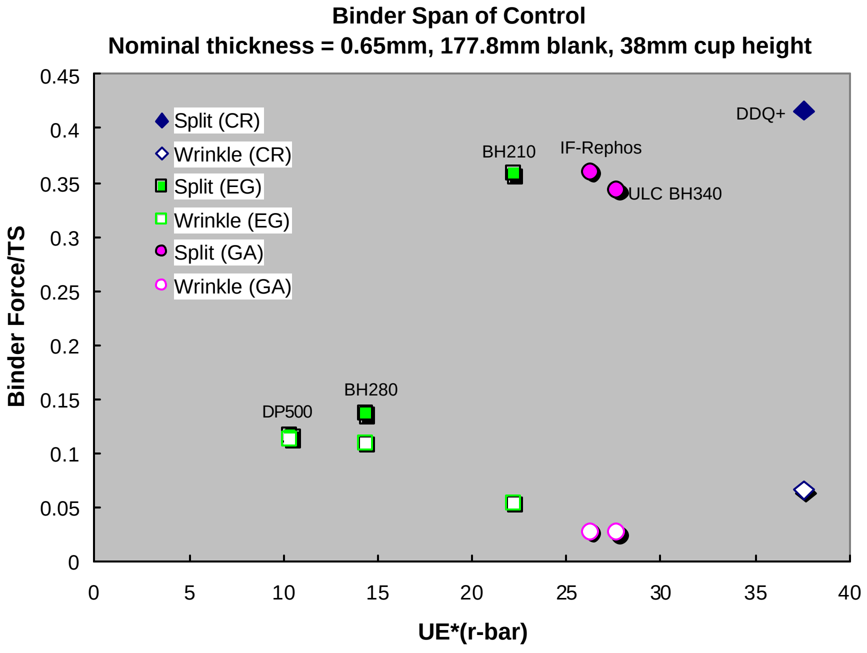

Figure 10.10: Binder Span of Control for steel grades of nominal thickness 0.65mm.

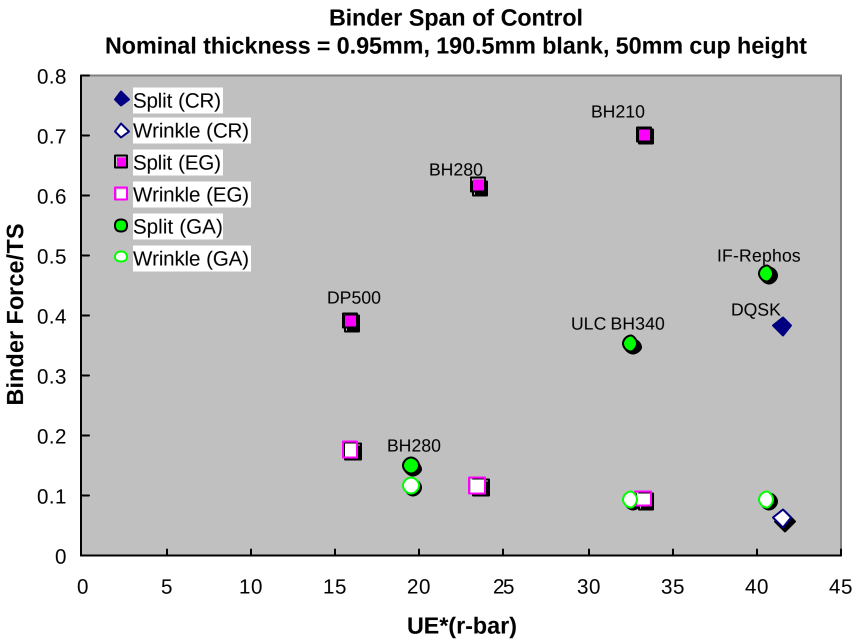

Figure 10.11: Binder Span of Control for steel grades of nominal thickness 0.95mm

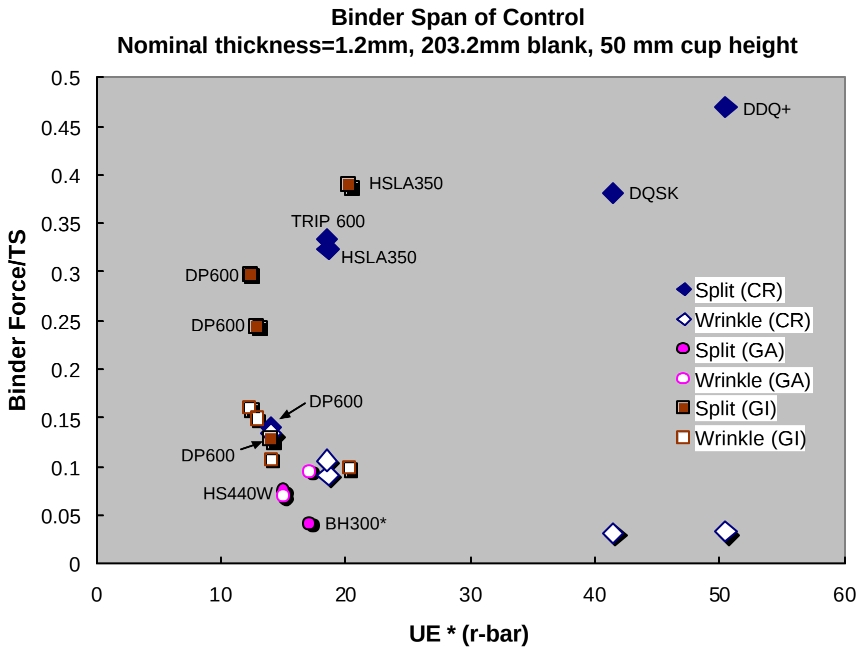

Figure 10.12: Binder Span of Control for some structural steels of nominal thickness 1.2mm

In general, it was found that, the operating windows for EG and GI steel lots were larger than the CR, and GA steel lots. Among the AHSS (DP600 and TRIP600), from Table 10.4, it can be seen that the operating window was the largest for the TRIP600 steel. This is probably caused by the higher n-value of the TRIP steel, delaying the onset of necking. Interestingly, among the UHSS, the only steel grade with any safe operating window was M190. For this tooling geometry, at a given binder force, if the force pulling the metal is greater than the restraint caused by the binder force, metal starts to pull in. In the case of M190, because of its high strength, any small strain will result in a large pulling force, thereby causing easy draw-in of the metal from the flange.

The results presented in Table 10.4 and Figures 10.10-10.12, are cases where the binder span of control was determined for one combination of blank size, cup height and lubricant. To examine the sensitivity of the binder span of control to test variables, additional testing was conducted on 1.19mm CR DP600 (2P). In these tests the wrinkle and split limits were determined for different cup heights. Two lubricants, Quaker EGL-1 ship oil and prelube were used to evaluate the sensitivity to the lubricant type. The ship oil was observed to have a lesser viscosity than the prelube. Figure 10.13 shows the results of this testing, where the wrinkle and split limits are shown as a function of cup height for the two lubricants.

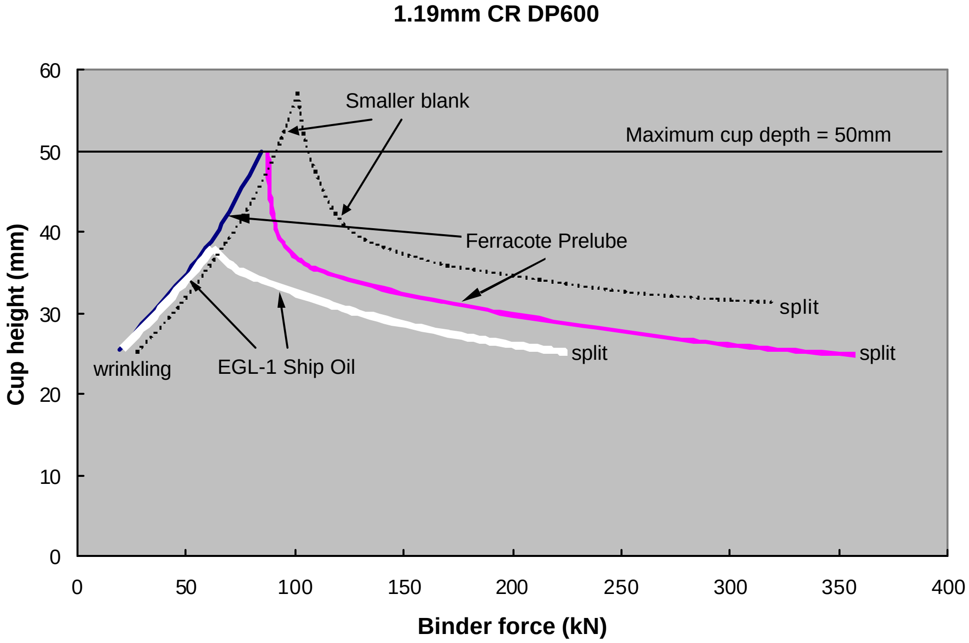

Figure 10.13: Effect of cup height, lubricant type and blank size on the binder span of control for 1.19mm CR DP600 (2P).

Figure 10.13 gives a more complete understanding of binder span of control as a function of the different test variables. The intersection point of the wrinkle and split lines for a given lubricant is the maximum cup depth that can be formed for the particular combination of blank size and lubricant. As seen in Figure 10.13, use of prelube results in a significantly higher operating window than using the lighter ship oil. The maximum cup depth that could be formed with the prelube is also higher than with the ship oil. Also shown in the figure are two dotted lines showing possible limits for a blank of a reduced size. The intersection point is presumed to be higher for a smaller blank because of easier flow through the binder. Figure 10.13 thus provides insights that help interpret the data in Table 10.4. As seen in Table 10.4, some steels show a very small safe window, for the particular combination of blank size, cup height, lubrication and tooling. Figure 10.13 shows that it is possible to obtain higher operating windows using a different lubricant, reducing the cup height or the blank size. A more complete comprehension of binder span of control would thus necessitate a much larger experimental matrix comprising of different lubricant types, blank sizes, cup heights.

10.6.3:Strain Measurement

Figures 10.14 through 10.24 show the major, minor and thickness strain distributions for the steels in the program. The strain distributions are presented in the diagonal direction. The center of the square cup corresponds to a value of 0 on the X-axis. The location corresponding to the punch entry radius was the eventual failure location. All the plots have similar shapes and features showing strain localization at or near the punch entry radius (X between 48mm and 60mm in the figures). For all cases shown here, it can be seen that the location of punch entry radius is characterized by significantly positive major and minor strains, showing a peak both for major and minor strains. In all the figures, the different steels are identified by their lot code. Complete mechanical properties corresponding to the different lots could be found in Section 2. All three strains, i.e. major, minor and thickness strains are presented in the same plot. To avoid clutter, the results for only two or three lots are presented in each plot. When examining these plots, it would be worthwhile to note that some lots show a more pronounced peak than others. From a formability perspective, a peaked feature in a strain distribution is undesirable representing strain localization, indicating that failure by necking or splitting is imminent. None of the samples showed any necking.

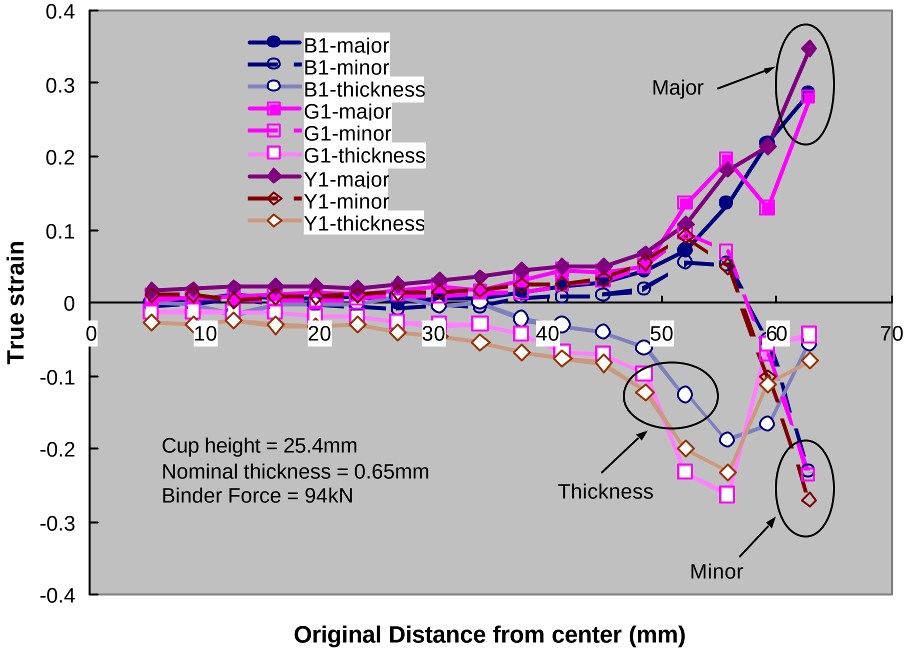

Figure 10.14: Major, minor and thickness strain distribution for lots 0.7 EG BH210 (B1), 0.66mm EG DP500 (G1) and 0.7mm DDQ+ (Y1) along the diagonal of the square cup.

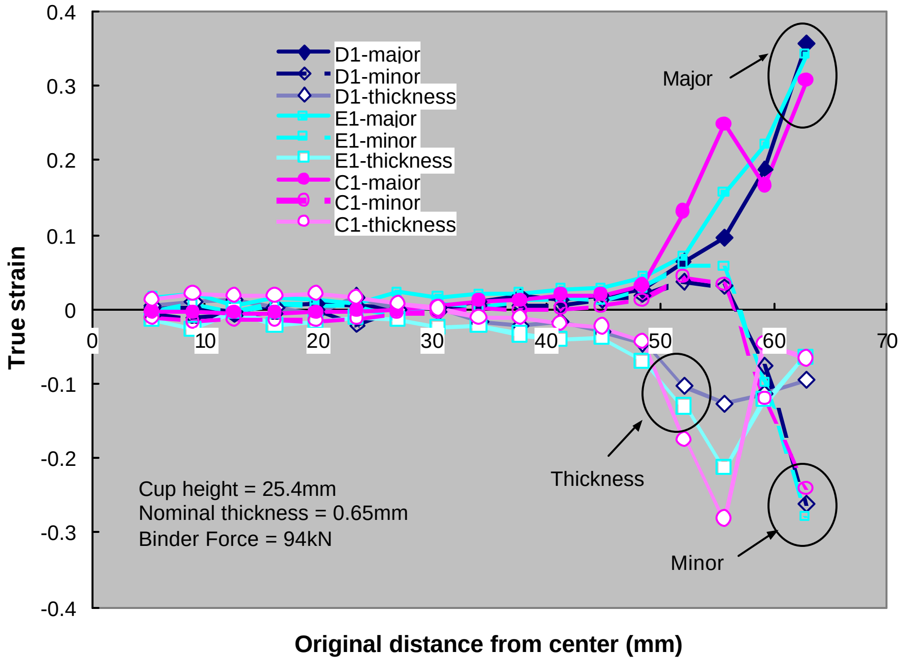

Figure 10.15: Major, minor and thickness strain distributions for 0.74mm ULC BH340 (D1), 0.63mm IF-Rephos (E1) and 0.7mm DDQ+ (Y1) along the diagonal of the square cup.

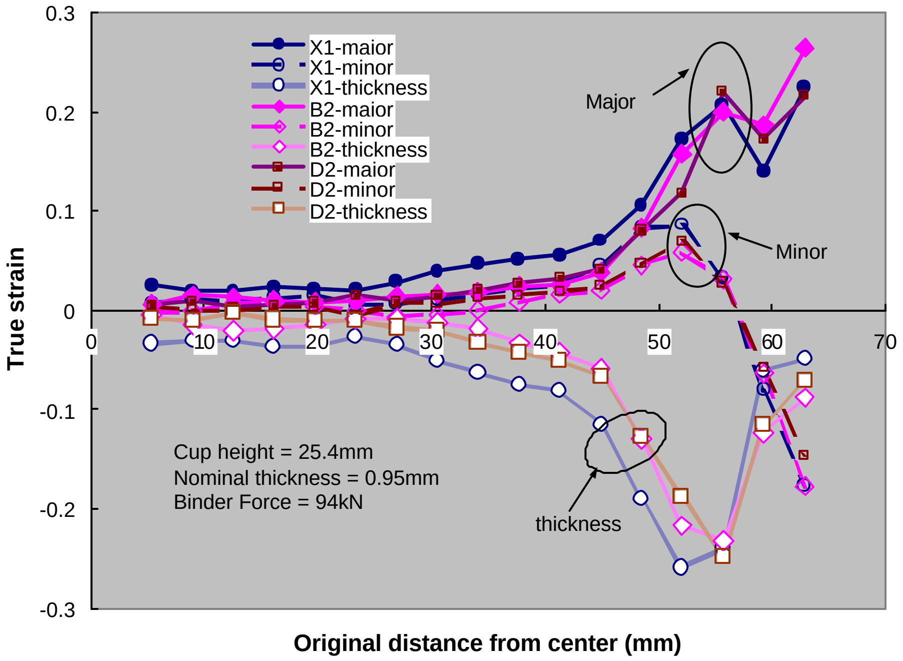

Figure 10.16: Major, minor and thickness strain distributions for 0.77mm CR DQSK (X1), 0.93mm EG BH210 (B2), 1.02mm GA ULC BH340 (D2) along the diagonal of the square cup.

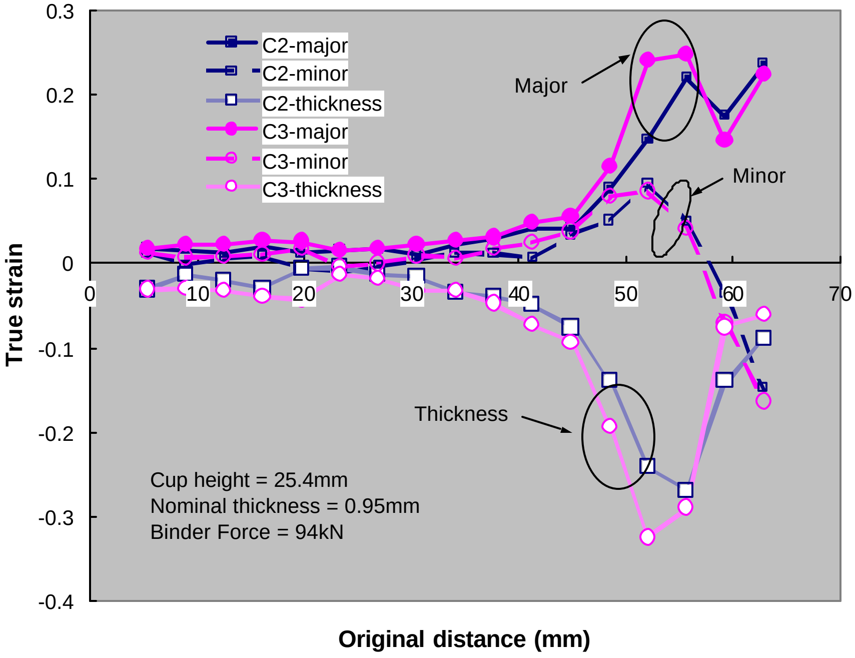

Figure 10.17: Major, minor and thickness strain distributions for 1mm EG BH280 (C2) and 1.04mm GA BH280 (C3) along the diagonal of the square cup.

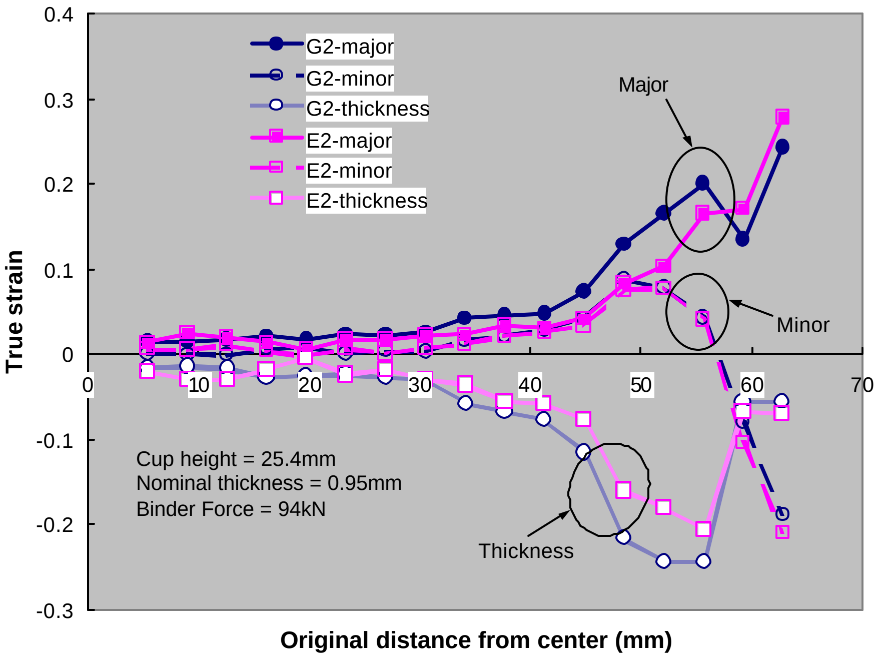

Figure 10.18: Major, minor and thickness strain distributions for 0.8mm EG DP500 (G2) and 0.89mm GA IF-Rephos (E2) along the diagonal of the square cup.

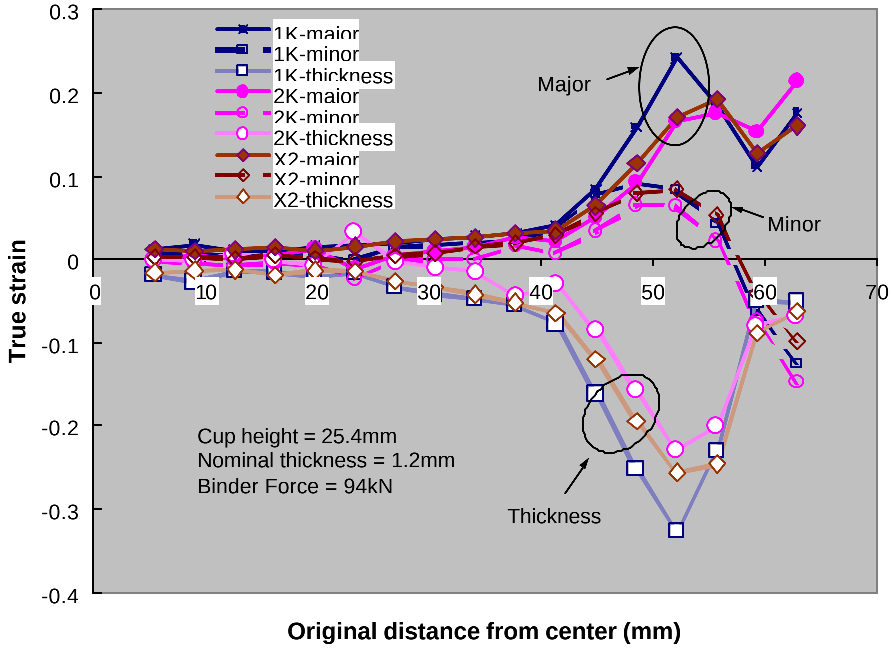

Figure 10.19: Major, minor and thickness strain distributions for 1.24mm GA BH300 (1K), 1.19mm GI BH300 (2K) and 1.19mm CR DQSK (X2) along the diagonal of the square cup.

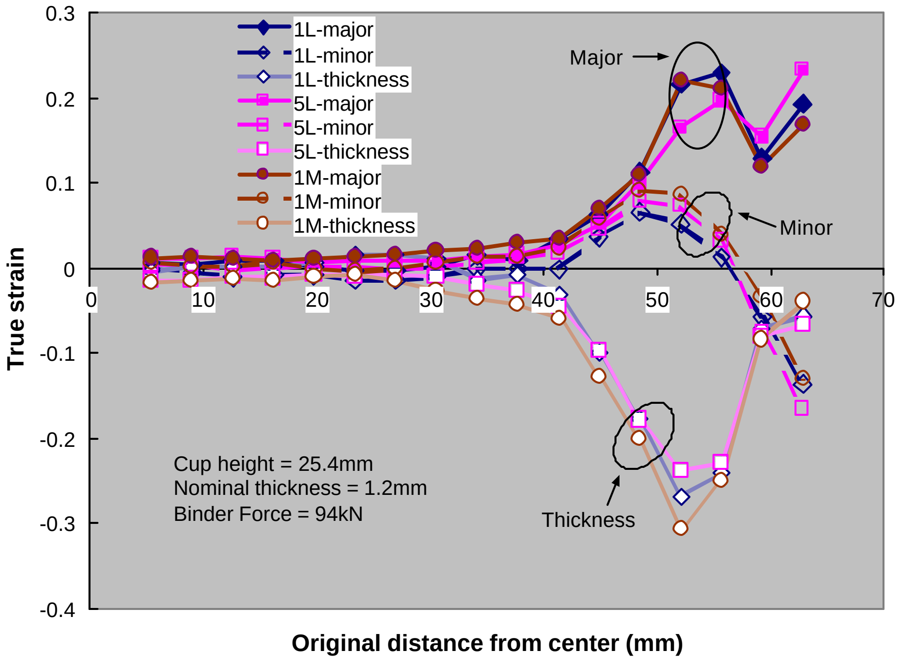

Figure 10.20: Major, minor and thickness strain distributions for 1.16mm GI HSLA350 (1L), 1.21mm CR HSLA350 (5L) and 1.24mm HS440W(1M) along the diagonal of the square cup.

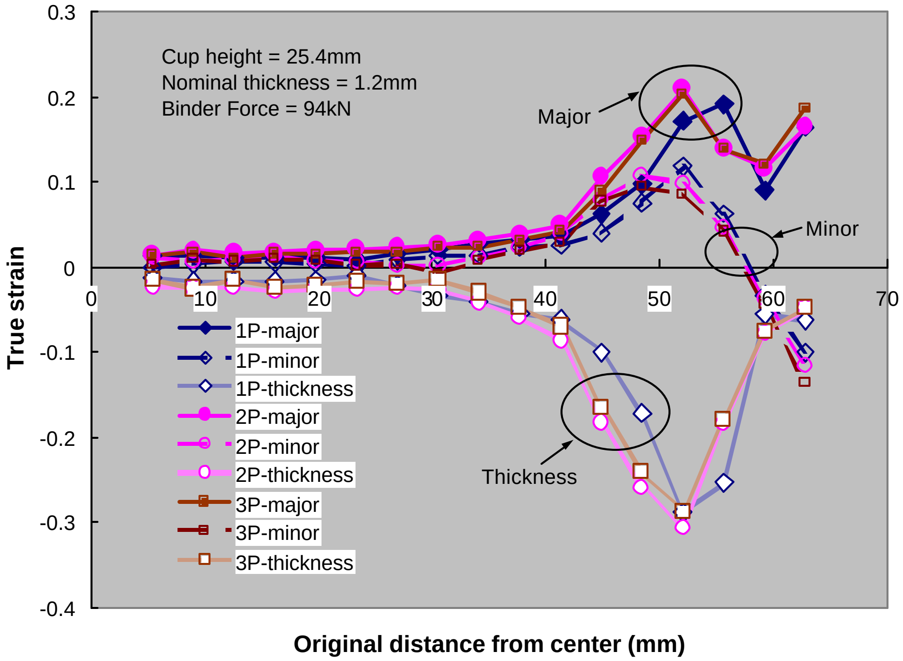

Figure 10.21: Major, minor and thickness strain distributions for 0.96mm GI DP600 (1P), 1.19mm CR DP600 (2P) and 1.39mm GI DP600 (3P) along the diagonal of the square cup.

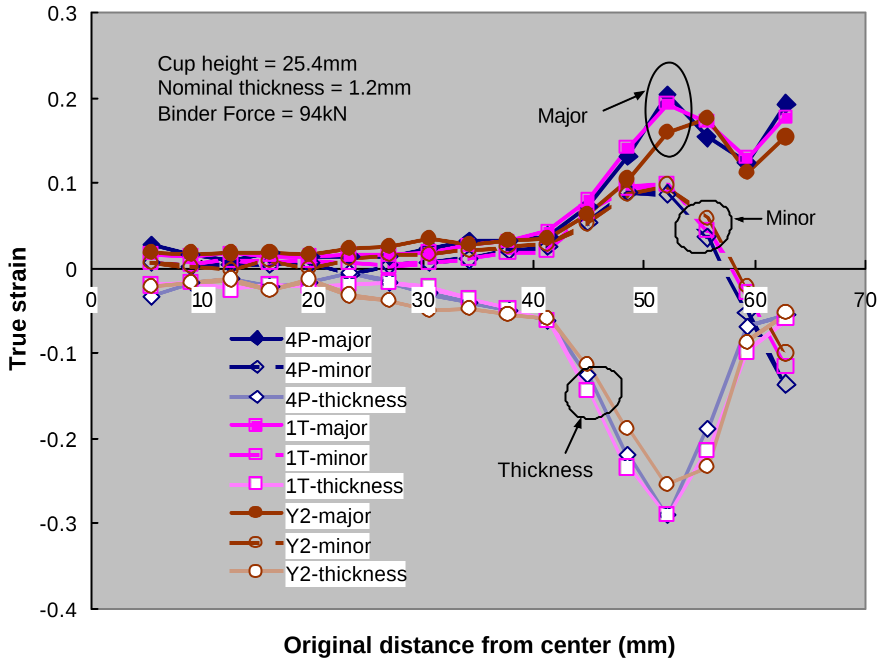

Figure 10.22: Major, minor and thickness strain distributions for 1.23mm GI DP600 (4P), 1.4mm CR TRIP600 (1T) and 1.19mm CR DDQ+ (Y2) along the diagonal of the square cup.

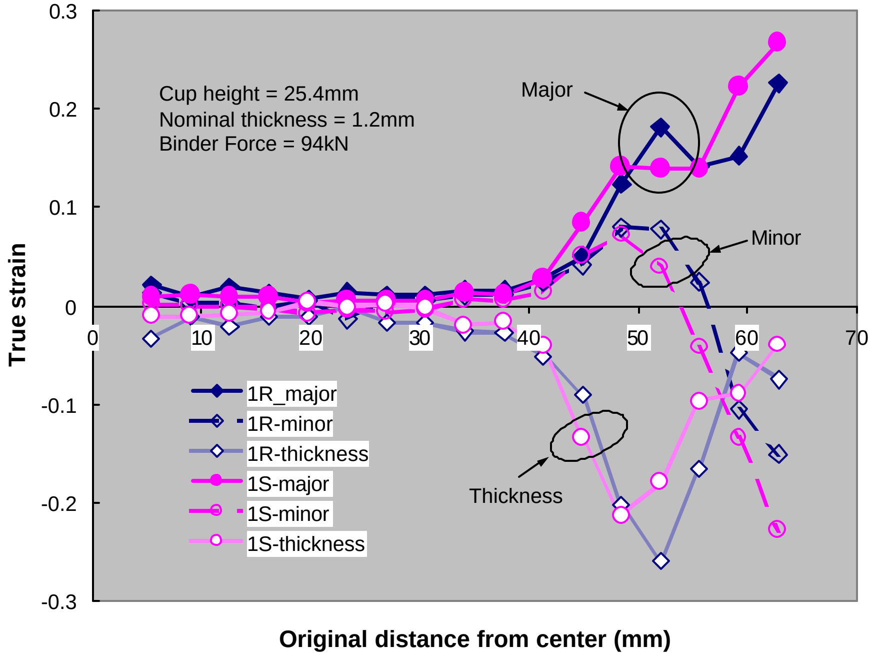

Figure 10.23: Major, minor and thickness strain distributions for 1.2mm GI DP800 (1R) and 1.15mm CR DP980 (1S) along the diagonal of the square cup.

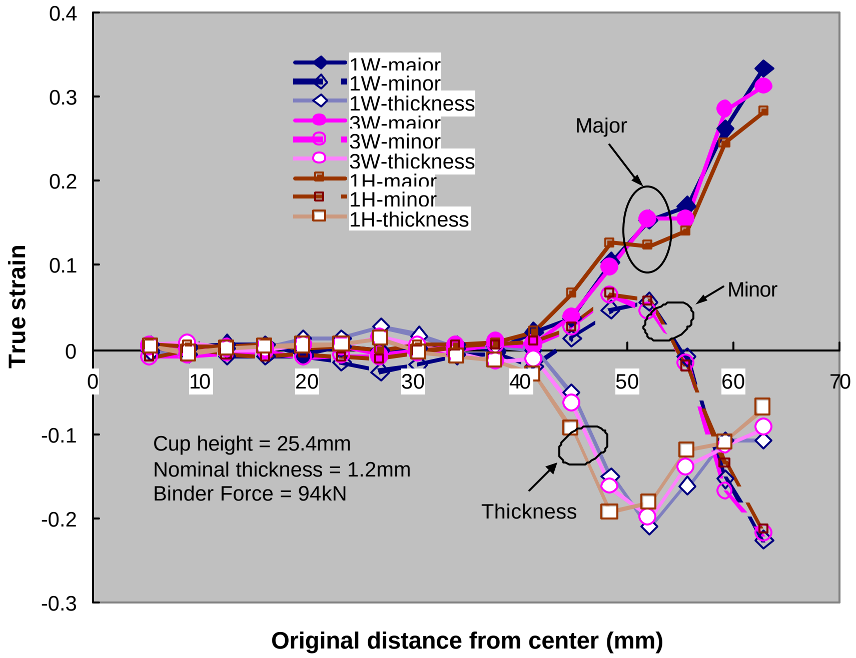

Figure 10.24: Major, minor and thickness strain distributions for 1.32mm GI RA830 (1W), 1.25mm CR RA830 (3W) and 1.03mm CR M190 (1H) along the diagonal of the square cup.

Examination of the strain distributions reveals that at the critical location, the material is stretched positively in both directions (biaxial straining). From these results, it can be seen that the Square Draw test evaluates formability under biaxial straining conditions. Also noteworthy is the fact that for some of the UHSS in the program (RA 830 and M190), the true thinning strain for safe parts is approximately -0.2, (engineering thinning strain of 18%), a value not normally associated with UHSS. This is probably related to the fact that in the FLC, the left hand side is a line of constant thickness strain, but on the right hand side, the safe thickness strain increases with increasing biaxiality. Results from strain measurements not only indicate a higher than expected formability for the UHSS, but also shows the potential for stamping these steels with appropriate die and process engineering. As seen in Figures 10.14-10.24, some lots show a more peaked strain distribution than others. The difference in strain distributions can be attributed to difference in mechanical properties, and coating differences.

10.7 Discussion

For all three measures of formability evaluated in this test: (1) Failure height (2) Binder Span of Control and (3) Strain measurement, it was seen that higher the value of UE*(r-bar) for a given lot, the better the forming performance of the steel grade under stretch-draw conditions. The parameter UE*(r-bar) can thus be considered as a fundamental performance metric for stretch drawability.

The effect of coating on the results of the Square Draw test was also very significant. Considering the skin panel steels, for steels with similar mechanical properties, EG steel lots had a better forming performance than the GA lots. For the structural steels, GI steels exhibited better formability than the uncoated (CR) or the GA lots. Results from this test demonstrate the importance of friction between the steel and tooling. It is to be noted that these results are valid only for the particular lubricant used in this study. The influence of different lubricants on stretch-drawability might be an interesting area to explore. The test method could also be used to determine the formability of a particular lubricant + steel combination.

One of the important uses of the results of the Square Draw test would to provide FE analysts with formability data against which to benchmark models for AHSS. By comparing predictions of strain distributions, and failure heights with experimental data, it would be possible to examine the effect of different yield functions, material hardening models, failure criteria used in formability simulation practice. The geometry is simple enough to enable the use of commercial FE codes or more research-oriented codes used by researchers at auto companies and universities.

10.8 Conclusions

1. Stretch drawability as measured in the Square Draw test was found to be strongly influenced by UE*(r-bar) when metal flow is restricted. The higher this value for a given steel lot, the better is the forming performance under stretch-draw conditions.
2. The influence of the protective coating on the results of the Square Draw test was very strong. For skin panel steels showing similar mechanical properties, it was found that the formability of EG steel lots was better than the GA steel lots. For structural steels, GI steels showed a better forming performance than GA steels.
3. Strain measurements of formed cups indicate the occurrence of biaxial straining at the eventual failure location.

References

Section 2

2.1 ASTM E-8-01, Standard Test Methods for Tension Testing of Metallic Materials, ASTM International, 100 Barr Harbor Drive, PO Box C700, West Conshohocken, PA 19428-2959.
2.2 C. Wong, *Improved Method for Instantaneous n-value Calculation*, Ispat Inland internal memo, March 7, 2002.

Section 3

3.1 P. S. Fallansbee, *High Strain Rate Compression Testing*, Metals Handbook, Ninth Edition, Vol. 8, p. 190, ASM, 1985.
3.2 B. Yan and K. Xu, *High Strain Rate Behavior of Advanced High Strength Steels for Automotive Applications*, in 44th MWSP Conference Proceedings, Vol. XI, 2002, pp. 493-507.

Section 4

4.1 W. C. Leslie, The Physical Metallurgy of Steels, McGraw-Hill International Book Company, 1982, p. 162.
4.2 M. G. Stout and A. D. Rollett, *Large Strain Bauschinger effect in FCC metals and Alloys*, Met. Trans. A, 21A, 3201-3213, 1990.
4.3 R. Sowerby and D. K. Uko, *Review of Certain Aspects of the Bauschinger Effect in Metals*, Materials Science and Engineering, 41, pp. 43-58, 1979

Section 5

5.1 S. P. Keeler and W. G. Brazier, "Relationship between Laboratory Material Characterization and Press-Shop Formability", Microalloying 75, pp. 517-530.
5.2 Bernard S. Levy, Private Communication
5.3 S. P. Keeler, The Bead Correction Factor, Training Manual for the Enhanced FLC Project, Auto/Steel Partnership, 2000 Town Center, Suite 320, Southfield, MI.

Section 6

6.1 K. Matsudo, K. Osawa, M. Yoshida, *Prediction of punched surface stretch flangeability of steel sheets*, Sheet Metal Forming and Formability, Proceedings of the 10th Biennial Congress, IDDRG, April 1978, pp. 325-334.
6.2 M. Sudo, M. Higashi, H. Hori, T. Iwai, S. Kambe, Z. Shibata, *Effects of microstructure on the mechanical properties of multi-phase sheet steels*, Transactions of the ISIJ, Vol. 21, 1981, pp. 820-827.
6.3 M. Sudo, I. Tsukatani, Z. Shibata, *Effect of microstructure on the plastic anisotropy and mechanical properties of triphase sheet steel*, Conf. on Metallurgy of Continuous-Annealed Sheet Steel, Dallas, TX, Feb. 1982, pp. 301-319

6.4 M. Sudo, I. Kokubo, *Microstructure-mechanical property relationships in multi-phase steel sheet*,

Scandinavian Journal of Metallurgy, 13 (1984), pp. 329-342.
6.5 S. Hashimoto, M. Sudo, K. Mimura, T. Hosoda, *Effect of microstructure on mechanical properties of C-Mn high strength hot rolled sheet*, Trans. ISIJ, Vol. 26, 1986, pp. 985-992.
6.6 T. Kato, M. Shinozaki, K. Tsunoyama, T. Irie, N. Aoyagi, *Properties of newly-developed hot-rolled high-strength sheet steels with phosphorus*, Int. J. of Materials and Product Technology, vol. 2, 1987, pp. 356-376.
6.7 I. Machida, M. Narita, R. Kureura, M. Morita, N. Aoyagi, M. Sano, *Reduction in weight of steel wheels by development of 780 MPa-grade hot rolled steel sheets*, SAE Technical paper # 940536, SAE International, Warrendale, PA.
6.8 H. Asano, N. Matsuzu, A. Itami, K. Koyama, *Development of high strength steel sheet with excellent stretch formability for automotive applications*, SAE Technical paper # 940943, SAE International, Warrendale, PA.
6.9 S. Nomura, H. Fukuyama, S. Nakai, N. Nagao, N. Komatsubara, Development of high-strength hot-rolled sheet products for automotive application, South East Asia Iron and Steel Institute, Session 9, 2/1-12
6.10 K. Sugimoto, Y. Shimizu, J. Sakaguchi, T. Kashima, *Microstructure and formability of high strength TRIP-Aided bainitic sheet steels*, 40th MWSP Conf. Proc. ISS, 1998, pp. 275-281.
6.11 K. Sugimoto, A. Nagasaka, M. Kobayashi, S. Hashimoto, *Effects of retained austenite parameters on warm stretch-flangeability in TRIP-aided dual-phase sheet steels*, ISIJ International, vol. 39 (1999), pp. 56-63.
6.12 K. Sugimoto, J. Sakaguchi, T. Iida, T. Kashima, *Stretch-flangeability of a high strength TRIP bainitic sheet steel*, ISIJ International, vol. 40 (2000), pp. 920-926.
6.13 K. Sugimoto, K. Nakano, S. Song, T. Kashima, *Retained austenite characteristics and stretch flangeability of high-strength low-alloy TRIP type bainitic sheet steels*, ISIJ International, vol. 42(2002), No. 4, pp- 450-455.
6.14 Z. Milosevic, F. Moussy, *Simulation of sheared edge behavior in stretch flanging by a modified Fukui test,* Advanced Technology of Plasticity 1987, vol. II, Stuttgart, FRG, Aug. 1987, pp. 697-702.
6.15 M. Y. Demeri, *The axi-symmetric stretch flanging of sheet metal*, 15th Biennial congress of the IDDRG, May 1988, pp. 231-236.
6.16 N.-M. Wang, M. L. Wenner, *An analytical and experimental study of stretch flanging*, Int. J. Mech. Sci. 1974, vol. 16, pp. 135-143.
6.17 N.-M. Wang, L. K. Johnson, S. C. Tang, *Stretch flanging of V-shaped sheet metal blanks*, J. Applied Metalworking, vol. 3 No. 3, July 1984, pp. 281-291.
6.18 S. Dudra and S. Shah, *Stretch flanges: Formability and trimline development*, J. Materials Shaping Technology, vol. 6, no. 2, 1988, pp. 91-101.
6.19 M. Y. Demeri, S. C. Tang, *Computer simulation and experimental validation of stretch flanging*, J. Materials Shaping Technology, (1991), vol. 9, pp. 241-251.
6.20 C. T. Wang, G. Kinzel, T. Altan, *Failure and wrinkling criteria and mathematical modeling of shrink and stretch flanging operations in sheet metal forming*, J. Materials Processing Technology, 53 (1995) pp. 759-780.
6.21 M. J. Worswick and M. J. Finn, *The numerical simulation of stretch flange forming*, Int. Journal of Plasticity, 16 (2000) pp. 701-720.

Section 7

7.1 P. L. Charpentier, *Influence of Punch Curvature on the Stretching Limits of Sheet Steel*, Met. Trans. A, vol. 6A, Aug. 1975, pp. 1665-1669
7.2 M. Y. Demeri, "The Stretch-Bend Forming of Sheet Metal", J. Applied Metalworking, 1981, vol.2, no. 1, pp. 3-10.
7.3 O. S. Narayanaswamy, and M. Y. Demeri, "Analysis of the Angular Stretch Bend Test", Novel Techniques in Metal Deformation Testing, edited by R. H. Wagoner, publication of The

Metallurgical Society of AIME

Section 8

8.1 M. Huang, J. C. Gerdeen, *"Springback of Doubly Curved Developable Sheet Metal Surface – An Overview",* SAE940938, 1994
8.2 R. H. Wagoner, *"Fundamental Aspects of Springback in Sheet Metal Forming"*, NUMISHEET2002, Korea, 2002
8.3 C. T. Wang, *"An Industrial Outlook for Springback Predictability, Measurement Reliability, and Compensation Technology*", NUMISHEET2002, Korea, 2002
8.4 Y. C. Liu, *"Springback Reduction in U-Channels – 'Double Bend' Technique",* Journal of Applied Metalworking, Vol. 3, No. 2, 1984
8.5 R. A. Ayres, *"SHAPESET: A Process to Reduce Sidewall Curl Springback in High-Strength Steel Rails"*, Journal of Applied Metalworking, Vol. 3, No. 2, 1984
8.6 R. G. Davies, *"Side-Wall Curl in High-Strength Steels"*, Journal of Applied Metalworking, Vol. 3, No. 2, 1984
8.7 Z. T. Zhang, and D. Lee, *"Springback Analysis and Control in Forming Two-Step Rail-Shaped Sheet Metal Parts"*, SAE 960596, 1996
8.8 R. J. Del Vecchio, Understanding Design of Experiments, Hanser Publishers, Munich, 1997
8.9 D. C. Montgomery, Design and Analysis of Experiments, 5th Edition, John Wiley & Sons, Inc., New York, 2001
8.10 D. J. Wheeler, and R. W. Lyday, Evaluating The Measurement Process, SPC Press Inc., Tennessee, 1984

Section 9

9.1 Standardized Dent Test Procedure Manual, June 1999, Auto/Steel Partnership, Southfield, MI.

9.2 S. Sriram, J. G. Speer, and D. K. Matlock, *Material and Design Factors Influencing the Quasi-Static Dent Resistance of Steel Body Panels*, SAE Paper, 1999-01-0025
9.3 S. Sriram, *Effect of Stamping and Styling on Dent Resistance*, 43rd MWSP Conf. Proc., ISS, vol. XXXIX, 2001

Appendix A: Data for Bending Under Tension Limits

Table A.1: Heights at failure and fracture locations for the Angular Stretch Bend test for all lots

Lot Code	Material	Thickness (mm)	R/t ratio	Failure heights (mm)	Std. Dev.	Failure Location
X1	DQSK	0.77	1.30	39.40	0.20	Punch
			4.81	57.43	0.37	Punch
			9.74	62.03	NA	Punch, Sidewall
			16.24	62.80	0.54	Sidewall
Y1	DDQ+	0.7	1.43	44.20	0.44	Punch
			3.56	58.31	0.66	Punch
			7.16	61.84	0.34	Punch, Sidewall
			14.29	64.50	0.61	Sidewall
X2	DQSK	1.19	1.26	41.20	0.31	Punch
			4.21	55.20	0.25	Punch
			8.41	59.85	0.65	Punch, Sidewall
			21.03	56.91	0.04	Sidewall
Y2	DDQ+	1.19	1.25	43.39	0.18	Punch
			4.17	57.01	0.13	Punch
			8.34	61.37	0.29	Punch, Sidewall
			20.85	60.33	0.67	Sidewall
B1	BH210	0.7	1.43	34.58	0.28	Punch
			3.58	46.04	0.93	Punch
			7.16	50.79	0.51	Punch
			14.29	54.23	0.67	Punch, Sidewall
B2	BH210	0.93	1.12	30.51	0.32	Punch
			4.16	45.84	0.28	Punch
			8.43	50.26	0.49	Punch
			14.06	55.18	0.65	Punch, Sidewall
C1	BH280	0.71	1.41	28.00	0.29	Punch
			3.51	38.46	0.40	Punch
			7.05	45.81	0.27	Punch
			14.09	51.93	0.22	Punch, Sidewall
C2	BH280	1	1.00	25.53	0.42	Punch
			3.70	40.71	0.24	Punch
			7.51	46.07	0.17	Punch
			12.52	49.91	0.84	Die exit
C3	BH280	1.04	0.96	26.78	0.18	Punch
			3.56	40.37	0.23	Punch
			7.21	47.59	0.08	Punch
			12.03	53.86	0.15	Punch, Sidewall

D1	ULC BH340	0.74	1.36	35.09	0.26	Punch
			3.38	46.78	0.06	Punch
			6.79	51.38	0.47	Punch
			13.55	54.05	0.28	Punch, Sidewall
D2	ULC BH340	1.02	0.98	32.18	0.11	Punch
			3.62	47.85	0.11	Punch
			7.34	52.72	0.41	Punch
			12.24	55.98	0.93	Punch, Sidewall
E1	IF-Rephos	0.63	1.37	41.73	0.13	Punch
			3.41	51.96	0.27	Punch
			6.86	55.91	0.38	Punch
			13.69	58.78	0.18	Punch, Sidewall
E2	IF-Rephos	0.89	1.11	35.28	1.08	Punch
			4.11	50.77	0.49	Punch
			8.33	54.61	0.41	Punch
			13.90	57.79	0.04	Punch, Sidewall
G1	DP500	0.66	1.52	26.86	0.95	Punch
			3.78	35.03	1.34	Punch
			7.60	37.80	0.60	Punch
			15.17	40.45	2.40	Punch
G2	DP500	0.81	1.25	24.06	0.40	Punch
			4.62	36.04	0.18	Punch
			9.37	38.74	0.36	Punch
			15.62	42.24	NA	Punch
1K	BH300	1.24	1.21	26.53	0.10	Punch
			4.03	37.46	0.19	Punch
			8.07	42.59	1.29	Punch
			20.16	43.87	0.77	Sidewall
2K	BH300	1.19	1.26	32.21	0.20	Punch
			4.21	45.86	0.32	Punch
			8.41	50.18	0.50	Punch, Sidewall
			21.03	50.55	1.64	Sidewall
1L	HSLA 350	1.16	1.28	24.13	0.26	Punch
			4.27	37.53	0.42	Punch
			8.54	44.37	0.67	Punch
			21.34	50.39	0.43	Sidewall
5L	HSLA 350	1.21	1.24			Punch
			4.13	33.88	0.34	Punch

			8.27	39.73	0.43	Punch
			20.67	43.43	0.44	Sidewall
2L	HSLA 350	1.62	1.54	23.63	0.14	Punch
			4.64	35.26	0.49	Punch
			7.72	41.23	0.14	Punch
			15.45	45.42	0.95	Sidewall
1M	HS 440W	1.24	1.24	26.13	0.50	Punch
			4.03	37.02	0.15	Punch
			8.07	42.38	0.94	Punch
			20.16	42.79	0.21	Sidewall
2M	HS 440W	1.58	1.58	28.02	0.05	Punch
			4.75	39.12	0.05	Punch
			7.91	43.47	1.47	Punch
			15.82	44.72	0.10	Sidewall
1P	DP600	0.96	1.57	24.33	0.74	Punch
			5.22	33.08	1.29	Punch
			10.44	37.33	1.38	Punch
			26.10	36.12	1.71	Punch
2P	DP600	1.19	1.25	24.42	1.02	Punch
			4.17	35.27	0.55	Punch
			8.34	39.85	1.69	Punch
			20.85	40.29	1.57	Punch
3P	DP600	1.39	1.06	19.18	0.46	Punch
			3.55	27.40	1.70	Punch
			7.09	29.26	1.21	Punch
			17.73	31.78	2.34	Punch
4P	DP600	1.23	1.21	21.60	0.46	Punch
			4.03	31.61	0.20	Punch
			8.07	35.87	1.14	Punch
			20.16	38.30	1.43	Punch
5P	DP600	1.64	1.53	27.90	0.84	Punch
			4.58	36.92	1.99	Punch
			7.63	40.77	2.14	Punch
			15.26	42.94	2.24	*
6P	DP600	1.49	1.68	23.27	0.60	Punch
			5.03	32.01	0.95	Punch
			8.39	35.45	0.54	Punch
			16.77	37.58	0.51	Punch
1T	TRIP 600	1.4	1.07	33.52	0.26	Punch
			3.58	46.06	0.59	Punch
			7.16	52.43	0.22	Punch

			17.89	55.30	0.53	Sidewall
2T	TRIP 600	1.6	1.56	36.15	0.15	Punch
			4.69	48.28	0.11	Punch
			7.82	52.54	0.29	Punch
			15.64	55.52	0.42	Sidewall
1R	DP800	1.2	1.25	17.84	0.98	Punch
			4.17	24.99	0.61	Punch
			8.34	29.27	0.34	Punch
			20.85	33.22	0.62	Punch
2R	DP800	1.59	1.57	15.41	NA	Punch
			4.72	18.69	2.06	Punch
			7.87	21.40	2.35	Punch
			15.74	25.70	NA	Punch
1S	DP980	1.15	1.30	16.01	0.20	Punch
			4.34	22.36	0.17	Punch
			8.69	27.06	0.21	Punch
			21.72	31.21	0.34	Punch, Sidewall
2S	DP980	1.52	1.65	17.65	0.07	Punch
			4.94	23.85	0.18	Punch
			8.23	27.78	0.33	Punch
			16.45	31.89	0.54	Punch, Sidewall
1W	RA 830	1	1.16	7.12	0.05	Punch
			3.86	14.52	0.48	Punch
			7.72	17.99	0.56	Punch
			19.29	20.53	0.72	Die
2W	RA 830	1.55	1.61	10.30	0.58	Punch
			4.84	17.53	3.73	Punch
			8.07	23.11	0.73	Die Exit
			16.13	24.93	0.31	Die Exit
3W	RA 830	1.25	1.20	8.31	0.37	Punch
			4.00	10.18	0.31	Punch
			8.00	16.26	NA	Punch
			20.00	20.60	1.85	Die
4W	RA 830	1.8	1.56	9.45	0.42	Punch
			4.69	13.31	0.27	Punch
			7.82	15.46	0.16	Punch
			15.64	17.93	1.19	Die
1H	M 190	1.03	1.48	12.15	0.34	Punch

Appendix B: Springback and Curl Data for the Channel Draw Test

Table B.1: Baseline steels

Lot Code	Testing condition	Springback		Sidewall Curl	
		Mean	Std. Dev.	Mean	Std. Dev.
X1	$A_SB_SC_S$	3.49	0.36	430.6	31.7
	$A_SB_SC_L$	2.04	0.21	1101.5	318.5
	$A_SB_LC_S$	4.19	0.30	466.5	40.9
	$A_SB_LC_L$	2.96	0.07	1136.2	148.9
	$A_LB_SC_S$	5.18	0.27	698.4	42.6
	$A_LB_SC_L$	2.81	0.18	1142.5	127.4
	$A_LB_LC_S$	6.21	0.09	370.3	11.0
	$A_LB_LC_L$	4.31	0.33	712.2	75.3
X2	$A_SB_SC_S$	2.25	0.12	1246.9	178.7
	$A_SB_SC_L$	0.29	0.21	**5644.5**	N/A
	$A_SB_LC_S$	3.54	0.14	929.4	729.2
	$A_SB_LC_L$	0.90	0.07	**5382.8**	N/A
	$A_LB_SC_S$	3.25	0.25	1039.4	251.7
	$A_LB_SC_L$	2.01	0.21	**1652.1**	N/A
	$A_LB_LC_S$	4.96	0.07	540.1	16.5
	$A_LB_LC_L$	3.17	0.24	1526.9	462.1
Y1	$A_SB_SC_S$	3.44	0.07	416.3	5.5
	$A_SB_SC_L$	2.25	0.21	768.6	118.5
	$A_SB_LC_S$	4.19	0.07	522.0	6.4
	$A_SB_LC_L$	2.23	0.07	803.7	130.0
	$A_LB_SC_S$	4.48	0.25	876.8	174.0
	$A_LB_SC_L$	2.11	0.24	867.0	65.8
	$A_LB_LC_S$	5.95	0.12	482.5	23.9
	$A_LB_LC_L$	3.15	0.14	966.6	70.3
Y2	$A_SB_SC_S$	1.87	0.35	**2016.9**	N/A
	$A_SB_SC_L$	0.19	0.25	**7150.3**	N/A
	$A_SB_LC_S$	2.64	0.09	**2650.1**	N/A
	$A_SB_LC_L$	0.49	0.14	**2104.9**	N/A
	$A_LB_SC_S$	2.25	0.41	981.5	26.1
	$A_LB_SC_L$	1.19	0.25	1495.0	338.0
	$A_LB_LC_S$	3.73	0.15	788.8	115.6
	$A_LB_LC_L$	2.23	0.18	**2677.4**	N/A

Table B.2: Skin Panel steels

Lot Code	Testing condition	Springback		Sidewall Curl	
		Mean	Std. Dev.	Mean	Std. Dev.
B1	$A_SB_SC_S$	4.57	0.00	178.9	5.2
	$A_SB_SC_L$	4.14	0.00	267.6	2.3
	$A_SB_LC_S$	5.30	0.12	200.1	7.4
	$A_SB_LC_L$	5.01	0.31	330.7	3.9
	$A_LB_SC_S$	7.45	0.31	238.5	11.5
	$A_LB_SC_L$	6.38	0.00	304.3	14.5
	$A_LB_LC_S$	8.48	0.07	180.3	2.6
	$A_LB_LC_L$	7.07	0.07	255.1	6.8
B2	$A_SB_SC_S$	4.00	0.06	265.6	7.4
	$A_SB_SC_L$	3.37	0.21	649.2	57.7
	$A_SB_LC_S$	4.96	0.07	309.6	10.5
	$A_SB_LC_L$	4.00	0.16	777.1	65.9
	$A_LB_SC_S$	6.09	0.23	314.6	9.5
	$A_LB_SC_L$	5.34	0.27	492.7	79.6
	$A_LB_LC_S$	6.93	0.28	235.8	9.8
	$A_LB_LC_L$	5.80	0.12	412.9	29.1
C1	$A_SB_SC_S$	5.56	0.18	133.1	3.9
	$A_SB_SC_L$	4.62	0.30	190.9	3.4
	$A_SB_LC_S$	6.64	0.14	137.8	1.1
	$A_SB_LC_L$	5.15	0.16	216.1	12.7
	$A_LB_SC_S$	8.85	0.13	168.0	3.3
	$A_LB_SC_L$	6.30	0.18	241.4	15.4
	$A_LB_LC_S$	10.03	0.14	150.8	1.9
	$A_LB_LC_L$	7.26	0.36	217.4	10.9
C2	$A_SB_SC_S$	2.25	0.12	269.5	12.3
	$A_SB_SC_L$	1.96	0.21	809.4	154.9
	$A_SB_LC_S$	2.88	0.24	310.9	5.4
	$A_SB_LC_L$	2.18	0.45	1199.2	79.5
	$A_LB_SC_S$	6.23	0.31	289.7	8.3
	$A_LB_SC_L$	5.32	0.32	447.3	15.7
	$A_LB_LC_S$	7.83	0.36	205.6	4.2
	$A_LB_LC_L$	5.39	0.07	397.9	15.4
C3	$A_SB_SC_S$	4.43	0.24	277.3	8.0
	$A_SB_SC_L$	3.00	0.30	1082.7	344.2
	$A_SB_LC_S$	5.75	0.14	330.1	31.1
	$A_SB_LC_L$	3.30	0.25	1478.4	70.1
	$A_LB_SC_S$	6.16	0.41	297.9	12.6
	$A_LB_SC_L$	4.57	0.12	561.5	77.9
	$A_LB_LC_S$	7.33	0.43	239.9	5.2
	$A_LB_LC_L$	5.71	0.14	506.4	28.9

D1	$A_SB_SC_S$	5.15	0.10	157.5	3.6
	$A_SB_SC_L$	4.19	0.14	256.5	12.7
	$A_SB_LC_S$	5.44	0.00	158.7	2.9
	$A_SB_LC_L$	5.20	0.15	279.7	4.2
	$A_LB_SC_S$	7.98	0.07	214.0	2.4
	$A_LB_SC_L$	6.38	0.12	281.8	11.5
	$A_LB_LC_S$	9.00	0.13	163.9	3.7
	$A_LB_LC_L$	7.12	0.12	250.5	5.6
D2	$A_SB_SC_S$	4.09	0.18	308.1	7.7
	$A_SB_SC_L$	2.47	0.12	1148.4	285.2
	$A_SB_LC_S$	4.72	0.20	340.3	9.0
	$A_SB_LC_L$	2.67	0.07	**2300.4**	N/A
	$A_LB_SC_S$	5.22	0.41	398.3	29.4
	$A_LB_SC_L$	3.49	0.18	765.2	101.3
	$A_LB_LC_S$	6.35	0.28	278.9	11.9
	$A_LB_LC_L$	4.38	0.38	892.2	146.1
E1	$A_SB_SC_S$	5.51	0.06	126.6	0.9
	$A_SB_SC_L$	4.89	0.14	151.2	4.8
	$A_SB_LC_S$	5.39	0.09	128.0	1.3
	$A_SB_LC_L$	5.25	0.15	164.0	0.9
	$A_LB_SC_S$	7.93	0.47	219.8	16.5
	$A_LB_SC_L$	6.59	0.12	256.0	12.6
	$A_LB_LC_S$	8.90	0.18	163.8	2.8
	$A_LB_LC_L$	7.74	0.12	239.9	6.7
E2	$A_SB_SC_S$	4.41	0.24	192.1	7.8
	$A_SB_SC_L$	3.44	0.18	683.9	109.8
	$A_SB_LC_S$	5.30	0.12	212.4	11.8
	$A_SB_LC_L$	4.26	0.22	865.7	239.9
	$A_LB_SC_S$	5.39	0.07	364.6	25.2
	$A_LB_SC_L$	4.00	0.39	627.2	144.2
	$A_LB_LC_S$	6.57	0.18	239.5	5.3
	$A_LB_LC_L$	5.01	0.33	591.6	76.9
G1	$A_SB_SC_S$	8.19	0.24	79.8	4.6
	$A_SB_SC_L$	6.38	0.12	97.5	2.3
	$A_SB_LC_S$	8.52	0.20	83.2	4.7
	$A_SB_LC_L$	6.90	0.28	95.3	1.0
	$A_LB_SC_S$	12.46	0.17	113.1	2.0
	$A_LB_SC_L$	8.90	0.13	142.5	6.0
	$A_LB_LC_S$	13.41	0.13	107.7	1.0
	$A_LB_LC_L$	10.29	0.23	144.5	4.3
G2	$A_SB_SC_S$	7.02	0.12	95.8	1.3
	$A_SB_SC_L$	5.99	0.14	135.1	8.4
	$A_SB_LC_S$	7.81	0.00	94.1	1.0
	$A_SB_LC_L$	6.45	0.10	121.5	4.9
	$A_LB_SC_S$	10.72	0.17	129.5	2.4
	$A_LB_SC_L$	8.02	0.30	179.6	6.2
	$A_LB_LC_S$	12.58	0.27	120.2	3.0
	$A_LB_LC_L$	8.45	0.35	179.5	3.9

Table B.3 Structural steels

Lot Code	Testing condition	Springback		Sidewall Curl	
		Mean	Std. Dev.	Mean	Std. Dev.
1K	$A_SB_SC_S$	6.71	0.18	195.0	6.6
	$A_SB_SC_L$	4.48	0.14	505.1	32.7
	$A_SB_LC_S$	7.00	0.21	194.6	3.2
	$A_SB_LC_L$	5.97	0.29	444.9	22.8
	$A_LB_SC_S$	6.71	0.24	239.0	7.0
	$A_LB_SC_L$	5.37	0.56	420.0	11.3
	$A_LB_LC_S$	8.10	0.23	214.7	3.3
	$A_LB_LC_L$	6.02	0.21	467.6	45.6
2K	$A_SB_SC_S$	5.01	0.53	219.4	7.6
	$A_SB_SC_L$	4.72	0.35	372.7	10.7
	$A_SB_LC_S$	6.59	0.30	213.2	9.9
	$A_SB_LC_L$	6.02	0.27	383.9	10.2
	$A_LB_SC_S$	6.64	0.37	252.9	4.0
	$A_LB_SC_L$	5.30	0.24	410.0	19.0
	$A_LB_LC_S$	7.17	0.15	226.9	8.2
	$A_LB_LC_L$	5.92	0.32	464.6	29.8
1L	$A_SB_SC_S$	4.12	0.15	189.2	0.1
	$A_SB_SC_L$	5.01	0.18	358.3	8.8
	$A_SB_LC_S$	5.90	0.07	203.6	3.4
	$A_SB_LC_L$	5.66	0.24	402.5	38.1
	$A_LB_SC_S$	4.89	0.55	220.6	9.1
	$A_LB_SC_L$	5.25	0.21	383.7	28.3
	$A_LB_LC_S$	5.99	0.14	197.8	6.3
	$A_LB_LC_L$	5.92	0.24	437.4	26.6
2L	$A_SB_SC_S$	4.77	0.18	366.4	24.6
	$A_SB_SC_L$	3.10	0.27	1446.2	323.8
	$A_SB_LC_S$	6.31	0.00	363.0	8.2
	$A_SB_LC_L$	3.73	0.18	**1638.1**	N/A
	$A_LB_SC_S$	4.86	0.20	343.1	8.2
	$A_LB_SC_L$	3.97	0.50	727.2	12.8
	$A_LB_LC_S$	6.09	0.00	329.2	4.1
	$A_LB_LC_L$	4.45	0.22	1007.4	0.5
1M	$A_SB_SC_S$	6.33	0.50	198.7	7.8
	$A_SB_SC_L$	4.60	0.19	524.8	47.6
	$A_SB_LC_S$	6.57	0.14	193.5	3.8
	$A_SB_LC_L$	5.59	0.24	474.6	43.1
	$A_LB_SC_S$	6.62	0.14	233.0	2.7
	$A_LB_SC_L$	5.10	0.07	420.6	27.3
	$A_LB_LC_S$	7.98	0.19	223.8	4.8
	$A_LB_LC_L$	6.26	0.39	474.4	19.5
2M	$A_SB_SC_S$	5.08	0.12	311.2	17.2
	$A_SB_SC_L$	4.84	0.32	365.6	13.3
	$A_SB_LC_S$	5.73	0.44	335.6	29.2
	$A_SB_LC_L$	5.97	0.46	384.6	19.6
	$A_LB_SC_S$	5.18	0.07	298.5	6.0
	$A_LB_SC_L$	4.98	0.18	343.0	12.8
	$A_LB_LC_S$	6.14	0.27	295.6	19.9
	$A_LB_LC_L$	5.92	0.24	328.6	31.3

1P	$A_SB_SC_S$	8.31	0.12	115.5	1.8
	$A_SB_SC_L$	6.93	0.22	165.9	4.8
	$A_SB_LC_S$	10.01	0.26	109.5	1.2
	$A_SB_LC_L$	7.98	0.07	153.1	2.4
	$A_LB_SC_S$	10.55	0.18	138.1	2.2
	$A_LB_SC_L$	8.17	0.20	221.7	6.6
	$A_LB_LC_S$	12.02	0.13	123.9	1.2
	$A_LB_LC_L$	8.78	0.24	199.7	6.9
2P	$A_SB_SC_S$	6.81	0.12	151.4	1.2
	$A_SB_SC_L$	5.54	0.30	335.5	16.7
	$A_SB_LC_S$	8.12	0.13	147.2	3.5
	$A_SB_LC_L$	6.76	0.09	356.8	34.3
	$A_LB_SC_S$	8.55	0.07	167.4	5.5
	$A_LB_SC_L$	6.52	0.12	314.5	19.7
	$A_LB_LC_S$	9.37	0.21	164.9	3.9
	$A_LB_LC_L$	7.17	0.15	317.0	15.5
3P	$A_SB_SC_S$	7.17	0.00	150.5	0.9
	$A_SB_SC_L$	6.14	0.07	241.7	10.1
	$A_SB_LC_S$	8.52	0.23	152.3	3.4
	$A_SB_LC_L$	7.29	0.09	248.5	8.1
	$A_LB_SC_S$	8.24	0.00	191.7	1.7
	$A_LB_SC_L$	6.38	0.12	318.7	15.9
	$A_LB_LC_S$	9.30	0.00	183.3	0.5
	$A_LB_LC_L$	7.55	0.07	322.5	9.8
4P	$A_SB_SC_S$	8.55	0.18	131.3	1.9
	$A_SB_SC_L$	6.40	0.17	198.1	8.3
	$A_SB_LC_S$	9.40	0.38	125.5	4.1
	$A_SB_LC_L$	7.88	0.31	198.9	1.3
	$A_LB_SC_S$	10.15	0.32	155.2	1.3
	$A_LB_SC_L$	8.10	0.15	245.6	6.1
	$A_LB_LC_S$	11.46	0.07	146.3	1.8
	$A_LB_LC_L$	8.78	0.12	224.0	10.0
5P	$A_SB_SC_S$	5.68	0.15	199.7	4.7
	$A_SB_SC_L$	5.20	0.03	570.0	36.3
	$A_SB_LC_S$	7.05	0.17	195.1	7.3
	$A_SB_LC_L$	6.26	0.26	643.9	66.2
	$A_LB_SC_S$	5.97	0.33	241.1	9.9
	$A_LB_SC_L$	4.62	0.07	512.0	37.0
	$A_LB_LC_S$	7.88	0.44	226.2	8.5
	$A_LB_LC_L$	6.40	0.54	611.2	64.9
6P	$A_SB_SC_S$	7.17	0.00	152.8	2.6
	$A_SB_SC_L$	5.95	0.12	237.1	5.6
	$A_SB_LC_S$	9.00	0.22	154.3	3.7
	$A_SB_LC_L$	7.05	0.39	235.2	9.2
	$A_LB_SC_S$	8.81	0.42	177.0	6.8
	$A_LB_SC_L$	7.00	0.34	252.7	10.8
	$A_LB_LC_S$	10.46	0.23	168.4	4.5
	$A_LB_LC_L$	7.79	0.15	255.1	2.0

1T	$A_SB_SC_S$	6.45	0.12	166.9	0.9
	$A_SB_SC_L$	5.15	0.27	481.5	31.5
	$A_SB_LC_S$	7.79	0.38	169.6	6.3
	$A_SB_LC_L$	6.45	0.20	492.1	27.3
	$A_LB_SC_S$	7.07	0.09	209.6	4.4
	$A_LB_SC_L$	5.63	0.19	463.0	31.5
	$A_LB_LC_S$	8.45	0.21	203.9	6.9
	$A_LB_LC_L$	6.59	0.44	520.0	9.2
2T	$A_SB_SC_S$	7.02	0.12	184.1	6.2
	$A_SB_SC_L$	4.94	0.27	670.4	45.6
	$A_SB_LC_S$	7.67	0.21	191.9	1.9
	$A_SB_LC_L$	6.28	0.15	775.0	33.3
	$A_LB_SC_S$	8.24	0.00	214.1	2.9
	$A_LB_SC_L$	6.28	0.18	491.3	51.5
	$A_LB_LC_S$	8.66	0.35	208.3	8.6
	$A_LB_LC_L$	7.14	0.15	534.6	27.0
1R	$A_SB_SC_S$	9.52	0.06	107.0	1.4
	$A_SB_SC_L$	8.69	0.22	136.1	1.7
	$A_SB_LC_S$	11.28	0.43	105.5	0.9
	$A_SB_LC_L$	9.63	0.13	136.1	4.4
	$A_LB_SC_S$	12.69	0.42	117.7	2.8
	$A_LB_SC_L$	9.59	0.15	146.5	5.4
	$A_LB_LC_S$	13.82	0.03	116.2	1.8
	$A_LB_LC_L$	10.76	0.23	144.1	2.5
2R	$A_SB_SC_S$	7.95	0.36	159.2	1.7
	$A_SB_SC_L$	7.64	0.24	181.0	4.4
	$A_SB_LC_S$	9.16	0.30	164.6	1.3
	$A_SB_LC_L$	8.83	0.42	187.5	3.6
	$A_LB_SC_S$	9.26	0.03	172.9	2.8
	$A_LB_SC_L$	8.64	0.15	186.2	9.3
	$A_LB_LC_S$	10.55	0.28	175.2	4.1
	$A_LB_LC_L$	9.82	0.07	201.8	1.5
1S	$A_SB_SC_S$	12.85	0.21	76.3	1.5
	$A_SB_SC_L$	9.21	0.35	140.0	1.9
	$A_SB_LC_S$	15.27	0.17	71.9	2.5
	$A_SB_LC_L$	11.00	0.30	130.6	2.5
	$A_LB_SC_S$	17.02	0.38	81.9	5.9
	$A_LB_SC_L$	12.23	0.27	132.7	6.1
	$A_LB_LC_S$	20.00	0.21	76.8	3.4
	$A_LB_LC_L$	13.61	0.16	127.2	1.8
2S	$A_SB_SC_S$	11.07	0.40	118.2	1.7
	$A_SB_SC_L$	7.40	0.18	250.7	8.5
	$A_SB_LC_S$	13.47	0.46	112.8	0.4
	$A_SB_LC_L$	9.47	0.23	261.6	7.9
	$A_LB_SC_S$	13.82	0.12	119.5	1.3
	$A_LB_SC_L$	9.40	0.23	186.4	3.7
	$A_LB_LC_S$	16.22	0.25	115.1	1.5
	$A_LB_LC_L$	10.60	0.22	189.4	3.4

1W	$A_SB_SC_S$	9.40	0.33	146.7	2.1
	$A_SB_SC_L$	9.26	0.26	157.4	2.7
	$A_SB_LC_S$	11.95	0.07	141.8	3.6
	$A_SB_LC_L$	11.88	0.12	154.3	2.4
	$A_LB_SC_S$	11.79	0.23	143.7	3.7
	$A_LB_SC_L$	11.28	0.25	159.3	4.3
	$A_LB_LC_S$	13.84	0.26	124.3	2.0
	$A_LB_LC_L$	13.66	0.33	131.2	3.8
2W	$A_SB_SC_S$	8.38	0.27	210.4	7.7
	$A_SB_SC_L$	8.33	0.22	256.1	5.7
	$A_SB_LC_S$	11.14	0.40	220.4	8.8
	$A_SB_LC_L$	10.53	0.18	273.8	7.5
	$A_LB_SC_S$	10.55	0.28	179.7	5.5
	$A_LB_SC_L$	9.66	0.21	204.4	11.8
	$A_LB_LC_S$	12.65	0.37	165.6	3.4
	$A_LB_LC_L$	11.51	0.38	179.1	7.7
3W	$A_SB_SC_S$	10.67	0.38	113.8	2.9
	$A_SB_SC_L$	9.19	0.18	137.9	1.6
	$A_SB_LC_S$	12.53	0.55	117.4	3.7
	$A_SB_LC_L$	10.97	0.29	145.8	5.8
	$A_LB_SC_S$	13.38	0.09	118.6	2.1
	$A_LB_SC_L$	12.18	0.00	129.4	0.7
	$A_LB_LC_S$	15.36	0.17	108.3	2.9
	$A_LB_LC_L$	13.77	0.20	124.9	2.1
4W	$A_SB_SC_S$	7.74	0.36	567.2	19.6
	$A_SB_SC_L$	7.36	0.07	724.6	60.7
	$A_SB_LC_S$	10.62	0.18	528.1	44.6
	$A_SB_LC_L$	10.20	0.07	663.2	78.4
	$A_LB_SC_S$	9.45	0.00	245.7	9.5
	$A_LB_SC_L$	8.62	0.07	257.0	12.3
	$A_LB_LC_S$	11.02	0.17	226.1	7.4
	$A_LB_LC_L$	10.72	0.30	240.2	10.3
1H	$A_SB_SC_S$	23.21	0.77	56.6	1.6
	$A_SB_SC_L$	21.75	2.91	59.2	3.0
	$A_SB_LC_S$	25.72	0.64	53.5	1.3
	$A_SB_LC_L$	18.28	2.99	58.2	1.4
	$A_LB_SC_S$	24.34	1.01	65.0	1.2
	$A_LB_SC_L$	27.69	1.70	68.8	1.4
	$A_LB_LC_S$	27.02	0.50	60.9	1.2
	$A_LB_LC_L$	33.33	1.40	62.8	1.2
2H	$A_SB_SC_S$	14.07	0.28	80.8	6.5
	$A_SB_SC_L$	12.37	0.03	98.1	2.0
	$A_SB_LC_S$	18.86	0.54	69.0	1.6
	$A_SB_LC_L$	15.95	0.29	87.2	3.5
	$A_LB_SC_S$	20.15	0.41	81.5	3.9
	$A_LB_SC_L$	17.54	0.79	101.6	5.0
	$A_LB_LC_S$	23.25	0.31	75.0	3.4
	$A_LB_LC_L$	17.97	0.22	116.1	15.8

5L	$A_SB_SC_S$	5.49	0.35	512.2	36.8
	$A_SB_SC_M$	4.74	0.07	986.3	176.4
	$A_SB_SC_L$	1.29	0.07	**3450.1**	N/A
	$A_SB_MC_S$	5.32	0.09	455.3	27.4
	$A_SB_MC_M$	4.57	0.20	877.6	50.7
	$A_SB_MC_L$	1.38	0.12	**5708.6**	N/A
	$A_SB_LC_S$	6.42	0.27	546.4	53.4
	$A_SB_LC_M$	5.61	0.27	1118.5	68.4
	$A_SB_LC_L$	2.71	0.42	**1901.1**	N/A
	$A_MB_SC_S$	6.16	0.06	208.0	5.9
	$A_MB_SC_M$	5.80	0.21	256.1	7.1
	$A_MB_SC_L$	5.03	0.12	586.9	70.4
	$A_MB_MC_S$	5.95	0.12	212.9	9.7
	$A_MB_MC_M$	5.87	0.12	271.7	12.6
	$A_MB_MC_L$	4.82	0.07	501.3	25.7
	$A_MB_LC_S$	6.97	0.34	195.0	6.3
	$A_MB_LC_M$	6.19	0.18	254.9	2.0
	$A_MB_LC_L$	5.90	0.14	582.1	54.3
	$A_LB_SC_S$	6.90	0.07	250.2	8.9
	$A_LB_SC_M$	6.16	0.26	283.4	10.7
	$A_LB_SC_L$	5.46	0.24	455.5	8.7
	$A_LB_MC_S$	7.17	0.38	211.5	2.8
	$A_LB_MC_M$	6.62	0.24	272.7	15.6
	$A_LB_MC_L$	5.46	0.24	409.0	30.6
	$A_LB_LC_S$	7.64	0.39	219.6	4.8
	$A_LB_LC_M$	7.07	0.18	278.2	12.7
	$A_LB_LC_L$	6.28	0.17	459.4	32.6
2P	$A_SB_SC_S$	5.49	0.12	197.6	4.9
	$A_SB_SC_M$	5.18	0.35	298.0	12.9
	$A_SB_SC_L$	3.37	0.22	931.3	100.6
	$A_SB_MC_S$	5.97	0.17	192.1	4.0
	$A_SB_MC_M$	5.47	0.12	310.4	7.8
	$A_SB_MC_L$	3.34	0.31	1117.6	118.7
	$A_SB_LC_S$	7.43	0.09	205.2	2.7
	$A_SB_LC_M$	6.66	0.23	351.0	14.6
	$A_SB_LC_L$	4.12	0.24	**1626.2**	N/A
	$A_MB_SC_S$	6.81	0.12	151.4	1.2
	$A_MB_SC_M$	6.78	0.24	190.0	2.4
	$A_MB_SC_L$	5.54	0.30	335.5	16.7
	$A_MB_MC_S$	7.79	0.24	147.0	0.4
	$A_MB_MC_M$	6.66	0.20	196.4	5.2
	$A_MB_MC_L$	5.80	0.16	348.0	28.5
	$A_MB_LC_S$	8.12	0.13	147.2	3.5
	$A_MB_LC_M$	7.43	0.13	188.3	6.3
	$A_MB_LC_L$	6.76	0.09	356.8	34.3
	$A_LB_SC_S$	8.55	0.07	167.4	5.5
	$A_LB_SC_M$	7.52	0.30	218.5	13.0
	$A_LB_SC_L$	6.52	0.12	314.5	19.7
	$A_LB_MC_S$	8.69	0.18	173.3	6.1
	$A_LB_MC_M$	8.05	0.26	217.1	13.2
	$A_LB_MC_L$	6.86	0.14	336.6	40.0
	$A_LB_LC_S$	9.37	0.21	164.9	3.9
	$A_LB_LC_M$	8.83	0.30	214.2	4.2
	$A_LB_LC_L$	7.17	0.15	317.0	15.5

Appendix C: Normalized Ratios for Channel Draw Test

Table C.1: Ratios of tooling radii/thickness, tool gap/thickness and Drawbead Force/Plane Strain Yield Strength

Material		Gauge (mm)	Ratios										
			A						B		C		
			Punch radius/thickness			Die radius/thickness			Clearance/thickness		Bead force/plane strain F_y		
Code	Steel		A_L Large (10.1mm)	A_M Middle (6.3mm)	A_S Small (3.3mm)	A_L Large (10.0mm)	A_M Middle (6.5mm)	A_S Small (3.0mm)	B_L t+0.002"	B_S t+0.5t	C_L High	C_M Middle	C_S Low
Baseline													
X1	DQSK	0.77	13.1	8.2		13.0	8.4		1.07	1.50	0.84		0.38
X2	DQSK	1.19	8.5	5.3		8.4	5.5		1.04	1.50	0.89		0.44
Y1	DDQ+	0.70	14.5	9.1		14.4	9.4		1.07	1.50	0.77		0.40
Y2	DDQ+	1.19	8.5	5.3		8.4	5.4		1.04	1.50	1.15		0.54
Skin Panels													
B1	BH210	0.70	14.5		4.7	14.4		4.3	1.07	1.50	0.50		0.23
B2	BH210	0.93	10.8		3.5	10.7		3.2	1.05	1.50	0.62		0.27
C1	BH280	0.71	14.2		4.6	14.1		4.2	1.07	1.50	0.46		0.23
C2	BH280	1.00	10.1		3.3	10.0		3.0	1.05	1.50	0.63		0.29
C3	BH280	1.04	9.7		3.2	9.6		2.9	1.05	1.50	0.68		0.30
D1	ULC BH340	0.74	13.6		4.4	13.5		4.0	1.07	1.50	0.54		0.25
D2	ULC BH340	1.02	9.9		3.2	9.8		2.9	1.05	1.50	0.83		0.36
E1	IF340	0.63	16.0		5.2	15.9		4.8	1.08	1.50	0.58		0.33
E2	IF340	0.89	11.3		3.7	11.2		3.4	1.06	1.50	0.83		0.35
G1	DP500	0.66	15.4		5.0	15.2		4.6	1.08	1.50	0.56		0.22
G2	DP500	0.81	12.4		4.1	12.3		3.7	1.06	1.50	0.65		0.26
Structural													
1K	BH300	1.24	8.1	5.1		8.1	5.2		1.04	1.50	0.76		0.31
2K	BH300	1.19	8.5	5.3		8.4	5.5		1.04	1.50	0.69		0.30
1L	HSLA340	1.16	8.7	5.4		8.6	5.6		1.04	1.50	0.53		0.25
5L	HSLA340	1.21	8.3	5.2	2.7	8.2	5.4	2.5	1.04	1.50	0.51	0.34	0.23
2L	HSLA340	1.62	6.2	3.9		6.2	4.0		1.03	1.50	0.93		0.44
1M	HS440W	1.24	8.2	5.1		8.1	5.2		1.04	1.50	0.77		0.33
2M	HS440W	1.58	6.4	4.0		6.3	4.1		1.03	1.50	0.52		0.39
1P	DP600	0.96	10.6	6.6		10.5	6.8		1.05	1.50	0.73		0.29
2P	DP600	1.19	8.5	5.3	2.8	8.4	5.5	2.5	1.04	1.50	0.85	0.56	0.37
3P	DP600	1.39	7.3	4.5		7.2	4.7		1.04	1.50	0.82		0.39
4P	DP600	1.23	8.2	5.1		8.1	5.3		1.04	1.50	0.73		0.31
5P	DP600	1.64	6.1	3.8		6.1	4.0		1.03	1.50	0.98		0.42
6P	DP600	1.49	6.8	4.2		6.7	4.4		1.03	1.50	0.75		0.35
1T	TRIP600	1.40	7.2	4.5		7.1	4.6		1.04	1.50	0.83		0.38
2T	TRIP600	1.60	6.3	3.9		6.3	4.1		1.03	1.50	0.90		0.40
1R	DP800	1.20	8.4	5.2		8.3	5.4		1.04	1.50	0.62		0.32
2R	DP800	1.59	6.4	4.0		6.3	4.1		1.03	1.50	0.57		0.40
1S	DP980	1.15	8.8	5.5		8.7	5.7		1.04	1.50	0.47		0.20
2S	DP980	1.52	6.6	4.1		6.6	4.3		1.03	1.50	0.55		0.24
1W	RA850	1.32	7.6	4.8		7.6	4.9		1.04	1.50	0.38		0.29
2W	RA830	1.53	6.6	4.1		6.5	4.2		1.03	1.50	0.34		0.27
3W	RA830	1.25	8.1	5.0		8.0	5.2		1.04	1.50	0.37		0.25
4W	RA830	1.80	5.6	3.5		5.6	3.6		1.03	1.50	0.39		0.31
1H	M190	1.03	9.8	6.1		9.7	6.3		1.05	1.50	0.29		0.18
2H	M190	1.58	6.4	4.0		6.3	4.1		1.03	1.50	0.24		0.04

Appendix D: The Scree Plot Analysis

The effect of a factor (a process variable or an interaction) on springback, in the current study, is defined by the change of springback produced by different settings of this factor. For instance, the effect of tooling radii (factor A) on springback is defined by the difference of springback with two different tool sets used in test. Given the range of strength and thickness of sample materials studied, the effect varies considerably from lot to lot. To compare them in a scree plot, the effects are normalized by converting the effect to a percentage of the maximum effect found for the material. The sign of the effect is ignored. As all normalized effects vary from 0 to 100%, they can be compared in a single scree plot.

As an illustration of this technique, the springback and curl for 0.96mm GI DP600 steel are listed in Table D. 1. There are eight results for the springback and curl, respectively, for all the designed experimental conditions. The effect of tooling radii (factor A) on the springback (or curl) is obtained from the average of all differences of four comparisons, namely, $A_SB_SC_S$ with $A_LB_SC_S$, $A_SB_SC_L$ with $A_LB_SC_L$, $A_SB_LC_S$ with $A_LB_LC_S$, and $A_SB_LC_L$ with $A_LB_LC_L$. It is clearly seen that, in each comparison, the difference of springback (or curl) only represents the effect of change of tooling radii (factor A) as the tool gap and drawbead penetration (factor B and C) remain the same. From Table D. 1, the differences of springback for four comparisons are 2.24, 1.24, 2.01 and 0.80, respectively, and the effect of factor A on springback is 1.57. The effects of other factors on springback (or curl) can be calculated similarly (Table D.1).

Table D. 1: Test results for 0.96mm GI DP600 steel (1P)

Testing Conditions	Ave. Springback (Degree)	Std. Dev. Springback (Degree)	Ave. Radius of Curl (mm)	Std. Dev. Radius of Curl (mm)
$A_SB_SC_S$	8.31	0.12	115.5	1.8
$A_SB_SC_L$	6.93	0.22	165.9	4.8
$A_SB_LC_S$	10.01	0.26	109.5	1.2
$A_SB_LC_L$	7.98	0.07	153.1	2.4
$A_LB_SC_S$	10.55	0.18	138.1	2.2
$A_LB_SC_L$	8.17	0.20	221.7	6.6
$A_LB_LC_S$	12.02	0.13	123.9	1.2
$A_LB_LC_L$	8.78	0.24	199.7	6.9

Once the effects of all factors are determined, they are normalized with the maximum effect. In this case, the drawbead penetration (factor C) has the maximum effect on both the springback and curl. The normalized results are listed in Table D. 2.

Table D. 2: Normalized effects for 0.96mm GI DP600 (1P)

Factor	Springback		Radius of Curl	
	Ave. Effect (Degree)	Norm. Effect (%)	Ave. Effect (mm)	Norm. Effect (%)
A (tool radii)	1.57	70	33.3	51
B (tool gap)	1.21	54	-12.2	19
C (drawbead penetration)	-2.26	100	64.9	100
AB	-0.17	7	-5.9	9
AC	-0.55	24	14.8	23
BC	-0.38	17	-2.1	3
ABC	-0.05	2	-1.8	3

The scree plots of all materials tested in the program are shown in Figure D. 1 to D.10. The meaning of the different factors used in the plots can be found in Table 8.2.

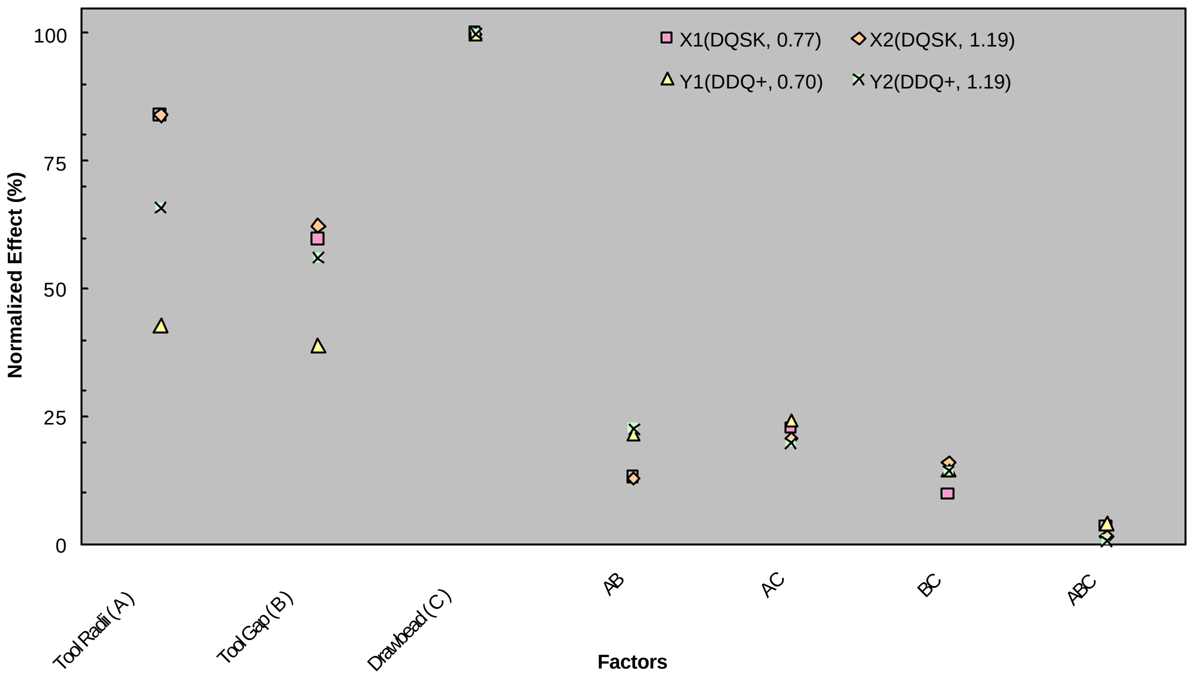

Figure D.1: The scree plot of effects of factors on springback (Baseline steel)

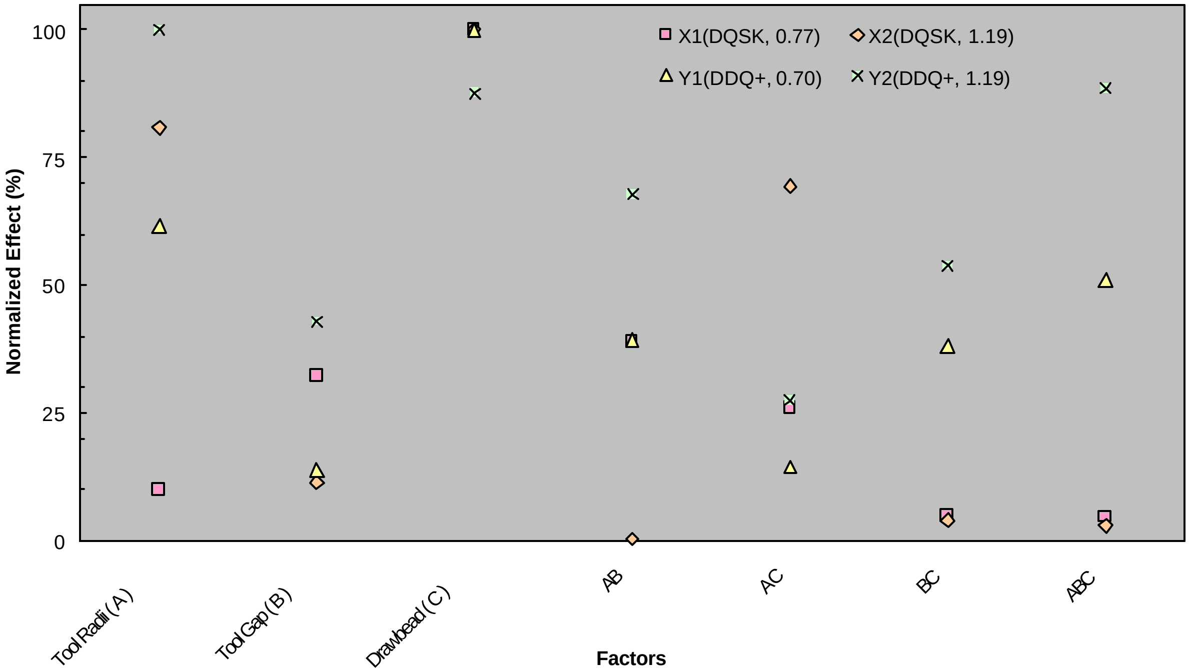

Figure D.2: The scree plot of effects of factors on sidewall curl (Baseline steel)

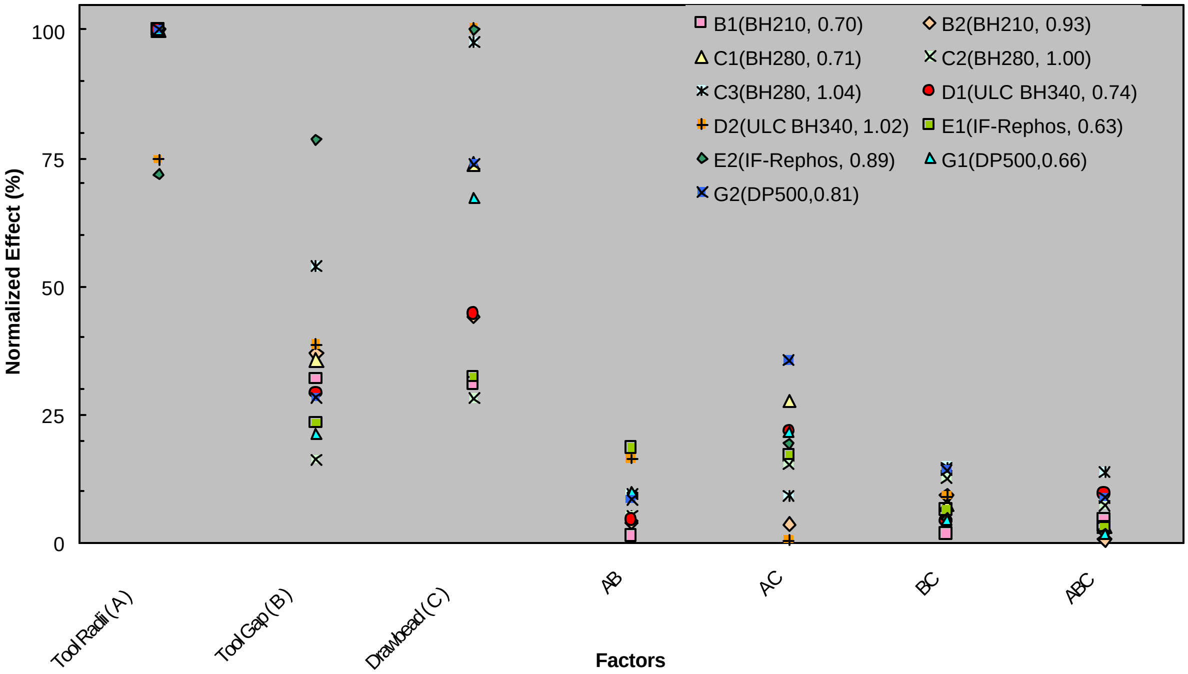

Figure D.3: The scree plot of effects of factors on springback (Skin panel steel)

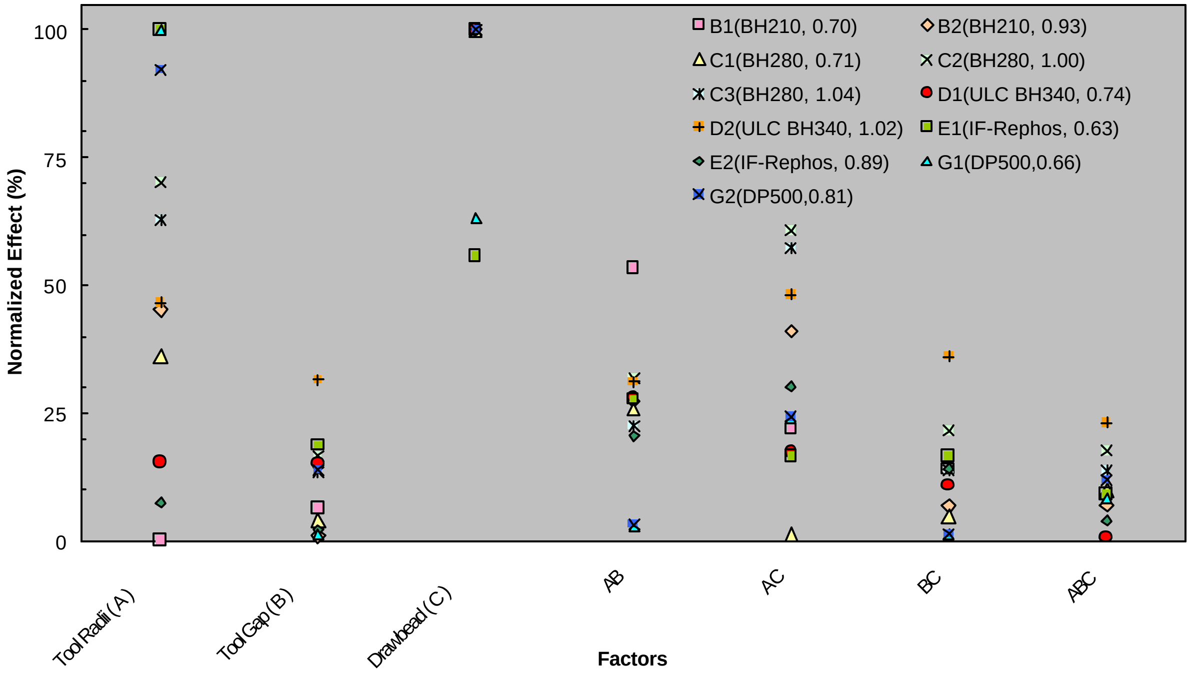

Figure D.4: The scree plot of effects of factors on sidewall curl (Skin panel steel)

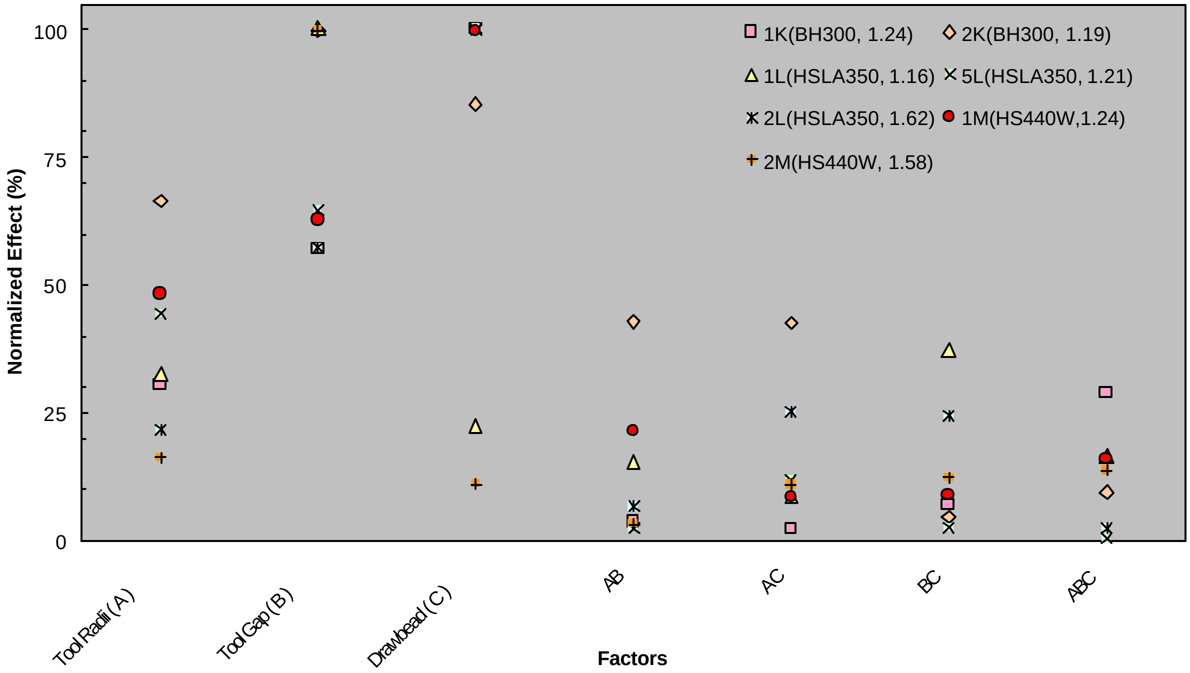

Figure D.5: The scree plot of effects of factors on springback (Structural HSS)

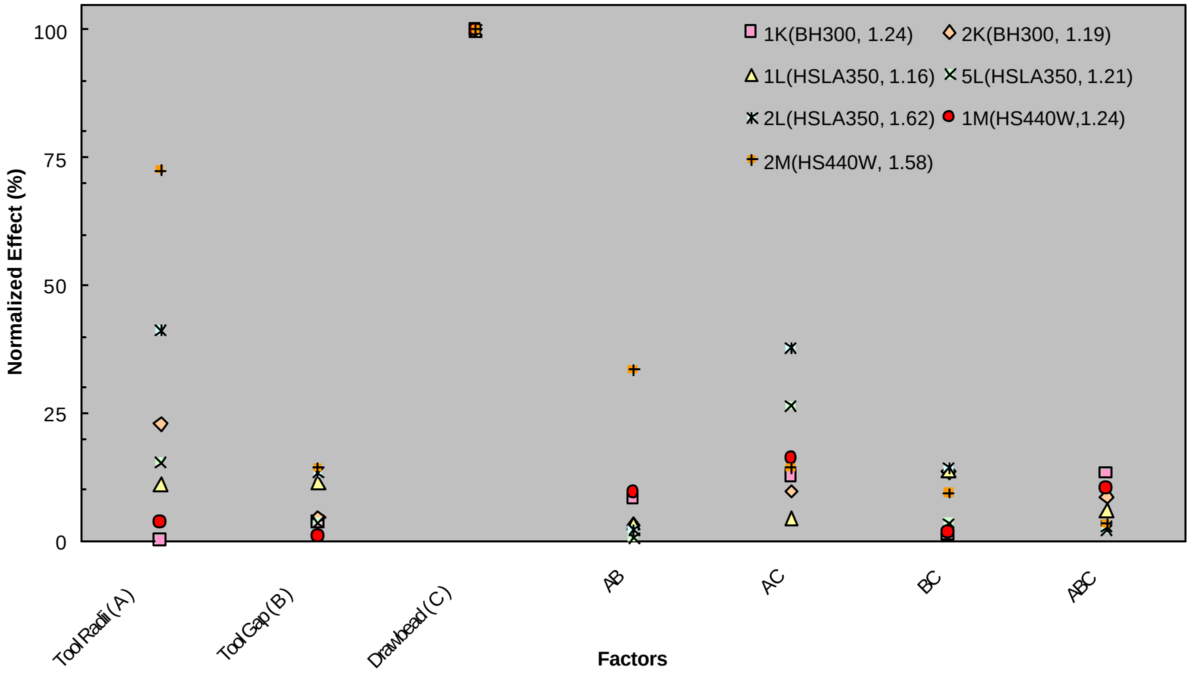

Figure D.6: The scree plot of effects of factors on sidewall curl (Structural HSS)

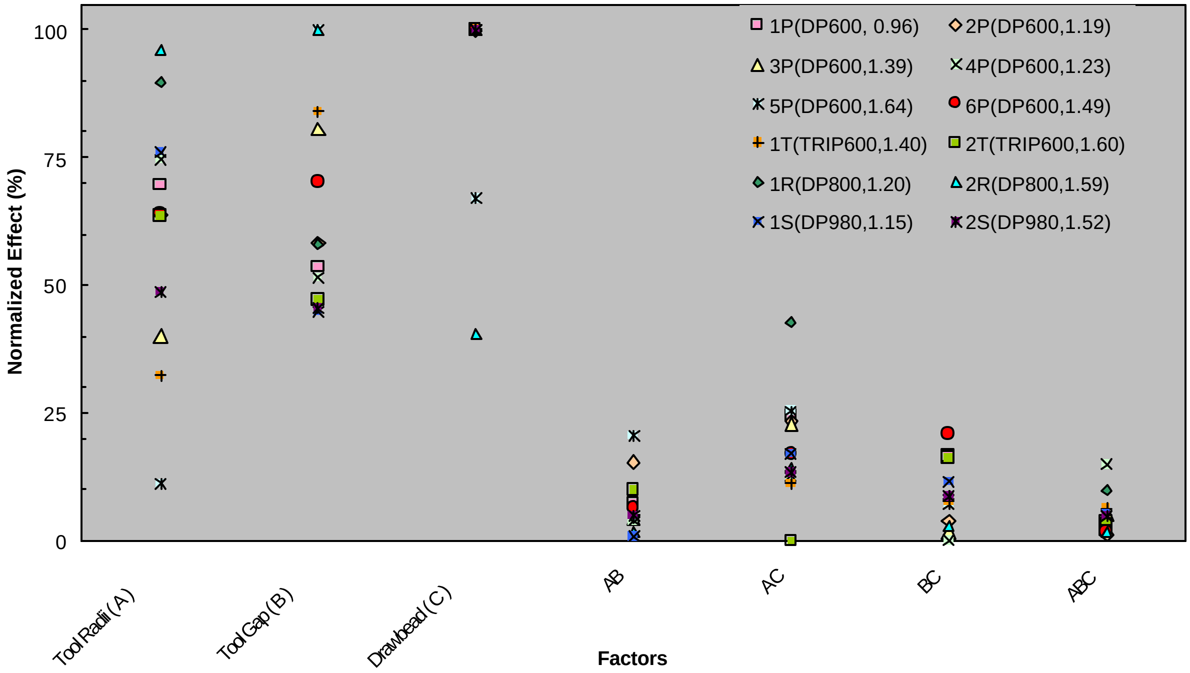

Figure D.7: The scree plot of effects of factors on springback (Structural AHSS)

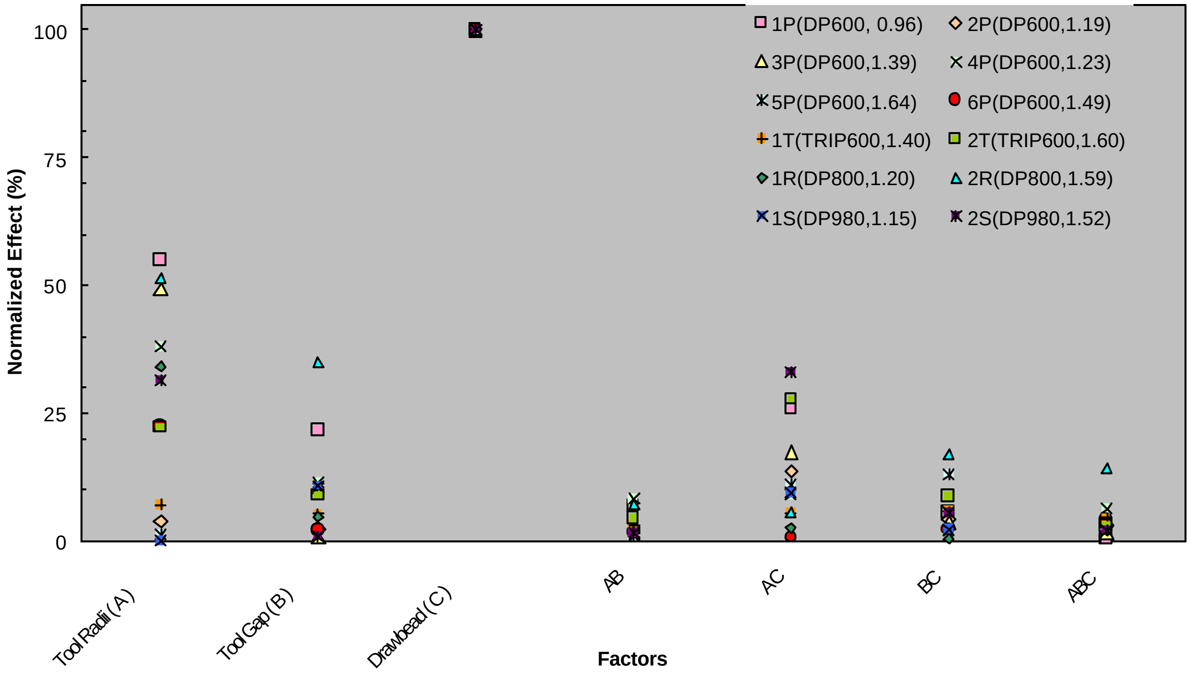

Figure D.8: The scree plot of effects of factors on sidewall curl (Structural AHSS)

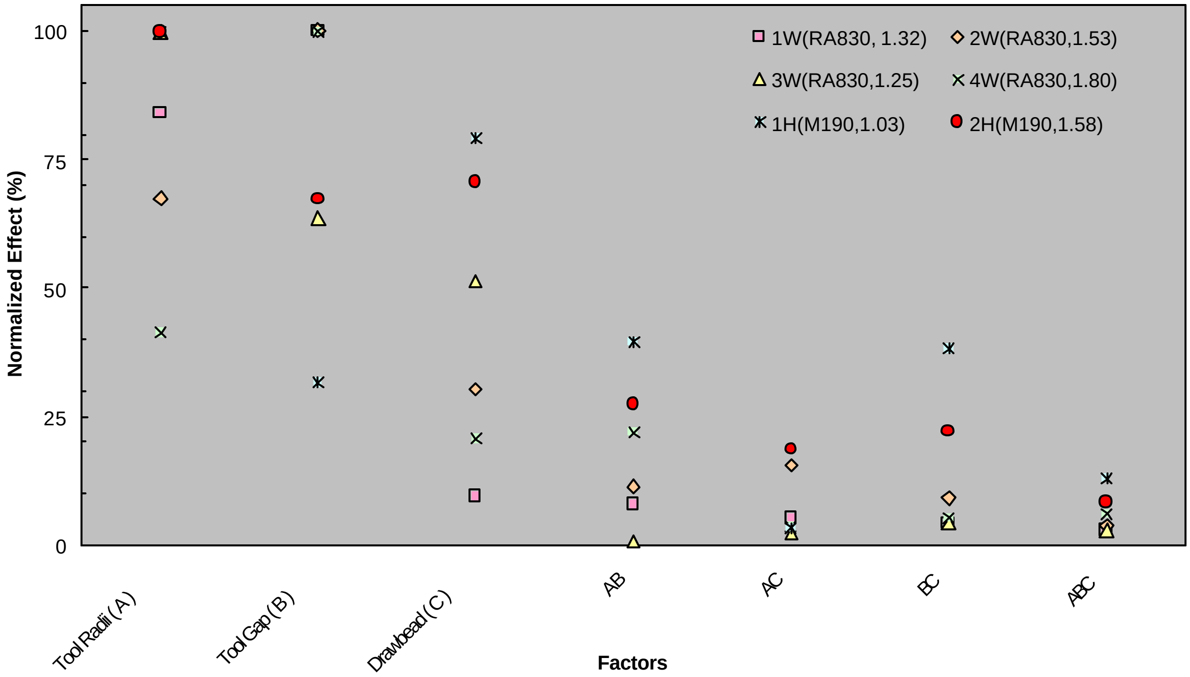

Figure D.9: The scree plot of effects of factors on springback (Structural UHSS)

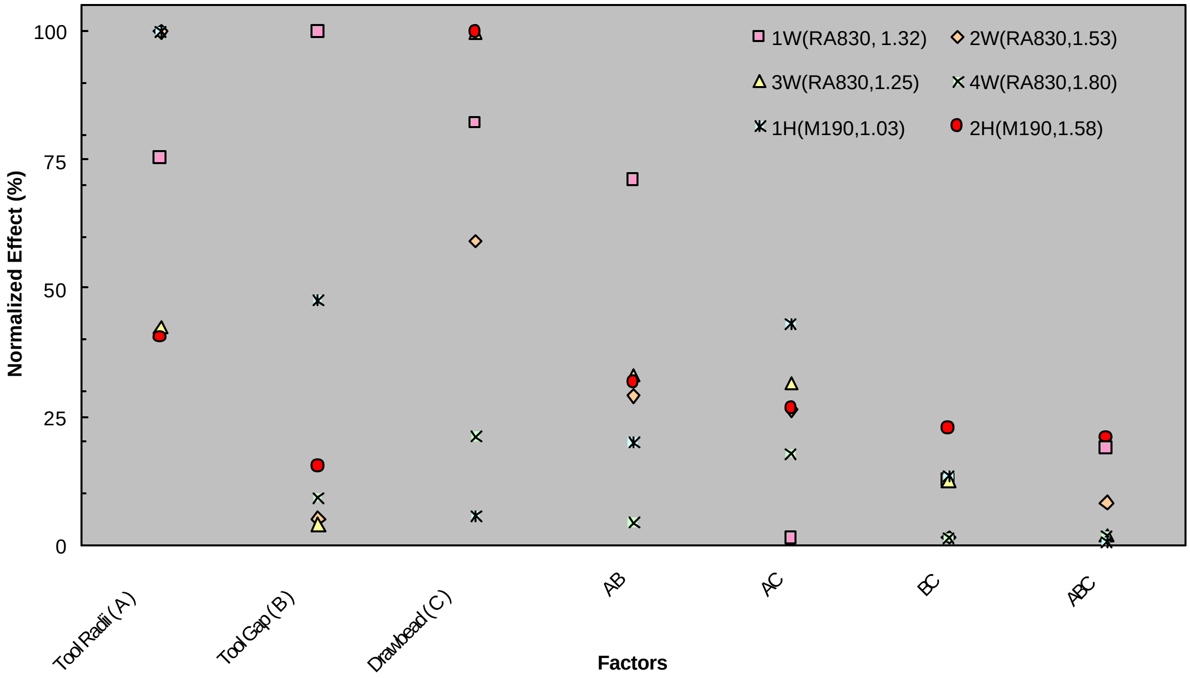

Figure D.10: The scree plot of effects of factors on sidewall curl (Structural UHSS)

Appendix E: Springback and Curl Analysis for Two Steel Groups

The effect of three factors on the springback and curl of two steel groups are plotted in the Figure E.1 to E.12. The conclusions resulted from the analysis can be found in section 8.7.2.

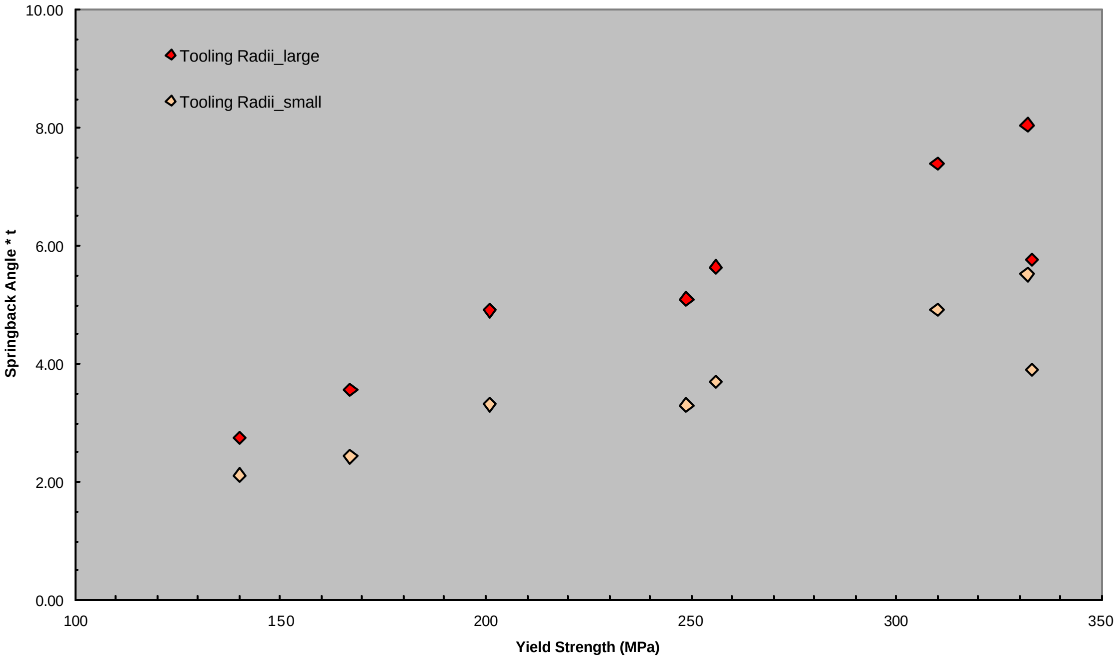

Figure E.1: The effect of tooling radii on springback (0.70mm group)

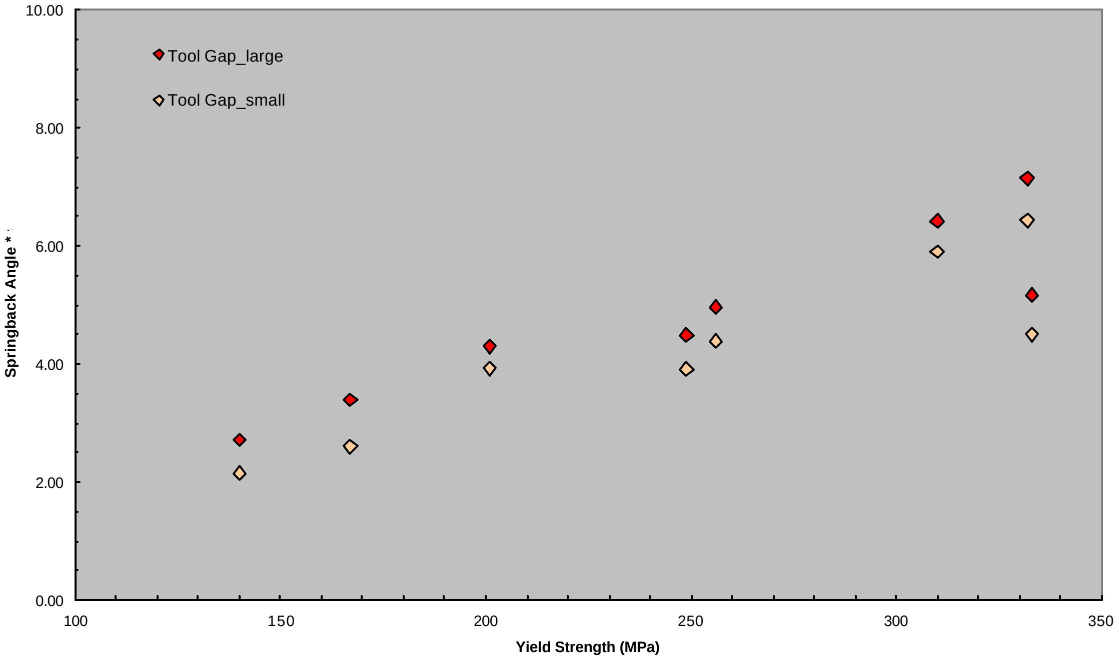

Figure E.2: The effect of tool gap on springback (0.70mm group)

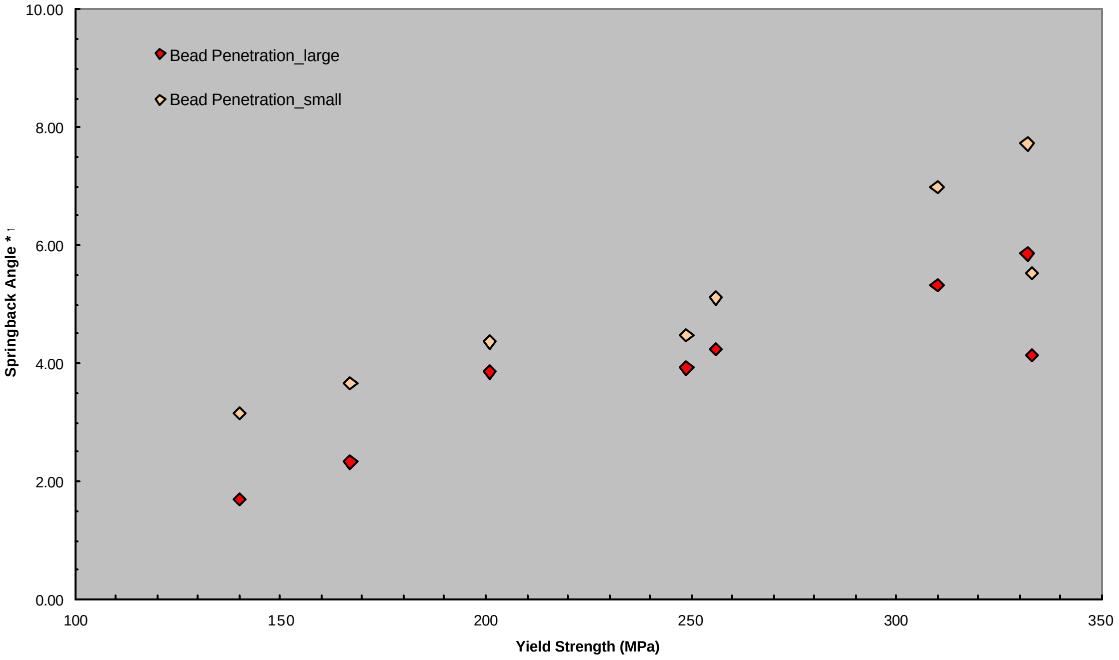

Figure E.3: The effect of drawbead restraining force on springback (0.70mm group)

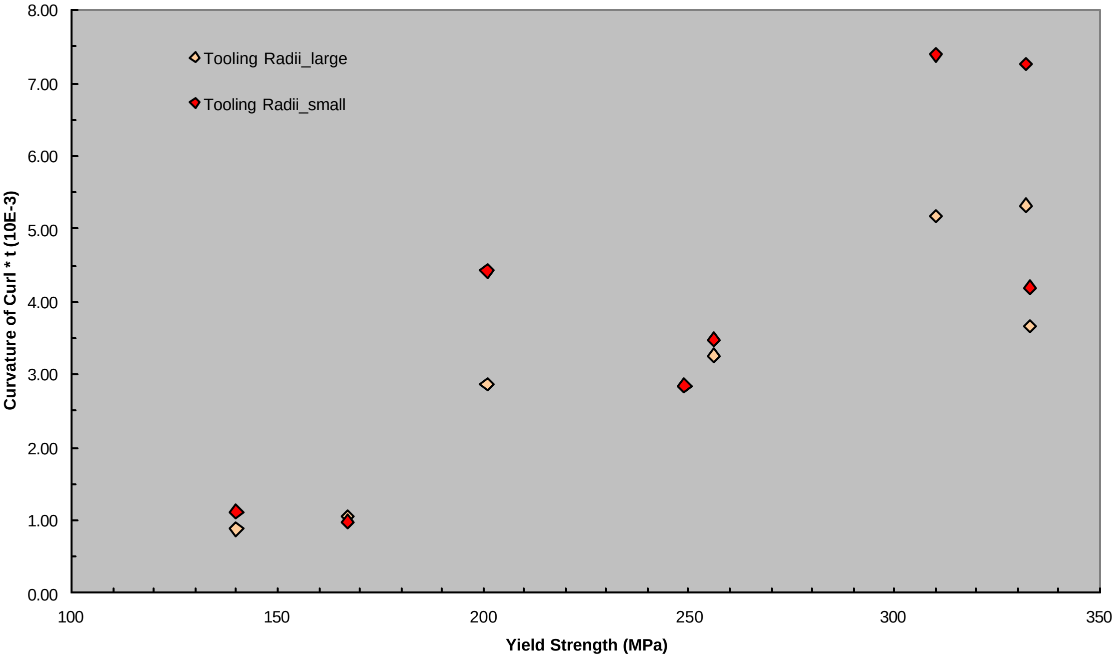

Figure E.4: The effect of tooling radii on sidewall curl (0.70mm group)

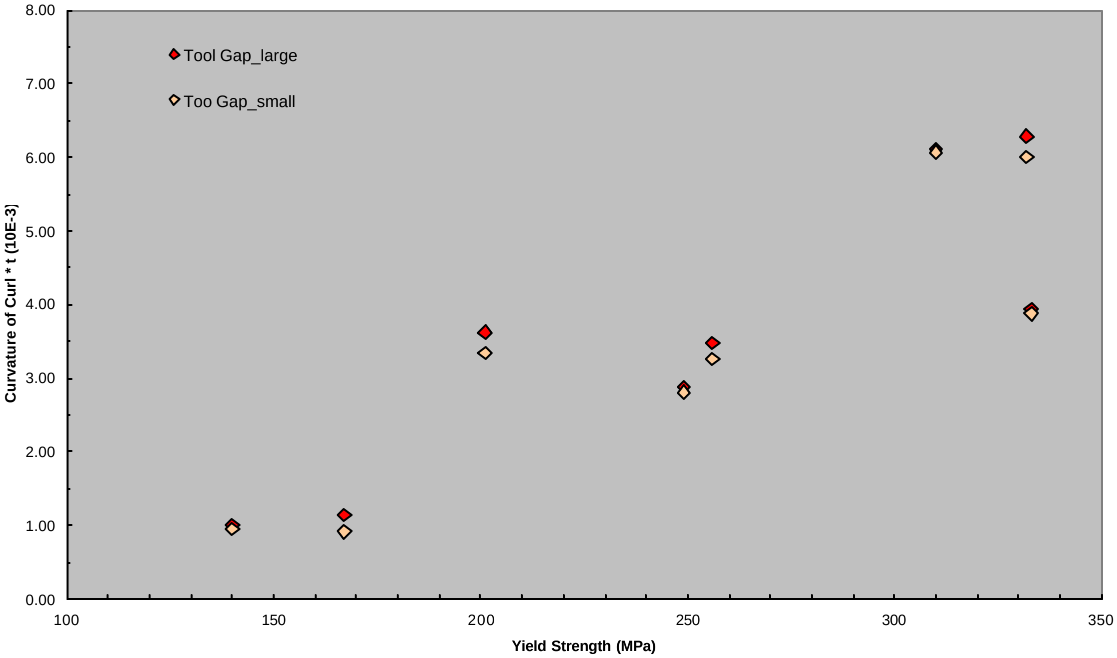

Figure E.5: The effect of tool gap on sidewall curl (0.70mm group)

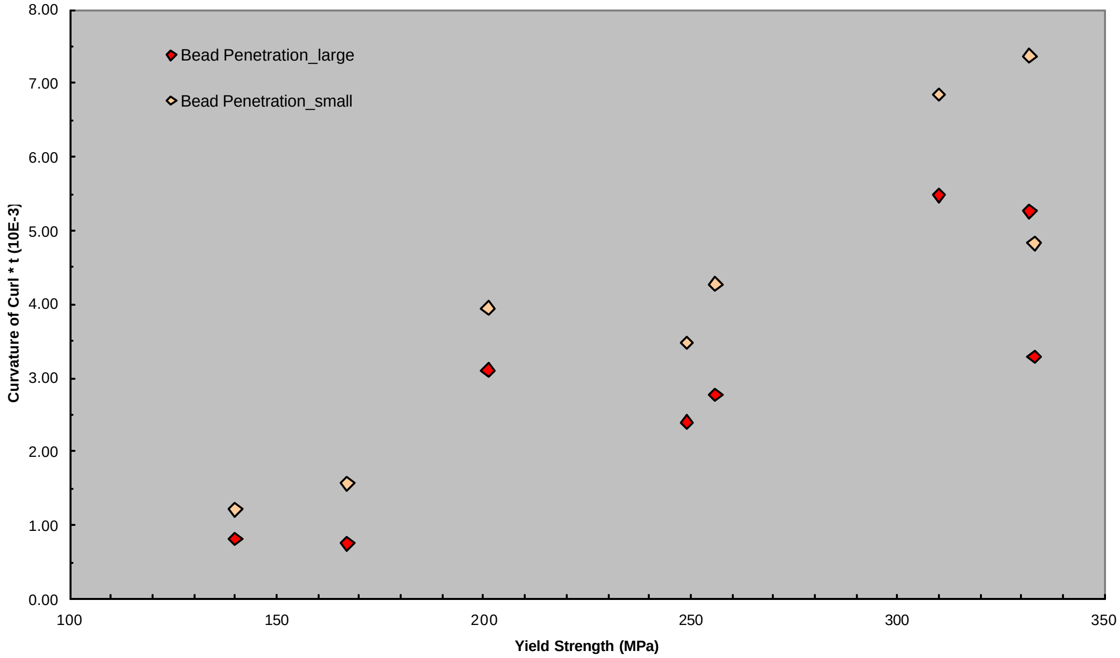

Figure E.6: The effect of drawbead restraining force on sidewall curl (0.70mm group)

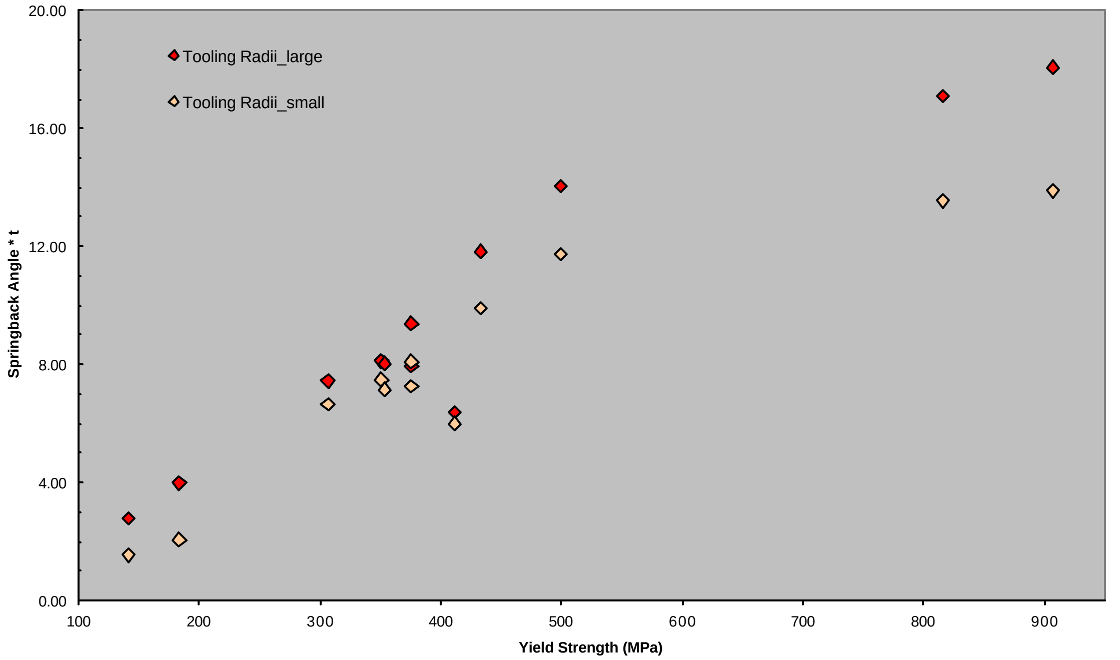

Figure E.7: The effect of tooling radii on springback (1.20mm group)

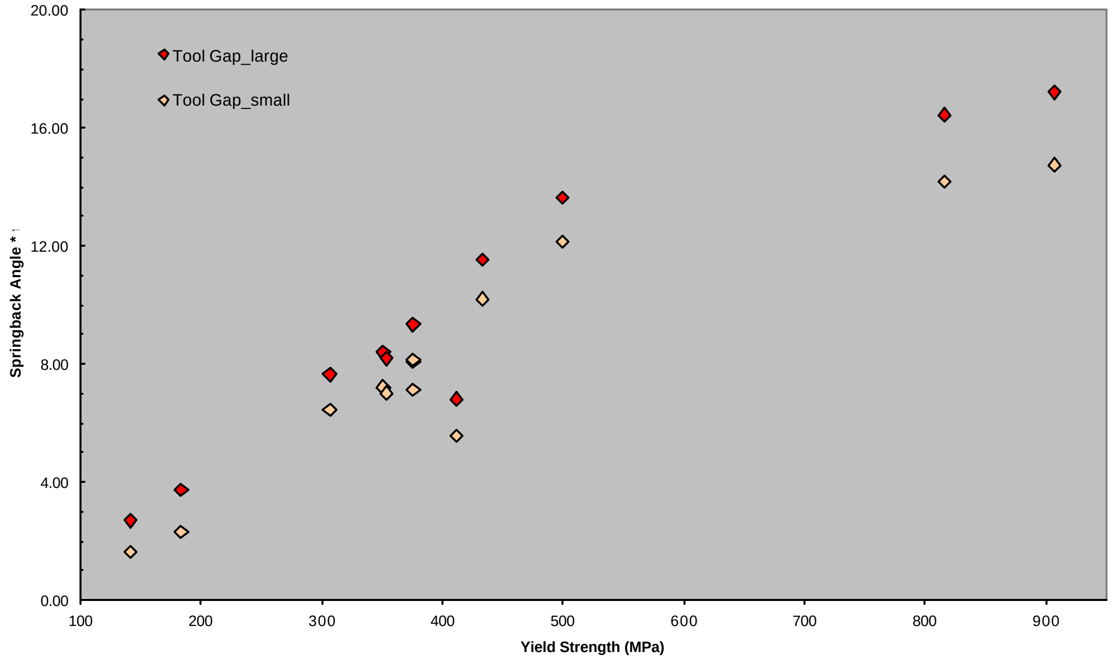

Figure E.8: The effect of tool gap on springback (1.20mm group)

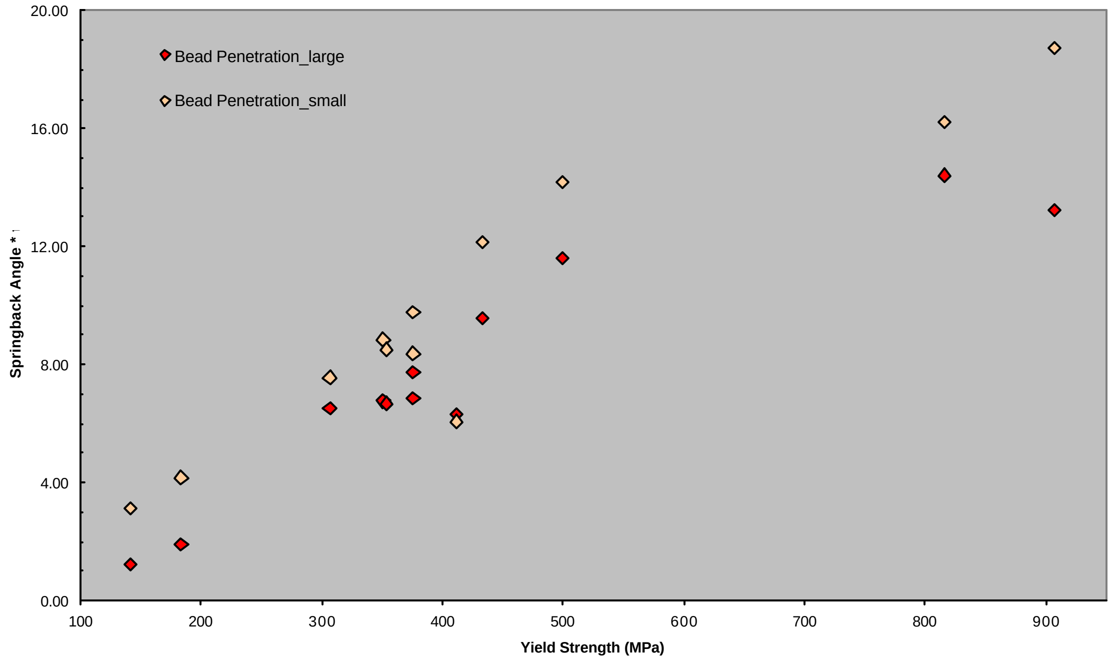

Figure E.9: The effect of drawbead restraining force on springback (1.20mm group)

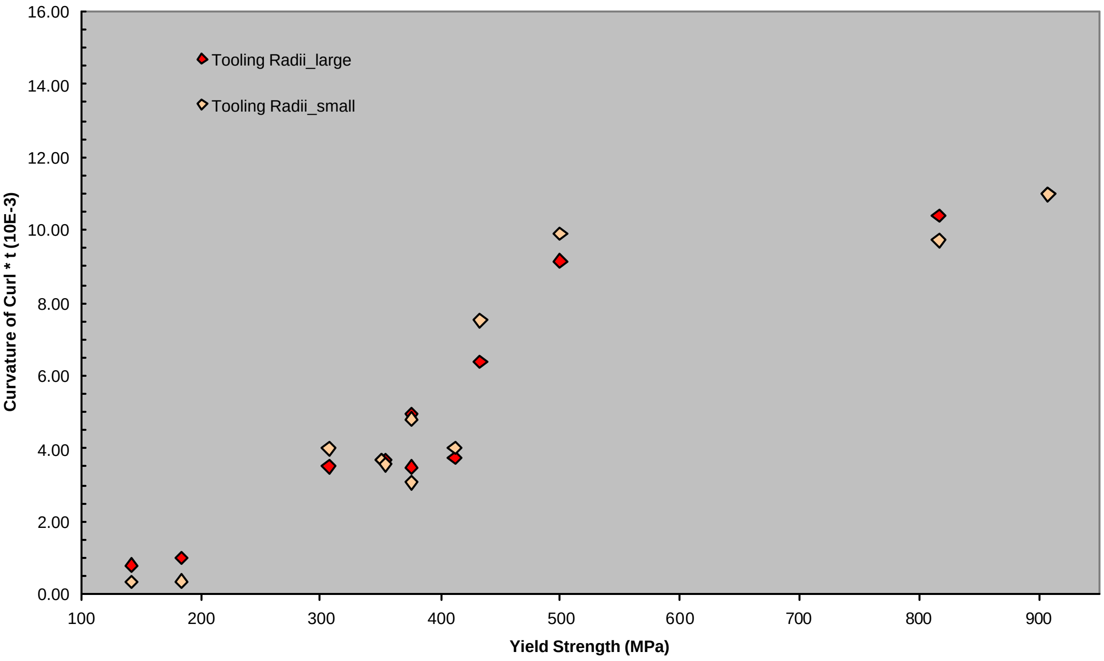

Figure E.10: The effect of tooling radii on sidewall curl (1.20mm group)

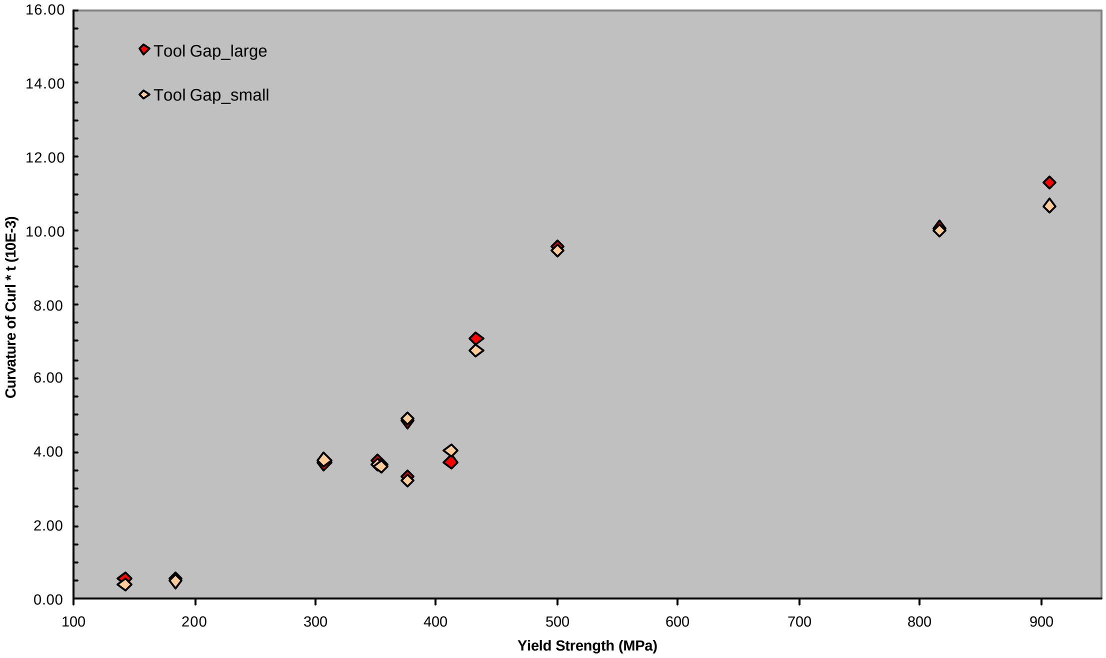

Figure E.11: The effect of tool gap on sidewall curl (1.20mm group)

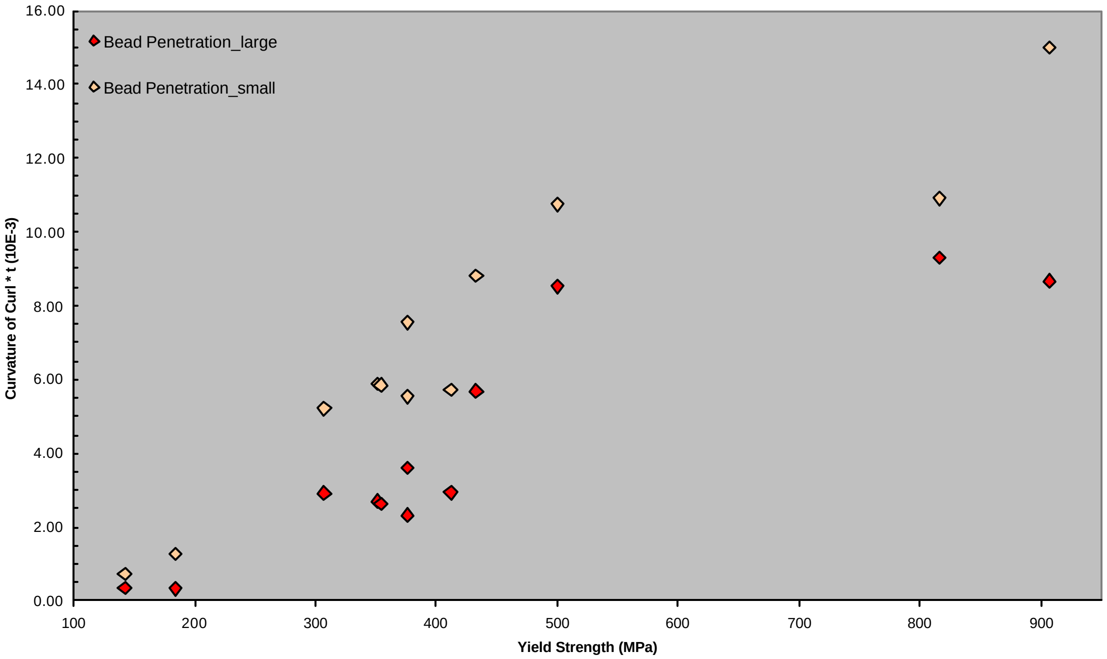

Figure E.12: The effect of drawbead restraining force on sidewall curl (1.20mm group)

Appendix F: Data for Square Draw Test

Table F.1: Failure heights for Square Draw test. The italicized entries are cups without splitting

Lot Code	Blank Size (mm)	Punch Height (mm)	
		Avg. (mm)	Std. Dev. (mm)
X1	*190.5*	*49.88*	*0.01*
	203.2	35.54	0.02
	228.6	28.00	0.00
X2			
	203.2	*49.48*	*0.00*
	228.6	33.09	0.01
	279.4	25.40	0.00
Y1	190.5	30.04	0.06
	203.2	26.15	0.01
	228.6	21.44	0.02
Y2			
	203.2	*49.51*	*0.01*
	228.6	37.32	0.00
	279.4	29.27	0.01
B1	190.5	26.55	0.32
	203.2	22.97	0.02
	228.6	16.77	0.49
B2	*190.5*	*49.86*	*0.01*
	203.2	*49.74*	*0.02*
	228.6	27.79	0.01
C1	190.5	22.53	0.01
	203.2	20.72	0.02
	228.6	15.92	0.14
C2	*190.5*	*49.86*	*0.00*
	203.2	*49.71*	*0.02*
	228.6	24.72	0.01
C3	190.5	27.56	0.02
	203.2	24.74	0.00

	228.6	**21.94**	**0.00**
D1	**190.5**	**23.42**	**0.28**
	203.2	**20.67**	**0.01**
	228.6	**16.90**	**0.01**
D2	*190.5*	*49.87*	*0.01*
	203.2	**31.09**	**0.01**
	228.6	**25.64**	**0.14**
E1	**190.5**	**27.08**	**0.58**
	203.2	**23.23**	**0.00**
	228.6	**19.44**	**0.02**
E2	*190.5*	*49.92*	*0.01*
	203.2	*49.77*	*0.01*
	228.6	**26.18**	**0.12**
G1	**190.5**	**25.38**	**0.01**
	203.2	**21.35**	**0.03**
	228.6	**16.35**	**0.03**
G2	*190.5*	*49.52*	*0.01*
	203.2	**38.23**	**0.01**
	228.6	**23.75**	**0.03**
1K			
	203.2	**26.69**	**0.02**
	228.6	**21.85**	**0.02**
	279.4	**17.59**	**0.02**
2K			
	203.2	*49.48*	*0.01*
	228.6	**41.63**	**0.02**
	279.4	**25.13**	**0.03**
1L			
	203.2	*49.33*	*0.00*
	228.6	**26.80**	**0.02**
	279.4	**19.47**	**0.01**
5L			
	203.2	*49.22*	*0.01*

	228.6	27.61	0.02
	279.4	19.97	0.00
1M			
	203.2	27.01	0.01
	228.6	22.65	0.00
	279.4	18.82	0.01
1P			
	203.2	*48.98*	*0.00*
	228.6	24.05	0.01
	279.4	18.85	0.01
2P			
	203.2	38.84	0.00
	228.6	24.87	0.02
	279.4	20.35	0.02
3P			
	203.2	46.70	0.01
	228.6	22.02	0.01
	279.4	18.67	0.02
4P			
	203.2	48.83	0.02
	228.6	25.46	0.02
	279.4	18.62	0.01
1T			
	203.2	*49.02*	*0.00*
	228.6	33.97	0.01
	279.4	23.22	0.02
1R			
	203.2	34.76	0.02
	228.6	19.38	0.02
	279.4	16.26	NA
1S			
	203.2	*48.44*	*0.01*
	228.6	20.41	0.00
	279.4	13.76	0.02
1W			
	203.2	45.01	0.01
	228.6	14.20	0.03
	279.4	7.42	0.04

3W			
	203.2	*48.59*	*0.02*
	228.6	**15.51**	**0.03**
	279.4	**7.24**	**0.00**

1H			
	203.2	*48.21*	*0.13*
	228.6	**15.10**	**0.05**
	279.4	**9.47**	**0.11**